Université de Liège
Faculté des Sciences

Study of the Cape Ghir upwelling filament using variational data analysis and regional numerical model

Charles Troupin
Department of Astrophysics, Geophysics and Oceanography
GeoHydrodynamics and Environment Research laboratory

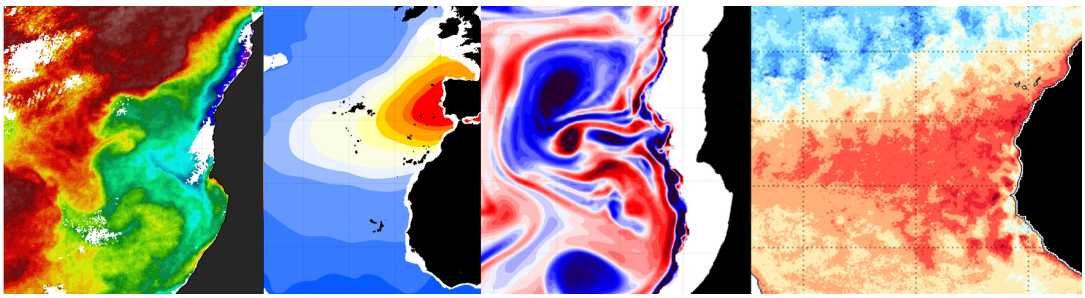

Thesis submitted for the degree of
Docteur en Sciences

August 2011

Université de Liège
Faculté des Sciences

Study of the Cape Ghir upwelling filament using variational data analysis and regional numerical model

Charles Troupin
Department of Astrophysics, Geophysics and Oceanography
GeoHydrodynamics and Environment Research laboratory

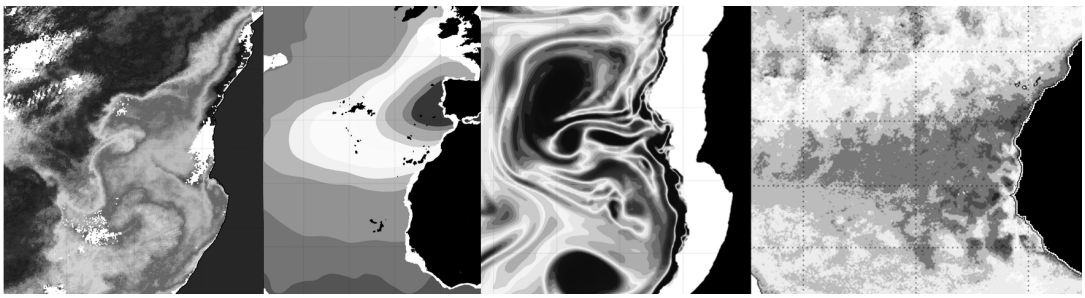

Thesis submitted for the degree of
Docteur en Sciences

August 2011

Acknowledgments

A doctoral thesis is like a long journey. And like in any journey, there are many road companions, who all contributed to this thesis. These lines are for them.

Jean-Marie Beckers guided me into the fascinating world of ocean modeling, always with a perfect blend of freedom in my choices and advices on the directions to follow. I appreciated his trust when he involved me in SeaDataNet European project since the beginning of my thesis.

During my stays at the *Facultad de Ciencias del Mar*, University of Las Palmas de Gran Canaria (ULPGC), I learned a lot about physical oceanography thanks to Pablo Sangrà. He always made his best to facilitate my stays there, and I enjoyed to confront our point of views about the filament dynamics. I am really grateful for his invitation to participate to the CAIBEX cruise in summer 2009, my first real contact with the ocean.

My colleagues at the GHER: Aida, Jaya, Ngu, Mahdia, Marie-Eve, Alexander, Arthur, Damien, Dieudonné, Fabian, Luc, Mohamed, with a special mention to Nadine and Charlotte for solving all our non-scientific problems. They were always available for discussion, ranging from cloud classifications to Italian coffee, and of course, a little bit of oceanography.

In Las Palmas de Gran Canaria I had the opportunity to work with Evan Mason, who taught me how to use ROMS model (and lots of other things) and Francisco Machín, who always explained with simple words, the complex regional oceanography of the region. Also many thanks to the other colleagues there: Isis, Laura, Mar, Mónica, Borja, Gheorghe, Marc, Timothée, ...and to the friends I had there: Ana, Berta, Amanda, Iñaki, Mikel, Pablo, and *mi novia* Davinia.

The success of the CAIBEX cruise on board *Sarmiento de Gamboa* was made possible by the efficiency and professionalism of the ship crew and the cruise Chief Scientist, Javier Arístegui (ULPGC). With them I could understand the real value of *in situ* measurements, and also the pleasure to eat with force 7 at sea...

A few words to my colleagues and friends of the *B5a-Tuesday-noon* running team, as well as to Hubert and the *Super-Gym* members.

My parents and family supported me in all the possible ways, including (too) numerous trips to the airport.

Abstract

Aim Upwelling filaments are shallow, elongated structures of cool waters often visible in the regions of coastal upwelling. The present thesis aims to improve our knowledge on the mechanisms responsible for the generation of filaments.

Location the study is centered on the Canary Current Upwelling system, located off northwest Africa, in particular around Cape Ghir (30°38'N, 9°53'W), where these filaments are frequently observed.

Methods

- We compiled historical in situ data to build a high-resolution climatology of temperature and salinity in the region of interest using the Data Interpolating Variational Analysis (Diva) method.
- We ran the experiments with the numerical model ROMS to investigate the processes responsible for the filament generation.
- We collected in situ measurements during a cruise in August-September 2009, in the frame of the CAIBEX project, in the filament area and analyzed them to get a detailed description of the Cape Ghir filament, its variability and its biogeochemical characteristics.
- We computed anomalies of several variables with respect to a long-term mean to examine the time-evolution of the Canary Current Upwelling system.

Results The climatology showed improvements with respect to existing products, especially in the coastal area, and was a valuable asset to provide initial and boundary conditions for the numerical model. The results of the simulations underlined the role of the wind in the filament generation and confirmed our assumption of a mechanism based on the potential vorticity balance. Preliminary analysis of the cruise data allowed us to characterize the filament physical and biological properties, in particular we observed the signal of a subsurface (at a depth of 300 m) anticyclonic eddy on the northern flank of the filament, also present in the numerical model outputs. Anomalies for the year 2010 revealed a widespread warming over the tropical and subtropical Atlantic Ocean and a diminution of the upwelling activity. We attributed these anomalies to a weakening of the winds, itself related to a strongly negative North Atlantic Oscillation (NAO) index.

Résumé

But Les filaments d'upwelling sont des structures d'eau froide peu profondes et allongées souvent visible dans les régions d'upwelling côtier. La présente thèse a pour but d'améliorer notre connaissance des mécanismes responsables de la formation de filaments.

Zone l'étude est centrée sur le système d'upwelling du Courant des Canaries, situé au large du nord-ouest de l'Afrique, en particulier autour du Cape Ghir (30°38'N, 9°53'O), où ces filaments sont fréquemment observés.

Méthodes

- Nous avons assemblé des données in situ historiques afin de construire une climatologie à haute résolution pour la température et la salinité dans la région d'intérêt en utilisant la méthode d'Interpolation de Données par Analyse Variationnelle (Diva).
- Nous avons procédé à des expériences avec le modèle numérique ROMS pour examiner les processus responsables de la génération de filaments.
- Nous avons collecté des mesures in situ durant une campagne en mer en août-septembre 2009, dans le cadre du projet CAIBEX, dans la zone du filament et les avons exploitées de manière à obtenir une description détaillée du filament de Cap Ghir, sa variabilité et ses caractéristiques biogéochimiques.
- Nous avons calculé les anomalies de plusieurs variables par rapport à une moyenne à long terme afin d'examiner l'évolution dans le temps du système d'upwelling du Courant des Canaries.

Résultats La climatologie a montré des améliorations par rapport à des produits existants, particulièrement dans la zone côtière, a été un précieux atout pour fournir des conditions initiale et aux limites au modèle numérique. Les résultats des simulations ont souligné le rôle du vent dans la génération du filament et ont confirmé notre hypothèse de mécanisme basé sur l'équilibre de la vorticité potentielle. Les analyses préliminaires des données de la campagne nous ont permis de caractériser les propriétés physiques et biologiques du filament, en particulier nous avons observé le signal d'un tourbillon anticyclonique sous la surface (à une profondeur de 300 m) sur la flanc nord du filament, également présent dans les sorties du modèle numérique. Les anomalies de l'année 2010 ont révélé un réchauffement étendu sur l'Océan Atlantique tropical et subtropical et une diminution de l'activité de l'upwelling. Nous avons attribué ces anomalies à un affaiblissement des vents, lui-même relié à un indice d'Oscillation Nord Atlantique (NAO) fortement négatif.

Resumen

Objetivo Los filamentos de afloramiento son estructuras someras y alargadas formadas por agua fría y visibles a menudo en las regiones de afloramiento costero. La presente tesis se propone mejorar nuestro conocimiento sobre los mecanismos responsables de la generación de filamentos.

Localización El estudio se centra sobre el sistema de afloramiento de la Corriente de Canarias, situado frente a la costa noroeste de África, en particular alrededor del Cabo Ghir (30°38'N, 9°53'O), donde estos filamentos son observados con frecuencia.

Métodos

- Compilamos datos in situ históricos para construir una climatología de alta resolución de temperatura y salinidad en la región de interés, empleando el método de Interpolación de Datos por Análisis Variacional (Diva).
- Realizamos experimentos con el modelo numérico ROMS para investigar los procesos responsables de la generación de filamentos.
- Reunimos medidas in situ durante una campaña en agosto-septiembre de 2009, en el marco del proyecto CAIBEX, en la zona del filamento y los analizamos para obtener una descripción detallada del filamento de Cabo Ghir, su variabilidad y sus características biogeoquímicas.
- Calculamos anomalías de varias variables con respecto a promedios a largo plazo para examinar la evolución temporal del sistema de afloramiento de la Corriente de Canarias.

Resultados La climatología mostró mejoras con respecto a productos existente, especialmente en la zona costera, y fue una ventaja valiosa para proporcionar condiciones iniciales y de borde al modelo numérico. Los resultados de las simulaciones resaltaron el papel del viento en la generación de filamentos y confirmaron nuestra hipótesis de un mecanismo basado sobre el balance de vorticidad potencial. Análisis preliminares de los datos de la campaña nos permitieron caracterizar las propriedades físicas y biológicas del filamento, en particular observamos la señal de un remolino anticiclónico subsuperficial (a 300 m de profundidad) en el flanco norte del filamento, tambien presente en las salidas del modelo numérico. Las anomalías del año 2010 revelaron un calentamiento extendido sobre el océano Atlántico tropical y subtropical y una disminución de la actividad del afloramiento. Atribuimos estas anomalías a una debilitación de los vientos, esto mismo relacionado a su vez con un indice de Oscilación del Atlántico Norte (NAO) fuertemente negativo.

Thesis preview

The thesis has been prepared with a four-year grant of the *Fonds pour la formation à la Recherche dans l'Industrie et dans l'Agriculture* (FRIA) from the National Fund for the Scientific Research (FRS-FNRS, Belgium). It provided contributions to SeaDataNet project, an Integrated Infrastructure Initiative of the EU Sixth Framework Programme, and CAIBEX projects (CTM2007-66408-C02-01/MAR), funded by the Spanish Ministry of Education and Science.

It was supervised by Prof. Jean-Marie Beckers, GeoHydrodynamics and Environment Research (GHER), AGO department, University of Liège, and Dr. Pablo Sangrà, *Departamento de Física, Facultad de Ciencias del Mar*, University of Las Palmas de Gran Canaria, Spain.

The thesis is organized as follows: in Chapter 1, we give a general description of the physical processes of upwelling and filaments, along with an overview of the Canary Current system. Chapter 2 is dedicated to the creation of a climatology around the region of interest by means of the Data Interpolating Variational Analysis (Diva) method. In Chapter 3 the results of the Regional Ocean Model System (ROMS) numerical model provides insight into the mechanisms responsible for the filament formation. The data collected during CAIBEX cruise are presented in Chapter 4 and used for the model validation. Finally in Chapter 5, we examine the evolution of the NW Africa upwelling over the last years by means of in situ and remote sensing measurements.

The relations between the different parts of the present work are symbolized by the arrow in Fig. 1. The introduction describes the main concepts and the characteristics of the coastal upwelling. The climatology is used for providing initial and boundary conditions to the numerical model, which in turn acts as a tool to control the quality of the gridded fields. Both are related to the CAIBEX cruise: the model helps to decide on the sampling strategy, while the data collected during the cruise are employed for the validation; the climatology constitutes a reference to compare the CAIBEX observations with. The latter could enrich the climatological data base in the future. The study of the time-evolution of the Canary Current system benefits from the climatology, which can again serve as a background, whereas numerical experiments with new forcing conditions could be prepared based on the observed or predicted atmospheric changes in the upwelling system.

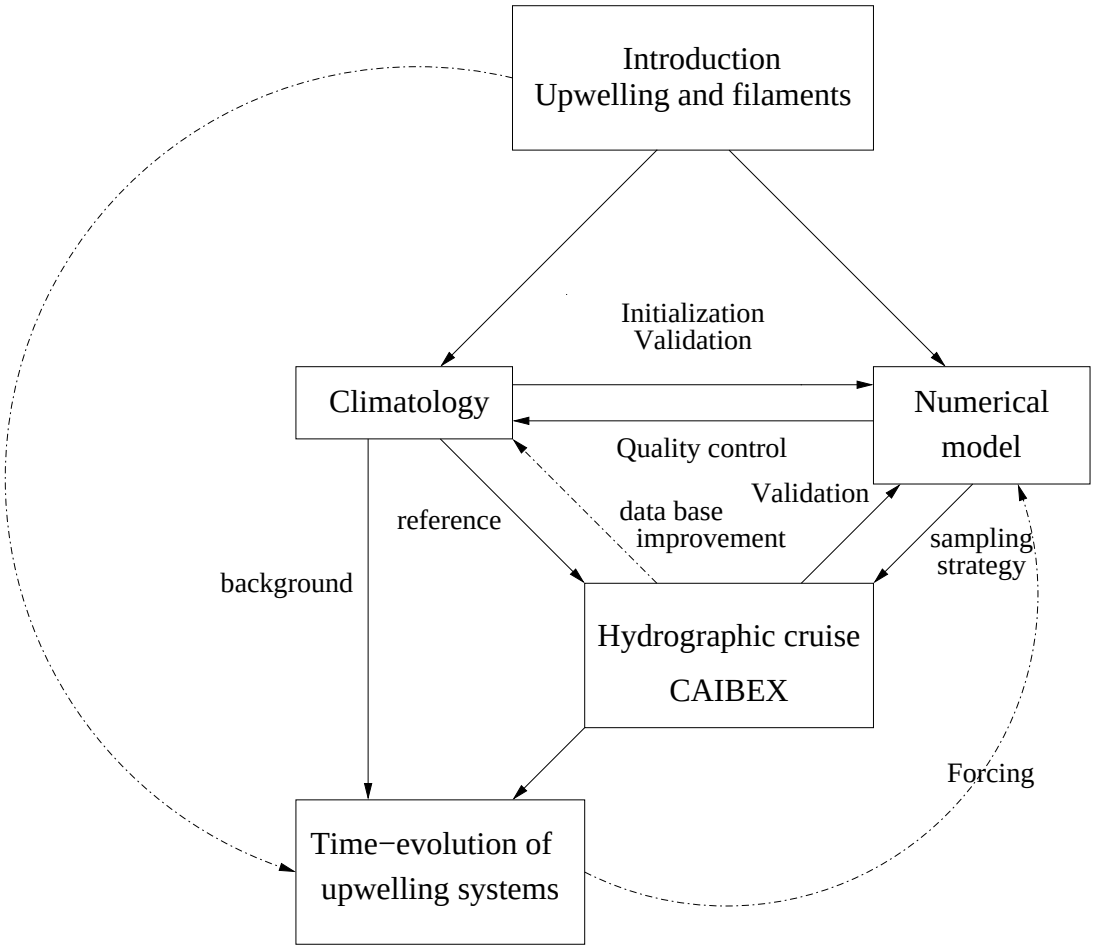

Figure 1: Rectangles denote chapters of the thesis and the arrow, the link between them. Dashed lines denote work in progress. After the introduction, two directions were explored: data analysis (Climatology) and numerical modeling. Both are then combined in the frame of the CAIBEX cruise.

Acronyms

ADCP	Acoustic Doppler Current Profiler
AVHRR	Advanced Very High Resolution Radiometer
BC	Boundary currents
CTD	Conductivity, Temperature, Depth
CGP	Cape Ghir Plateau
COADS	Comprehensive Ocean-Atmosphere Data Set
CV	Cross-validation
CZCS	Coastal Zone Color Scanner
DIVA	Data Interpolating Variational Analysis
EBC	Eastern boundary current
EBUS	Eastern boundary upwelling system
GCV	Generalized cross-validation
GEBCO	General Bathymetric Chart of the Oceans
GODAE	Global Ocean Data Assimilation Experiment
ICES	International Council for the Exploration of the Sea
LME	Large Marine Ecosystems
MEDAR	Mediterranean Data Archeology and Rescue
MLD	Mixed-layer depth
MODIS	Moderate Resolution Imaging Spectroradiometer
NADW	North Atlantic Deep Water
NAO	North Atlantic Oscillation
NPP	Net primary production
OA	Objective analysis
OBC	Open boundary condition
PAR	Photosynthetically available radiation
PIC	Particulate inorganic carbon
POC	Particulate organic carbon
PV	Potential vorticity
QuikSCAT	Quick Scatterometer
ROMS	Regional Oceanic Modeling System
RMS	Root mean square
SeaWiFS	Sea-viewing Wide Field-of-view Sensor
SCOW	Scatterometer Climatology of Ocean Winds
SST	Sea Surface Temperature
STD	Standard deviation
VIM	Variational Inverse Model
WOD	World Ocean Database
WOA	World Ocean Database
WOCE	World Ocean Circulation Experiment
XBT	Expendable Bathythermograph

Contents

Chapter 1

Introduction: Upwelling and filaments

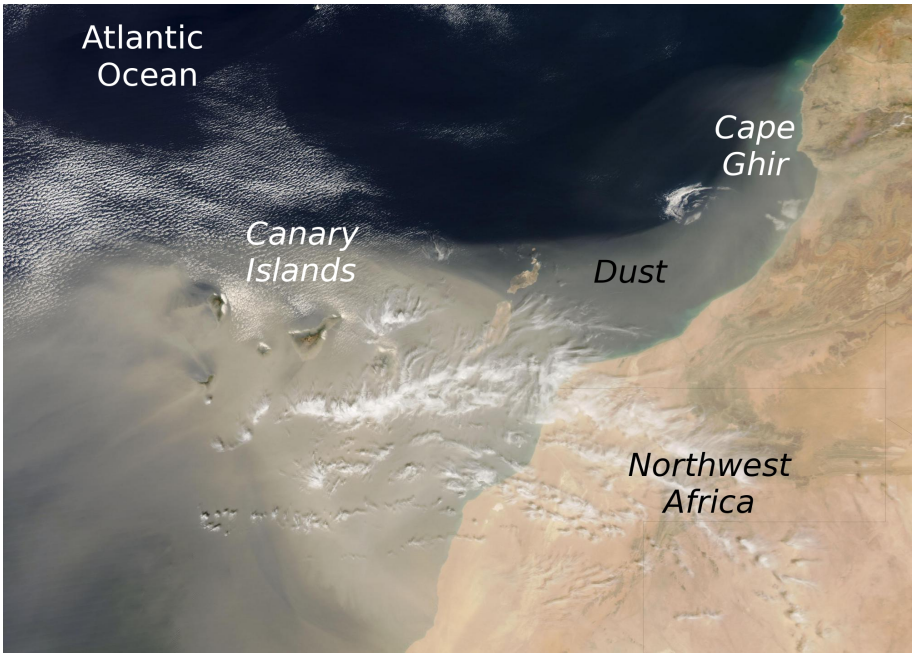

MODIS-Aqua true-color image of Cape Ghir region on March 10, 2007.
Adapted from NASA Earth Observatory
http://earthobservatory.nasa.gov/NaturalHazards/view.php?id=18106

The present chapter is dedicated to the description (mechanism, observations, modeling) of coastal upwelling and filaments, and serves as an introduction of the main concepts used in the next chapters. Since filaments are intimately related to upwelling, it is necessary to first describe this process.

Contents

1.1 Upwelling

In general terms, the American Meteorological Society glossary (http://amsglossary.allenpress.com/glossary/) defines an upwelling as "*an ascending motion of subsurface water by which water from deeper layers is brought into the surface layer*". There are different processes responsible for the ascending motion. According to the process in play, several types of upwelling are distinguished:

The coastal upwelling, generated by the wind blowing along the coast in a favorable direction, during a sufficiently long period, as will be described in details in the next sections.

The equatorial upwelling (e.g., Cromwell, 1953; Wyrtki, 1981): close to the Equator, trade winds tend to blow westward. In the northern hemisphere, the Ekman transport is directed northward, while in the southern hemisphere, it is directed southward. This divergence of the flow generates an upward velocity along the equator.

The ice-edge upwelling (e.g., Van Heijst, 1984; Alexander & Niebauer, 1981; Tang & Ikeda, 1989): its origin is the different stress exerted on the water by the ice or the air. A diverge of the horizontal flow is generated near the ice-edge, resulting in a compensating vertical velocity.

1.1.1 Coastal upwelling

A *coastal upwelling* can be defined as a *near-shore circulation induced into a stratified rotating ocean by the surface wind* (e.g., O'Brien & Hurlburt, 1972). This short definition contains several essential points:

Near-shore circulation: the process typically takes place in a limited region near to the coast.

Stratification: the fluid presents vertical variations of density.

Rotation: Earth rotation is necessary to promote the upwelling.

Winds: as will be shown later, the main forcing is the wind.

In geophysical fluid dynamics, upwelling is the typical process that combines both rotation and stratification effects.

1.1.2 Mechanism

The base explanation of coastal upwelling (e.g., Stewart, 2008; Cushman-Roisin & Beckers, 2011) is quite simple. The situation is summarized in Fig. 1.1: when wind blows during a sufficiently long time with a constant direction, it provokes a mean transverse transport,

called *Ekman drift*. The Ekman drift points at 90 degrees with respect to wind direction, and is directed to its right (left) in the northern (southern) hemisphere.

Let us assume that we are in the northern hemisphere, with the wind blowing along a north-south oriented coast. If the wind blows southward (i.e., with the coast to its left), it creates an Ekman drift directed offshore, so that a water depletion occurs near the coast. To compensate for it, subsurface waters tend to move upward. The water depletion generates a low pressure zone along the coast, which in turn creates a geostrophic current with the same direction as the wind, called *upwelling jet*. It is noteworthy to mention that it is not the wind that generates directly this jet, but rather the low pressure arising from the water depletion.

Along meridional-oriented coastlines situated at the east side of oceans, the conditions favorable to coastal upwelling are met when winds are southward (northward) in the northern (southern) hemisphere, that is to say, when winds are equatorward.

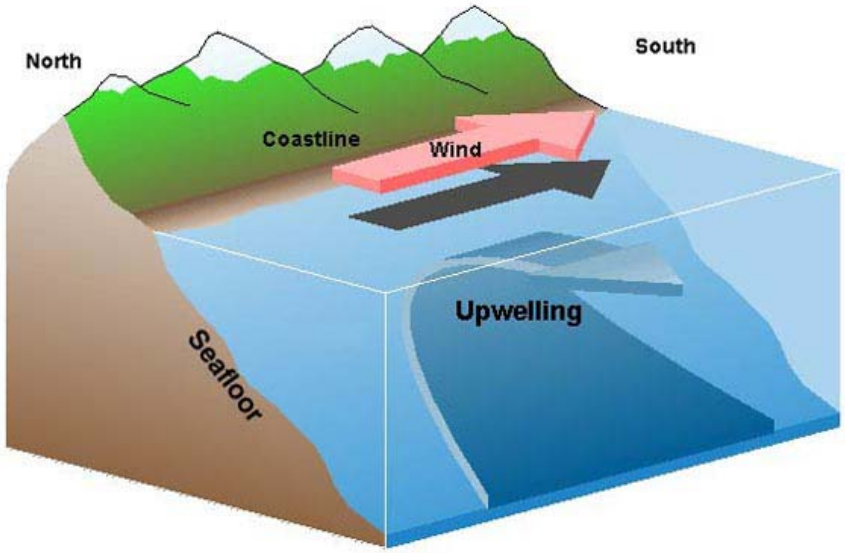

Figure 1.1: Cartoon of a coastal upwelling in the northern hemisphere. Source: Ocean Explorer, http://oceanexplorer.noaa.gov/explorations/02quest/background/upwelling/upwelling.html.

1.1.3 Characteristics

As upwelled waters come from deeper zones (below the thermocline), they are cooler and have a higher content in nutrients. These characteristics make them identifiable through satellite images (Section 1.1.4). Usually, surface waters are depleted of nutrients (phosphates, nitrates, ...), but when the nutrient-rich waters reach the surface layers, where the sun light can penetrate, they are able to sustain an enhanced biological activity (blooms of phytoplankton). Phytoplankton are eaten by zooplankton, which are eaten by small fish, themselves eaten by larger fishes. All in all, they constitute the base for animals higher in the food chain (seabirds, marine mammals, ...).

The alongshore component of the wind is responsible for the upwelling, while the

shore-ward component may bring moist air over the cooler upwelled waters. When the incoming air enters the coastal zone, it cools and forms a thin atmospheric boundary layer. The humidity contained in the air is condensed, fog or low stratus clouds are formed. Such fog conditions are typical in the upwelling areas in summer (Fig. 1.2). The warmer air above the boundary layer inhibits vertical convection. The air column is more stable, and the precipitations are weak. This explains why the lands adjacent to coastal upwelling are often deserts: the Atacama desert (Chile), the Namib desert (southwest Africa), Baja California desert (U.S.A.) and the Atlantic coastal desert of Morocco. Upwelled cold water also inhibits formation of tropical cyclones, since such tropical systems derive their energy from warm surface waters (usually when temperature is higher than 26.5°C, e.g., Graham & Barnett, 1987).

Figure 1.2: Reduced visibility due to fog in the NW Africa upwelling. Photograph taken on August 21, 2009, close to Moroccan coast, during CAIBEX campaign. Surface temperature is about 16° C.

1.1.4 Identification

The parts of the ocean where coastal upwellings take place are easily identified using Sea Surface Temperature (SST) images. According to the definition given previously, upwelled waters are characterized by a temperature lower than in the open ocean at the same latitude. Figure 1.3 was obtained by combining all the SST measurements made by the Moderate Resolution Imaging Spectroradiometer sensor (MODIS, `http://modis.gsfc.nasa.gov/`) aboard Aqua satellite (`http://aqua.nasa.gov/`), from February 1, 2002, to January 29, 2008. These data are obtained through the Ocean Color web page (Feldman & McClain, 2010).

From this global view of the surface temperature, we can detect four regions of coastal upwelling, often referred to as *upwelling systems*:

1. The California (Current) upwelling system, located along the west coast of north

America;

2. The Peru-Chile (Current) upwelling system, also called Humboldt Current;
3. The Canary Current upwelling system, located off northwest Africa;
4. The Benguela upwelling system, along the coasts of Namibia and South Africa.

All these regions share a characteristic: they are located in the eastern part of the main subtropical gyres (Fig. 1.4). For this reason, they are designated as the *Eastern Boundary Current Upwelling Systems* (EBUS hereinafter). Another upwelling system, not visible on this SST map, exists in the Arabian Sea: the Somali Current System (e.g., Warren *et al.*, 1976; Swallow, 1980). The reason why the SST signature did not appear is that the upwelling is strongly seasonal, with its maximal intensity taking place during the boreal winter.

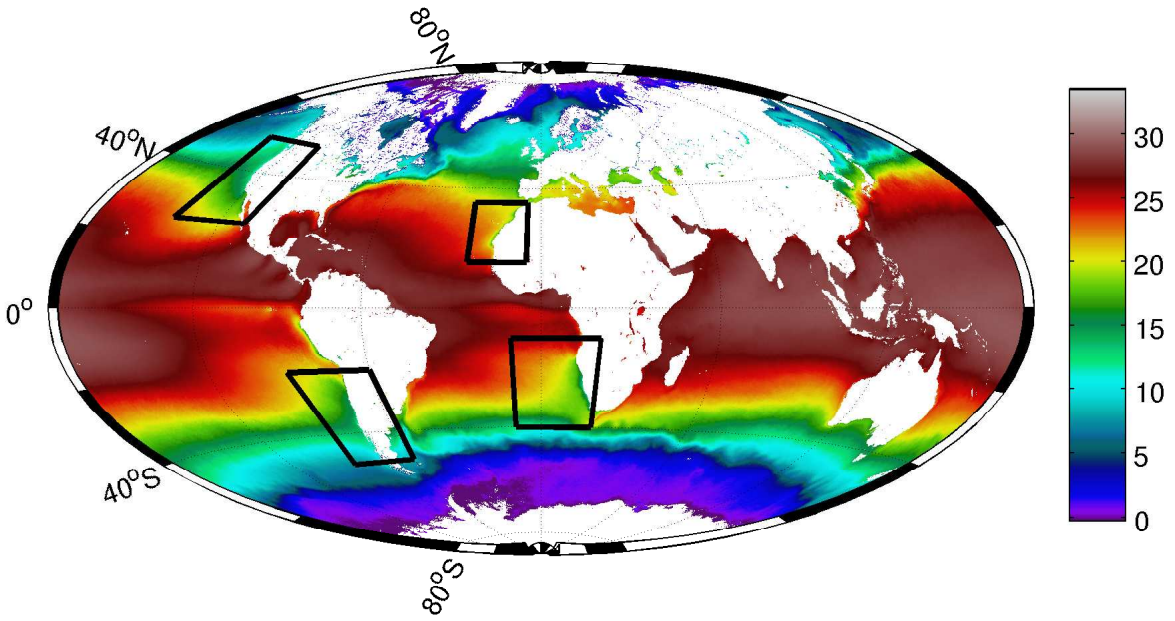

Figure 1.3: Mean SST over the global ocean, obtained from MODIS measurements between 2002 and 2008. The main upwelling areas (black rectangles) are located in the eastern parts of the subtropical gyres.

In order to verify the mechanism presented in Section 1.1.2, the SST map is compared with the annual wind vectors (Fig. 1.5), obtained from the Scatterometer Climatology of Ocean Winds (SCOW, Risien & Chelton, 2008). SCOW is a monthly climatology of wind and wind stress based on NASA's Quick Scatterometer measurements (QuikSCAT, `http://winds.jpl.nasa.gov/missions/quikscat/index.cfm`) and provides wind fields with a resolution of 0.25° and for latitudes between 70°S and 70°N. Unfortunately, QuikSCAT mission stopped on November 23, 2009.

The map confirms the equatorward wind direction along the eastern boundaries of the Atlantic and Pacific subtropical gyres. The seasonal and interannual variabilities of the wind fields can be strong, hence the location and intensity of the upwelling can also undergo significant variations.

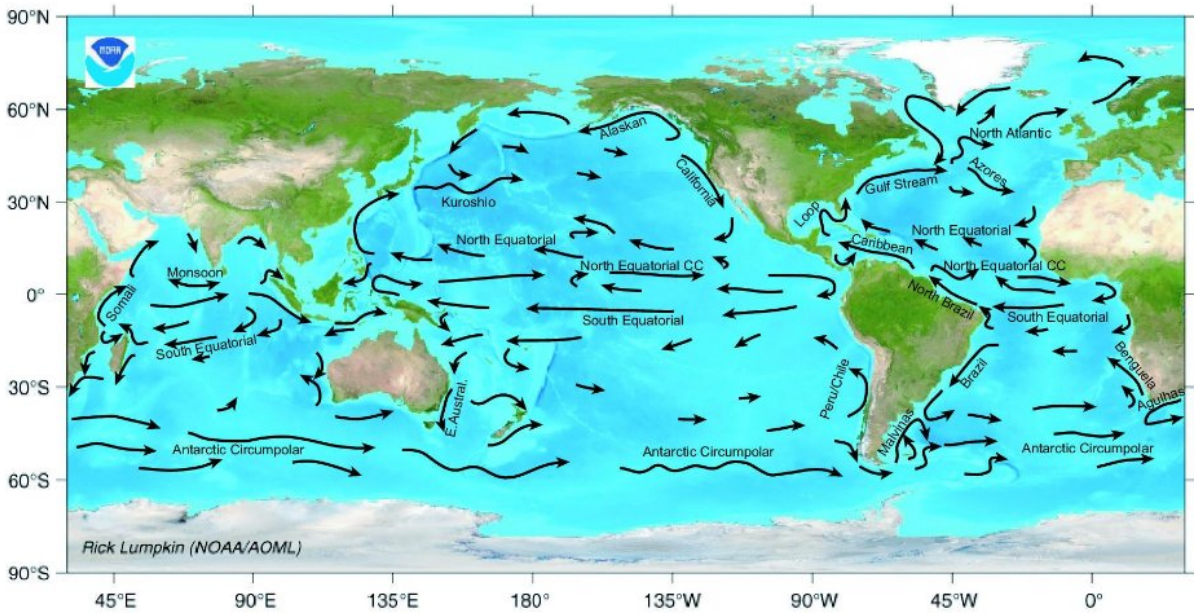

Figure 1.4: The main surface currents show that the four main upwelling systems are characterized by equatorward currents: Benguela, Canary, Peru-Chile and California (from NOAA's Adopt a Drifter Program, http://www.adp.noaa.gov/currents_map.html).

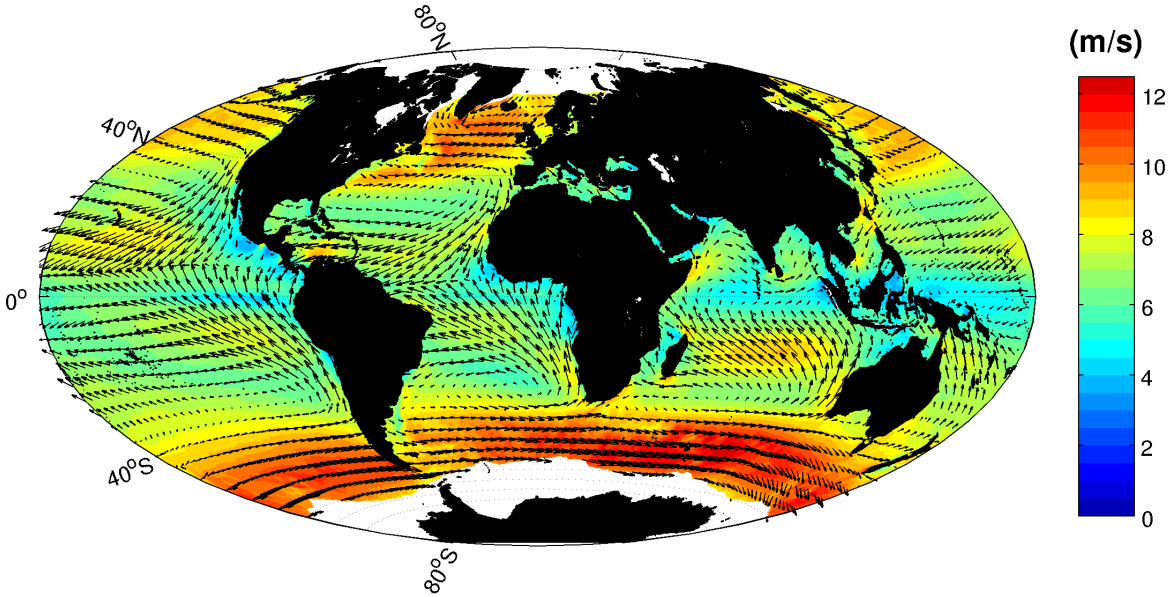

Figure 1.5: Annual mean wind velocity from the Scatterometer Climatology of Ocean Winds. The main upwelling systems are characterized by northeasterly (southeasterly) winds in the northern (southern) hemisphere.

1.1.5 Importance of the upwelling systems

By the injection of nutritive matter into the surface water, upwelling systems play a significant role in the marine ecosystems. According to Ryther (1969), upwelling areas represent only 0.1% of the total ocean surface (with 3.6×10^5 km^2) but have a mean productivity estimated around 300 gC m^{-2}yr^{-1} (versus 50 gC m^{-2}yr^{-1} for the open ocean) and a fish production of 12×10^7 tons (16×10^5 tons for the open ocean). Even if the delimitation of the main upwelling areas and the method to estimate the productivity have evolved during the last decades, these numbers underline the prominence of these areas in the ocean productivity.

More recently, Durand *et al.* (1998) estimated that the four major upwelling systems account for 30% of the global fish catch, while Jennings *et al.* (2001) stated that approximately 25% of the total global marine fish catches come from five upwelling areas that occupy only 5% of the total ocean. All except the California Current System have productivity close to 300 gC m^{-2} yr^{-1} (Tab. 1.1).

The four EBUS belong to the larger group of Large Marine Ecosystems (LME, `http://www.lme.noaa.gov/`). The group is made up of 64 LMEs and accounts for 80% of mean annual fisheries yields. Unfortunately, there are also the regions with the most overfishing, pollution and anoxia. It is estimated that they contribute around 12 trillion dollars annually to the global economy .

In this work, we are particularly interested by the Canary Current upwelling system, located in the eastern part of the north Atlantic subtropical gyre. In this region, the winds responsible for the upwelling are the trades, generated by the Azores high and the African thermal through, and which blow predominantly from the northeast. They reach their maximal intensity in summer, when the Azores high is at its northernmost position (Wooster *et al.*, 1976). The Azores high is centered at about 35°N, 35°W in summer and 33°N, 20°W in winter (Speth *et al.*, 1978).

Many countries are directly affected by the upwelling: Morocco, Mauritania, Guinea-Bissau, Guinea, Canary islands (Spain), Gambia, Cabo Verde, Senegal and Western Sahara. It is estimated that 0.77% of the total oceanic area of the region is protected. The population is about 58 millions, of which 70% are related to the Canary Current ecosystem (Heileman & Tandstad, 2009).

Table 1.1 compares the linear temperature trend in the four EBUS. When computed over the 1957-2006 period, all the linear trends are positive, with a mean value of 0.37°C (i.e., on average, the temperature increases at a rate of 0.0147°C per year). However, when computed over the 1982-2006 period, the trends for the Humboldt and California EBUS reveal a weak cooling. According to Bakun (1990), a global warming would have the effect of increasing the coastal upwelling, through the intensification of the pressure gradient between the continental thermal low and the Azores high, resulting in increased alongshore wind stress. Still, the temporal evolution of the EBUS is not trivial: it has to be examined carefully, since it also depends on the large scale circulation.

Table 1.1: Characteristics of the four EBUS (Belkin, 2009).

Upwelling	Surface ($\times 10^6$)	Productivity (g C m^{-2} yr^{-1})	Linear trend (°C)	
			1957-2006	1982-2006
California	2.2	< 150	0.32	-0.07
Humboldt	2.5	150-300	0.41	-0.10
Canary	1.1	> 300	0.48	0.52
Benguela	1.5	> 300	0.26	0.24

We present a global map of chlorophyll *a* concentration (Fig. 1.6) in order to demonstrate the remarkable biological activity in the upwelling systems. They are obtained from the Sea-viewing Wide Field-of-view Sensor (SeaWiFS, http://oceancolor.gsfc.nasa.gov/SeaWiFS/) aboard the Orbview-2 satellite. The average is computed using all the data from 1997 to 2010. The idea behind the measurements is that the color of the sea water varies as a function of the quantity of chlorophyll and other plant pigments present. The four EBUS exhibit high chlorophyll *a* concentrations in a thin band along the coast. Note that there are other areas with high chlorophyll *a*, but not associated with a low SST signal. In these cases, the increase of production is due to other processes, for example river discharge in the mouth of the Amazon or Congo rivers.

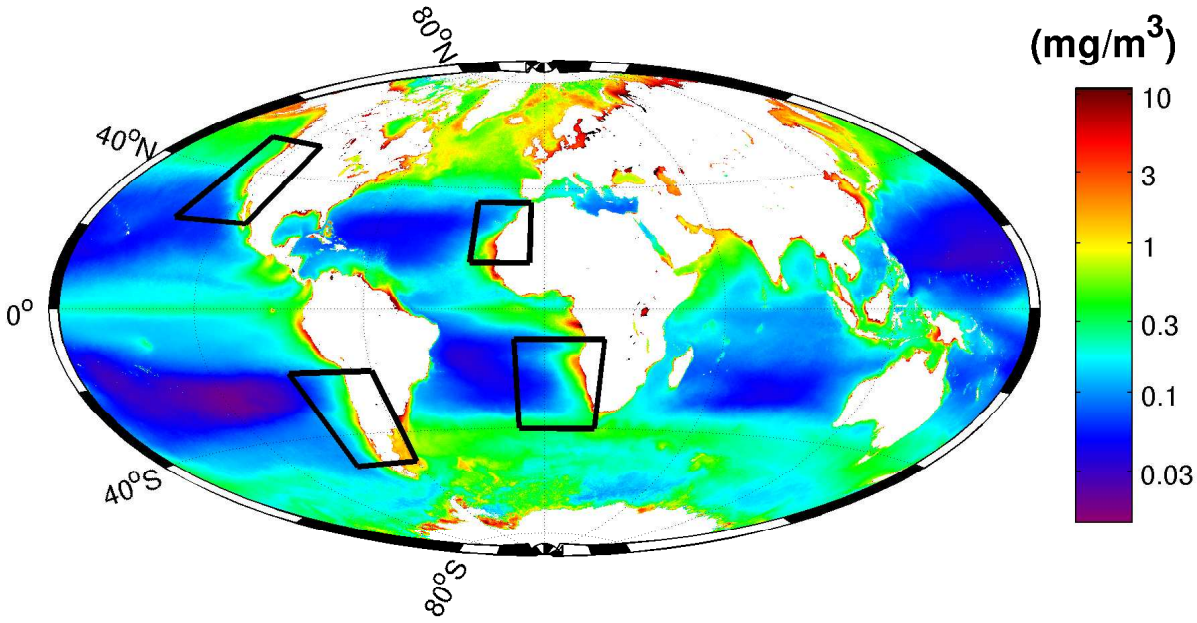

Figure 1.6: Mean chlorophyll a concentration (logarithmic scale) over the global ocean, obtained from SeaWiFS measurements between 1997 and 2010.

The relationship between low temperature and high chlorophyll *a* concentration is underlined in Fig. 1.7, which provides close-up views of the four EBUS. Let us recall that these images are constructed using several years of satellite data.

Using the chlorophyll concentration, SST and photosynthetically available radiation

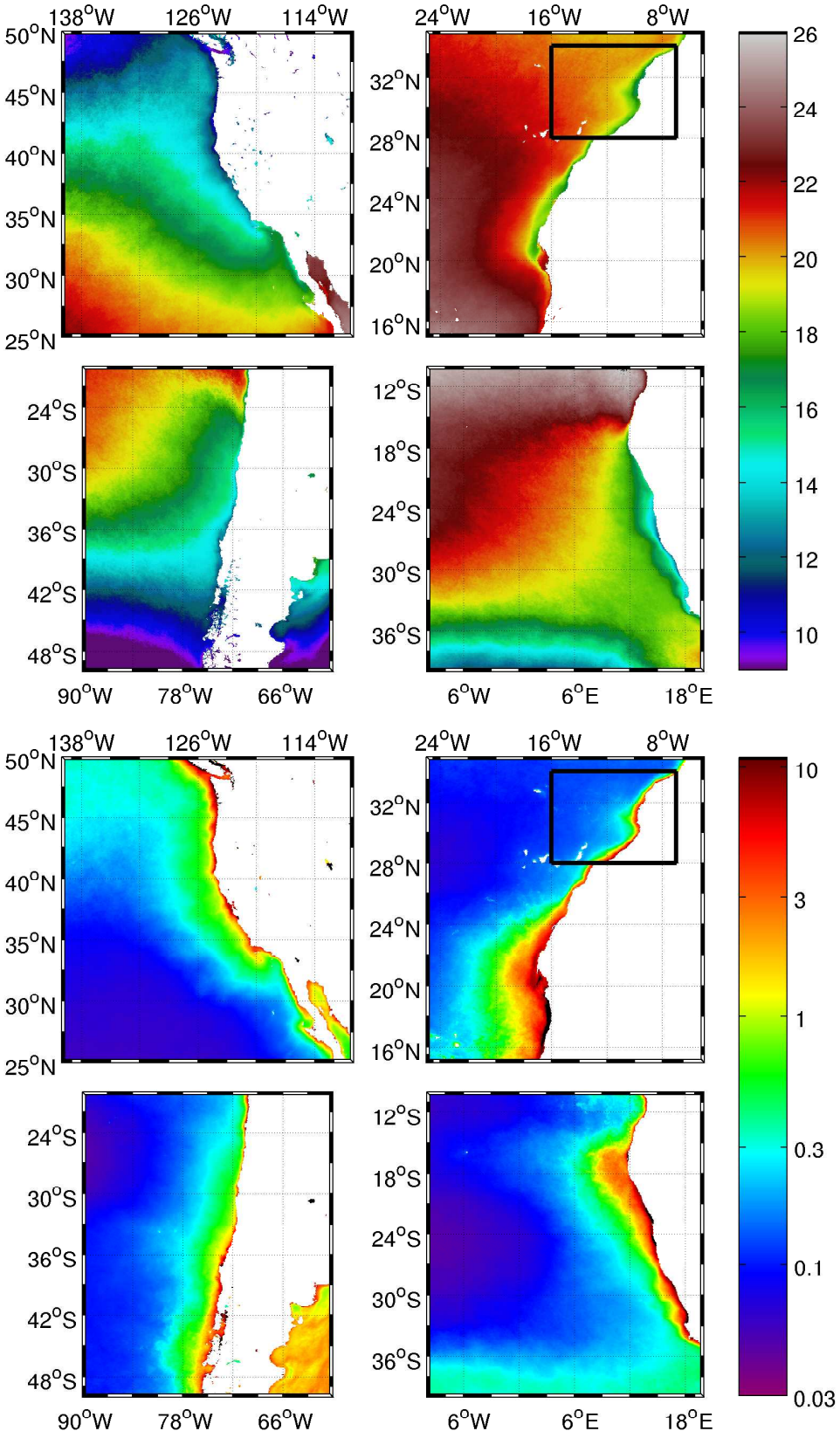

Figure 1.7: Close-up view of the SST (top) and chlorophyll a concentration (bottom; logarithmic scale) for the four main upwelling regions.

(PAR), it is possible to deduce the *net primary production* (NPP). NPP is the difference between the energy produced by the ecosystem and the energy consumed by respiration. The Vertically Generalized Production Model (VGPM, Behrenfeld & Falkowski, 1997) is an algorithm to compute NPP using these remote-sensed variables.

The corresponding fields are available at `http://www.science.oregonstate.edu/ocean.productivity/standard.product.php`. Chlorophyll concentration and SST are obtained from MODIS sensor, while PAR is provided by SeaWiFS sensor. *Euphotic depth* (depth reached by a sufficient amount of light to sustain photosynthesis) is estimated from chlorophyll concentration using the model of Morel & Berthon (1989). The mean annual field is computed using the data from 2002 to 2009. Figure 1.8 again evidences the role of the EBUS, where the highest production values are observed. The largest values are on the order of $10^3 - 10^4$ mg C $m^{-2}day^{-1}$ and occur very close to the coast.

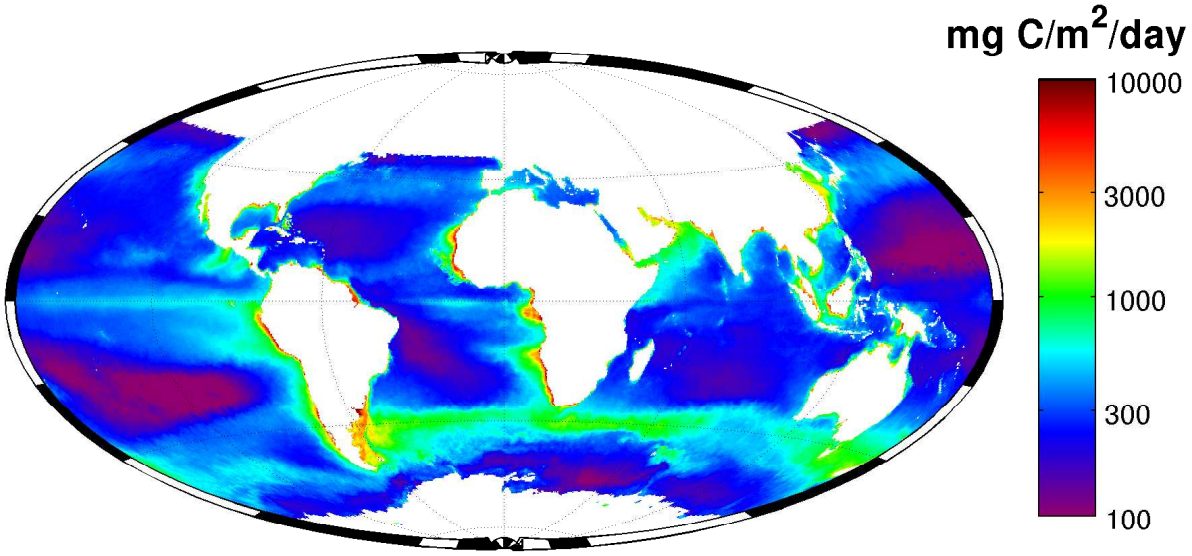

Figure 1.8: Mean annual VGPM-estimated net primary production, computed over the 2002-2009 period.

1.2 Upwelling filaments

The condition for the existence of a coastal upwelling is that the wind has to blow during a certain amount of time in a favorable direction. Let us consider the SST in the black rectangle of Fig. 1.7, centered on the Canary Current upwelling system, but this time for single days: August 26 and September 2, 2009. The images are again extracted from the Ocean Color web page, with a 4 km horizontal resolution. We observe a narrow, elongated structure of cool water oriented westward, at a latitude around 31°N (Fig. 1.9). Such a structure is called *upwelling filament*.

The core of the filament has a temperature below 19°C, while open ocean waters have a temperature above 22°C. The longitudinal extension exceeds 100 km in both cases presented in Fig. 1.9, whereas the width is variable, usually on the order of 10 km. The

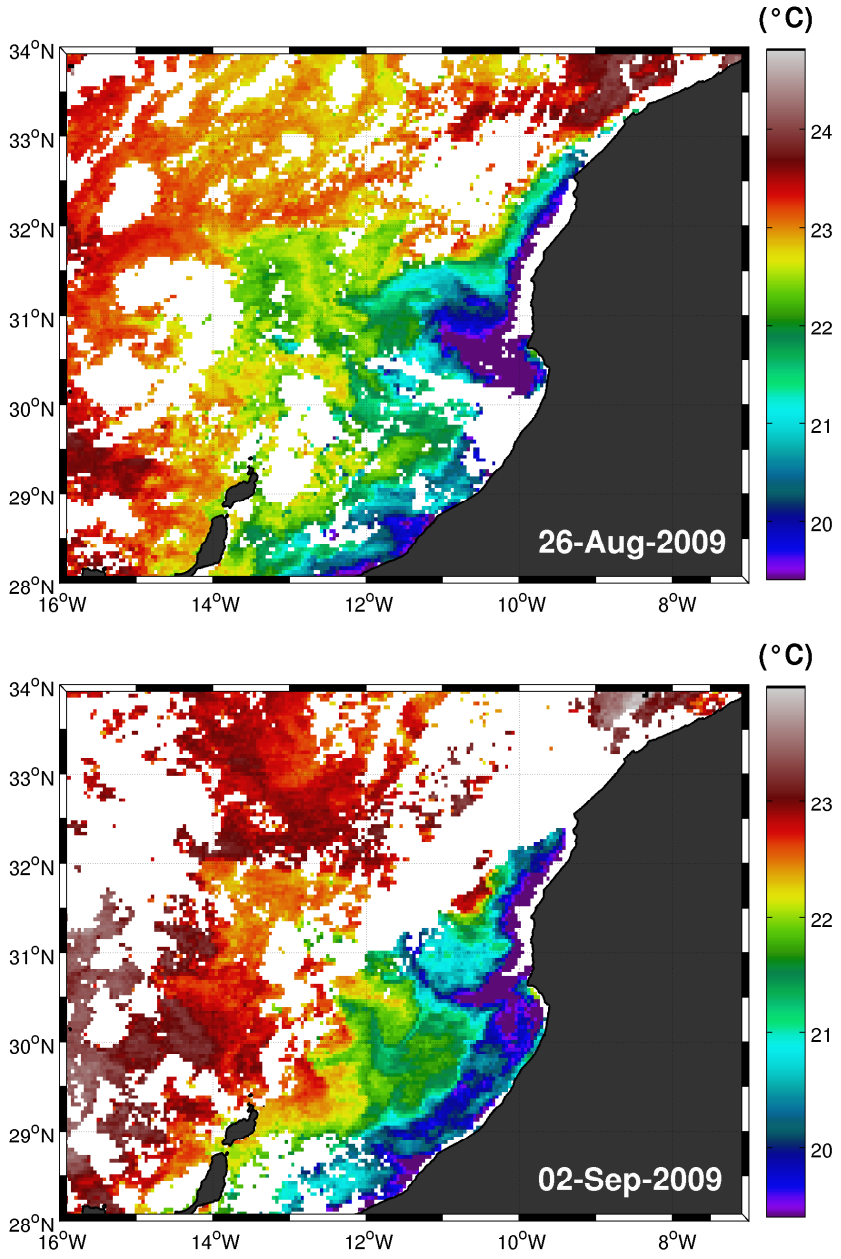

Figure 1.9: SST (MODIS-Aqua) off NW Africa on August 26 (top) and on September 2, 2009 (bottom).

filament seems to develop at the latitude of Cape Ghir (30°38'N). Though the images are separated by one week, the temperature structures are similar.

1.2.1 Roles

What makes upwelling systems important is their input of nutrient-enriched water to the surface layers of the ocean. What makes filaments worthy of interest is their capacity to export the enriched upwelling water toward the open ocean, resulting in high concentrations in phytoplanktons. Figure 1.10 shows the chlorophyll *a* concentration for the same days as in Fig. 1.9. Far away from the coasts, concentrations are weak, on the order of 0.01 mg/m^3. Within the upwelling, these concentrations reach values larger than 3 mg/m^3, and in the filament, similar values are observed.

Another consequence of the filaments is the exportation of particulate organic carbon (POC, Arístegui *et al.*, 2006; Neuer *et al.*, 2002; Gabric *et al.*, 1993; García-Muñoz *et al.*, 2005) as far as 700 km offshore. The POC plays an important role in the carbon cycle. Álvarez-Salgado *et al.* (2007) underlined the few number of studies with measurements of carbon in the coastal upwelling systems. They estimated that filaments export 2.5 to 4.5 more carbon than the Ekman transport. They also estimated that the Cape Ghir filament exports 2 to 3 times more primary production than the other filaments in the same region (e.g., Cape Juby, Cape Bojador; see Fig. 1.14 for the localization of the main capes). With field data obtained from September 26 to October 2, 1997, García-Muñoz *et al.* (2005) determined that the Cape Ghir filament was responsible for the exportation of 63% of the total annual production.

1.2.2 Historical observations

In situ measurements

Filaments have been first observed during the late 1970's–early 1980's in the California Current System through in situ measurements (e.g., Brink, 1983; Brink *et al.*, 1984; Mooers & Robinson, 1984) and satellite images (see next section). Intensive surveys were carried out during multidisciplinary projects along the U.S. northwest coast:

The Coastal Ocean Dynamics Experiment (CODE, Kosro & Huyer, 1986; Beardsley & Lentz, 1987): it was carried out north of the San Francisco bay, from April 1981 to August 1982. The main objective was the study of the dynamical processes over the continental shelf, with the help of high-resolution and high-quality measurements (hydrographic data, drifters, satellite images and Acoustic Doppler Current Profiler (ADCP)). In particular, numerous measurements of the properties of the cold tongues extending from the coast were carried out.

The Coastal Transition Zone program (CTZ, Brink & Cowles, 1991, and the related papers in the same issue) took place off northern California in 1987-1988. The program was made up of large-scale and mesoscale surveys, along-filament studies (drifters) and modeling effort. It is certainly the most comprehensive program that has been undertaken for the study of filaments, and the data and results contained in the special issue [*Journal of Geophysical Research* **96 (C8)**, 1991] are still an invaluable reference for the future works.

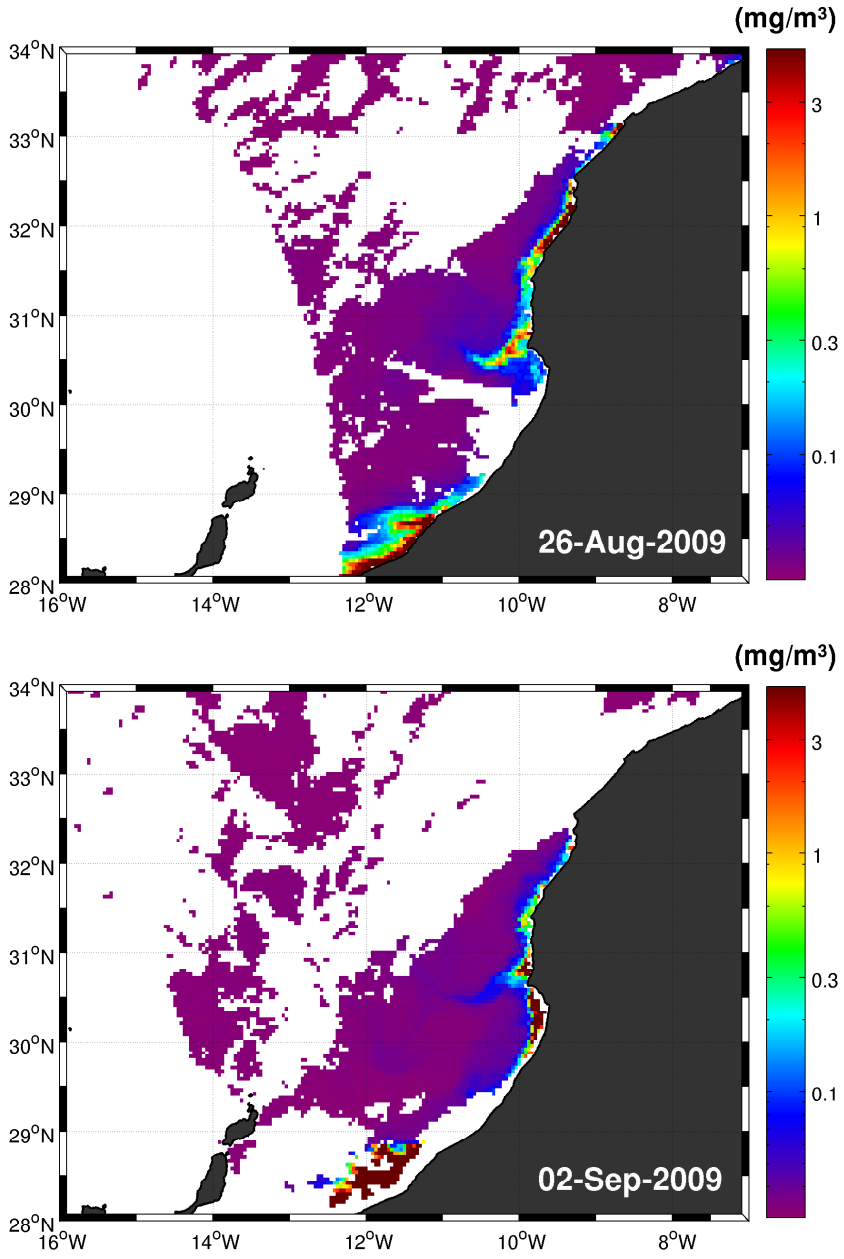

Figure 1.10: Chlorophyll a concentration (MODIS-Aqua) off NW Africa on August 26 (left) and on September 2, 2009 (right). Note the logarithmic color bar.

The Eastern Boundary Current experiment (EBC, Huyer *et al.*, 1998): it was conducted in 1993, during the upwelling season. It was made up of two surveys of the California Current using SeaSoar towed vehicle and ADCP.

All in all, these programs provided a better knowledge of the filament characteristic scales and setting up hypothesis on their mechanism of formation.

Concerning the NW Africa upwelling, numerous cruises in took place from the years 1970's, most of them being concentrated in the region between Cape Bojador (26°N) and Cape Blanc (21°N). We can mention the international projects help during the "International Decade of Ocean Exploration" (1971-1980):

The Cooperative Investigation of the Northern Part of the Eastern Central Atlantic (CINECA), a multidisciplinary study carried out between the Strait of Gibraltar and Dakar (Senegal) over the period 1970-77. It consisted of data compilation, monitoring of environmental and biological parameters and synoptic surveys by a large number of research vessels. Results were presented and discussed at a symposium in 1978 (Hempel, 1982).

The Coastal Upwelling Ecosystems Analysis (CUEA), with the objective to predict the response of the upwelling system to change by monitoring physical, biological or meteorological variables.

The presence of a poleward undercurrent over the continental slope was frequently reported (e.g., Hughes & Barton, 1974a,b; Johnson *et al.*, 1975; Mittelstaedt *et al.*, 1975; Mittelstaedt & Hamann, 1981). Hughes & Barton (1974a) performed intensive measurements off Cape Bojador and stated in their description of the upwelling: "*(...) although the isolines appear in general to follow the line of the edge of the continental shelf, there is nevertheless much irregularity in the recorded profiles because of the complicated nature of the surface distributions.*" Indeed, their Figure 2 shows what seems to be the signal of a filament at 25°N. Tomczak, (1973) already mentioned these *cold water patches* in the NW Africa upwelling, while Hughes & Barton (1974a) concluded on an increased upwelling intensity off Cape Bojador and Cape Blanc.

During the last two decades, the effects of filaments upon the marine ecosystems were further studied in the EBUS:

- The Peru-Chile upwelling system (e.g., Sobarzo & Figueroa, 2001; Marlín *et al.*, 2001);
- The Benguela upwelling system (e.g., Shillington *et al.*, 1990; Lutjeharms *et al.*, 1991; Nelson *et al.*, 1998; Cury & Shannon, 2004);
- The Canary Upwelling System (e.g., Haynes *et al.*, 1993; Hagen *et al.*, 1996; Barton *et al.*, 1998; Barton & Arístegui, 2004; Pelegrí *et al.*, 2005).

These surveys aimed to explain how the export of nutrient-rich, upwelled waters into the subtropical oligotrophic ocean takes place and what is its role on the enhancement of

Table 1.2: Typical scales of the filaments off NW Africa and the Iberian coast (Kostianoy & Zatsepin, 1996; Barton et al., 1998; Peliz et al., 2002; Pelegrí et al., 2005).

Scale	Unit	Value
Length	km	100-250
Width	km	10-75
Depth	m	100-150
Time of activity	days	3-10
T° difference	°C	1-2.5

primary production. The characteristic dimensions of the filaments located in the Canary Uwpelling System, obtained from previous cruises, are summarized in Table 1.2.

More recently, the project *Canaries-Iberian marine ecosystem Exchanges* (CAIBEX) was dedicated to the study of the physical and biological processes responsible for an enhancement of the production in the open ocean, notably the numerous upwelling filaments existing in off the coast of Galicia and NW Africa. In particular, the third leg of this project was conducted in the area near to Cape Ghir, with the objective of getting a high-resolution sampling of the filament properties. Analysis of data obtained during this cruise are the object of Chapter 4.

In order to assess the quantity of measurements available in the studied region, the temperature observations at 50 m deep are shown for the period 1900-2009 in March and September (Fig. 1.11). These data are obtained from the World Ocean Database 2009 (WOD09, Boyer *et al.*, 2009), available on-line at `http://www.nodc.noaa.gov/OC5/SELECT/dbsearch/dbsearch.html`. In this case, all the available instruments are selected.

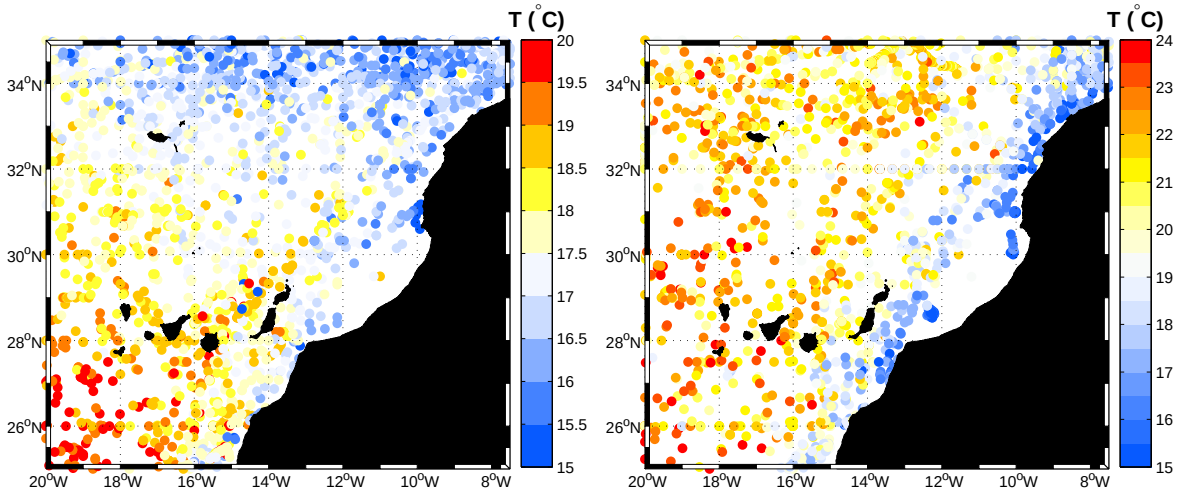

Figure 1.11: In situ temperature interpolated at 50 m in March (left) and September. Note the different color bars.

Even in this raw format, the maps provide a description of the main temperature features in the Canary upwelling system: the coastal upwelling is visible for both months,

with temperatures down to 15°C, while the open interior exhibits significantly higher values. Signals of cool water around 150-200 km west of the coast may be the due to the presence of a filament at the time of the measurements. In March, highest values occur in the lee of the Canary islands.

The maps also show that the number of data in the region of Cape Ghir is limited, considering that more than 100 years of measurements have been gathered. Furthermore the coastal area roughly comprised between 28°N and 30°N is almost void of data. The reason for this apparent lack of data is that the number of cruises was limited, or simply that some data have not have reached the database yet.

Remote sensing imagery

Due to their particular physical (low SST) and biological (high chlorophyll *a* concentration) characteristics, upwelling filaments suit particularly well to remote sensing imagery. Yet in the 1970, Bernstein *et al.* (1977) observed filaments – referred to as *cold tongues* at that time – and eddy structures in the California Current upwelling system, with visible and infrared satellite images. The in situ measurements obtained through the California Cooperative Oceanic Fisheries Investigations (CalCOFI, `http://www.calcofi.org/`) program permitted the validation of the satellite observations and the estimation of the vertical extent of the tongues.

With the advancements made in the domain of satellite imagery, other studies focused on the California Current system. Ikeda & Emery (1984) observed that the cold tongues extended preferentially from topography irregularities, in this case Cape Blanco, Cape Mendocino and Heceta Bank, a shallow submarine bank. By combining in situ data and satellite infrared images, Flament (1985) studied the evolution of a filament near Point Arena (38°55'N, 123°42'W). All these satellite data provided useful information about the filament typical scales and an insight into the mechanism responsible for their development.

One decade later, several satellite imagery analysis were carried off NW Africa and allowed the identification of the sites favorable to filament formation. Van Camp *et al.* (1991) analyzed SST from the Advanced Very High Resolution Radiometer (AVHRR) and chlorophyll pigment concentrations from the Coastal Zone Color Scanner (CZCS), and described mesoscale patters apparent in the upwelling front. Gabric *et al.* (1993) focused on the Cape Blanc filament with the help of phytoplankton pigment concentration images. This filament is frequently called the Cape Blanc *giant filament*, as it is a permanent structure with offshore extension of several hundred kilometers. Kostianoy & Zatsepin (1996) evaluated the exchange due to upwelling filaments in the Canary Current upwelling system, between 15°N and 25°N. Estimations of velocities were obtained by García-Weill *et al.* (1994) in the areas near to Cape Ghir and Dakhla (Western Sahara, 23°43'N, 15°57'W) exploiting pair of consecutive images. With an Empirical Orthogonal Function (EOF) technique, Hernández-Guerra & Nykjaer (1997) examined the main spatial and temporal patterns of SST off NW Africa. Their region of interest encompassed the main capes, known to be related to the triggering of filaments.

1.2.3 Generation mechanisms

The combination of in situ and satellite observations lead to the conclusion that the coastline irregularities and the wind forcing both play a role in the development of the filaments. Several mechanisms were proposed, though even today, there is not an overall agreement yet.

Ikeda & Emery (1984) assumed that filaments are formed by upwelling jet meanders triggered by the topography irregularities and developed through a baroclinic instability, associated with the shear between the surface equatorward current and the poleward undercurrent. In the frame of the CTZ program, Strub *et al.* (1991) proposed a set of mechanisms explaining the generation of these structures:

1. The *squirts*, created by the convergence of coastal wind-driven currents, or by the deflection of the flow by topographic obstacles, such as capes or offshore ridges.
2. The meandering of the equatorward jet, possibly induced by a baroclinic instability.
3. The jet inside a field of synoptic-mesoscale eddies. This hypothesis was also advanced by Mooers & Robinson (1984) and by Lutjeharms *et al.* (1991) for the Benguela upwelling system.

Most of the observations of filaments share a common characteristic: they are associated with irregularities of the coastline, or more generally, of the topography. Along the coast of NW Africa, numerous capes are known to be frequently affected by filaments, typically off Cape Ghir, Cape Juby, Cape Bojador and Cape Blanc (see Fig. 1.14 for the location of the main capes). Concerning the Cape Ghir filament, Hagen *et al.* (1996) proposed that the Cape Ghir Plateau (CGP hereinafter) located between between Cape Ghir and Cape Sim, was responsible for the formation of filaments. Along the Iberian Peninsula, Peliz *et al.* (2002) identified the Aveiro Canyon (41°45'N) as a possible trigger for the filaments. Castelao & Barth (2007) studied the effect of a cape in the separation of a jet. With an idealized model, they showed that when the radius of the cape increases (i.e., a more rounded cape), the separation takes longer to occur.

The wind has also be proposed as a possible engine for the filament. Brink & Cowles (1991) suggested that the role of the wind was only to drive the California Current, which then would become unstable. Castelao & Barth (2007) analyzed the impact of wind on the separation: an increased magnitude of the wind curl induces an earlier establishment of offshore jet, while a wind stress intensification itself does not promote detachment.

The *upwelling undercurrent*, an along-slope, poleward flow characteristic of the upwelling systems (e.g., Barton, 1989; Haynes & Barton, 1990), was assumed to interact with the upwelling jet, leading to the propagation of the flow further offshore and preventing it from returning to the shelf (e.g., Barth *et al.*, 2000; Peliz *et al.*, 2002).

Marshall & Tansley (2001) examined the conditions suitable to jet separation: according to their analytical developments, $\beta-$effect enhances the separation of eastern-boundary currents, while the separation is enhanced when such a jet flows in a direction where its depth increases (i.e., $\mathbf{u} \cdot \boldsymbol{\nabla} h > 0$).

To summarize, the processes assumed to play a role in the generation of an upwelling filament:

1. Interaction of the jet with the topography (capes and submarine banks).
2. Interaction of the jet with the undercurrent.
3. Influence of wind and wind curl.

The generation mechanism is further investigated in Chapter 3, where a high-resolution numerical model in implemented around Cape Ghir.

1.3 Modeling effort

As we have seen in Section 1.1.2, the basic mechanism of an upwelling is relatively simple: the Ekman transport generated by an along-shore wind (with a favorable direction) is compensated by an upward transport of deeper water. However, the detailed flow picture is more complicated. The low pressure created along the coast is responsible from an alongshore current, due to geostrophy. In the lower layer, a vertical stretching of the water column takes place, generating relative vorticity and a shear flow. The vertical displacement of the isopycnal surfaces creates lateral density gradients, which in turn are responsible for a vertical shear (*thermal wind* relation).

Moreover, we will have to take into account that:

- Wind is rarely uniform, neither in space, nor in time: there are periods of wind relaxation, intensification, but also change of wind direction and spatial structure.
- Coasts are not straight and bottom is not flat, then a sufficiently high resolution is necessary to accurately take them into consideration.

In this section we present an analytical model of upwelling and then concentrate our attention to regional models implemented in the Canary Upwelling system.

1.3.1 Concept of vorticity

As *vorticity* is involved in several analytical models of upwelling, but also in the generation mechanism of filaments proposed in Chapter 3, a few developments are provided here.

Absolute, relative and planetary vorticity

The vorticity of a fluid parcel is defined as the curl (or rotational; $\boldsymbol{\nabla}\times$ in mathematic symbols) of the velocity field $\mathbf{u}$ (e.g., Pedlosky, 1987):

$$\boldsymbol{\zeta} = \boldsymbol{\nabla} \times \mathbf{u}. \tag{1.1}$$

The *absolute* vorticity $\boldsymbol{\zeta_a}$ is simply the curl of the absolute velocity. In the case of the Earth, the absolute velocity is made up of the relative velocity and the Earth own velocity, i.e., $\mathbf{u_a} = \mathbf{u} + \boldsymbol{\Omega} \times \mathbf{r}$, where $\mathbf{r}$ is the position vector and Ω the Earth rotation speed. After simplifications, $\boldsymbol{\zeta_a}$ is expressed as:

$$\boldsymbol{\zeta_a} = \boldsymbol{\zeta} + 2\boldsymbol{\Omega}. \tag{1.2}$$

The second term of the previous equation is referred to as *planetary* vorticity. The vertical component of the relative vorticity is obtained by multiplying Eq. (1.1) by a vertical unit vector $\mathbf{k}$:

$$\mathbf{k} \cdot (\boldsymbol{\nabla} \times \mathbf{u}) = \frac{\partial v}{\partial x} - \frac{\partial u}{\partial y} = \zeta, \tag{1.3}$$

The vertical component of the planetary vorticity is:

$$2\boldsymbol{\Omega} \cdot \mathbf{k} = 2\Omega \sin\lambda = f, \tag{1.4}$$

where λ is the latitude.

Potential vorticity

For a barotropic fluid, the potential vorticity is the ratio between the sum of the planetary and relative vorticity, and the water column depth. The vertical component is

$$q = \frac{f + \zeta}{h} = \frac{f + \left(\frac{\partial v}{\partial x} - \frac{\partial u}{\partial y}\right)}{h} \tag{1.5}$$

From this simple definition, several mechanisms that modify the potential vorticity appear:

1. The change of the Coriolis parameter by moving north or south (β effect).
2. The change of the flow relative vorticity.
3. The squeezing/stretching of the water column.

The expression is also valid for layered flows, provided h is defined as a differential thickness, dependent on the density vertical structure (Cushman-Roisin & Beckers, 2011):

$$h = -\Delta\rho \frac{\partial z}{\partial \rho}, \tag{1.6}$$

where $\Delta\rho$ is an arbitrary density difference.

Shear and orbital vorticity

If the relative vorticity is now expressed in natural coordinates ($\boldsymbol{\tau}$ along the jet, $\mathbf{n}$ across the jet), Eq. (1.3) reads:

$$\zeta = \frac{\partial V}{\partial n} - \kappa V, \tag{1.7}$$

with $V = \sqrt{u^2 + v^2}$, the flow velocity, and κ, the curvature. The first term of (1.7) is called *shear vorticity* and the second one *orbital vorticity* (Cushman-Roisin, 1993; Cushman-Roisin & Beckers, 2011). In the presence of large meridional displacements of the jet, the β effect also have to be considered in the vorticity balance.

1.3.2 Analytical models of upwelling

Numerous analytical models of upwelling were developed during the 1960-1970's (Hsueh & O'Brien, 1971; Hsueh & Kenney, 1972; Allen, 1973; Hurlburt & Thompson, 1973; Pedlosky, 1974, 1978a,b). They mainly differ by their working hypotheses and their degree of realism:

- homogeneous or stratified fluid;
- infinite depth, flat bottom or sloping bottom;
- f-plane or β-plane;
- uniform or non-uniform wind forcing.

The interest of these models is the possibility to examine the effects of the conditions on the realism of the solution and the deduction of orders of magnitude for the characteristic dimensions of an upwelling.

Here we present a simple analytical model, with the goal of deducing the typical time and space scales, and getting an insight on the mechanism. It is based on the model presented in Cushman-Roisin & Beckers (2011).

A linear upwelling model

The situation to be analyzed is summarized in Fig. 1.12: The wind acts along a vertical located on its left. The lower layer is assumed infinitely deep and motionless.

We also make the following assumptions:

1. reduced-gravity ocean on an $f-$plane;
2. we are in the northern hemisphere ($f > 0$);
3. there are no alongshore variations ($\frac{\partial \cdot}{\partial y} = 0$).

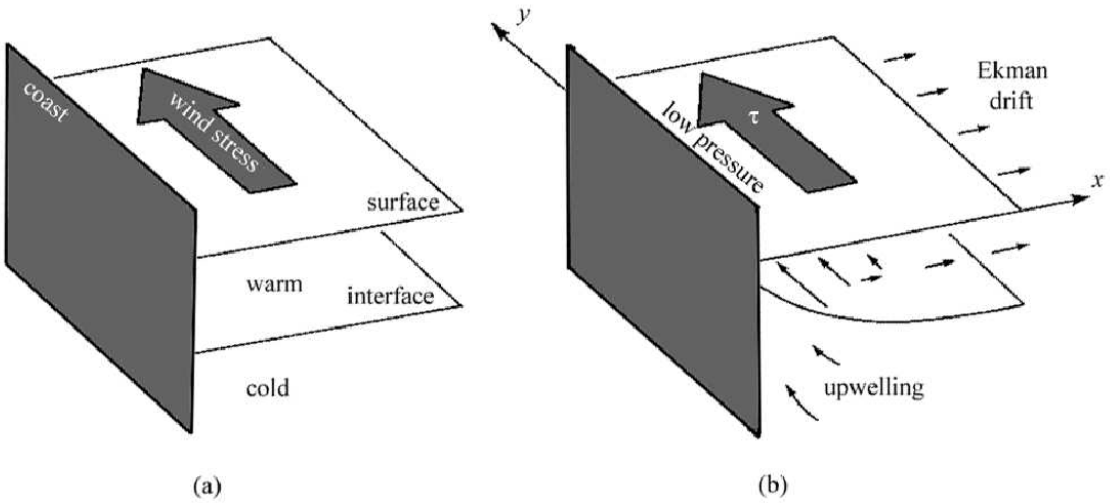

Figure 1.12: Schema of the coastal upwelling model. The wind blowing along the coast and toward the equator (a) generates an offshore Ekman transport, balanced by the upward motion of deep water (b). From Cushman-Roisin & Beckers (2011).

Equations: the translation of the previous assumptions provides:

$$\frac{\partial u}{\partial t} + u\frac{\partial u}{\partial x} - fv = -g'\frac{\partial h}{\partial x}, \tag{1.8a}$$

$$\frac{\partial v}{\partial t} + u\frac{\partial v}{\partial x} + fu = \frac{\tau}{\rho_0 h}, \tag{1.8b}$$

$$\frac{\partial h}{\partial t} + \frac{\partial}{\partial x}(hu) = 0, \tag{1.8c}$$

with the x and y axis as in Fig. 1.12 and $g' = \frac{\Delta\rho}{\rho_0}g$ the reduced gravity. We define $h = H - a$, where H is the depth of the undisturbed upper layer and a a small upward displacement of the interface. After linearization, the system (1.8a)-(1.8c) becomes:

$$\frac{\partial u}{\partial t} - fv = g'\frac{\partial a}{\partial x}, \tag{1.9a}$$

$$\frac{\partial v}{\partial t} + fu = \frac{\tau}{\rho_0 h}, \tag{1.9b}$$

$$-\frac{\partial a}{\partial t} + H\frac{\partial u}{\partial x} = 0. \tag{1.9c}$$

Initial and boundary conditions: we assume an initial state at rest, a zonal velocity equal to zero at the coast, and an unperturbed interface far from the coast. These three conditions reads:

$$\begin{aligned} u = v = a &= 0 \qquad \text{for } t = 0, \\ u &= 0 \qquad \text{at } x = 0, \\ a(x,t) &= 0 \qquad \text{for } x \to +\infty. \end{aligned}$$

Forcing: we consider time-fluctuating winds, represented by $\tau = \tau_0 \sin(\omega t)$, where τ_0 is constant in both space and time.

Solution: the structure of the system (1.9a)-(1.9c) invites to try a solution of the form:

$$u = u_0(x)\sin(\omega t), \tag{1.10a}$$
$$v = v_0(x)\cos(\omega t), \tag{1.10b}$$
$$a = a_0(x)\cos(\omega t). \tag{1.10c}$$

The substitution and the use of boundary and initial conditions yield the solution:

$$u_0(x) = \frac{f\tau_0}{\rho_0 H(f^2-\omega^2)}\left[1-\exp\left(-\frac{x}{R_\omega}\right)\right], \tag{1.11}$$
$$v_0(x) = \frac{\omega\tau_0}{\rho_0 H(f^2-\omega^2)}\left[1-\frac{f^2}{\omega^2}\exp\left(-\frac{x}{R_\omega}\right)\right], \tag{1.12}$$
$$a_0(x) = \frac{-f\,R_\omega\tau_0}{\rho_0 g' H-\omega}\exp\left(-\frac{x}{R_\omega}\right), \tag{1.13}$$

where the *modified deformation radius* has been defined as:

$$R_\omega = \sqrt{\frac{g'H}{f^2-\omega^2}}. \tag{1.14}$$

Interpretation: from this simple model, we can deduce that:

1. The upwelling signal is concentrated in a region comprised between the coast and a distance on the order of R_ω offshore.

2. For long periods of wind blowing, i.e., wind blows in the same direction during a long time longer than the inertial period ($f \gg \omega$), we have

$$R_\omega = \frac{\sqrt{g'H}}{f},$$

the radius of deformation. The vertical displacement a tends to increase since it is proportional to the ratio f/ω. Far offshore ($x \to +\infty$), the solution simplifies:

$$\begin{aligned} u &= \frac{\tau_0}{\rho_0 f H}\sin(\omega t), \\ v &= 0, \end{aligned}$$

that is to say, an Ekman drift.

3. For short period ($\omega > f$), R_ω is imaginary: the solution consists in oscillations and inertia-gravity waves propagating offshore.

Order of magnitude: with the typical values of the parameters

$$\begin{aligned} \mathcal{O}(g') &= \frac{1}{1000}10 = 10^{-2} m/s^2, \\ \mathcal{O}(H) &= 10^2 m, \\ \mathcal{O}(f) &= 10^{-4} s^{-1}, \end{aligned}$$

and if we assume that ($f \gg \omega$), we get $\mathcal{O}(R_\omega) = \sqrt{\frac{10^{-2}10^2}{10^{-8}}} \simeq 100$ km.

Finite-amplitude upwelling

This term refers to the case where the wind is sufficiently strong and blows for a sufficiently long time to force the density interface to reach the surface and generates a front. If winds keeps on blowing, the front moves offshore, and the cool water of the lower layer is exposed. In this situation, the non-linear terms of the equations cannot be discarded.

Equations: Eq. (1.8a) can be written as

$$\frac{d}{dt}(v + fx) = \frac{\tau}{\rho_0 h}. \tag{1.15}$$

If we define the derivation operator $\frac{d}{dt} = \frac{\partial}{\partial t} + u\frac{\partial}{\partial x}$, which represents the time derivative following a particle: $\frac{\partial}{\partial t}$ takes into account variations due to non-stationarity, while $u\frac{\partial}{\partial x}$ models variations coming from advection.

Initial conditions: we take a rest state ($v = 0$), with the particle located at $x = x_0$.

Forcing: we consider a wind event with a finite duration, i.e., from $t = t_{start}$ to $t = t_{end}$.

Solution: we integrate Eq. (1.15) over time:

$$(v+fx)_{t_{end}} - (v+fx)_{t_{start}} = \int_{t_{start}}^{t_{end}} \frac{\tau}{\rho_0 h}\, dt = I,$$

where I is called *wind impulse*. As an additional approximation, we assume the wind event is short enough to allow us to use local stress value and H instead of h. In this case, we calculate the wind impulse as

$$I \cong \frac{1}{\rho_0 H} \int_{t_{start}}^{t_{end}} \tau\, dt.$$

The initial conditions provides:

$$v + f(x - x_0) = I. \tag{1.16}$$

When there is no wind, (1.15) shows that $(v+fx)$ is conserved along the particle trajectory, so that the previous relation is still valid after the wind event. After the wind event, a stationary state ($\frac{\partial}{\partial t} = 0$) is be reached, and relation (1.8c) leads to:

$$u = 0 \qquad \text{and} \qquad v = \frac{g'}{f}\frac{\partial h}{\partial x}. \tag{1.17}$$

An additional relation is obtained by assuming that the wind is laterally uniform (i.e., $\frac{\partial \tau}{\partial x} = 0$), so that no potential vorticity is provided to fluid particles. In the present case, the conservation of potential vorticity is expressed as:

$$\frac{1}{h}\left(f + \frac{\partial v}{\partial x}\right) = \frac{f}{H}. \tag{1.18}$$

The resolution of the system (1.18)-(1.17) provides:

$$v = A\sqrt{\frac{g'}{H}} \exp\left(-\frac{x}{R}\right), \tag{1.19a}$$

$$h = H - A \exp\left(-\frac{x}{R}\right), \tag{1.19b}$$

where R is the radius of deformation and A, a constant of integration related to the amplitude of the upwelling.

Two cases have to be distinguished:

1. the interface does not rise enough to reach the surface: a particle with its initial position at $x = 0$ remains there. Equation (1.16) simplifies to $I = v$. The solution at $x = 0$ reads:

$$v = A\sqrt{\frac{g'}{H}},$$
$$h = H - A.$$

The condition for having an interface below the surface is $h = h - A > 0$, translates to a condition on the wind impulse:

$$I \leq \sqrt{g'H}. \tag{1.20}$$

2. The interface forms a front. A particle initially at the coast (i.e., $x_0 = 0$) reaches a position $x = d > 0$. At $x = d$, $h = 0$ and Eq. (1.19b) gives $A = H \exp\left(\frac{-d}{R}\right)$. The alongshore velocity v is deduced from (1.19a): $v = \sqrt{g'H}$, while the displacement of the interface is related to the wind impulse through (1.16):

$$d = \frac{I - v}{f} = \frac{I}{f} - \frac{\sqrt{g'H}}{f} = \frac{I}{f} - R. \tag{1.21}$$

In order to impose a positive value to the displacement d, we must have $I > \sqrt{g'H}$.

Interpretation: from (1.21), it can be shown that d is made up of two contributions:

1. An offshore Ekman drift: $\frac{I}{f}$.
2. A geostrophic adjustment, directed toward the shore: $-R$.

1.3.3 Experimental model

Narimousa & Maxworthy (1987) studied the effects of capes on the upwelling circulation using a rotating cylinder filled with two layers of water with different densities. A half cylinder played the role of the cape (Fig. 1.13). With this system, they were able to obtain filament-like structures, created by the divergence of the flow just downstream of the cape.

1.3.4 Numerical models

The previous section was dedicated to analytical models, from which we could extract a solution under some restrictive assumptions. We now focus on the numerical models able to reproduce filaments with realistic characteristics.

Requirements

Due to the particular features of the filaments, their modeling requires a set of particular conditions:

1. A sufficiently large domain, in order to correctly reproduce the large-scale features in which the filament is embedded (main currents, coastal upwelling, ...)

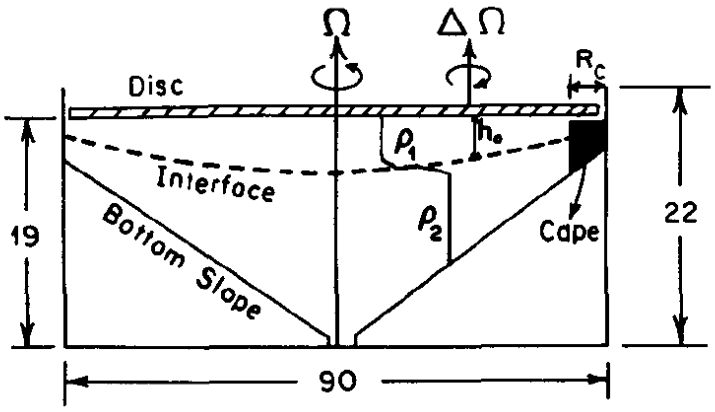

Figure 1.13: Cross section of the apparatus at the cape: the fluid in the tank is brough to rotation. The surface of the fluid is in contact with a rotating disk that models the wind stress. ρ_1 and ρ_2 denote the fluid densities, Ω the rotation speed of the tank, and R_C the radius of the cape. Lengths are measured in centimeters. Adapted from Narimousa & Maxworthy (1987).

2. A fine resolution: the filament typical width is quite small ($\mathcal{O}(10\ km)$) and the topographic features (capes, banks, ...) have to be correctly represented in the model.

These constraints often imply the use of nesting procedures along with adequate specifications of the *open boundary conditions* (OBCs).

3. The numerical dissipation has to be limited, so as to permit the simulation of instabilities.

4. The wind field has to be specified accurately, that is to say with good spatial and temporal resolutions, as it constitutes the main forcing of the upwelling.

Regional model implementation

With the improvements in computing resources, an increasing number of high-resolution models have been implemented in the four EBUS. Here we limit our review to the implementations made in the Canary Current upwelling system.

Spall (1990) used an eddy-resolving model covering the Canary basin to study the local circulation. With a horizontal resolution close to 35 km, the model could reproduce the main currents. The authors reported problems in the eddy kinetic energy values and in the representation of the Mediterranean water tongue, probably related to the specification of the OBCs.

In the framework of the CANIGO project (Canary Islands Azores Gibraltar Observations, Parrilla *et al.*, 2002), Johnson & Stevens (2000) used a 1/6°-resolution model in a region extending from the north of Portugal to the south of Canary islands, including the Azores Archipelago and the Strait of Gibraltar. Their simulations were able to generate the Cape Ghir filament, even if the horizontal resolution was not sufficient to obtain

a detailed description, and to show that the filament is stronger during the upwelling maximum.

Stevens *et al.* (2000) applied a similar model to the Iberian shelf-slope region and pointed out the need for a enhanced-resolution implementation in order to be able to model the effects of the capes. With a 1/12°-resolution model, Stevens & Johnson (2003) noted that filaments tend to appear at the same locations along the coast: at 25°30'N, 28°N (Cape Juby), 31°N (Cape Ghir) and 33°N, in agreement with satellite observations. However, their modeled filaments were too broad and penetrated too far offshore in comparison with observations.

With a 9 km-resolution model forced by seasonal wind, Batteen *et al.* (2000) studied the effects of the coastline on the eddy and filament structures in the Canary Current system. Despite using a flat bottom (4500 m depth), they were able to obtain filaments in agreement with field measurements and attached to the main capes. Their experiments underlined the role played by the wind in the generation of filaments and the importance of the coastline to obtain realistic locations. Another process-oriented study was conducted by Batteen *et al.* (2007) in the same area with a terrain-following, 3 km-resolution model. Filament structures were obtained off Cape Ghir when an iterative topography developed by Martinho & Batteen (2006) was used, while the Gaussian smoothed topography only generated little mesoscale activity.

Meunier *et al.* (2010) employed a 2-layer shallow water model on the f-plane in a simple geometric configuration to study the role of the bottom topography on the filament generations. They related the origin of filaments near a promontory with the generation of a potential vorticity anomaly when the upwelling current interacts with it.

With the objective of studying the seasonal variability of the Canary Current, Mason *et al.* (2011) implemented the ROMS model at a 7.5 km-resolution in a domain covering the northeast Atlantic. The choice of their grid and resolution allowed them to reproduce filaments at the main capes, including Cape Ghir, though their length largely exceeded the remote-sensing observations.

As the described modeling studies were not able to reproduce correctly the spatial and temporal characteristic of the Cape Ghir filament, or were centered on other regions, we used the Mason *et al.* (2008)'s model results to provide initial and boundary conditions to nested domains centered on Cape Ghir. The objective was twofold:

1. Obtain a reasonable representation of the filament.
2. Examine the mechanisms at the origin of the filaments off Cape Ghir.

To this end, several process-oriented numerical experiments were conducted. The results of these simulations are the object of Chapter 3.

1.4 The Cape Ghir region

Cape Ghir (named *Cape Heracles* in antiquity) is located on the western coast of Morocco, at 30°37'49"N, 9°53'20"W, about 40 km north of the city of Agadir. It is easily identified

on maps because of the change of concavity of the coastline (Fig. 1.14).

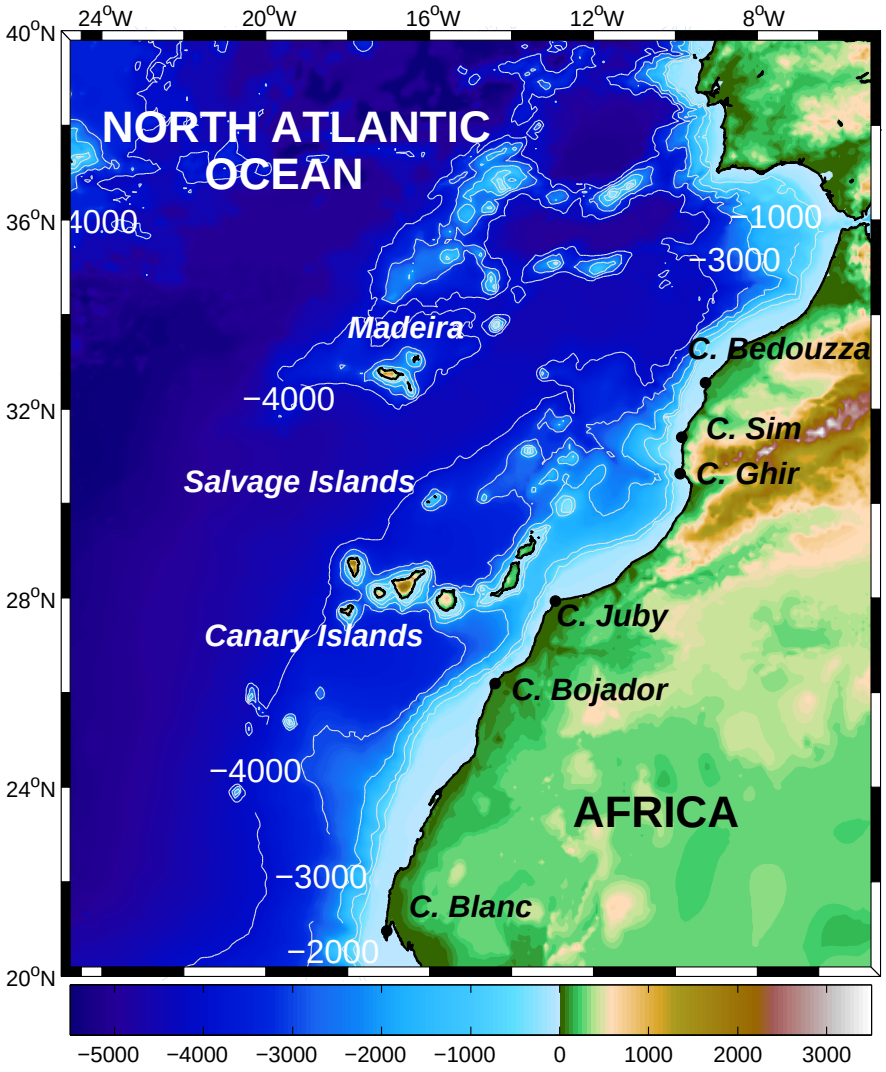

Figure 1.14: Topography of the studied region and main geographical features. Isobaths 500, 1000, 2000, 3000 and 4000 m are plotted in white.

1.4.1 Topography and bathymetry

Cape Ghir can be considered as the extension of the High Atlas range, which culminates at 4167 m above sea level (*Jbel Toubkal* mountain). The mountain range acts as as barrier that separates regions with different weather: the south, under the influence of Sahara desert and the north, with a Mediterranean climate.

The continental shelf is generally narrow along the northern part of the coast and wider along the southern part. Between Cape Ghir and Cape Sim (Fig. 1.14), a westward extension of the shelf is visible. This submarine bank is called the *Cape Ghir Plateau* (Hagen *et al.*, 1996) and is believed to play a role similar to other topographic features in the California Upwelling System: Heceta Bank (44°10'N, 124°45'W; e.g., Peffley &

O'Brien, 1976) or the submarine extension of Cape Mendocino (40°26'N, 124°25'W; e.g., Ikeda & Emery, 1984).

Within the Canary upwelling system lie two main archipelagos: Madeira and the Canary islands. The smallest Salvage islands (Portugal) are located between these two archipelagos at 30°4'N, 15°56'W.

1.4.2 Atmospheric features

Seasonal cycle

It is relevant to analyze the seasonal cycle of the atmospheric fields around Cape Ghir, in order to understand their influence on the water column dynamics. Here we used climatological atmospheric fields that we interpolated onto a position close to Cape Ghir. The point for the interpolation (31°N, 12°W) was chosen offshore in order to obtain conditions representative of the open ocean.

According to the meridional shift of the Azores high, the trade winds display marked seasonal variations (Wooster *et al.*, 1976). Strongest winds occur during summer months, with mean values above 8 m/s (Fig. 1.15). The intensity strongly decreases in winter and reaches values 50% lower than in summer. The freshwater flux (precipitation minus evaporation) is weak all year long (Fig. 1.16). Maximal precipitations usually occurs in winter, under the effect of Atlantic low-pressure systems. Short-wave radiations (Fig. 1.17) are maximal in June-July values with exceeding 250 W/m^2. The surface net heat flux is positive for most of the year, except from November to January-February.

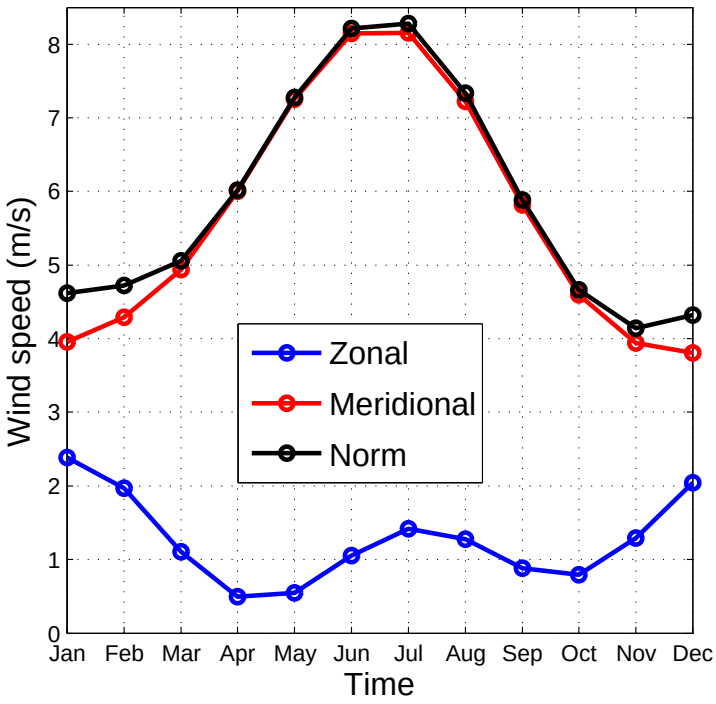

Figure 1.15: Monthly wind speed from SCOW, interpolated at 31° N, 12° W.

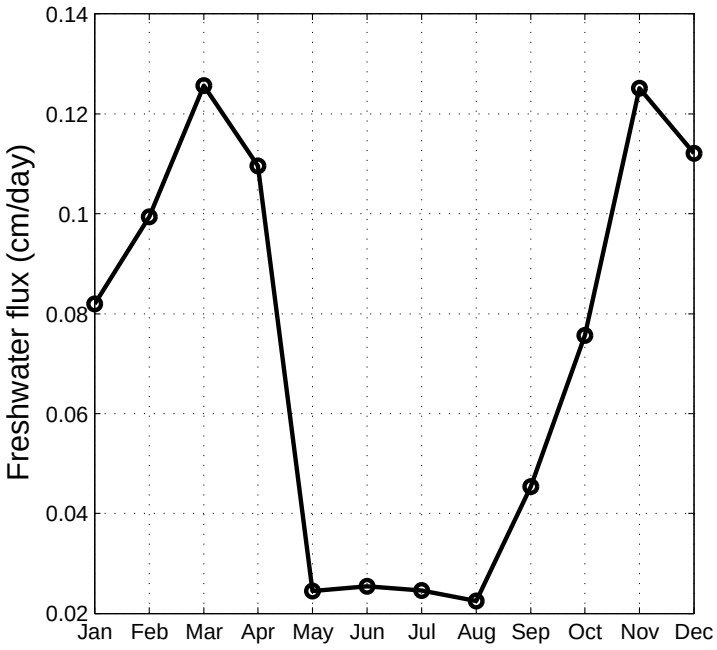

Figure 1.16: Monthly freshwater flux from COADS, interpolated at 31° N, 12° W.

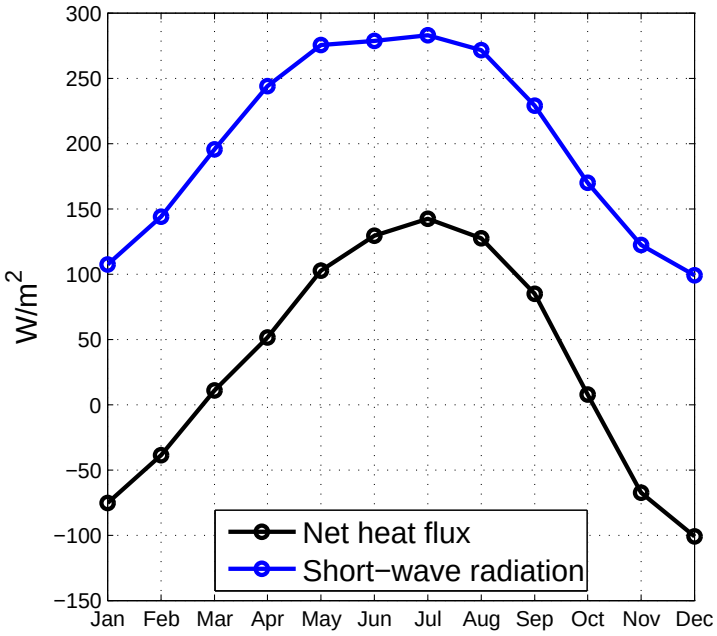

Figure 1.17: Monthly net heat flux and short-wave radiation from COADS, interpolated at 31° N, 12° W.

This set of atmospheric conditions drives the seasonal cycle of the mixed-layer depth (MLD), as shown in Fig. 1.18. The MLD was extracted from the 1994 version of the World Ocean Atlas (WOA94, Monterey & Levitus, 1997) at a grid point close to Cape Ghir. The situation is similar to the waters south of the Canary islands, as described in Troupin *et al.* (2010), who used a one-dimension model at 27°30'N, 15°30'W (south of Gran Canaria island) to study the seasonal cycle in that area. They showed that the development of a deep mixed layer (> 100 m) takes place in winter, under the effect of convective mixing. In spring, the stratification progressively strengthens until it reaches a minimum (below 20 m) in summer. The highest temperature are in late September-early October, when the net heat flux is still high, but the trade winds have weakened. The corresponding temperature field for the first 200 m of the water column is shown in Fig. 1.19.

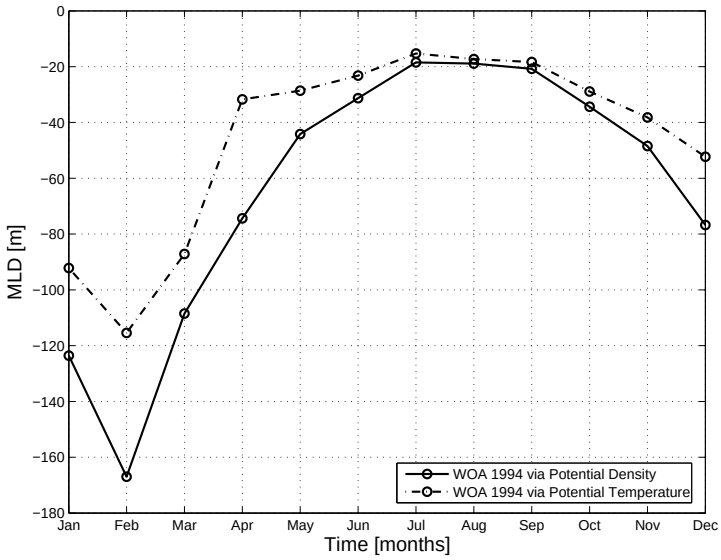

Figure 1.18: Seasonal cycle of the mixed-layer depth from the WOA94.

Aerosol input

Due to its proximity to the Sahara and Sahel deserts, the Cape Ghir region is frequently affected by input of aeolian dust. The dust input episodes, locally known as *calima*, generally last between 1 and 8 days, with a mean duration of 3 days. They tend to occur more frequently in winter, but with a strong inter-annual variability (Torres-Padrón *et al.*, 2002; Alonso-Pérez *et al.*, 2007). They are often associated with a rise of temperature and a decrease of relative humidity.

The most obvious impact is the reduced visibility, as evidenced by the satellite picture at the beginning of this chapter (p. 3). This results in perturbations in the satellite images, as dust may act similarly to clouds.

Dust inputs also play an important role from the point of view of biogeochemical cycles: the dust intrusion provide trace elements, such as aluminum, iron and manganese. Increases of chlorophyll *a* concentration and small phytoplankton induced by a dust storm

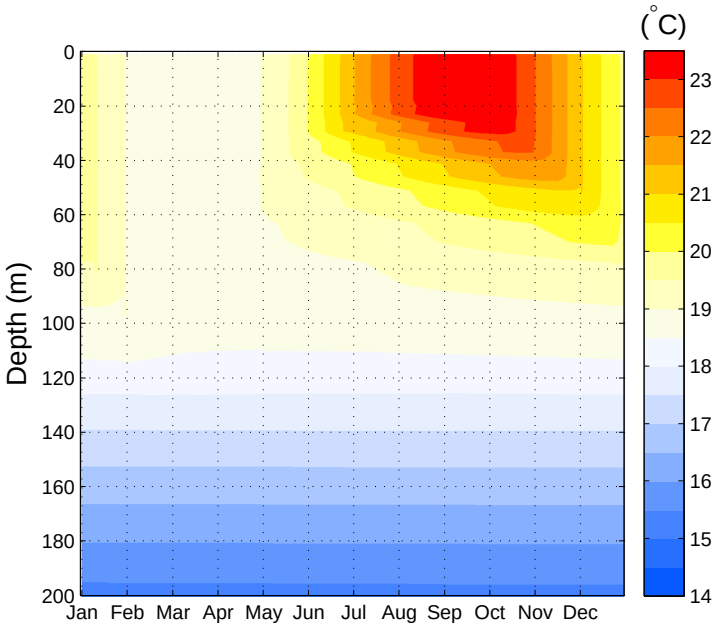

Figure 1.19: Seasonal cycle of the temperature obtained with the ROMS-1D model.

in February 2000 have been documented (Hernández-León *et al.*, 2004). According to Neuer *et al.* (2004), higher aerosol concentrations do not provoke higher primary production, though they did not discard the simulation of phytoplankton by the iron input. Jickells *et al.* (2005) stated that an atmospheric input of iron was necessary to sustain phytoplankton primary production in the open ocean.

Changes have been observed over the last decades: in the subtropical Eastern North Atlantic region, Alonso-Pérez *et al.* (2011) described an increase if the number of African dust intrusions, related to an intensification and an eastward shift of the Azores high.

1.4.3 Oceanographic characteristics

Currents

The main current of our region of study is the Canary Current, which lies between the Strait of Gibraltar and Cape Blanc. It is the extension of the Azores Current, which travels eastward between 32 and 35°N (Klein & Siedler, 1989). The Azores Current is the southern branch of the Gulf Stream and constitutes the northern part of the North Atlantic subtropical gyre. The Canary Current turns westward just north of the Cape Verde frontal zone, where it becomes the North Equatorial Current (Stramma & Schott, 1999). The latter constitutes the southern limb of the North Atlantic subtropical gyre. The Canary Current is present between the surface and 700-800 m depth. Its transport is estimated at 3 Sv (Stramma, 1984). Mason *et al.* (2011) related the seasonal variability of the current to counter-rotating structures generated close to Africa. An undercurrent circulates along the slope at depths near 300 m, coming from a region south of Cape Blanc (Gabric *et al.*, 1993; Machín *et al.*, 2006).

Close to Cape Ghir, other promontories have been shown to be the starting points of upwelling filaments: Cape Juby and Cape Bojador (Hernández-Guerra *et al.*, 1993).

When strongly developed, these filaments can reach some of the Canary islands and interact with the eddy field generated in their lee (e.g., Arístegui *et al.*, 1997; Barton *et al.*, 2004; Arístegui & Montero, 2005). The interest of studying the Cape Ghir filament specifically is that it is almost permanent, even in case of non upwelling favorable wind, and that it is not affected by the additional mesoscale activity generated by the islands.

Water masses

The temperature-salinity diagram (T-S diagram) constructed with the data available in the zone 7.5-20°W, 25-35°N (Fig. 1.20) reveals the existence of four distinct regions: two with a large variability and two with a tight T-S relationship (e.g., Hernández-Guerra *et al.*, 2001; Machín *et al.*, 2006). The four main water masses found are:

1. the Eastern North Atlantic Central Water (ENACW),
2. the Mediterranean Water (MW),
3. the Antarctic Intermediate Water (AAIW) and
4. the North Atlantic Deep Water (NADW).

Their main characteristics are summarized in Tab. 1.3. Apart from these four well-defined types, the surface waters (SW) are found in the first 100 m of the water column. They are characterized by a strong variability, due to the air-sea interactions and to the influence of the coastal upwelling.

According to the origin of the ENACW, two types are distinguished (e.g., Harvey, 1982): the subtropical type ($13°C<\mathrm{T}<15°C$) and the subpolar type ($11°C<\mathrm{T}<13°C$). The ENACW is the constituent of the main thermocline. In the lower thermocline lie the MW, contained in subsurface eddies (*meddies*) and the AAIW, carried by a northward current. An elegant way to delimit the different water masses is the isoneutral density (Jackett & McDougall, 1997). Machín *et al.* (2006) applied this method to four hydrographic cruises carried out north of the Canary archipelago. Their criteria for the neutral density are also summarized in Tab. 1.3.

Table 1.3: Water mass characteristics in the Canary Current system.

Water mass	Depth (m)	Temperature (°C)	Salinity	Neutral density (kg/m^3)
ENACW	$100 \leq d \leq 700$	$10 \lesssim T \lesssim 17$	$35 \lesssim T \lesssim 37$	$27.65 \leq \gamma_n < 27.38$
MW	$700 \leq d \leq 1600$	$T \lesssim 17$	$S \gtrsim 35.5$	$27.38 \leq \gamma_n < 27.922$
AIW	$700 \leq d \leq 1600$	$T \gtrsim 5$	$S \lesssim 35.3$	$27.38 \leq \gamma_n < 27.922$
NADW	$1600 \leq d \leq 4000$	$T \lesssim 6$	$34.8 \lesssim T \lesssim 35.6$	$\gamma_n \leq 27.922$

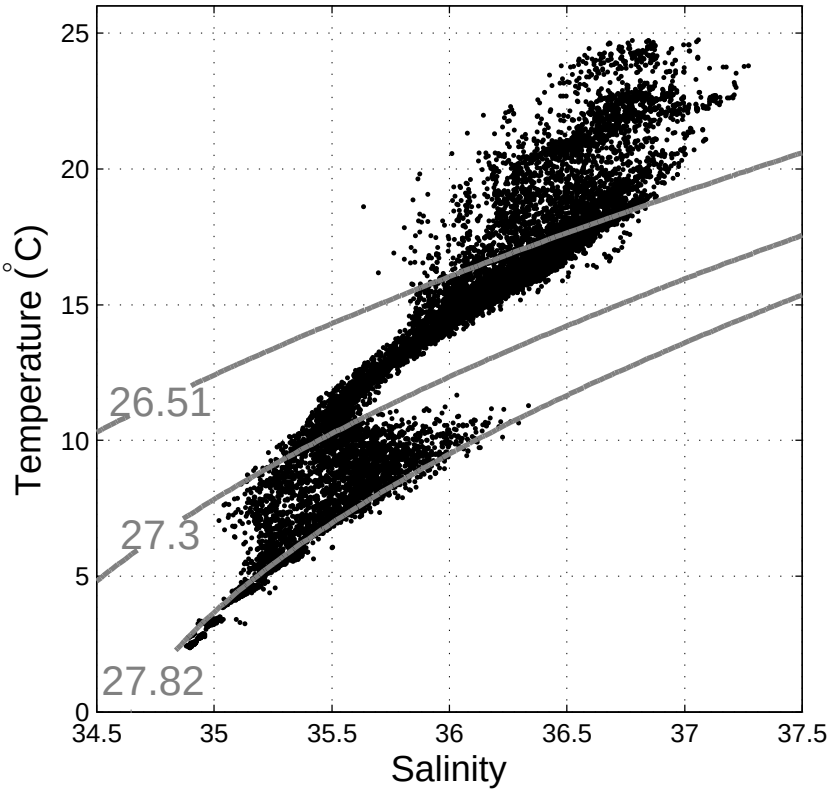

Figure 1.20: T-S diagram constructed using all the CTD data from the WOD09 in the Canary Current region (25°-35°N, 7°30'-20°W; same area as Fig. 1.11). Isoneutrals 26.51, 27.3 and 27.82 kg/m^3 separate different water masses.

References

Alexander, V. & Niebauer, H. J. (1981). Oceanography of the eastern Bering Sea ice-edge zone in spring. *Limnology and Oceanography*, **26(6)**: 1111–1125. URL http://www.jstor.org/pss/2835880

Allen, J. S. (1973). Upwelling and coastal jets in a continuously stratified ocean. *Journal of Physical Oceanography*, **3**: 245–257. doi:10.1175/1520-0485(1973)003<0245:UACJIA>2.0.CO;2.

Alonso-Pérez, S., Cuevas, E., Pérez, C., Querol, X., Baldasano, J. M., Draxler, R. & De Bustos, J. J. (2011). Trend changes of African airmass intrusions in the marine boundary layer over the subtropical Eastern North Atlantic region in winter. *Tellus B*, **63(2)**: 255–265. doi:10.1111/j.1600-0889.2010.00524.x. URL http://onlinelibrary.wiley.com/doi/10.1111/j.1600-0889.2010.00524.x/full

Alonso-Pérez, S., Cuevas, E., Querol, X., Viana, M. & Guerra, J. (2007). Impact of the Saharan dust outbreaks on the ambient levels of total suspended particles (TSP) in the marine boundary layer (MBL) of the Subtropical Eastern North Atlantic Ocean. *Atmospheric Environment*, **41(40)**: 9468–9480. doi:10.1016/j.atmosenv.2007.08.049. URL http://www.sciencedirect.com/science/article/B6VH3-4PKPH2D-2/2/abff8ec97022928d7f9bfda8cf5dad59

Álvarez-Salgado, X., Arístegui, J., Barton, E. D. & Hansell, D. A. (2007). Contribution of upwelling filaments to offshore carbon export in the subtropical Northeast Atlantic Ocean. *Limnology and Oceanography*, **52(3)**: 1287–1292. doi:10.4319/lo.2007.52.3.1287. URL http://www.aslo.org/lo/toc/vol_52/issue_3/1287.pdf

Arístegui, J., Álvarez Salgado, X. A., Barton, E. D., Figueiras, F. G., Hernández-León, S., Roy, C. & Santos, A. M. P. (2006). Oceanography and Fisheries of the Canary Current/Iberian region of the eastern North Atlantic. In A. Robinson & K. Berink (eds.), *The Sea: The Global Coastal Ocean: Interdisciplinary Regional Studies and Synthesis*, vol. 14, pp. 878–931. Harvard Univ. Press.

Arístegui, J. & Montero, M. F. (2005). Temporal and spatial changes in plankton respiration and biomass in the Canary Islands region: the effect of mesoscale variability. *Journal of Marine Systems*, **54(1-4)**: 65–82. doi:10.1016/j.jmarsys.2004.07.004.

Arístegui, J., Tett, P., Hernández-Guerra, A., Basterretxea, G., Montero, M. F., Wild, K., Sangrà, P., Hernández-León, S., Cantón, M., García-Braun, J., Pacheco, M. & Barton, E. D. (1997). The influence of island-generated eddies on chlorophyll distribution: a study of mesoscale variation around Gran Canaria. *Deep-Sea Research I*, **44**: 71–96. doi:10.1016/S0967-0637(96)00093-3.

Bakun, A. (1990). Global climate change and intensification of coastal ocean upwelling. *Science*, **247(4939)**: 198 –201. doi:10.1126/science.247.4939.198.

Barth, J. A., Pierce, S. D. & Smith, R. L. (2000). A separating coastal upwelling jet at Cape Blanco, Oregon and its connection to the California Current system. *Deep-Sea Research II*, **47**: 783–810. doi:10.1016/S0967-0645(99)00127-7.

Barton, E. (1989). The poleward undercurrent on the eastern boundary of the subtropical North Atlantic. In S. J. Neshyba, C. N. K. Mooers, R. L. Smith & R. T. Barber (eds.), *Poleward Flows along Eastern Ocean Boundaries*, pp. 82–95. Springer-Verlag, New York.

Barton, E. D. & Arístegui, J. (2004). The Canary Islands Coastal Transition Zone: Upwelling, eddies and filaments. *Progress in Oceanography*, **62(2-4)**: 67–69. doi:10.1016/j.pocean.2004.08.003.

Barton, E. D., Arístegui, J., Tett, P., Cantón, M., García-Braun, J., Hernández-León, S., Nykjaer, L., Almeida, C., Almunia, J., Ballesteros, S., Basterretxea, G., Escánez, J., García-Weill, L., Hernández-Guerra, A., López-Laatzen, F., Molina, R., Montero, M. F., Navarro-Pérez, E., Rodríguez, J. M., van Lenning, K., Vélez, H. & Wild, K. (1998). The transition zone of the Canary Current upwelling region. *Progress in Oceanography*, **41**: 455–504. doi:10.1016/S0079-6611(98)00023-8.

Barton, E. D., Arístegui, J., Tett, P. & Pérez, E. N. (2004). Variability in the Canary Islands area of filament-eddy exchanges. *Progress in Oceanography*, **62**: 71–94. doi:10.1016/j.pocean.2004.07.003.

Batteen, M. L., Martinez, J. R., Bryan, D. W. & Buch, E. J. (2000). A modeling study of the coastal eastern boundary current system off Iberia and Morocco. *Journal of Geophysical Research*, **105(C6)**: 14173–14195. doi:10.1029/2000JC900026.

Batteen, M. L., Martinho, A. S., Miller, H. A. & McClean, J. L. (2007). A process-oriented modelling study of the coastal Canary and Iberian Current system. *Ocean Modelling*, **18(1)**: 1–36. doi:10.1016/j.ocemod.2007.02.006.
URL http://www.sciencedirect.com/science/article/pii/S1463500307000376

Beardsley, R. C. & Lentz, S. J. (1987). The coastal ocean dynamics experiment collection: An introduction. *Journal of Geophysical Research*, **92(C2)**: 1455–1463. doi:10.1029/JC092iC02p01455.

Behrenfeld, M. J. & Falkowski, P. G. (1997). Photosynthetic rates derived from satellite-based chlorophyll concentration. *Limnology and Oceanography*, **42(1)**: 1–20.
URL http://www.jstor.org/stable/2838857

Belkin, I. M. (2009). Rapid warming of Large Marine Ecosystems. *Progress in Oceanography*, **81(1-4)**: 207–213. doi:10.1016/j.pocean.2009.04.011.

Bernstein, R. L., Breaker, L. & Whritner, R. (1977). California Current eddy formation: Ship, air, and satellite results. *Science*, **195(4276)**: 353–359. doi:10.1126/science.195.4276.353.

Boyer, T. P., Antonov, J. I., Baranova, O. K., Garcia, H. E., Johnson, D. R., Locarnini, R. A., Mishonov, A. V., O'Brien, T. D., Seidov, D., Smolyar, I. V. & Zweng, M. M. (2009). World Ocean Database 2009, Chapter 1: Introduction. Tech. rep., National Oceanographic Data Center, Ocean Climate Laboratory, Washington, D.C. 216 pp.
URL ftp://ftp.nodc.noaa.gov/pub/WOD09/DOC/wod09_intro.pdf

Brink, K. (1983). The near-surface dynamics of coastal upwelling. *Progress in Oceanography*, **12**: 223–257. doi:10.1016/0079-6611(83)90009-5.

Brink, K. H. & Cowles, T. J. (1991). The coastal transition zone experiment. *Journal of Geophysical Research*, **96(C8)**: 14637–14647. doi:10.1029/91JC01206.

Brink, K. H., Stuart, D. W. & Van Leer, J. C. (1984). Observations of the coastal upwelling region near 34°30'N of California: Spring 1981. *Journal of Physical Oceanography*, **14**: 378–391. doi:10.1175/1520-0485(1984)014<0378:OOTCUR>2.0.CO;2.

Castelao, R. M. & Barth, J. A. (2007). The role of wind stress curl in jet separation at a cape. *Journal of Physical Oceanography*, **37**: 2652–2671. doi:10.1175/2007JPO3679.1.

Cromwell, T. (1953). Circulation in a meridional plane in the central equatorial Pacific. *Journal of Marine Research*, **12**: 196–213.

Cury, P. & Shannon, L. (2004). Regime shifts in upwelling ecosystems: observed changes and possible mechanisms in the northern and southern Benguela. *Progress in Oceanography*, **60**: 223–243. doi:10.1016/j.pocean.2004.02.007.

Cushman-Roisin, B. (1993). Trajectories in Gulf Stream meanders. *Journal of Geophysical Research*, **98(C2)**: 2543–2554. doi:10.1029/92JC02059.

Cushman-Roisin, B. & Beckers, J.-M. (2011). *Introduction to Geophysical Fluid Dynamics: Physical and Numerical Aspects*. Academic Press, 2nd edn., 789 pp. ISBN 978-0-12-088759-0.

Durand, M.-H., Cury, P., Mendelssohn, R., Roy, C., Bakun, A. & Pauly, D. (eds.) (1998). *Global versus Local Changes in Upwelling Systems*. ORSTOM, Paris, 594 pp. ISBN 2-7099-1389-5.

Feldman, G. C. & McClain, C. R. (2010). Ocean Color Web, `http://oceancolor.gsfc.nasa.gov/`. NASA Goddard Space Flight Center, Eds. Kuring, N., Bailey, S. W., Franz, B. F., Meister, G., Werdell, P. J., Eplee, R. E., accessed October 4, 2010.

Flament, P. (1985). The evolving structure of an upwelling filament. *Journal of Geophysical Research*, **90**: 11765–11778. doi:10.1029/JC090iC06p11765.

Gabric, A. J., Garcia, L., van Camp, L., Nykjaer, L., Eifler, W. & Schrimpf, W. (1993). Offshore export of shelf production in the Cap Blanc giant filament as derived from Coastal Zone Color Scanner imagery. *Journal of Geophysical Research*, **98**: 4697–4712. doi:10.1029/92JC01714.

García-Muñoz, M., Arístegui, J., Pelegrí, J. L., Antoranz, A., Ojeda, A. & Torres, M. (2005). Exchange of carbon by an upwelling filament off Cape Ghir (NW Africa). *Journal of Marine Systems*, **54(1-4)**: 83–95. doi:10.1016/j.jmarsys.2004.07.005.

García-Weill, L., Nykjaer, L., Tejera-Cruz, A. & Cantón, M. (1994). Cálculo de velocidades oceánicas superficiales en el área del afloramiento del NW de África mediante imágenes del sensor AVHRR. *Revista de Teledetección*, **3**: 37–41.

Graham, N. E. & Barnett, T. P. (1987). Sea surface temperature, surface wind divergence, and convection over tropical oceans. *Science*, **238(4827)**: 657–659. doi:10.1126/science.238.4827.657.

Hagen, E., Zülicke, C. & Feistal, R. (1996). Near surface structures in the Cape Ghir filament off Morocco. **19(6)**: 577–598.

Harvey, J. (1982). θ-S relationships and water masses in the eastern North Atlantic. *Deep Sea Research Part A. Oceanographic Research Papers*, **29(8)**: 1021–1033. doi:10.1016/0198-0149(82)90025-5.
URL http://www.sciencedirect.com/science/article/B757K-48BD1JD-2C/2/555e3539115478e8f53af3d95f766550

Haynes, R. & Barton, E. D. (1990). A poleward flow along the Atlantic coast of the Iberian Peninsula. *Journal of Geophysical Research*, **95**: 11425–11442. doi:10.1029/JC095iC07p11425.

Haynes, R., Barton, E. D. & Pilling, I. (1993). Development, persistence and variability of upwelling filaments off the Atlantic Coast of the Iberian Peninsula. *Journal of Geophysical Research*, **98**: 22681–22692. doi:10.1029/93JC02016.

Heileman, S. & Tandstad, M. (2009). Canary Current LME. In K. Sherman & G. Hempel (eds.), *The UNEP Large Marine Ecosystems Report: A Perspective on Changing Conditions in LMEs of the World's Regional Seas. UNEP Regional Seas Report and Studies*, vol. 182, pp. 131–141. United Nations Environment Programme.

Hempel, G. (ed.) (1982). *The Canary current : studies of an upwelling system*. Rapports et Procès-Verbaux des Réunions, Conseil International pour l'Exploration de la Mer, vol. 180, Copenhagen, Denmark, 450 pp.

Hernández-Guerra, A., Arístegui, J. & Cantón, M. (1993). Phytoplankton pigment patterns in the Canary Islands area as determined using Coastal Zone Colour Scanner data. *International Journal of Remote Sensing*, **14(7)**: 1431–1437. doi:10.1080/01431169308953977.

Hernández-Guerra, A., López-Laatzen, F., Machín, F., de Armas, D. & Pelegrí, J. (2001). Water masses, circulation and transport in the eastern boundary current of the North Atlantic subtropical gyre. *Scientia Marina*, **65**: 177–186. doi:10.3989/scimar.2001.65s1177.

Hernández-Guerra, A. & Nykjaer, L. (1997). Sea surface temperature variability off North-West Africa: 1981-1989. *International Journal of Remote Sensing*, **18(12)**: 2539–2558. doi:10.1080/014311697217468.

Hernández-León, S., Almeida, C., Bécognée, P., Yebra, L. & Arístegui, J. (2004). Zooplankton biomass and indices of grazing and metabolism during a late winter bloom in subtropical waters. *Marine Biology*, **145(6)**: 1191–1200. doi:10.1007/s00227-004-1396-5.

Hsueh, Y. & Kenney, R. N. (1972). Steady coastal upwelling in a continuously stratified ocean. *Journal of Physical Oceanography*, **2**: 27–33. doi:10.1175/1520-0485(1972)002<0027:SCUIAC>2.0.CO;2.
URL http://journals.ametsoc.org/doi/abs/10.1175/1520-0485%281972%29002%3C0027%3ASCUIAC%3E2.0.CO%3B2

Hsueh, Y. & O'Brien, J. J. (1971). Steady coastal upwelling induced by an alongshore current. *Journal of Physical Oceanography*, **1(3)**: 180–186. doi:10.1175/1520-0485(1971)001<0180:SCUIBA>2.0.CO;2.
URL http://journals.ametsoc.org/doi/abs/10.1175/1520-0485%281971%29001%3C0180%3ASCUIBA%3E2.0.CO%3B2

Hughes, P. & Barton, E. D. (1974a). Physical investigations in the upwelling region of North West Africa on RRS Discovery Cruise 48. *Tethys*, **6**: 43–52.

Hughes, P. & Barton, E. D. (1974b). Stratification and water mass analysis in the upwelling area off NW Africa in April-May 1969. *Deep-Sea Research*, **21**: 611–628. doi:10.1016/0011-7471(74)90046-1.

Hurlburt, H. E. & Thompson, J. D. (1973). Coastal upwelling on a β-plane. *Journal of Physical Oceanography*, **3(1)**: 16–32. doi:10.1175/1520-0485(1973)003<0016:CUOAP>2.0.CO;2.
URL http://journals.ametsoc.org/doi/abs/10.1175/1520-0485%281973%29003%3C0016%3ACUOAP%3E2.0.CO%3B2

Huyer, A., Barth, J. A., Kosro, P. M., Shearman, R. K. & Smith, R. L. (1998). Upper-ocean water mass characteristics of the California Current, summer 1993. *Deep-Sea Research II*, **45**: 1411–1442. doi:10.1016/S0967-0645(98)80002-7.

Ikeda, M. & Emery, W. J. (1984). Satellite observations and modeling of meanders in the California Current system off Oregon and Northern California. *Journal of Physical Oceanography*, **14**: 1434–1450. doi:10.1175/1520-0485(1984)014<1434:SOAMOM>2.0.CO;2.

Jackett, D. R. & McDougall, T. J. (1997). A neutral density variable for the world's oceans. *Journal of Physical Oceanography*, **27(2)**: 237–263. doi:10.1175/1520-0485(1997)027<0237:ANDVFT>2.0.CO;2.

Jennings, S., Kaiser, M. & Reynolds, J. D. (2001). *Marine Fisheries Ecology*. Blackwell Science Ltd, Oxford. ISBN 978-0-632-05098-7.

Jickells, T. D., An, Z. S., Andersen, K. K., Baker, A. R., Bergametti, G., Brooks, N., Cao, J. J., Boyd, P. W., Duce, R. A., Hunter, K. A., Kawahata, H., Kubilay, N., laRoche, J., Liss, P. S., Mahowald, N., Prospero, J. M., Ridgwell, A. J., Tegen, I. & Torres, R. (2005). Global iron connections between desert dust, ocean biogeochemistry, and climate. *Science*, **308(5718)**: 67–71. doi:10.1126/science.1105959.
URL http://www.sciencemag.org/content/308/5718/67.abstract

Johnson, D. R., Barton, E. D., Hughes, P. & Mooers, C. N. K. (1975). Circulation in the Canary Current upwelling region off Cabo Bojador in August 1972. *Deep-Sea Research*, **22(8)**: 547–558. doi:10.1016/0011-7471(75)90035-2.

Johnson, J. & Stevens, I. (2000). A fine resolution model of the eastern North Atlantic between the Azores, the Canary Islands and the Gibraltar Strait. *Deep-Sea Research I*, **47**: 875–899. doi:10.1016/S0967-0637(99)00073-4.

Klein, B. & Siedler, G. (1989). On the origin of the Azores Current. *Journal of Geophysical Research*, **94(C5)**: 6159–6168. doi:10.1029/JC094iC05p06159.

Kosro, P. M. & Huyer, A. (1986). CTD and velocity surveys of seaward jets off northern California, July 1981 and 1982. *Journal of Geophysical Research*, **91**: 7680–7690. doi:10.1029/91JC00885.

Kostianoy, A. G. & Zatsepin, A. G. (1996). The West African coastal upwelling filaments and cross-frontal water exchange conditioned by them. *Journal of Marine Systems*, **7**: 349–359. doi:10.1016/0924-7963(95)00029-1.

Lutjeharms, J. R. E., Shillington, F. A. & Rae, C. M. D. (1991). Observations of extreme upwelling filaments in the Southeast Atlantic Ocean. *Science*, **253**: 774–776. doi:10.1126/science.253.5021.774.

Machín, F., Hernández-Guerra, A. & Pelegrí, J. L. (2006). Mass fluxes in the Canary Basin. *Progress in Oceanography*, **70**: 416–447. doi:10.1016/j.pocean.2006.03.019.

Marlín, V. H., Escribano, R., Delgado, L. E., Olivares, G. & Hidalgo, P. (2001). Nearshore circulation in a coastal upwelling site off the Northern Humboldt current system. *Continental Shelf Research*, **21(13-14)**: 1317 – 1329. doi:10.1016/S0278-4343(01)00022-X. URL http://www.sciencedirect.com/science/article/pii/S027843430100022X

Marshall, D. P. & Tansley, C. E. (2001). An implicit formula for boundary current separation. *Journal of Physical Oceanography*, **31**: 1633–1638. doi:10.1175/1520-0485(2001)031<1633:AIFFBC>2.0.CO;2.

Martinho, A. S. & Batteen, M. L. (2006). On reducing the slope parameter in terrain-following numerical ocean models. *Ocean Modelling*, **13(2)**: 166–175. doi:10.1016/j.ocemod.2006.01.003.
URL http://www.sciencedirect.com/science/article/pii/S1463500306000060

Mason, E., Colas, F., Molemaker, J., Shchepetkin, A., Sangrà, P. & McWilliams, J. C. (2008). Seasonal variability of the Canary Current system. In *Eastern boundary upwelling ecosystems: integrative and comparative approaches*. Las Palmas de Gran Canaria, Spain.
URL http://www.confmanager.com/main.cfm?cid=845&nid=7276

Mason, E., Colas, F., Molemaker, J., Shchepetkin, A. F., Troupin, C., McWilliams, J. C. & Sangrà, P. (2011). Seasonal variability of the Canary Current: a numerical study. *Journal of Geophysical Research*, **116**: C06001. doi:10.1029/2010JC006665.
URL http://www.agu.org/journals/jc/jc1106/2010JC006665/2010JC006665.pdf

Meunier, T., Rossi, V., Morel, Y. & Carton, X. (2010). Influence of bottom topography on an upwelling current: Generation of long trapped filaments. *Ocean Modelling*, **35(4)**: 277–303. doi:10.1016/j.ocemod.2010.08.004.

URL http://www.sciencedirect.com/science/article/B6VPS-50W1TPD-2/2/eac751cd6591c014f49603f2dea97c87

Mittelstaedt, E. & Hamann, I. (1981). The coastal circulation off Mauritania. *Deutsche Hydrographische Zeitschrift*, **34**: 81–118. doi:10.1007/BF02226483.

Mittelstaedt, E., Pillsbury, D. & Smith, R. (1975). Flow patterns in the Northwest African upwelling area. Results of measurements along 21°40' N during February - April 1974. JOINT-1. *Deutsche Hydrographische Zeitschrift*, **28**: 145–167. doi:10.1007/BF02232617.

Monterey, G. I. & Levitus, S. (1997). Climatological cycle of mixed layer depth in the world ocean. Tech. rep., U.S. Gov. Printing Office NOAA NESDIS. 5 pp.

Mooers, C. N. K. & Robinson, A. R. (1984). Turbulent jets and eddies in the California Current and inferred cross-shore transports. *Science*, **223(4631)**: 51–53. doi:10.1126/science.223.4631.51.

Morel, A. & Berthon, J.-F. (1989). Surface pigments, algal biomass profiles, and potential production of the euphotic layer: Relationships reinvestigated in view of remote-sensing applications. *Limnology and Oceanography*, **34(8)**: 1545–1562.
URL http://www.jstor.org/stable/2837038

Narimousa, S. & Maxworthy, T. (1987). On the effects of coastline perturbations on coastal currents and fronts. *Journal of Physical Oceanography*, **17(8)**: 1296–1303. doi:10.1175/1520-0485(1987)017<1296:OTEOCP>2.0.CO;2.
URL http://journals.ametsoc.org/doi/abs/10.1175/1520-0485%281987%29017%3C1296%3AOTEOCP%3E2.0.CO%3B2

Nelson, G., Boyd, A., Agenbag, J. & Duncombe Rae, C. (1998). An upwelling filament north-west of Cape Town, South Africa. *South African Journal of Marine Science*, **19**: 75–88. doi:10.2989/025776198784126953.

Neuer, S., Freudenthal, T., Davenport, R., Llinás, O. & Rueda, M.-J. (2002). Seasonality of surface water properties and particle flux along a productivity gradient off NW Africa. *Deep-Sea Research II*, **49(17)**: 3561–3576. doi:10.1016/S0967-0645(02)00098-X.
URL http://www.sciencedirect.com/science/article/B6VGC-46PBSFR-2/2/b09b82fcc786f0b569762f27ed245c55

Neuer, S., Torres-Padrón, M. E., Gelado-Caballero, M. D., Rueda, M. J., Hernández-Brito, J., Davenport, R. & Wefer, G. (2004). Dust deposition pulses to the eastern subtropical North Atlantic gyre: Does ocean's biogeochemistry respond? *Global Biogeochemical Cycles*, **18**: GB4020. doi:10.1029/2004GB002228.
URL http://www.agu.org/pubs/crossref/2004/2004GB002228.shtml

O'Brien, J. J. & Hurlburt, H. E. (1972). A numerical model of coastal upwelling. *Journal of Physical Oceanography*, **2(1)**: 14–26. doi:10.1175/1520-0485(1972)002<0014:ANMOCU>2.0.CO;2.
URL http://journals.ametsoc.org/doi/abs/10.1175/1520-0485%281972%29002%3C0014%3AANMOCU%3E2.0.CO%3B2

Parrilla, G., Neuer, S., Le Traon, P. Y. & Fernández-Suarez, E. (2002). Topical studies in oceanography: Canary Islands Azores Gibraltar Observations (CANIGO). Volume 1: Studies in the northern Canary Islands basin. *Deep-Sea Research II*, **49**: 3409–3413. doi:10.1016/S0967-0645(02)00104-2.

Pedlosky, J. (1974). On coastal jets and upwelling in bounded basins. *Journal of Physical Oceanography*, **4(1)**: 3–18. doi:10.1175/1520-0485(1974)004<0003:OCJAUI>2.0.CO;2.
URL http://journals.ametsoc.org/doi/abs/10.1175/1520-0485%281974%29004%3C0003%3AOCJAUI%3E2.0.CO%3B2

Pedlosky, J. (1978a). An inertial model of steady coastal upwelling. *Journal of Physical Oceanography*, **8(2)**: 171–177. doi:10.1175/1520-0485(1978)008<0171:AIMOSC>2.0.CO;2.
URL http://journals.ametsoc.org/doi/abs/10.1175/1520-0485%281978%29008%3C0171%3AAIMOSC%3E2.0.CO%3B2

Pedlosky, J. (1978b). A nonlinear model of the onset of upwelling. *Journal of Physical Oceanography*, **8(2)**: 178–187. doi:10.1175/1520-0485(1978)008<0178:ANMOTO>2.0.CO;2.
URL http://journals.ametsoc.org/doi/abs/10.1175/1520-0485%281978%29008%3C0178%3AANMOTO%3E2.0.CO%3B2

Pedlosky, J. (1987). *Geophysical Fluid Dynamics*. Springer-Verlag, 2nd edn., 728 pp. ISBN 0-387-96387-1.

Peffley, M. B. & O'Brien, J. J. (1976). A three-dimensional simulation of coastal upwelling off oregon. *Journal of Physical Oceanography*, **6(2)**: 164–180. doi:10.1175/1520-0485(1976)006<0164:ATDSOC>2.0.CO;2.
URL http://journals.ametsoc.org/doi/abs/10.1175/1520-0485%281976%29006%3C0164%3AATDSOC%3E2.0.CO%3B2

Pelegrí, J. L., Marrero-Díaz, A., Ratsimandresy, A., Antoranz, A., Cisneros-Aguirre, J., Gordo, C., Grisolía, D., Hernández-Guerra, A., Laíz, I., Martínez, A., Parrilla, G., Pérez-Rodríguez, P., Rodríguez-Santana, A. & Sangrà, P. (2005). Hydrographic cruises off northwest Africa: the Canary Current and the Cape Ghir region. *Journal of Marine Systems*, **54(1-4)**: 39–63. doi:10.1016/j.jmarsys.2004.07.001.
URL http://www.sciencedirect.com/science/article/pii/S0924796304002064

Peliz, A., Rosa, T. L., Santos, A. M. P. & Pissarra, J. L. (2002). Fronts, jets, and counter-flows in the Western Iberian upwelling system. *Journal of Marine Systems*, **35**: 61–77. doi:10.1016/S0924-7963(02)00076-3.

Risien, C. M. & Chelton, D. B. (2008). A global climatology of surface wind and wind stress fields from 8 years of QuikSCAT scatterometer data. *Journal of Physical Oceanography*, **38**: 2379–2413. doi:10.1175/2008JPO3881.1.

Ryther, J. H. (1969). Photosynthesis and fish production in the sea. *Science*, **166(3901)**: 72–76. doi:10.1126/science.166.3901.72.
URL http://www.jstor.org/stable/1727735

Shillington, F. A., Peterson, W. T., Hutchings, L., Probyn, T. A., Waldron, H. & Agenbag, J. J. (1990). A cool upwelling filament off Namibia, southwest Africa: preliminary measurements of physical and biological features. *Deep-Sea Research*, **37**: 1753–1772. doi:10.1016/0198-0149(90)90075-7.

Sobarzo, M. & Figueroa, D. (2001). The physical structure of a cold filament in a Chilean upwelling zone (Península de Mejillones, Chile, 23°S). *Deep-Sea Research I*, **48**: 2699–2726. doi:10.1016/S0967-0637(01)00031-0.

Spall, M. A. (1990). Circulation in the Canary Basin: A model/data analysis. *Journal of Geophysical Research*, **95**: 9611–9628. doi:10.1029/JC095iC06p09611.

Speth, P., Detlefsen, H. & Sierts, H.-W. (1978). Meteorological influence on upwelling off Northwest Africa. *Ocean Dynamics*, **31(3)**: 95–104. doi:10.1007/BF02227007.

Stevens, I., Hamann, M., Johnson, J. A. & Fiúza, A. F. G. (2000). Comparisons between a fine resolution model and observations in the Iberian shelf-slope region. *Journal of Marine Systems*, **26**: 53–74. doi:10.1016/S0924-7963(00)00038-5.

Stevens, I. & Johnson, J. (2003). A numerical modelling study of upwelling filaments off the NW African coast. *Oceanologica Acta*, **26**: 549–564. doi:10.1016/S0399-1784(03)00049-5.

Stewart, R. H. (2008). Introduction to physical oceanography. 353 pp.
URL http://oceanworld.tamu.edu/resources/ocng_textbook/contents.html

Stramma, L. (1984). Geostrophic transport in the warm water sphere of the eastern subtropical North Atlantic. *Journal of Marine Research*, **42**: 537–558. doi:10.1357/002224084788506022.

Stramma, L. & Schott, F. (1999). The mean flow field of the tropical Atlantic Ocean. *Deep-Sea Research II*, **46**: 279–303. doi:10.1016/S0967-0645(98)00109-X.
URL http://www.ingentaconnect.com/content/els/09670645/1999/00000046/00000001/art00109

Strub, P. T., Kosro, P. M., Huyer, A. & CTZ Collaborators (1991). The nature of cold filaments in the California Current system. *Journal of Geophysical Research*, **96(C8)**: 14743–14768. doi:10.1029/91JC01024.
URL http://www.agu.org/pubs/crossref/1991/91JC01024.shtml

Swallow, J. C. (1980). The Indian Ocean Experiment: Introduction. *Science*, **209(4456)**: 588. doi:10.1126/science.209.4456.588.
URL http://www.sciencemag.org/content/209/4456/588.2.full.pdf

Tang, C. & Ikeda, M. (1989). Ice-edge upwelling off the Newfoundland coast during LIMEX. *Atmosphere-Ocean*, **27(4)**: 658–681. doi:10.1080/07055900.1989.9649360.

Tomczak,, M. (1973). An investigation into the occurence and development of cold water patches in the upwelling region of N. W. Africa ("Meteor"-cruise 19). *"Meteor" Forschungsergebnisse, A*, **13**: 1–42.

Torres-Padrón, M. E., Gelado-Caballero, M. D., Collado-Sánchez, C., Siruela-Matos, V. F., Cardona-Castellano, P. J. & Hernández-Brito, J. J. (2002). Variability of dust inputs to the CANIGO zone. *Deep-Sea Research II*, **49(17)**: 3455–3464. doi:10.1016/S0967-0645(02)00091-7.

Troupin, C., Sangrà, P. & Arístegui, J. (2010). Seasonal variability of the oceanic upper layer and its modulation of biological cycles in the Canary Island region. *Journal of Marine Systems*, **80(3-4)**: 172–183. doi:10.1016/j.jmarsys.2009.10.007.
URL http://www.sciencedirect.com/science/article/B6VF5-4XMKB67-1/2/326bcf54e891969eb6191ec534805d35

Van Camp, L., Nykjaer, L., Mittelstaed, E. & Schlittenhard, P. (1991). Upwelling and boundary circulation off Northwest Africa as depicted by infrared and visible satellite observations. *Progress in Oceanography*, **26(4)**: 357–402. doi:10.1016/0079-6611(91)90012-B.

Van Heijst, G. J. F. (1984). An analytical model for ice-edge upwelling. *Geophysical & Astrophysical Fluid Dynamics*, **29(1-4)**: 155–177. doi:10.1080/03091928408248188.

Warren, B., Stommel, H. & Swallow, J. (1976). Water masses and patterns of flow in the Somali Basin during the southwest monsoon of 1964. *Deep Sea Research and Oceanographic Abstracts*, **13(5)**: 825–860. doi:10.1016/0011-7471(76)90907-4.
URL http://www.sciencedirect.com/science/article/B757H-48BCGM5-D9/2/2ebb132aad5e1b657e80e2c106d6f455

Wooster, W. S., Bakun, A. & McLain, D. R. (1976). The seasonal upwelling cycle along the eastern boundary of the North Atlantic. *Journal of Marine Research*, **34**: 131–140.

Wyrtki, K. (1981). An estimate of equatorial upwelling in the Pacific. *Journal of Physical Oceanography*, **11(9)**: 1205–1214. doi:10.1175/1520-0485(1981)011<1205:AEOEUI>2.0.CO;2.
URL http://journals.ametsoc.org/doi/abs/10.1175/1520-0485%281981%29011%3C1205%3AAEOEUI%3E2.0.CO%3B2

Chapter 2

Climatology of the northeast Atlantic Ocean

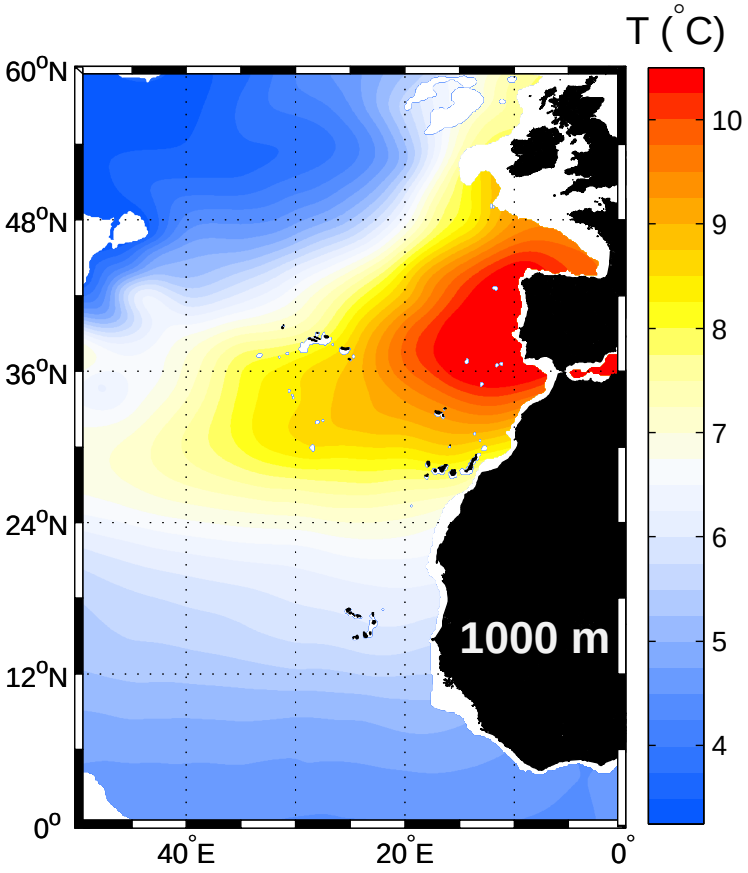

Annual temperature field at 1000 m depth.

This chapter is focused on the construction of a high-resolution climatology in the northeastern Atlantic using the Data-Interpolating Variational Analysis (Diva) method. After a description of the method, the results obtained in the NE Atlantic are presented.

Two articles are related to this chapter:

1. Troupin, C., F. Machín, M. Ouberdous, D. Sirjacobs, A. Barth, and J.-M. Beckers (2010), High-resolution climatology of the North-East Atlantic using Data-Interpolating Variational Analysis (Diva), *Journal of Geophysical Research*, **115**, C08005, doi:10.1029/2009JC005512.

2. Troupin, C., D. Sirjacobs, M. Rixen, P. Brasseur, J.-M. Brankart, A. Barth, A. Alvera-Azcárate, A. Capet, M. Ouberdous, F. Lenartz, M.-E. Toussaint and J.-M. Beckers, Advanced Data Interpolating Variational Analysis. Application to climatological data, submitted to *Ocean Modelling*.

Contents

2.1 Introduction

Gridded fields of hydrographic properties constitute a highly demanded product in a wide range of applications in oceanography, going from simple visualization purposes to initialization of numerical model and quality-check of newly acquired data. A climatology is defined as a set of such gridded fields, computed at different levels, either in the global ocean or in one sub-region.

Many techniques allow the creation of climatologies using in situ measurements. They differ in the way data are treated (individual or groups), the choice of vertical coordinate system (pressure or density), the a posteriori filters applied to the results and, above all, the mathematical background for solving the griding problem.

Generally, two main approaches have to be distinguished for data griding:

The interpolation: it implies a strict passage of the solution through the points of data, but it is obviously not adapted for the creation of climatologies, given the nature of the considered data.

The approximation (or analysis): it provides a solution that does not necessarily contains all the data points: the reconstructed field is forced to be relatively close to the data points, or put in other words, the separation between data and analyzed field is adjusted.

Approximation techniques are particularly well adapted to oceanographic measurements, since these latter are contaminated by several sources of errors or noise with respect to climatological values, making the use of strict interpolation obsolete.

The most popular global climatologies are the successive versions of the World Ocean Atlas (WOA, Levitus, 1982; Levitus & Boyer, 1994; Stephens *et al.*, 2002; Locarnini *et al.*, 2006, 2010), produced by the U.S. National Oceanographic Data Center (NODC) Ocean Climate Laboratory (OCL). They provide 1°-resolution fields on 33 isobaric levels and were prepared using the large data set contained in the World Ocean Database (WOD hereinafter), which is continuously enriched by contributions of national data centers around the world. The last version of the database contains more than 9 million stations, available without restriction. In the WOA, the gridded fields are obtained with an objective analysis (OA) scheme, following the method described in Barnes (1964). Although these atlas are still frequently used for initializing numerical models (e.g., Chassignet *et al.*, 2003; Marchesiello *et al.*, 2003), they suffer from a lack of resolution, specially in the coastal zones.

A 1/4° WOA climatology was also developed (referred to as WOA01, Boyer *et al.*, 2005), yet coastal zones are still not adequately covered. This is a paradox characteristic of many climatologies, since coastal areas are generally more surveyed than the open ocean (see Figs. 2.1 and 2.2). Another concern of this climatology is the application of smoothing filters on the resulting fields, in order to remove the noise coming from limited data coverage and small smoothing radius (Chang & Chao, 2000).

Gouretski & Koltermann (2004) prepared the World Ocean Circulation Experiment (WOCE) Global Hydrographic Climatology (WGHC) on 45 standard levels with a 0.5-

by-0.5° resolution. They worked with a combined data set including WOD98 and WOCE. Observations were separated into two groups: reference data, composed of high-quality observations (around twenty thousand profiles), and historical data (around one million profiles). The first group served as a reference for validating historical data and treating systematic biases. Potential density surface were used for averaging on deep layers, while isobaric surfaces were preferred for upper layers. The correlation function was a Gaussian form with a decorrelation length scale R. To account for smaller-scale processes in shallow region, R was computed as a function of the distance between a given point and the coast. The problem of basin separation was solved by applying Optimal Interpolation (OI) individually on different sub-regions of the ocean, the coherence between the solution being assured by zones of overlap. Their method provided tighter T-S sequences compared with WOA01, but the OI method did not allow them to consider the effect of coastlines and to have sufficient resolution. Moreover, by the time their climatology was produced, they could not consider important data sources, such as Coriolis or Mediterranean Data Archeology and Rescue (MEDAR, `http://www.ifremer.fr/medar/`).

On a more regional scale, Lozier *et al.* (1995) proposed a North Atlantic climatology based on a database enriched with respect to the WOD. As the data coverage was improved and the size of the domain reduced, they were able to use a smaller smoothing radius in the interpolation, thus representing features absent from the WOA94. Another enhancement is the use of isopycnic levels instead of isobaric ones, allowing for a better conservation of water mass structures. Despite these modifications, their results also suffer from the coastal issue, since observations located in regions shallower than 200 meters were removed from their data set.

A recurring drawback of many methods is the use of an isotropic correlation length in horizontal planes, while numerous physical processes often have different characteristics according to the direction (e.g., cross-shore vs. along-shore variations). Kim *et al.* (2007) avoid this drawback by applying a two-step method to produce 5 km-resolution gridded fields off the U.S. West coast:

1. the data are averaged on a high-resolution sparse grid;
2. the averages are mapped on a regular grid using Objective Analysis (OA, Gandin, 1965) with anisotropic correlation length.

Nevertheless, the data binning prior to their analysis may constitute a loss of the information contained in the data.

Ridgway *et al.* (2002) use locally weighted regression (also called *loess mapping*, Cleveland & Devlin, 1988) on a combination of data sets for producing gridded fields around Australia. Their technique provides solutions to the referred problems, as it allows for anisotropy and topographical effect considerations. The resulting fields have a resolution that depends on the data coverage. The bias induced by the irregular temporal data coverage is removed by fitting the data to annual and semi-annual harmonic components. The method requires a large number of adjustable parameters, hence making the analysis less objective and more difficult to adapt to a particular region. The authors also reported problems related to spatial sampling, such as instability in regions void of data, unrealistic temperature inversion, or effect of data clusters.

Eventually, none of the climatologies that were described provides the user with complementary error fields, except the WGHC (Gouretski & Koltermann, 2004): they computed an absolute formal error as the product of the property variance and the relative error of the objective analysis.

A different approach to the griding problem, called process-convolution method (PCM; e.g., Higdon *et al.*, 1998; Swall, 1999) has been recently developed and applied to hydrographic fields. The principle of the method is to represent a dependent process by the convolution of simple independent processes, using a kernel that varies with space and time, allowing for flexibility in modeling the spatial dependence (Calder & Cressie, 2007). Therefore the PCM has the capacity of accounting for the temporal component of the data, which was systematically ignored in the previous approaches.

Higdon (1998) applied this method to the temperature in the North Atlantic Ocean. As very few time series are available, the temporal dependencies of the kernel are not obvious to detect, hence they relied on standard variogram structures to fill in the gap. Because the numerical cost is important, the kernel was only determined at a limited number of locations. Lemos & Sansó (2006) worked on the temperature variability in the Portugal Current System using a similar approach. They employed a Gaussian kernel with horizontal and vertical standard deviations of 2° of arc and 60 m, respectively, but the choice of these values for the parameters is not related to the data or to physical processes. Moreover the horizontal resolution was limited to 2° because of numerical cost.

More recently, North Atlantic SST was analyzed by (Lemos & Sansó, 2009). The kernel they applied allows the consideration of anisotropic and non-stationary fields. The resulting fields have the same large scale patterns than the WOA, but presents a better distinction of water masses. The estimation of the kernel parameters requires a substantial increase of the computational cost. This can constitute a temporary obstacle to the generation of a complete climatology (i.e., applying the same procedure to several variables at various depth levels).

Having reviewed different methods, the objective is settled to the construction of a regional climatology with a griding method that fulfills the following conditions:

1. to deal with a great number of individual data, without needing to work with averaged values or data bins;
2. to take into account coastline and topography effects in a natural way, without additional parametrization;
3. to generate coherent error maps;
4. to rely on a limited number of parameters, estimated in an objective way.

In addition, the technique implemented shall have reasonable computational time, both for analyzed and error fields, so that it can be run routinely on several depth levels and time periods without requiring huge computational resources.

The selected approach is called the Data-Interpolating Variational Analysis (Diva, Troupin *et al.*, 2011), an implementation of the Variational Inverse Method (VIM, Brasseur

& Haus, 1991; Brasseur, 1994), since this method satisfies all our requirements. It was successfully applied to the Mediterranean Sea for physical (Brasseur *et al.*, 1996; Rixen *et al.*, 2005a,b) and biological variables (Denis-Karafistan *et al.*, 1998; Karafistan *et al.*, 2002), and to the South China Sea (Uu & Brankart, 1997). More recently, global gridded maps at the ocean surface were generated by Tyberghein *et al.* (2011) for various physical and chemical variables, in the frame of a project focused on marine species distribution. The griding method has also been implemented within Ocean Data View software (ODV, Schlitzer, 2002), which provides an easy way to perform simple analyzes. Finally, another option for two-dimensional analyzes is the web interface been developed by Barth *et al.* (2010).

The methodology presented in this chapter is suitable to any region of the global ocean. For the sake of simplicity, we limit ourselves to a subregion of the Atlantic Ocean. This zone constitutes a pertinent choice for the application of Diva, since it gives the opportunity to deal with complex systems, such as the NW Africa upwelling system, the Strait of Gibraltar, the presence of Archipelagos (Canary, Madeira, Azores etc.), sea mounts, or the river plumes.

The present chapter is organized as follows: Section 2.2 describes the preparation of the data and the preprocessing steps; Section 2.3 gives an overview of Diva theory and of the selection of parameters for producing the climatology; Section 2.4 is dedicated to the analyzed and error fields, while Section 2.5 emphasizes the improvements brought by the method and the new data set; conclusions and future works are the subject of Section 2.6.

2.2 Data set preparation

As data coverage is an essential factor in the climatology quality, we strive to create the most complete database for our region of sake.

2.2.1 Sources

Data were gathered from several databases (Tab. 5.1) including only CTD and bottle measurements. XBT data are known to exhibit systematic error due to incorrect fall rate (Hanawa & Yasuda, 1992). Although correcting equations are available (Hanawa *et al.*, 1994), the decision to stick only to CTD and bottles was preferred, at least for the present version of the climatology. Moreover, it is necessary to know which type of XBT is considered (e.g., T4, T5, etc.) to apply the suitable correction. Unfortunately, the XBT type is rarely directly available. Nevertheless, conclusions drawn from the present work are still applicable to data sets made up of data types other than CTD and bottles.

Within each individual database, when previously quality-controlled data were available, they were preferred to raw data. Fig. 2.1 indicates the profiles locations for each database: coastal areas are particularly well covered, mostly near France, Spain and England. Mediterranean Sea and Gibraltar Strait benefit from a high data density, thanks to the MEDAR/MedAtlas II project. The north-western part of the domain (Newfoundland and Labrador shelves) is also well surveyed, as it is the zone where mixing between North

Atlantic Current warm waters and cold Labrador Current takes place (Gyory *et al.*, 2011). The least covered zone is by far the central part of the subtropical gyre, as only 7.9% of the data are located between 30-50°W and 10-30°N, with an average of about 600 profiles per 5°W box (Fig. 2.2).

Table 2.1: Data sources. The third and fourth column indicate the number of profiles before quality control and duplicate elimination for temperature and salinity, respectively. (*) World Ocean Database 2005; (**) International Council for the Exploration of the Sea.

Source	URL	Number of profiles T	S
WOD05 (*)	http://www.nodc.noaa.gov/OC5/WOD05/pr_wod05.html	304714	303103
Hydrobase2	http://www.whoi.edu/science/PO/hydrobase/	235016	235016
ICES (**)	http://www.ices.dk/Ocean/data.asp	45552	45002
MedAtlas2	http://www.ifremer.fr/medar/cdrom_database.htm	9413	9425
Coriolis	http://www.coriolis.eu.org	4367	4358
Local Campaigns	–	2330	2321
	Total:	**601392**	**599225**

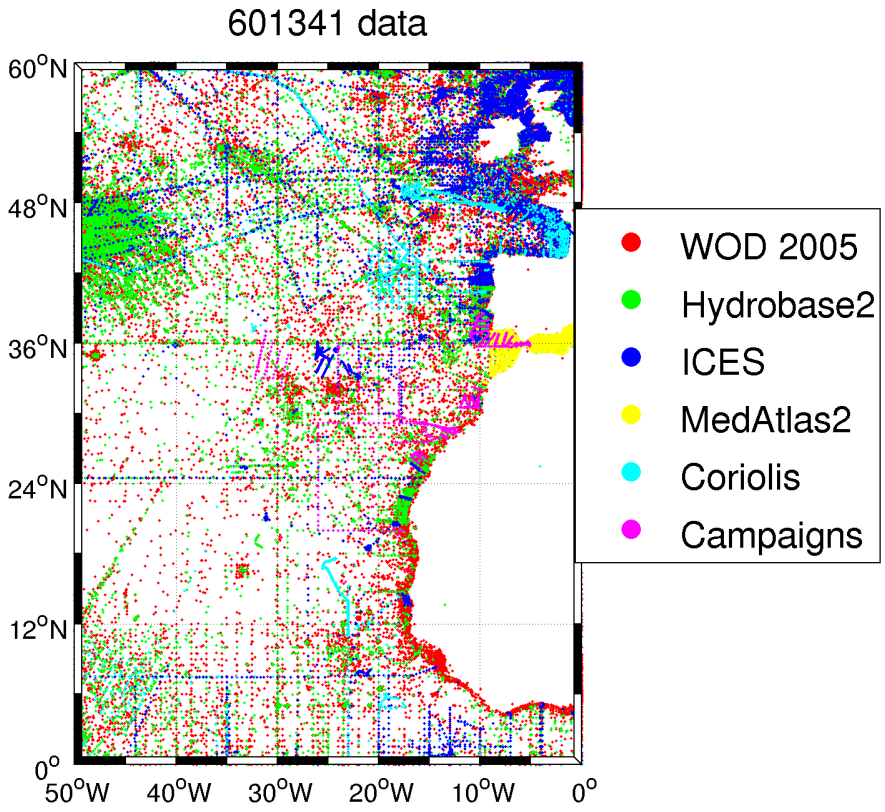

Figure 2.1: Localization of the profiles by data set. Note that WOD05 data are not always visible due to overlay with other databases.

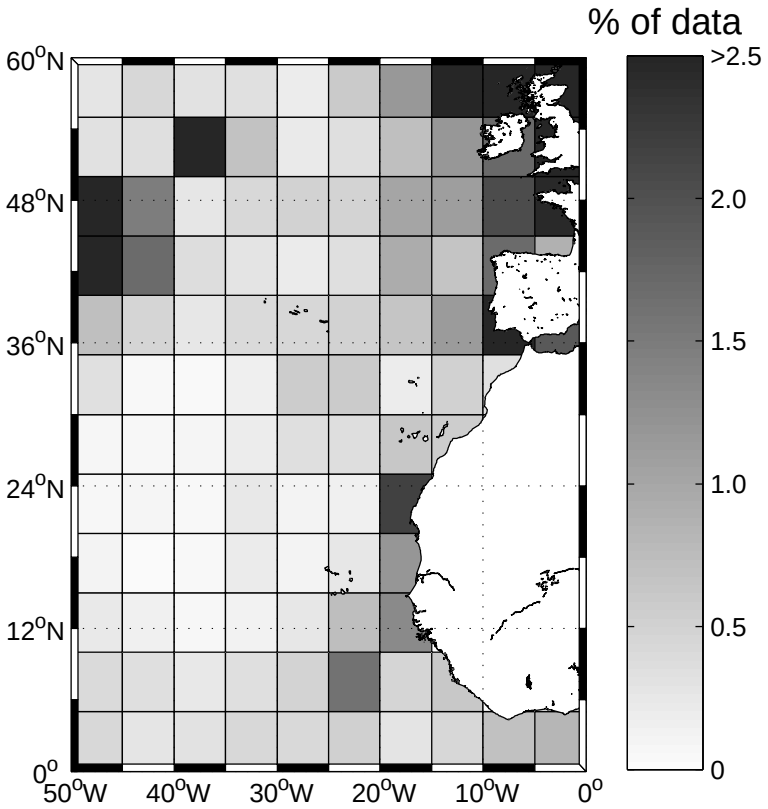

Figure 2.2: Relative data density on a 5°-by-5° grid. Dark rectangles contains the most data.

2.2.2 Pre-processing

Duplicate detection

The first step to obtain our database is the detection and removal of data duplicates. Otherwise, data analyzes would be biased in places where two (or more) identical data are present, as the data weight at these locations would be artificially multiplied. The criterion to detect duplicates is the following: two profiles measured at the same time (year, month and day, as more precise information are not always available) and separated by a distance shorter than a chosen threshold, are consider as duplicates, except if they belong to the same cruise. In that case, distance between two successive casts may be very small. We supposed that data sources taken individually are exempt of duplicates.

Results from the duplicate removal process are summarized in Tab. 2.2: out of 601341 casts, 270949 duplicates were found, mainly between WOD05 and HydroBase2. This result was predictable as HydroBase2 is made up of the 2001 version of the World Ocean Database (Conkright *et al.*, 2002) and several other hydrographic sources.

Working with a combination of sources instead of a unique one leads to an increase of 8% in the number of profiles with respect to the WOD05. Changes induced by using this new data set will be addressed in Section 2.5.3.

Table 2.2: Number of profiles and duplicates by database.

Database	Duplicates	(%)	After duplicate removal
WOD05	–	–	304714
Hydrobase2	225341	95.9	9675
ICES	34388	75.5	11164
MedAtlas2	7375	78.4	2038
Coriolis	3009	68.9	1358
Local Campaigns	836	35.9	1494
			Total: **330443**

Vertical coordinate system

Each database has a vertical coordinate system that is expressed in depth (meters) or in pressure (dbar). In the surface layers, working with any of the two makes almost no difference, but at greater depths a unique system has to be decided to ensure coherence between measurements.

Elaborated formulas require the knowledge of both temperature and salinity to convert pressure to depth. However, salinity measurements are less available than temperature. This is why we used a simpler method described in Saunders (1981). This formulation brings correction around 10 meters at 1 km depth and around 100 meters at 5 km depth. This correction yield results where the error is always smaller than 1 m if the depth does not exceed 7500 dbar.

Quality control

Even if a priori controlled data are used, further quality control (QC) procedures have to be applied. A first simple QC based on the range of the observations was implemented in order to remove obvious outliers. The ranges for temperature and salinity were obtained for the North Atlantic basin and the Mediterranean Sea following the tables of Johnson *et al.* (2006). The adaptation of the acceptable ranges in the Mediterranean Sea is decisive to allow for higher salinities through the water column. This first step only discarded a negligible amount of the data, but was essential to clean out evident outliers or remaining exclusion values. The second step consisted in checking the vertical gradient of temperature and salinity: values outside a prescribed range, similarly to Johnson *et al.* (2006). These two steps were performed on the profiles themselves.

The third QC was performed after the vertical interpolation: the domain was decomposed into 5°-by-5° tiles in which mean value and standard deviation (STD) were computed. Values falling outside $\pm N_{STD}\times$ STD around the mean were discarded. Locarnini *et al.* (2006) used different values for N_{STD}, depending whether they were considering coastal or open ocean zone. Typically, N_{STD} was assigned a higher value in the tiles containing coasts in order to take into account the higher variability in coastal areas, due for instance to upwelling or river discharge. Nevertheless, we decided to keep the value

$N_{STD} = 3$ for each tile, as the number of removed data was relatively small: 0.7% of the data were considered as outliers using this STD criterion.

Vertical interpolation

The weighted parabolic interpolation (WPI, Reiniger & Ross, 1968) is applied to the profiles to obtain the temperature and salinity fields at standard vertical levels (Tab. 2.3), similar to those of the WOA. This interpolation method is used in numerous oceanographic climatologies, such as the WOA and the MedAtlas (Fichaut *et al.*, 2003). It is preferred to other methods because it does not generate non-physical oscillations in the interpolated profiles. The original WPI routine was slightly modified, so that if any value is recorded within 5 m of the surface, this value is directly used as the surface value.

Table 2.3: Standard depth levels (in meters) selected for the vertical interpolation of the profiles.

Level no.	Depth (m)	Level no.	Depth (m)	Level no.	Depth (m)
1	5500	12	1300	23	250
2	5000	13	1200	24	200
3	4500	14	1100	25	150
4	4000	15	1000	26	125
5	3500	16	900	27	100
6	3000	17	800	28	75
7	2500	18	700	29	50
8	2000	19	600	30	30
9	1750	20	500	31	20
10	1500	21	400	32	10
11	1400	22	300	33	0

2.2.3 Statistics and distributions

The distribution of data by decade is shown in Fig. 2.3(a): most of the data (72.3%) were acquired after 1970, with a peak between 1980 and 1990 (28.1% of the total number of profiles). The negative trend of the number of available data in the last decades is due to the time lag between data acquisition and their public availability in databases. This is also observed in other similar works (e.g., Lozier *et al.*, 1995; Gouretski & Koltermann, 2004).

The monthly distribution (Fig. 2.3(b)) underlines the contrast between summer and winter regarding the number of available data: August is the month with the most profiles (more than 40703) while December has about 60% less data. Similar observations are made on every depth layer. This irregular distribution has to be taken into account when computing annual fields, otherwise results would be biased by the highest data coverage during summer months. For this reason, annual fields are computed by averaging the monthly means. Doing so, the uneven seasonal distribution is partially overcome. On average, 42.6% of the profiles go below 500 m, 31.9% below 1000 m and only 12.9% below 2000 m.

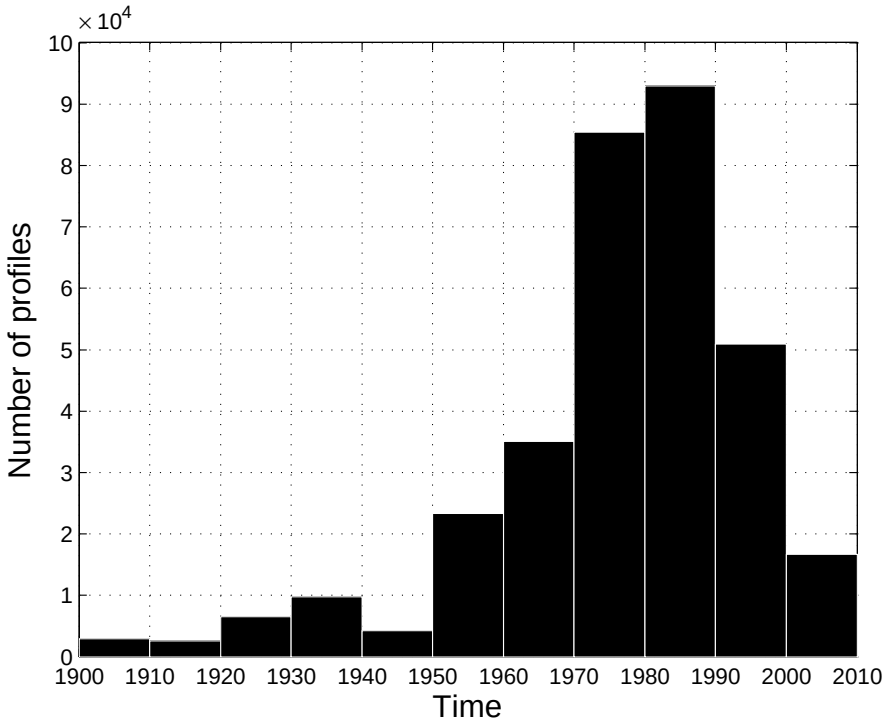

(a)

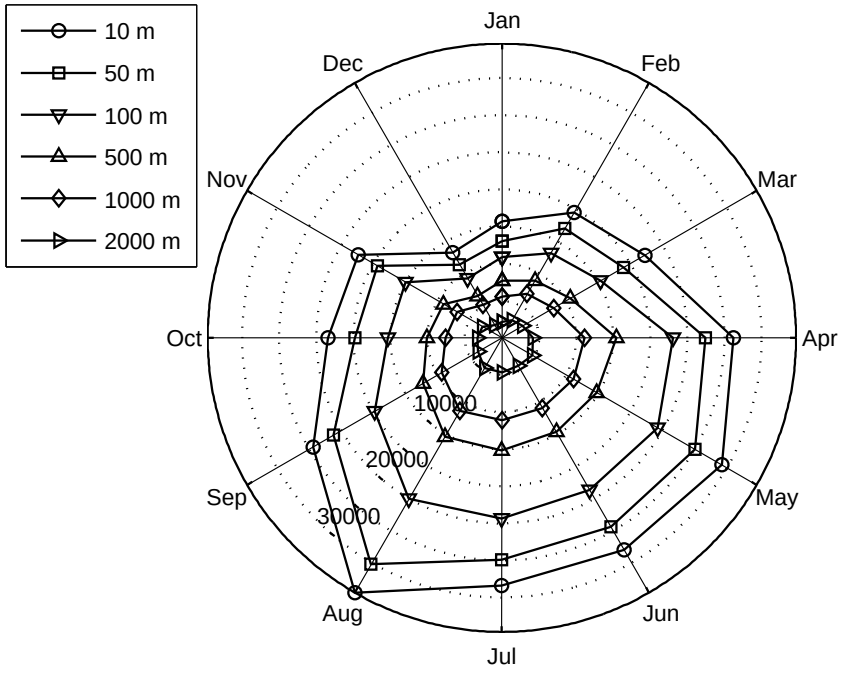

(b)

Figure 2.3: Time histogram of data (a) and monthly distribution at various depths (b); dotted circle are separated by 5000 units. The apparent decrease of data number in the last two decades comes from the delay between the acquisition of data at sea and their incorporation into accessible database.

2.3 Analysis method

The code of Diva method is freely available for download at http://modb.oce.ulg.ac.be/projects/1/diva.

2.3.1 Formulation

Let us consider a set of N_d observations d_j, located at positions $\mathbf{r}_j$. The idea is to find a field φ sufficiently close to the data, but whose variations are not too large. In a mathematical form, the problem consists of finding φ that minimizes the functional J:

$$J[\varphi] = \sum_{j=1}^{N_d} \mu_j \left[d_j - \varphi(\mathbf{r}_j)\right]^2 + \|\varphi\|^2 \tag{2.1}$$

with

$$\|\varphi\|^2 = \int_D \left(\alpha_2 \boldsymbol{\nabla}\boldsymbol{\nabla}\varphi : \boldsymbol{\nabla}\boldsymbol{\nabla}\varphi + \alpha_1 \boldsymbol{\nabla}\varphi \cdot \boldsymbol{\nabla}\varphi + \alpha_0 \varphi^2\right) dD, \tag{2.2}$$

where $\boldsymbol{\nabla}$ is the gradient operator and $\boldsymbol{\nabla}\boldsymbol{\nabla}\varphi : \boldsymbol{\nabla}\boldsymbol{\nabla}\varphi$ is the squared Laplacian of the field φ.

The functional is composed of two penalty terms: the first for the smoothness of the solution, the second for the compatibility of the data. The first term of the right-hand side of (2.1) (compatibility term) takes into account the distance between observations and reconstructed field, so that coefficients μ_j penalizes misfits between data and analysis; if the variational principle was only composed of this term, the solution would be the pure interpolation of the data, as the minimum would be obtained when $d_j = \varphi(x_j, y_j)$ for $j = 1, \ldots, N_d$. As stated in the introduction, this solution is not adapted to hydrographic data, due to their inherent noise.

The second term, made explicit in (2.2), is the smoothness term. It constitutes a measure of the field regularity. The expression within the integral is a positive-definite operator and remains invariant with respect to any rotation of the reference frame (Brasseur & Haus, 1991). α_0 penalizes the field norm, α_1 penalizes gradients and α_2 penalizes variability. Without loss of generality α_2 is chosen to be equal to one, since function (2.1) is homogeneous.

This formulation is referred to as Variational Inverse Method (VIM, Brasseur & Haus, 1991; Brasseur *et al.*, 1996). Under some conditions, smoothing splines, utilized in the VIM method, and OI are strictly equivalent (McIntosh, 1990; Bennet, 1992). This provides an argument to statistically justify the method.

2.3.2 Parameter determination

Parameters α_0, α_1 and μ_j may be determined from the data themselves, following developments from (Brasseur *et al.*, 1996). Let us assume that $\mu_j = \mu$, for $j = 1, \ldots, N_d$, i.e., all data have the same weight.

Writing Eq. (2.1) and (2.2) in non-dimensional form (with $\frac{1}{L}\tilde{\boldsymbol{\nabla}} = \boldsymbol{\nabla}$, L being a characteristic length of the problem), we have

$$J[\varphi] = \sum_{j=1}^{Nd} \mu[d_j - \varphi(x_j, y_j)]^2 + \int_{\tilde{D}} \left(\frac{1}{L^4} \tilde{\boldsymbol{\nabla}}\tilde{\boldsymbol{\nabla}}\varphi : \tilde{\boldsymbol{\nabla}}\tilde{\boldsymbol{\nabla}}\varphi + \frac{\alpha_1}{L^2} \tilde{\boldsymbol{\nabla}}\varphi \cdot \tilde{\boldsymbol{\nabla}}\varphi + \alpha_0 \varphi^2 \right) L^2 \, d\tilde{D}, \tag{2.3}$$

and multiplying by L^2:

$$J[\varphi] = \sum_{j=1}^{Nd} \mu L^2[d_j - \varphi(x_j, y_j)]^2 + \int_{\tilde{D}} \left(\tilde{\boldsymbol{\nabla}}\tilde{\boldsymbol{\nabla}}\varphi : \tilde{\boldsymbol{\nabla}}\tilde{\boldsymbol{\nabla}}\varphi + \alpha_1 L^2 \tilde{\boldsymbol{\nabla}}\varphi \cdot \tilde{\boldsymbol{\nabla}}\varphi + \alpha_0 L^4 \varphi^2 \right) d\tilde{D}. \tag{2.4}$$

The coefficient α_0 fixes the length scale over which variations are significant to move the kernel function of the norm (2.2) from one to zero:

$$\alpha_0 L^4 = 1. \tag{2.5}$$

μL^2 fixes the relative weight on data (signal, σ^2) versus regularization (noise, ϵ^2):

$$\mu L^2 = 4\pi \frac{\sigma^2}{\epsilon^2} = 4\pi\lambda, \tag{2.6}$$

where λ is the *signal-to-noise ratio*. The coefficient α_1 fixes the influence of gradients:

$$\alpha_1 L^2 = 2\xi, \tag{2.7}$$

where ξ is a non-dimensional parameter close to one if the gradients are to be penalized with a similar weight than the second derivatives. In the following, ξ is chosen equal to 1. Equations (2.5) and (2.6) show that the coefficients of the variational principle are related to the data through two parameters:

1. the *correlation length* L, which translates the distance over which a given data influence its neighborhood; it will be determined by fitting the correlation between the data to the theoretical kernel function of (2.2).

2. the signal-to-noise ratio λ, which gives an indication of the confidence one can have in a data point, thus it measures the closeness between the data and the analysis; it can be estimated by a generalized cross-validation (GCV) technique (Brankart & Brasseur, 1996).

Correlation length

Correlation length is first estimated on each level and for each month by fitting the data correlation function to an analytical form (Brasseur *et al.*, 1996). Then, for each month, a smoothing filter is applied over the different layers to remove possible irregularities. Such irregularities may arise from data clustering, outliers, or insufficient amount of measurements in a given layer. Finally, the monthly profiles of correlation length are averaged

in order to have smooth transition from one month to the other. Indeed, correlation length undergoes large variations from one month to the other. An example is given for the surface: from January to June, estimated correlation length has a value between 1.5 and 1.8° of arc (approximately 200 km), whereas in September, the reached value is close to 10° (more than 1000 km). Data spatial distribution is a possible explanation of such strong variations, this is why we applied the time-averaging.

Figure 2.4 shows the correlation length L as a function of depth: from the surface to around 800-1000 m, L undergoes an increase that may be attributed to the weaker influence of atmosphere and to the presence of more homogeneous water masses. Below 1000 m, L decreases with depth and reaches a minimum at 3500 m. Values of L for temperature and salinity are similar for most of the water column, as they start to diverge from 3500 to 5500 m depth.

It seems surprising that the value of L at 3500 m is lower than at the surface. Nevertheless, we believe that the evolution of L is related to the distributions of water masses, as detailed in Section 2.4.1. To ensure that it is not an artifact of the data distribution, the same fitting tool was applied to the fields extracted from a high-resolution solution, generated with the ROMS model (Mason *et al.*, 2011) in the same region of interest, and to another gridded climatology (WOA05). This comparison showed that the variation of L follows a similar evolution in both cases (Fig. 2.5).

The justification of the variability of the water masses distribution with depth would require a more detailed study, which is not in the scope of the present work. Nevertheless, we believe that the Mid Atlantic Ridge may also play a role in the separation of the water properties.

The tool for estimating the correlation length is more efficient when numerous data are available, hence the values computed at higher depths may be affected by a higher degree of uncertainty.

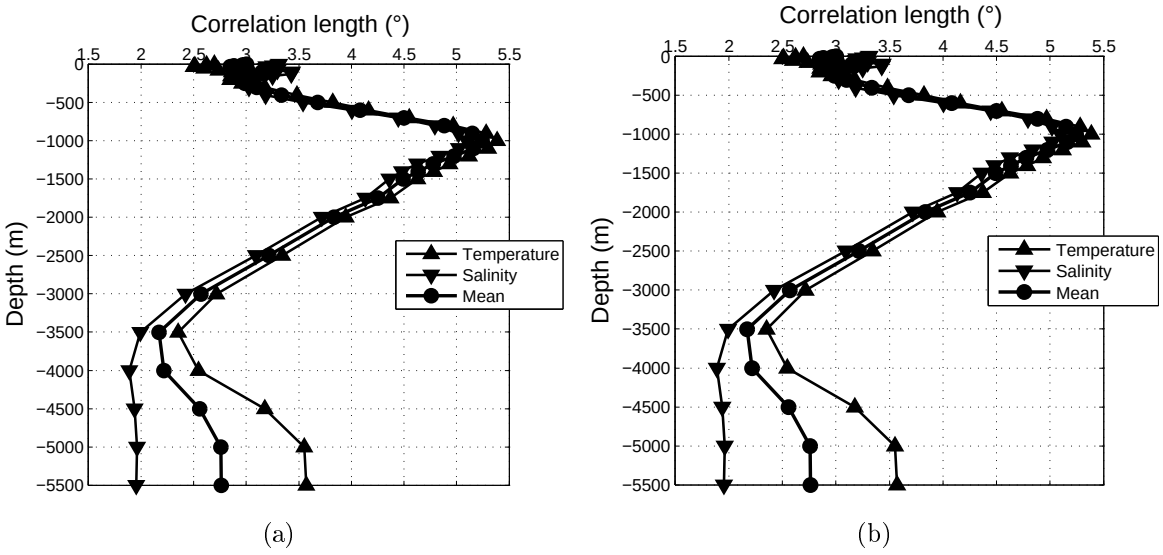

Figure 2.4: Monthly-averaged profile of correlation length for temperature (a) and salinity (b).

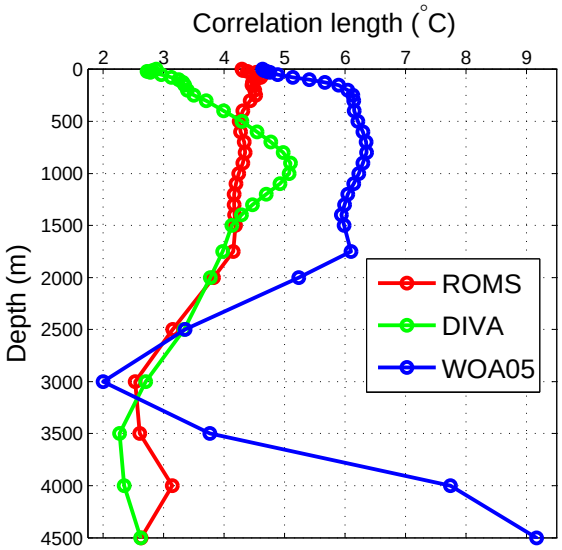

Figure 2.5: Correlation length estimated from ROMS results, WOA05 climatology, and Diva data set.

Signal-to-noise ratio

We performed the analyzes with constant and uniform value for signal-to-noise ratio $\lambda = 1$. The values of λ provided by cross-validation and generalized cross-validation were generally too high, so that the resulting analysis fields were too noisy and do not represent climatological conditions, since they display numerous small-scale features or sometimes even reveal the tracks of particular cruises. The choice of λ is difficult: in the case of a climatology, the error is not only instrumental, but it also comes from the *error of representativity*: a climatological field (hence representative of large time scales) is generated using measurements coming from several campaigns (hence having a smaller scale variability). Unfortunately, this kind of error cannot be easily quantified.

The reason why high signal-to-noise ratio values arise from the use of (G)CV is the following: the GCV tries to find the value of λ that makes minimal a global estimate of the analysis error variance, Θ, called the *generalized cross validator*, and defined as follows (Wahba & Wendelberger, 1980):

$$\Theta^2 = \frac{1}{N}\sum_{i=1}^{N}\hat{\theta}_i^2, \tag{2.8}$$

where N is the number of data and

$$\hat{\theta}_i^2 = \frac{(d_i - \tilde{d}_i)^2}{(1 - A_{ii})^2}. \tag{2.9}$$

In Eq. (2.9), d_i is the data at location $\mathbf{x} = \mathbf{x_i}$, $\tilde{d}_i$ is the analysis at $\mathbf{x_i}$ when data i is discarded, and $\mathbf{A}$ is the matrix that links analysis and data, according to

$$\tilde{\mathbf{d}} = \mathbf{A}\mathbf{d}. \tag{2.10}$$

The problem of this formulation when applied to oceanographic data, is that such data are not independent, for instance observations of a given cruise made during a relatively short time interval. In that case, GCV yields to very high values for the signal-to-noise ratio, which are incompatible with the nature of a climatology. For this reason λ was assigned a constant value.

2.3.3 Background field

The field $\varphi(\mathbf{r})$ to reconstruct is decomposed into two terms: a background field $\varphi_b(\mathbf{r})$ and a perturbation $\varphi'(\mathbf{r})$. It is the perturbation that is substituted in (2.2), otherwise the mean value of the field would be also minimized. Hence the background field acts as the solution obtained in regions far away from data. It constitutes the first guess of the field to reconstruct.

In the present implementation, $\varphi_b(\mathbf{r})$ is chosen as a least-square linear regression of the data. Such a background fields aims to remove the mean and the spatial trend (e.g., a meridional temperature gradient) from the original data. Configurations using semi-norm analysis ($\alpha_0 = 0$, Brasseur *et al.*, 1996) did not yield significant difference, except near the Amazon River plume: this zone is characterized by strong salinity variations, going from nearly 0 to 30 over a few hundreds kilometers in the first 20 m of the water column (Lentz & Limeburner, 1995). In this particular situation, semi-normed background field may lead to unrealistic negative values.

2.3.4 Kernel function

The Euler-Lagrange differential equation corresponding to the variational principle (2.1) reads (e.g., Brasseur *et al.*, 1996):

$$\alpha_2 \Delta^2 \varphi - \alpha_1 \Delta \varphi + \alpha_0 = \sum_{j=1}^{N_d} \mu_i \left(\varphi - d_j\right) \delta\left(\mathbf{r} - \mathbf{r}_j\right) \tag{2.11}$$

where Δ is the Laplacian operator and δ is the Dirac delta function. If $\mathbf{d}$ is the vector containing the data, the solution of (2.11) is written as

$$\varphi = \mathbf{k}^T \mathbf{D}^{-1} \mathbf{d},$$

with

$$D_{ij} = K(\mathbf{r}_i, \mathbf{r}_j) + \frac{1}{\mu}\delta_{ij}, \tag{2.12}$$

$$k_i = K(\mathbf{r}, \mathbf{r}_i), \tag{2.13}$$

where δ_{ij} stands for the delta of Kronecker ($\delta_{ij} = 1$ if $i = j$, $\delta_{ij} = 0$ if $i \neq j$), $K(\mathbf{r}, \mathbf{r}_i)$ is the kernel of the equation

$$\alpha_2 \Delta^2 \varphi - \alpha_1 \Delta \varphi + \alpha_0 = \delta(\mathbf{r} - \mathbf{r}_j).$$

Let us consider $\alpha_2 = 1$, $\alpha_1 = 2/L^2$ and $\alpha_0 = 1/L^4$ and an infinite domain (where infinite means that boundaries are distant enough from the data in comparison to the correlation length): in this particular case, the solution reads

$$K(\mathbf{r}, \mathbf{r}_j) = K(\mathbf{r} - \mathbf{r}_j) = K(r) = \frac{L^2}{4\pi} \frac{r}{L} K_1\left(\frac{r}{L}\right), \tag{2.14}$$

with K_1, the modified Bessel function of the second kind (Abramowitz & Stegun, 1964, page 359). As the domain is infinite, the solution does only depend on the distances r between positions $\mathbf{r}$ and $\mathbf{r}_j$, not on the positions themselves.

Effect of the parameters on the kernel

For practical purposes, the solution K is not computed, but it is still instructive to represent it in the case of an infinite domain and a unique data with a value of 1, located at the origin. In the example of Fig. 2.6(a), the correlation length is set to 1.0 (arbitrary units): in absence of boundaries, the solution is isotropic and goes from 1 at the origin to zero away from the origin.

The form of the kernel is a function of the analysis parameter L and is represented in Fig. 2.6(b), where K is plotted as a function of the ration r/L; the signal-to-noise ratio is assigned a high value ($\lambda = 1000$).

This trivial example illustrates the role of the parameters L and λ on the analysis:

1. An increase of L extends the influence region of the data, i.e., the effect of the data is felt at larger distances.
2. λ does not modify the kernel, but makes the analysis not so close to the observation: there is less confidence in the data, hence the definition of approximation.

2.3.5 Solver

Minimization of (2.1) is performed by a finite-element (FE) method, hence the need for generating a triangular FE mesh. Since the functional (2.1) is only defined in the sea, the minimization is limited to the zone defined by the coastline at surface or by the isobath corresponding to the depth of interest, so the FE mesh should only cover that zone (e.g., Fig. 2.7). For practical purposes, the real domain is split into N_e triangular FEs, so that the variational principle is expressed as the sum:

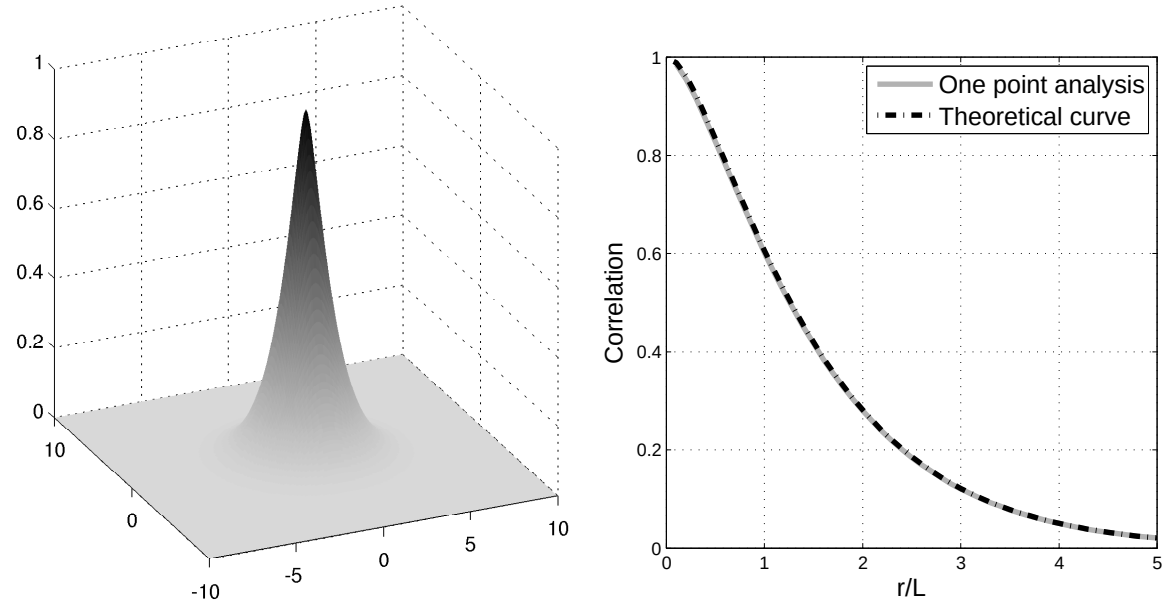

(a) (b)

Figure 2.6: (a) Analysis of a single data point with $\lambda = 1000.0$ and no background field; (b) Analysis of a single point along the $x-$axis (grey curve) and the theoretical kernel function (dashed black curve).

$$J[\varphi] = \sum_{e=1}^{N_e} J_e(\varphi_e). \tag{2.15}$$

In each element, the solution is a combination of shape functions (3rd-order polynomials) and the continuity between elements is assured by identification of adjacent connectors:

$$\varphi_e(\mathbf{r_e}) = \mathbf{q_e}^T \mathbf{s}(\mathbf{r_e}), \tag{2.16}$$

with $\mathbf{q}$, the connectors (the new unknowns) and $\mathbf{r_e}$, the position in a local coordinate system. Substituting (2.16) in (2.15) and using the variational principle (2.1), it comes

$$J_e(\mathbf{q_e}) = \mathbf{q_e}^T \mathbf{K_e} \mathbf{q_e} - 2\mathbf{q_e}^T \mathbf{g_e} + \sum_{i=1}^{N_{d_e}} \mu_i d_i, \tag{2.17}$$

where $\mathbf{K_e}$ is the local stiffness matrix, constructed from the integration of the shape functions, and $\mathbf{g}$ is a vector which depends on local data. On the whole domain, (2.17) reads

$$J(\mathbf{q}) = \mathbf{q}^T \mathbf{K} \mathbf{q} - 2\mathbf{q_e}^T \mathbf{g_e} + \sum_{i=1}^{N_d} \mu_i d_i, \tag{2.18}$$

of which the minimum is reached when

$$\mathbf{q} = \mathbf{K}^{-1}\mathbf{g}. \tag{2.19}$$

Matrix $\mathbf{K}$ has a size approximatively proportional to the number of degrees of freedom of the system, but can be very sparse if the elements are properly sorted. In that case the number of operations to invert $\mathbf{K}$ is approximatively proportional to the power 5/2 of the number of degrees of freedom.

To map the data on the finite element mesh, a transfer operator $\mathbf{T_2}$, dependent on the shape functions, is applied:

$$\mathbf{g} = \mathbf{T_2}(\mathbf{r})\mathbf{d},$$

and finally, to have the solution at any location inside the domain, another transfer $\mathbf{T_1}$ is applied:

$$\boldsymbol{\varphi}(\mathbf{r}) = \mathbf{T_1}(\mathbf{r})\mathbf{q}.$$

Combining the two previous equations, the relation between φ, the interpolated field at location $\mathbf{r}$, and the data vector $\mathbf{d}$ is obtained:

$$\boldsymbol{\varphi} = \mathbf{T_1}(\mathbf{r})\mathbf{K}^{-1}\mathbf{T_2}(\mathbf{r})\mathbf{d}. \tag{2.20}$$

The asset of this resolution method is twofold:

1. from the point of view of physics: data can only influence a zone that is physically connected to it through the mesh;
2. from the point of view of numerics: for a large number of data, the method requires less operations than OI.

It is instructive to compare meshes from the right and middle figures: at 500 m, Mediterranean Sea and Atlantic Ocean are separated, whereas at 125 m, the finite-element mesh links one zone to the other. Implications of this property are analyzed in Section 2.5.1.

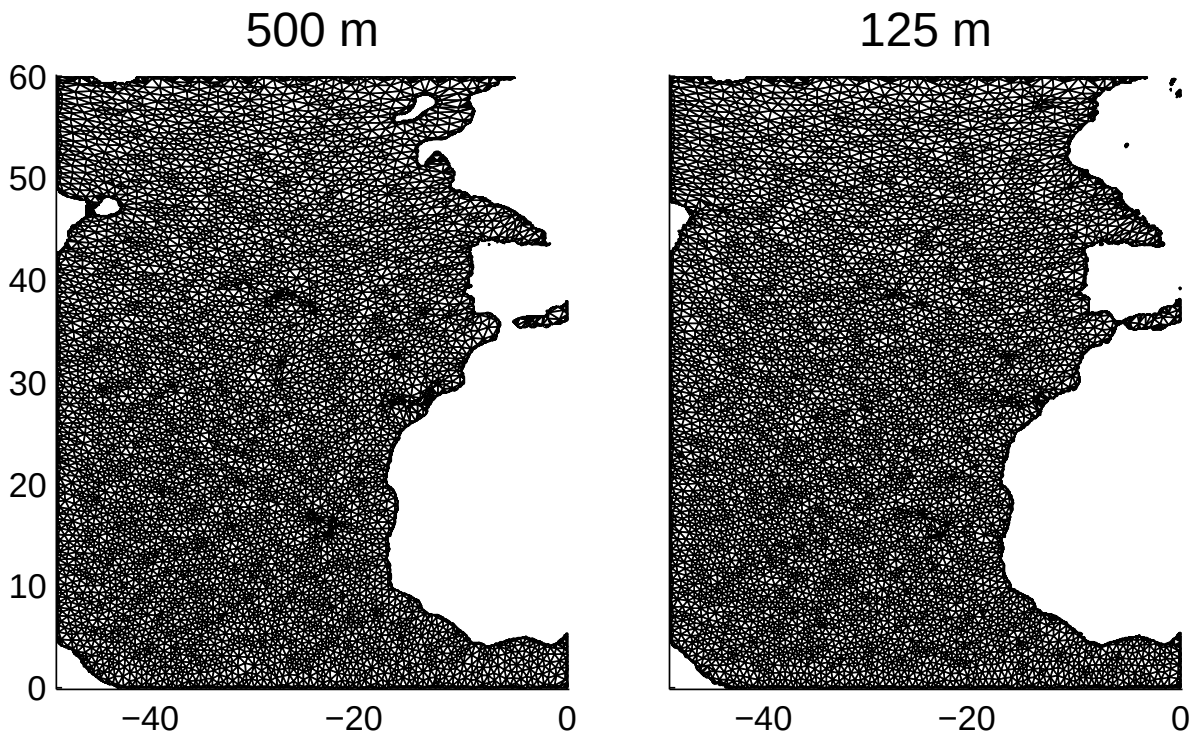

Figure 2.7: Finite-element meshes created at 500 and 125 m. Isobaths are generated from Digital Bathymetric Data Base Variable Resolution (DBDB-V) topography.

Topography and coastlines

Coastlines are necessary to delimit the area covered by the finite element mesh. Reference depths are chosen from surface to 5500 m, similarly to other large-scale climatologies. Depth contours are created using the Digital Bathymetric Data Base Variable Resolution (DBDBV, US Navy), a 5 minute-resolution bathymetry. The General Bathymetric Chart of the Oceans (GEBCO, Hunter & Macnab, 2003; Ward, 2010, with a resolution going up to 30 arc-seconds) was also considered, but for the region of sake, it generated too many small contours, which makes the FE mesh difficult to generate. Using high-resolution bathymetries is probably more advisable in the cases of less extended regions. Another option is simply to decrease the resolution of the GEBCO bathymetry.

Finite-element mesh

Once the contours are created, meshes are constructed on each of the 33 levels (Fig. 2.7) with a scale $L_e = 1/3°$. This value is a compromise between resolution and computational time, since mesh generation is a costly operation. As within each triangular element, the solution is a combination of shape functions (3rd-order polynomials), features with scale approximatively larger or equal to $L_e/3$ can be resolved. Meshes are generated only once and then stored for further operations.

2.3.6 Outlier detection

An automatic outlier detection is implemented within Diva. It is based on a comparison between the data-analysis residual and the expected standard deviation (Troupin *et al.*, 2011). This outlier detection algorithm has the asset of being applied during the analysis itself, so it does not require a priori information on the data. It will be shown in Section 2.5 that this step is essential to guarantee the quality of the analysis.

2.4 Results

Temperature and salinity fields generated with the data described in Section 2.2 and the methodology presented in Section 2.3 have been produced on monthly, seasonal and annual basis, on 33 standard depth levels (Tab. 2.3). Gridded fields of 0.1°-resolution are displayed on the GHER server at `http://gher-diva.phys.ulg.ac.be/web-vis/clim.html` in the directory GHER, with the name NEAtlantic and are available for download at `http://gher-diva.phys.ulg.ac.be:8080/GHER/NEAtlantic/` (OPeNDAP) and at `http://gher-diva.phys.ulg.ac.be/data/GHER/NEAtlantic/`.

2.4.1 Annual fields

The annual fields are computed by averaging all the monthly fields. Several levels are mapped in Fig. 2.8 to illustrate some of the outputs. An exhaustive description of water properties and formation across the entire domain is not in the scope of the present paper. The interested reader will find this information in other relevant publications (e.g., Lozier *et al.*, 1995; van Aken, 2000a,b, 2001). The objective is limited to a more simple description of typical temperature and salinity fields, with a focus on the link between property dispersion diagram and data-derived parameters presented in Section 2.3.2.

To have a first validation of the results, the T-S diagrams presented here were compared to those obtained from the WOA05 and from a high-resolution numerical model covering the same region (Mason *et al.*, 2011). In the three cases, the diagrams display comparable features concerning the water mass distribution. The observations made in the next sections about the water mass structure seem quite coherent.

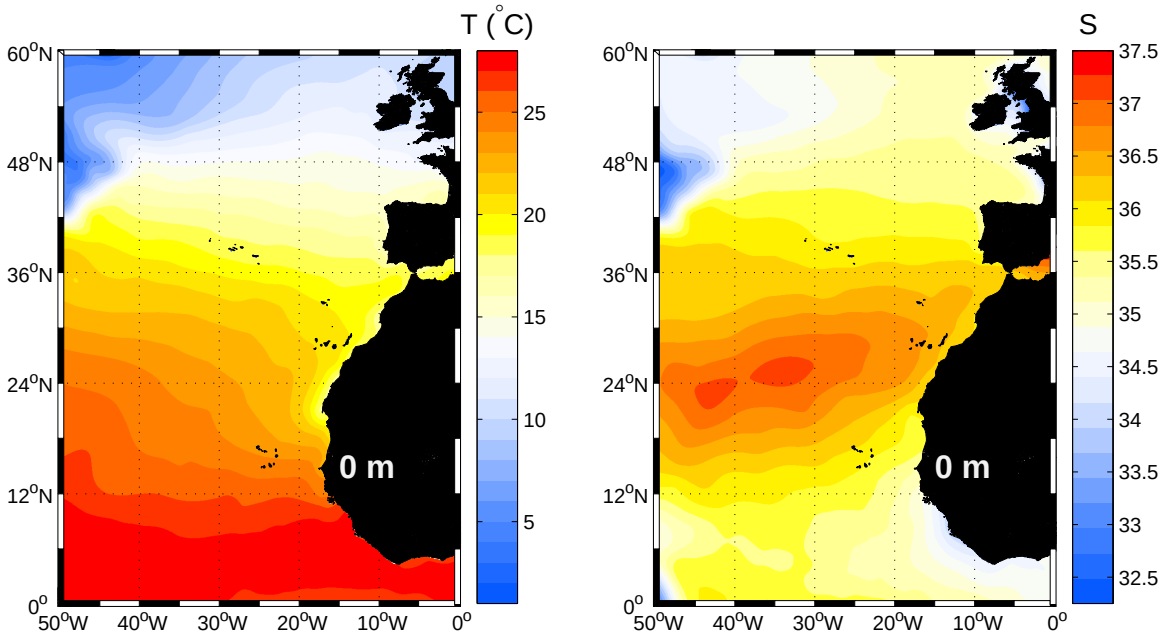

(a) (b)

Figure 2.8: Annual temperature (left) and salinity fields (right) at 0, 250, 700, 1300 and 3500 m. Black surfaces indicate surface land mask while white surfaces represent depth contours.

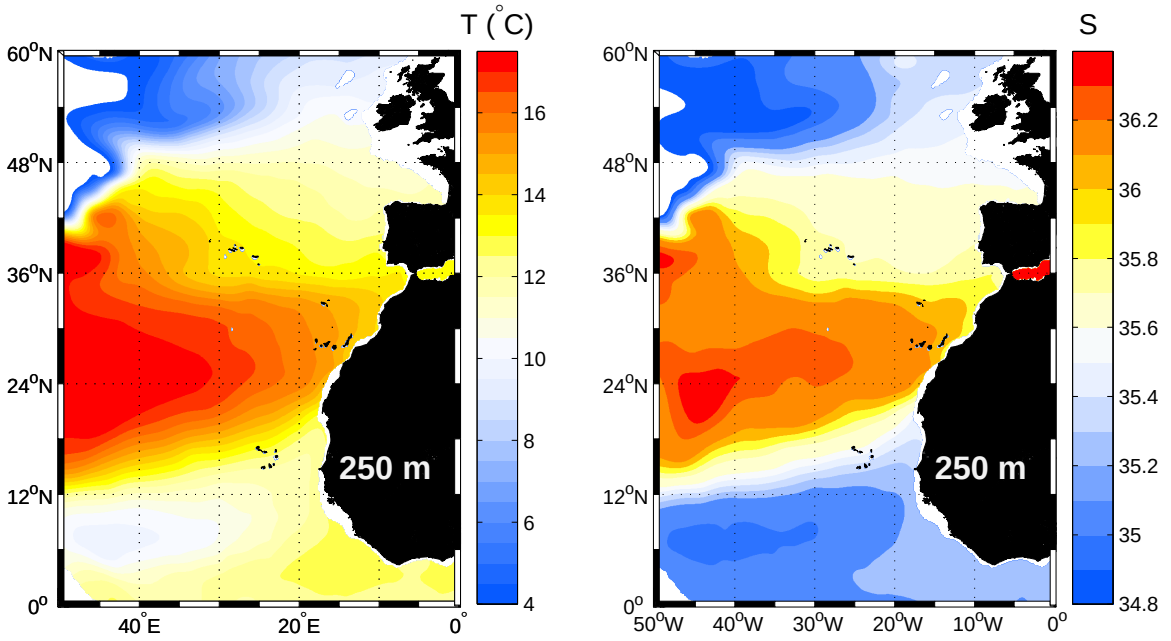

(c) (d)

Figure 2.8: continued.

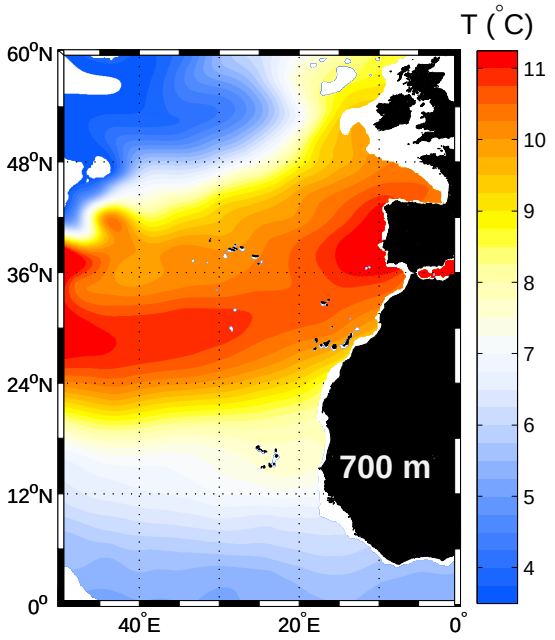

(e)

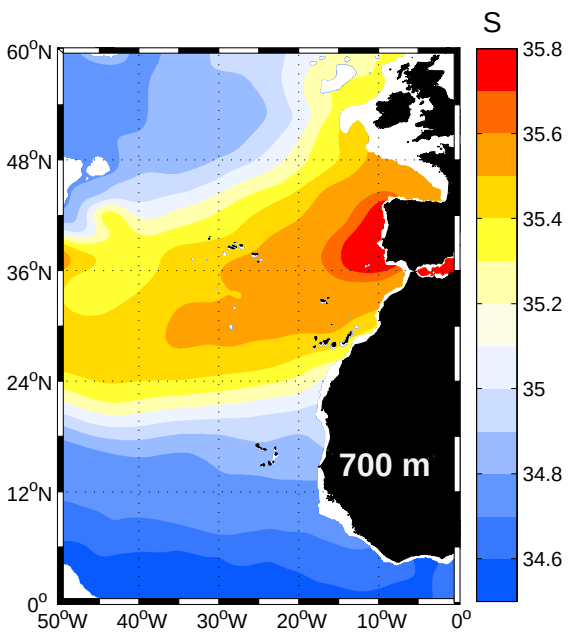

(f)

Figure 2.8: continued.

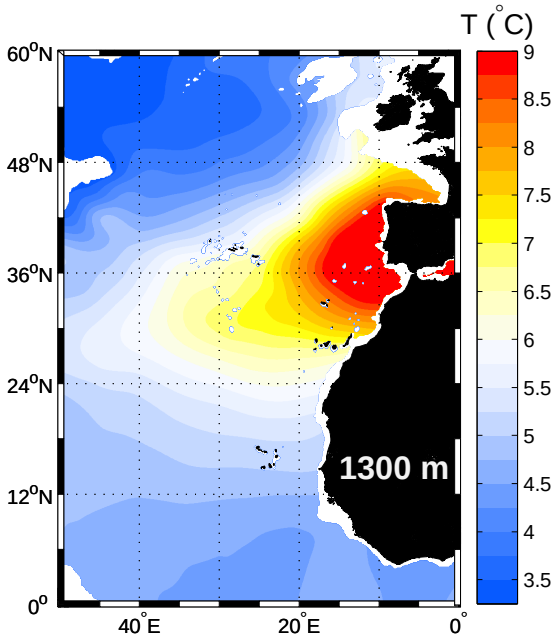

(g)

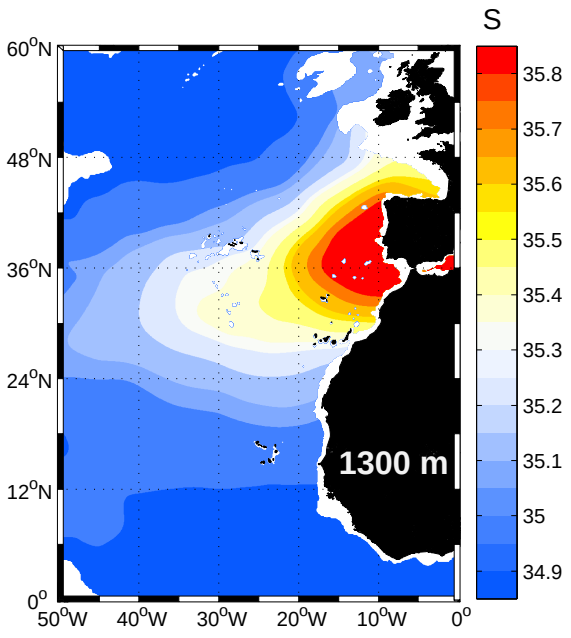

(h)

Figure 2.8: continued.

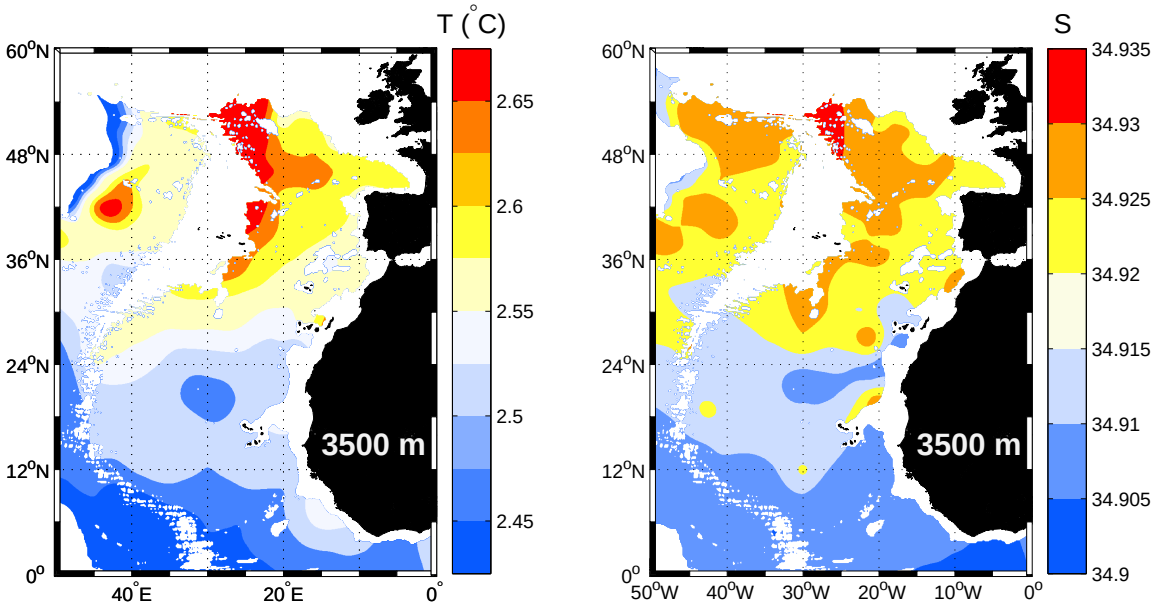

Figure 2.8: continued.

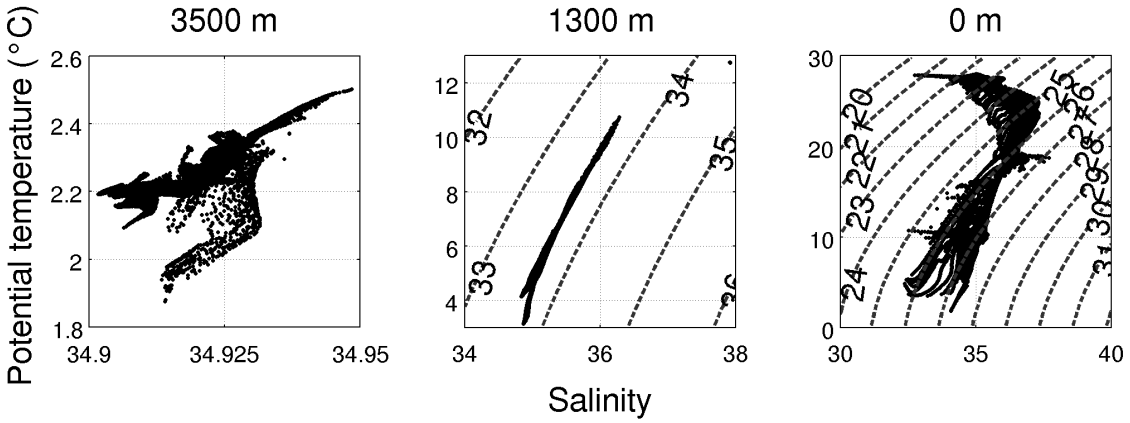

Figure 2.9: T-S diagrams at 0, 1300, and 3500 m.

Near-surface fields

The highest salinity values are observed in the central part of the subtropical gyre and in the Mediterranean Sea, where evaporation overcomes freshwater flux. Four zones are characterized by low salinity:

1. coastal zones of France and England,
2. the southwestern part the domain,
3. the Gulf of Guinea and

4. the Labrador region.

The three formers undergo the effects or river discharge, while the latter has combined effects of melting ice and rivers.

The general temperature structure is a meridional gradient due to different solar radiation. Exceptions lie in the Labrador Sea and in the northwest Africa region, where upwelling is visible from the Strait of Gibraltar to Cape Blanc (20°30'N). In the northwestern part of the domain, strong temperature and salinity gradients appear, and a front separates cold, fresh waters and warm, salty waters. These strong gradients remain visible up to about 700 m.

Another front is observed south of the subtropical gyre (Fig. 2.8), where the westward North Equatorial Current (NAC) makes the connection between South Atlantic Water and North Atlantic Central Water (Lozier *et al.*, 1995).

T-S diagram (Fig. 2.9, left) evidences the presence of numerous water masses as well as the strong surface variability, consequence of the air-sea exchanges. This may constitute an explanation for the low values observed for the correlation length in comparison with the values at higher depth (Fig. 2.4). The strong scattering of properties is mainly observed in the first 100 m of the water column.

Intermediate depth fields

At 700 m, a region of warmer water is limited to the south by a front between North Atlantic and South Atlantic waters and to the north by strong gradients described in the previous section. The salinity map from Fig. 2.8 reveals a clear separation between high-salinity Mediterranean Waters (MW) and Atlantic waters. Between 1000 and 1500 m, the maximal values of temperature and salinity appear near the Iberian Peninsula and Gibraltar.

The lower scattering of properties is underlined by T-S diagram (Fig. 2.9, middle), where a limited number of water masses seems to be present at this level. Such situation is representative of depth levels between 200 and 1750 m, with an overall tendency of decreasing dispersion when depth is increased. As stated before, the same observations were made on the T-S diagrams constructed using WOA and high-resolution model (ROMS) results (not shown here).

Deep-water fields

At higher depths, variations of temperature and salinity are very weak with respect to what is observed at surface. Physical separation between western and eastern Atlantic basins is evidenced by the field differences across the boundary, even if small amounts of North East Atlantic Deep Water (NEADW) is able to flow though the small gaps of the mid-Atlantic ridge.

In the northwestern part of the domain, a zone of low temperature (Fig. 2.8, left) is probably to be the signature of Denmark Strait Overflow Water (DSOW), which crosses

Denmark Strait (between Greenland and Iceland) to reach the Labrador Sea (Lazier *et al.*, 2002). Highest temperatures are located in the northern zone of the eastern basin, centered west of Spain, and is attributed to North Atlantic Deep Water (NADW).

Figure 2.9 (right) shows broad scattering in the property distribution, in agreement with the correlation-length plot (Fig. 2.4) where the minimal value appears around 3500 m, both for temperature and salinity. Similar T-S diagrams are found between 2500 and 5500 m.

2.4.2 Error fields

Along with the analyzed fields, it is often instructive to have the associated error fields, reflecting the confidence one can have in the results. Basically, the error is expected to depend on two factors: the data coverage and the noise on data. OI method provides a way to compute an error estimate, according to the formula:

$$e^2(\mathbf{r}) = \sigma^2 - \mathbf{g}(\mathbf{r})^T \mathbf{D}^{-1} \mathbf{g}(\mathbf{r}) \tag{2.21}$$

where σ^2 is the variance of the true anomaly field, $\mathbf{g}(\mathbf{r})$ is the covariance of the data with respect to the true field (which is dependent on the location $\mathbf{r}$), and $\mathbf{D}$ is the data covariance matrix. For large data sets, such as those used for climatology production, the operation (2.21) is costly, since it requires the inversion of the covariance matrix $\mathbf{D}$.

McIntosh (1990) and Bennet (1992) demonstrated the equivalence between smoothing splines and OI, under the condition of identity of covariance function of OI and reproducing kernel for norm splines. Brankart & Brasseur (1998) and Rixen *et al.* (2000) used this identity to derive an error expression for the VIM. In practice the data input of the analysis tool for an error calculation is a vector containing the covariance of data points with respect to the point where the error estimate is to be calculated. Rixen *et al.* (2000) showed that, for large grids, VIM becomes numerically cheaper than OI when the number of data is larger than the number of degrees of freedom of the finite element mesh. This method will be referred to as hybrid method and is one of the three implemented in Diva.

In the OI method, the term $\mathbf{g}(\mathbf{r})^T \mathbf{D}^{-1}$ is the analysis operator, i.e., the operator that relates the data to the analyzed field. To compute the error field, the analysis operator has to be applied to $\mathbf{g}(\mathbf{r})$ (2.21). The problem comes down to evaluate $\mathbf{g}(\mathbf{r})$.

Recent developments detailed in Troupin *et al.* (2011) permitted the derivation of the real covariance function through the execution of Diva. At each point at which the error is needed, two analyzes are performed: the first one is made with the already existing LU decomposition (decomposition into a product of a lower triangular matrix L and an upper triangular matrix U) of one Diva execution to calculate the error, the other with an existing LU decomposition of another Diva execution to calculate the covariance function.

An additional simplification provides the poor man's error indicator: instead of applying the analysis operator to $\mathbf{g}(\mathbf{r})$, it is applied to a vector of the size of the data, but filled with σ^2. It constitutes the quickest method, since the error is evaluated at every grid points in only one operation. Nevertheless, the error fields computed this way are systematically underestimated.

An application is presented in Fig. 2.10: relative (to the field variance) error fields for temperature are computed on a $0.5 \times 0.5°$ grid for the temperature in January at 2000 m. In these figures, the standard deviation (in °C) is represented. In each case, the importance of data coverage is underlined, as the main error region occur in a zone that approximatively spreads from 10 to 20°W and from the equator to 12°W and totally void of data. Another location where high errors are observed is within the small isolated contours within the Middle Atlantic Ridge. The difference with the previous region is that these small contours are not physically connected to the rest of the ocean in the horizontal layer, illustrating the disconnection of error field in non-adjacent area.

Figures 2.10(b) and (c) show very similar error fields, meaning that in the present case, the hybrid approach was sufficient to correctly estimate the covariance function. The poor man's version yields lower values over the whole domain. However, it efficiently provides a qualitative mapping of the error estimate, which can later be used to produce a mask over the analyzed fields.

Eventually, similar error computations were carried out at different levels and at different times of the year, both for temperature and salinity. They revealed the same conclusions concerning the error distribution and the importance of data coverage.

2.5 Discussion

2.5.1 Comparison with World Ocean Atlas

To have an overall validation of the method, maps of analyzed fields are compared with the 1°-resolution WOA05 (Fig. 2.11). Even if this first comparison is mainly visual, it confirms that without sophisticated quality control or any application of posterior filtering on the fields, Diva is able to reproduce features comparable to those of WOA05.

However, the lack of resolution of WOA05 (and other recent climatologies, such HydroBase and WOCE GHC) is particularly visible near the coasts and around archipelago (e.g., Canary Islands, Azores). Also, interior seas and channels (Mediterranean Sea, English Channel, Strait of Gibraltar) are not covered at all by the latter climatologies.

Separation between basins

Salinity analysis around the Strait of Gibraltar are presented in Fig. 2.12. The objective of this example is to illustrate the mixing of waters with OA (WOA05) and Diva methods. In the right panel (WOA05), a zonal gradient visible on both side of the strait: the radius of influence of the OA method has propagated the high-salinity information westward, while the Mediterranean waters are supposed to sink and flow into the Atlantic Ocean at higher depths. The analysis provided by Diva is different, as the flow of less-saline Atlantic water into the Mediterranean Sea is clearly visible.

Another instructive example is found in Brasseur *et al.* (1996), where in situ measurements in the Mediterranean Sea are analyzed using both OA and VIM. In the OA

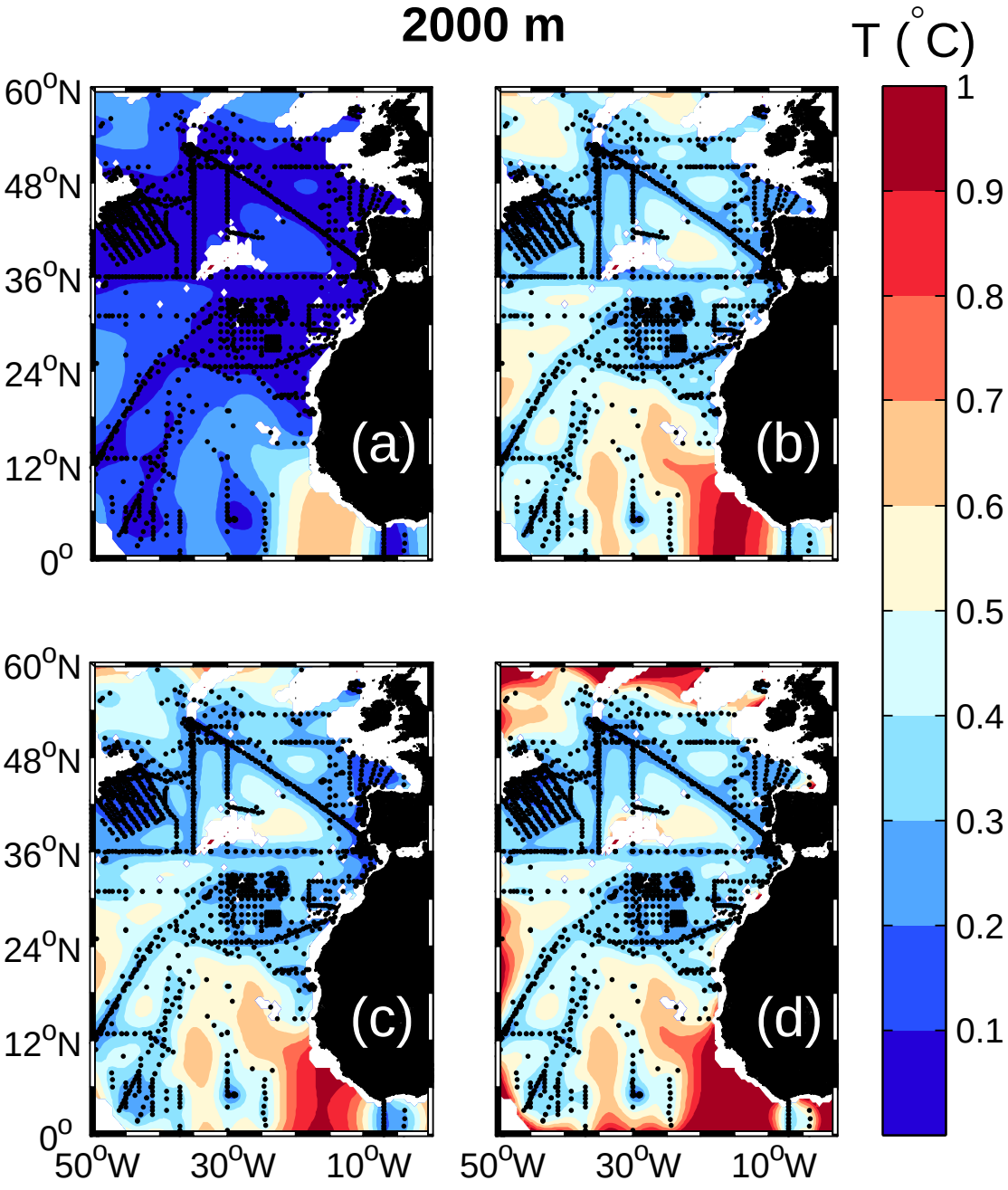

Figure 2.10: Relative error fields computed with the different methods for temperature in January at 2000 m: (a) poor man's error estimate, (b) hybrid method, (c) real covariance function and (d) real covariance with boundary effect. Black circles indicate data locations.

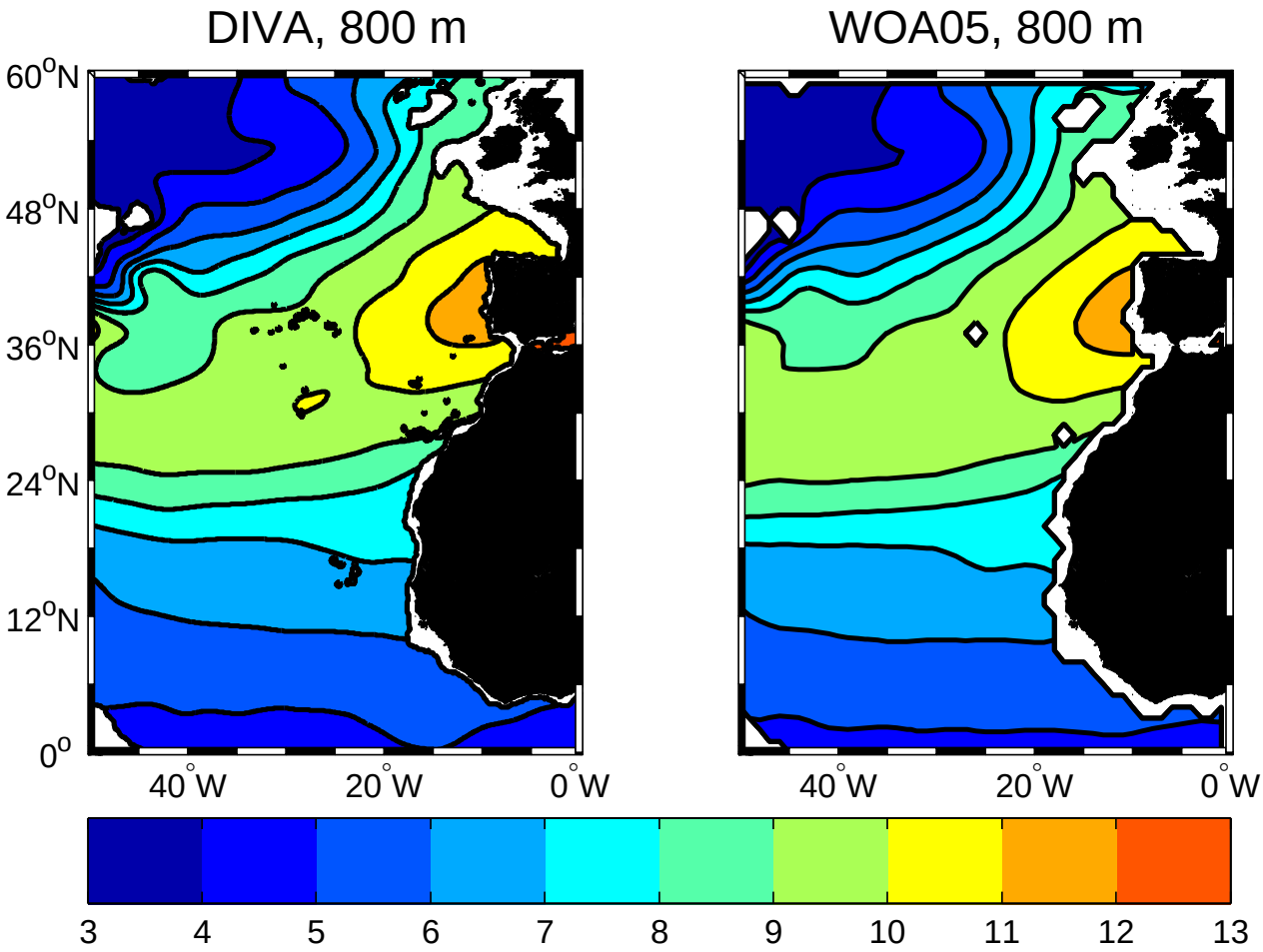

Figure 2.11: Annual temperature fields at 800 m from Diva (a) and from WOA05 (b).

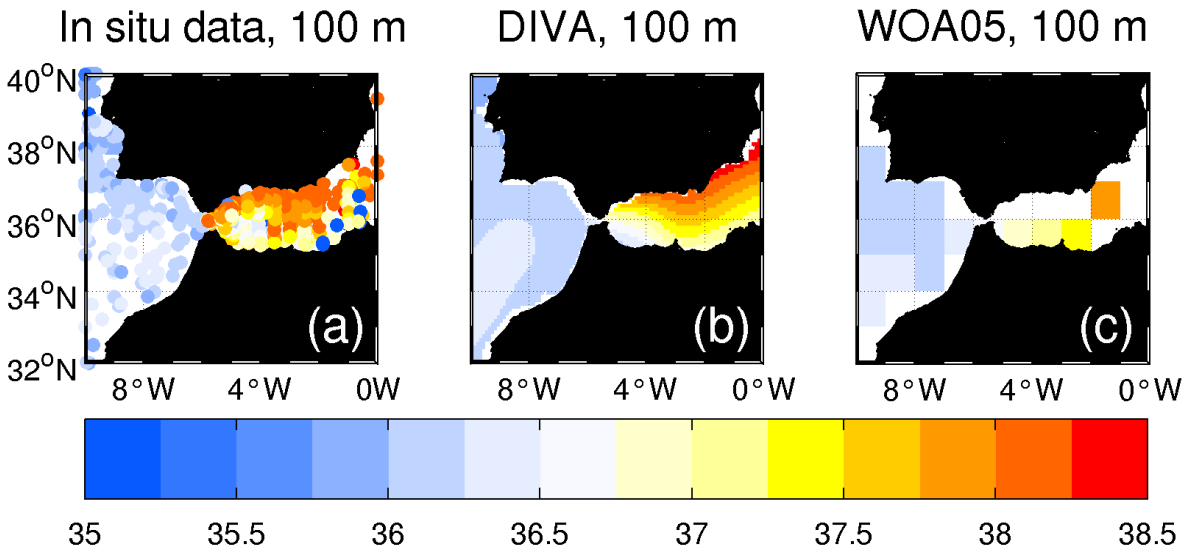

Figure 2.12: Salinity observations in July at 100 m around the Strait of Gibraltar (a) and corresponding analysis from Diva (b) climatology and WOA05 (c).

solution, it appears that low-salinity coastal waters in the Adriatic Sea influence waters in the Tyrrhenian Sea, while the two are separated by Italy.

Coastal area

This particular example concentrates on Cape Blanc (20°N, Mauritania) upwelling region, in order to show the impact of a better resolution near the coast. It is essential to stress that this illustration did not require a new analysis, but is merely an enlargement of a determinate zone, in order to show features that would not be easily visible on the global map.

The Cape Blanc region is characterized by a permanent upwelling (e.g., Barton *et al.*, 1998) and a quasi-permanent filament (Van Camp *et al.*, 1991; Gabric *et al.*, 1993). This structure has been frequently sampled, making available a large number of data. South of the Cape (between 15 and 21°N) lies a mesoscale cyclonic gyre. Its position varies over the year, but it is still present all year long.

To illustrate these features, the temperature field is extracted at 50 m in August from the Diva and WOA05 climatologies (Fig. 2.13). North of the cape, the characteristics of the fields are similar, except that in the left panel, the temperature reaches lower values, characteristic of the coastal upwelling. However, this first difference can be, at least partly, attributed to the grid resolution of the two climatologies, and to the mode of representation of the fields (contours).

A more interesting feature is the eddy visible south of the cape in the left panel. As the data sets used are not too different (Section 2.5.3), the difference between the two fields is attributed to the analysis method itself: WOA05 uses 1° square temperature averages as input of the objective analysis program (Locarnini *et al.*, 2006). The averaging

is responsible for the smoothing of the field and may generate the loss of information contained in the data.

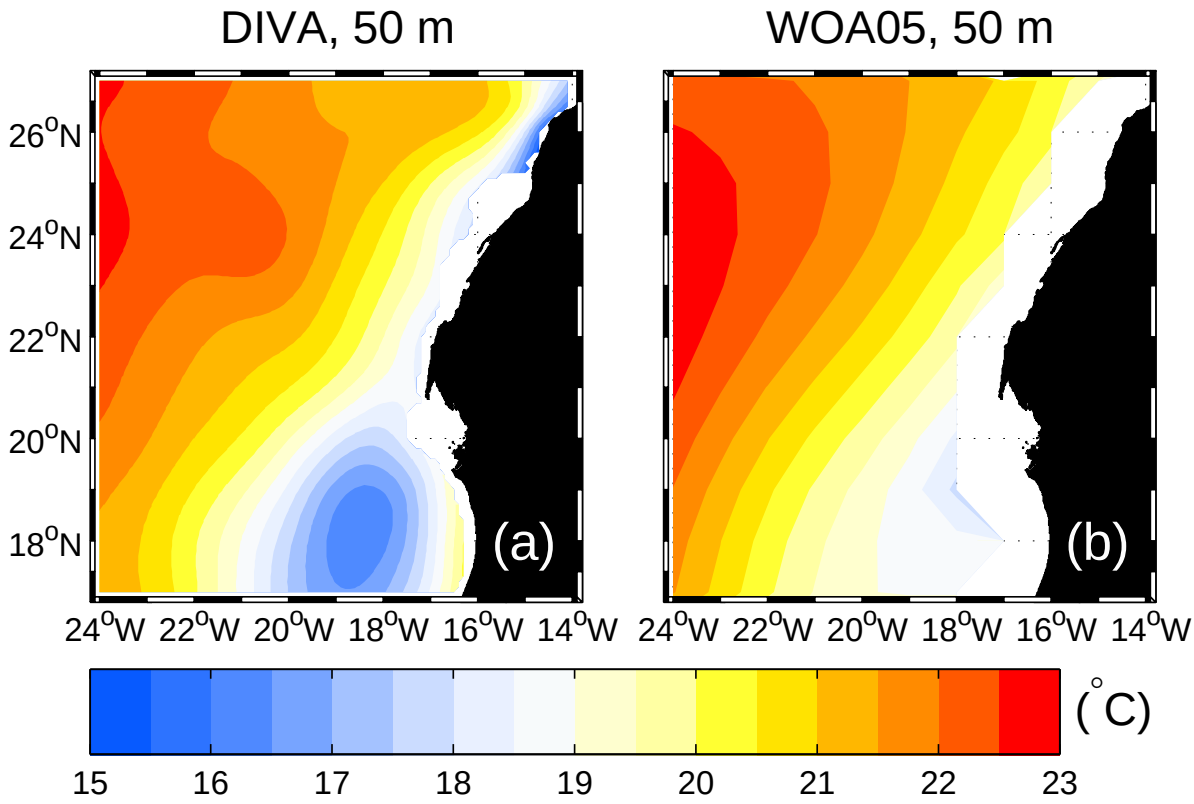

Figure 2.13: Temperature fields in August at 50-m depth, (a) from Diva climatology (b) from WOA05.

2.5.2 Outlier detection

As part of the analysis, an automatic quality control routine is applied. The objective is to remove data that create irregularities in the analyzed fields but that were not previously detected by a priori quality checks (as described in Section 2.2.2). Such data may not be defined as outliers, since their value is situated within an acceptable range and since they do not differ from the local ($5° \times 5°$) mean with more than three STD's. But they are not compatible with the construction of a climatology, which supposes relatively regular fields, i.e., exempt of very local variation.

An application is shown in Fig. 2.14: on the right side (no QC), several small salinity structures (indicated by black arrows), referred as bull's eye in Lozier *et al.* (1995), are visible, for example south of the Azores. These structures may be attributed to suspect data and the latter shall be removed in the final version of the climatological field, even if the measurement in itself is correct. On the left is the field after removal of the suspect observations: the bull's eyes have been eliminated.

Typically, these observations may arise from campaigns that aimed to sample small scale structures (eddies, meddies, filaments etc). If the number of such observations is

small with respect to the total number of data in the region, Diva quality control will be able to detect them automatically. Otherwise, if these observations represent a significant proportion of the available data in the region, they will be considered as good data, thus the small scale structure will be present in the final analyzed field. If it is the case, data have to be removed by hand. A concrete example is a meddy sampled during a cruise in June 1982, with a clear signature from 700 to 1300 m depth: numerous data points come from this cruise, and the traditional outliers detection criterion are not able to spot them.

The difference between the two fields (with and without outliers) is mapped in Fig. 2.15, along with the suspect data locations. The first striking fact is that most of the suspect data are located near Newfoundland and Labrador shelves. As outlined in Section 2.2.1, this zone is characterized by a strong variability, due to the encounter of Gulf Stream and Labrador Current. Nevertheless, the removal of numerous data in this region did not strongly affect the analyzed field. This is simply explained by the large number of measurements available (see Fig. 2.2).

A second important feature is that the greatest differences between the two fields occur in the southwest part of the domain, next to the Brazilian shelf. The color bar reveals that waters are saltier in the case where outliers are removed. This is attributed to the localized influence of the Amazon fresher water, transported north-westward by the North Brazil Current.

It is to highlight that the data responsible for the small salinity patches were detected, even if their number was relatively important in the case of the south Azores region. This section is concluded by the important comment that the decision of removing or not suspect data has to be made by the user himself. The decision should be made in agreement with the pursued goal, considering that analyzing climatological data is different than working with synoptic data sets. Generally, a good knowledge of the physical processes in the region of interest is a necessary step toward the finalization of a climatology.

2.5.3 Benefits from using aggregated data set

As described in Section 2.2, the climatology presented in this Chapter is constructed upon an aggregated data set, which includes the WOD. Two questions arise from this specificity:

- Is it worth working with such data sets, or put in other words, is it worth dedicating time to produce new data sets from several sources?
- How does it translate, in terms of temperature and salinity, to the analyzed fields?

The answers to these questions obviously depend on the location of the additional data with respect to the original database, WOD in this case, and on their quality.

Analyzed fields are compared with and without the additional observations, as illustrated in Fig. 2.16, which shows temperature fields in October at 700 m. These fields are representative of general features that were obtained for other depths, months or variables. Two possibilities have to be considered:

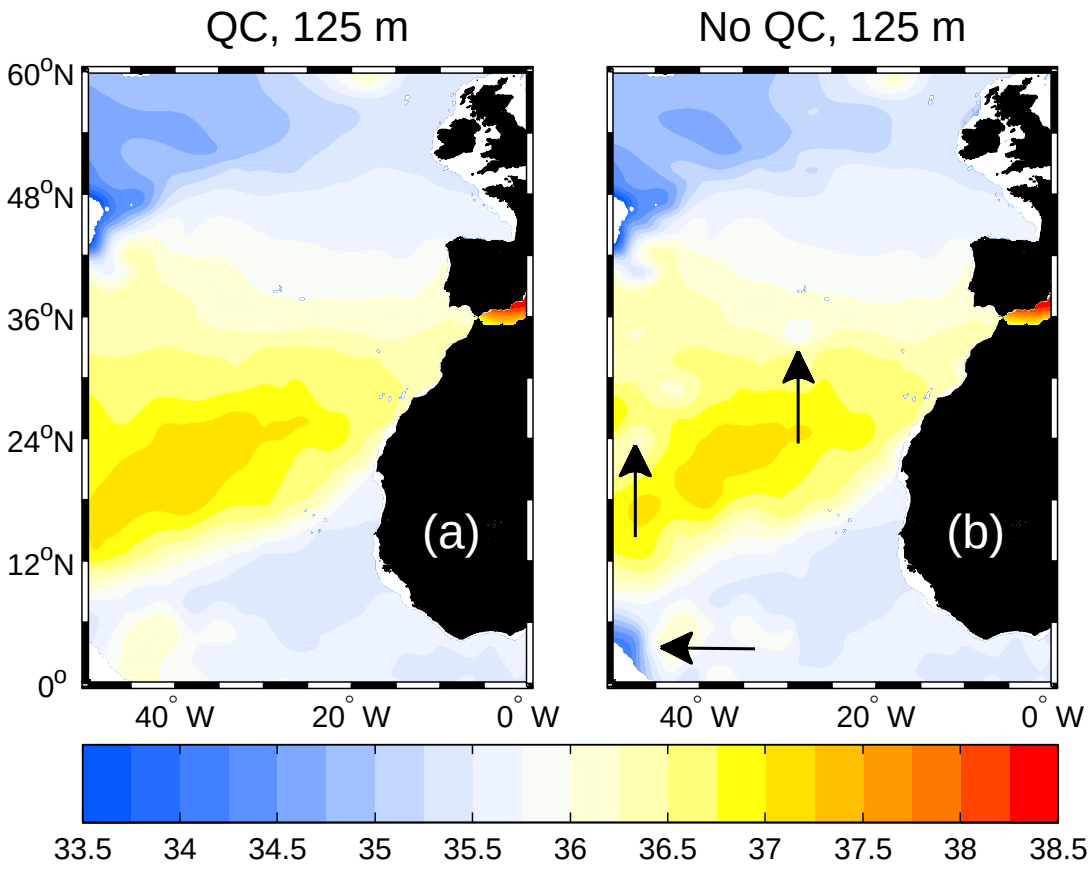

Figure 2.14: Salinity field in January at 125 m, with (a) and without (b) Diva quality check. Arrows indicate areas where largest differences occur.

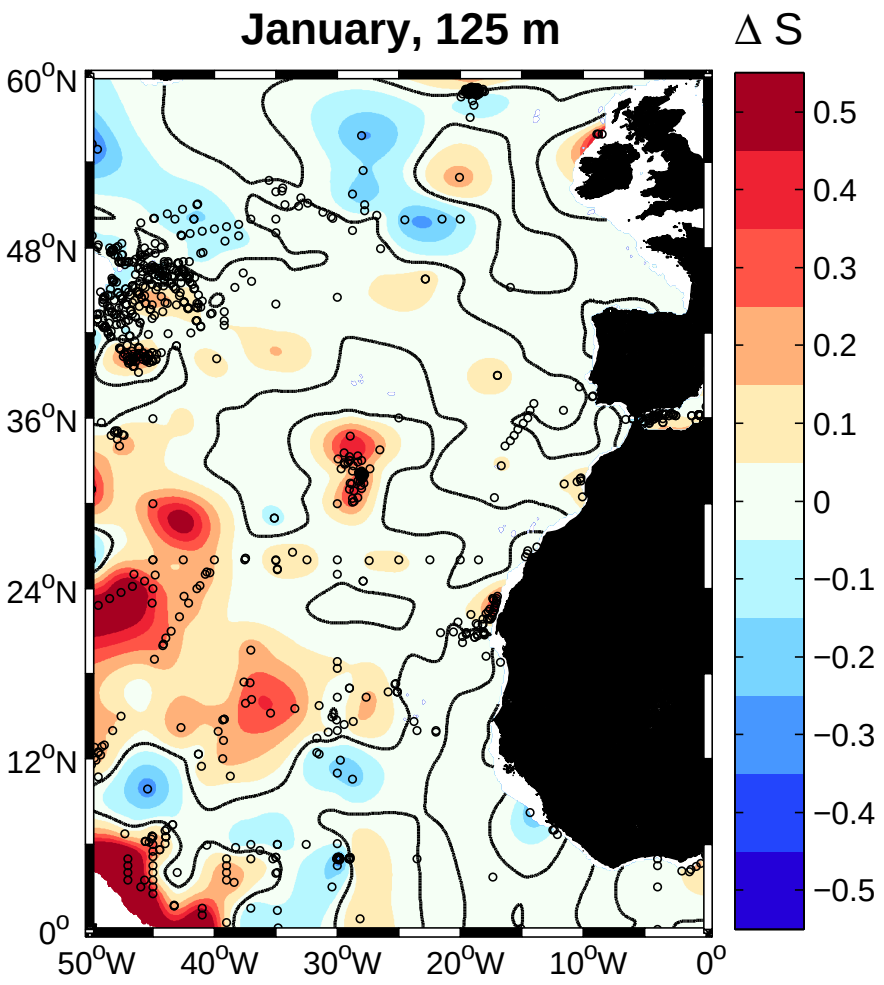

Figure 2.15: Salinity difference between analyzed fields without and with suspect data in January at 125 m. Suspect observations are denoted by black circle. Isohalines are separated by $\Delta S = 0.1$, thick lines represent isohaline $\Delta S = 0$. Red color indicates higher salinity for the no-outlier field.

1. additional data are found where data coverage is already good.

2. additional data manage to fill in the gaps left by the initial coverage.

For the domain of interest, it is mainly the situation described in the first case: the initial data coverage was already good, and the additional observations were almost always located in already sampled zones. This is why the two fields are relatively close (Fig. 2.17, lower than 0.1°C) within a large area. Nevertheless, large differences between the fields occur locally, for instance south of the Grand Banks of Newfoundland (between 36 and 42°N). Justifying these differences is quite delicate. A first hypothesis is that data have undergone stricter quality control before their inclusion into WOD than into the other individual databases (Section 2.2.1). The second hypothesis is that these data are indeed correct and have to be included in the analysis. For example, if the measurements were made during campaigns under particular oceanographic or atmospheric conditions, they might perturb the field constructed using observations from the initial data set. As the Newfoundland region is known for its strong variability, the latter hypothesis turns out to be plausible. The solution to confirm one of the hypothesis would be to apply again the WOD quality checks to all the other databases prior to their merging.

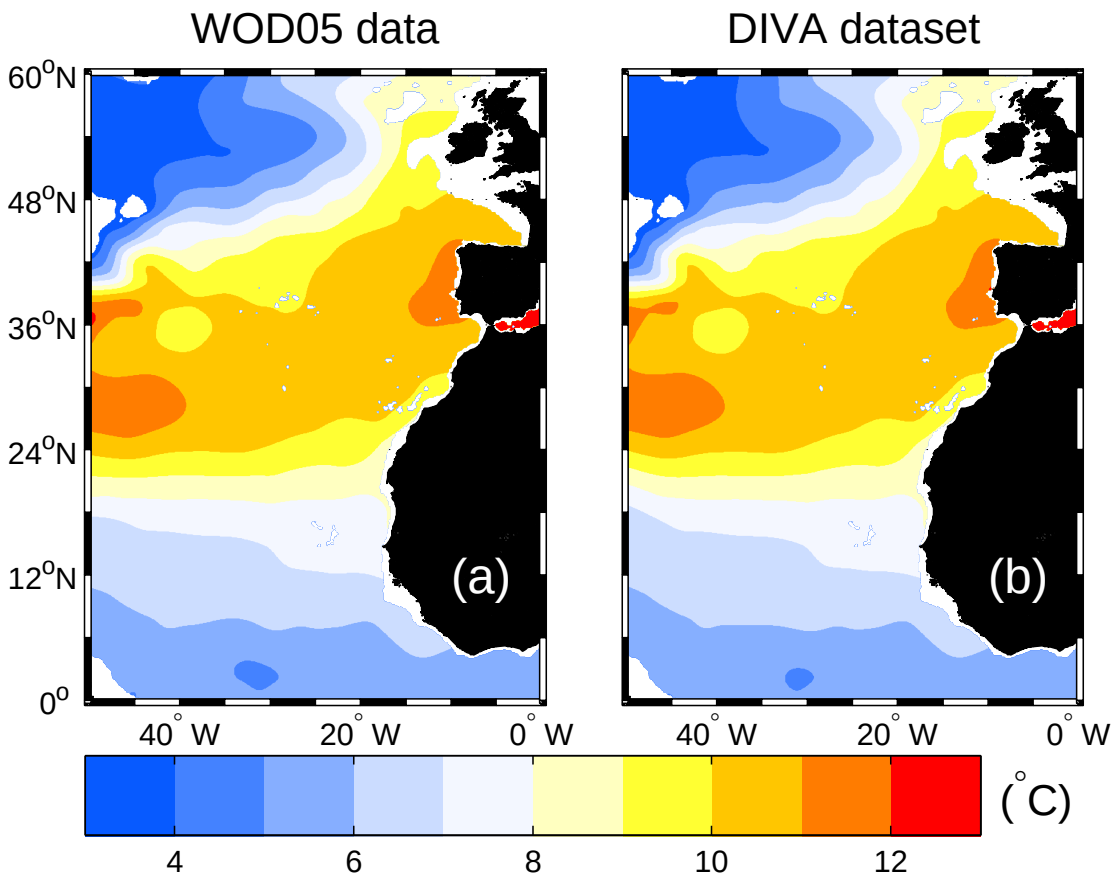

Figure 2.16: Temperature fields in October at 700-m depth, as obtained from WOD (a) and merged (b) data sets.

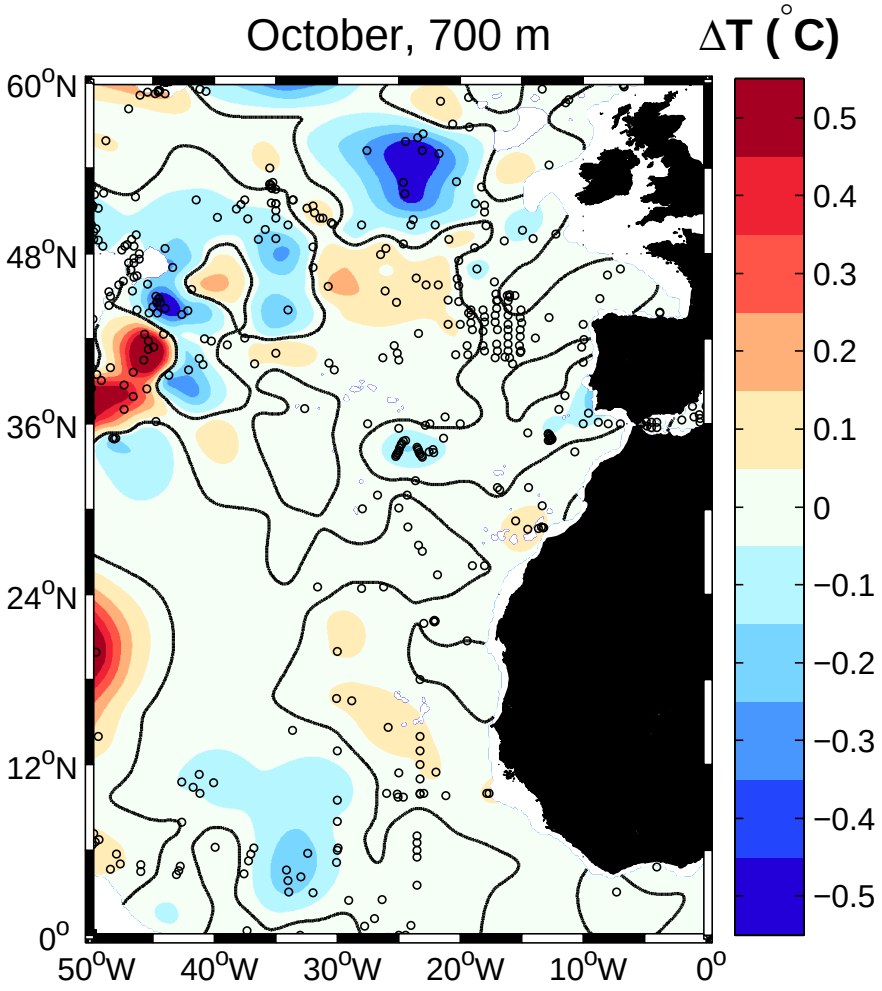

Figure 2.17: Difference between the temperature fields in October; thick lines represent $\Delta T = 0$).

2.6 Conclusions

We present a practical application of the software Diva on an aggregation of several data sets in the North East Atlantic. Diva possesses numerous advantages over recently developed climatologies: this objective method is applicable in any region of the ocean and implies a limited number of parameters needed to go from raw data to the gridded climatology. The innovation in the present work is two-fold:

1. the database, constructed by assembling data sets from various sources and eliminating the resulting duplicates.
2. the method, of which the benefits were reviewed along this paper: high resolution output grid, consideration of physical boundaries in the analysis process, low number of parameters, determined in objective way, efficient finite-element solver, and generation of associated error fields. The latter is of particular importance, as most of currently available climatologies do not offer this feature.

Comparisons with WOA05 reveal a better representation of the coastal zones, which are usually the most sampled regions. Also, the physical separation of water masses (i.e., through bottom topography) shown in Section 2.5.1 highlights the coherence of the variational method.

Concerning the relevance of using aggregated database, the results obtained here did not show significant improvements, that is to say the overall data coverage was only slightly enhanced, since the new data were mostly situated in regions already well sampled. However, this small amount of extra data was sufficient to create visible differences in the analyzed fields. It remains to evidence if this is due to a real addition of information from the new data, or if it is an effect of insufficient quality control in each individual database. Nevertheless, the construction of local climatologies on more reduced regions may certainly benefit from the use of gathered data sets.

Finally, the method outlined here is very general, hence it can be applied to any region of the World Ocean, provided the data have been properly prepared.

2.6.1 Possible improvements

Many developments are expected to be made in the future:

1. Extension of the selected types of instruments for the new database: they will not be limited only to CTD's and bottles, but will also include profiling floats. XBT's and MBT's constitute valuable sources of information on the ocean characteristics and are expected to help increasing the data coverage, thus decreasing the error fields. Once again, the obstacle to overcome is the preparation of data, for instance the quality control and correction of instrument systematic errors. Nevertheless, the first tests we performed to create this new database showed that the additional observations are mostly concentrated where data are already present. This is why it is believed that the general results will not undergo substantial modifications.

2. Use of isopycnic coordinates instead of isobaths. The principle of Diva is to perform analysis in horizontal planes, whatever the vertical coordinates are. The task will consist in transforming depth surfaces into density surfaces, prior to the analysis, and then to switch back to depths after it.

3. Combined analysis of in situ and remote sensing data for the surface fields: satellite images provide high-resolution temperature fields that can certainly help improving the analysis at surface. The difficulty is to take into account the possible bias that exist between satellite and in situ data (e.g., Reynolds *et al.*, 2002). A preliminary work by Alvera-Azcárate *et al.* (2011) was dedicated to the study of the statistics of in situ and satellite data in a common region (Western Mediterranean Sea). They showed that the bias and the RMS error between the two kinds of measurement depend on the instrument and the database considered.

2.6.2 Exploitation of the fields

Recently Mason *et al.* (2011) studied the Canary Basin circulation using the NE Atlantic climatology to construct their initial and boundary conditions for temperature and salinity, instead of the widespread WOA. For the initialization, the original fields were simply interpolated horizontally and vertically onto the model grid. In order to avoid aliasing problems, the climatology resolution was reduced to 0.25°, instead of the 0.1° in the original version. The signal-to-noise ratio was slightly increased in order to have less smooth fields as initial condition.

For the boundary condition extraction, the procedure described in Mason *et al.* (2010) was applied: it consists of a one-way nesting tool where the conditions are set in order to limit the wave reflection at the open boundaries of the domain. The combination of this procedure with the new climatology provided encouraging results, namely improvements in the representation of the Azores Current. In this particular application, the correct detection of outliers was of primary importance to assure physically acceptable fields: even small hydrostatic instabilities present in early versions of the climatology had dramatic influences on the model outputs. This highlights the advantage of having a numerical model running in the same area as the climatology.

2.6.3 Application to other regions

As stated previously, the method described to produce regional climatologies is sufficiently general to be applied to other area. This was done for the Mediterranean Sea, with the objective of providing initial and boundary conditions for a numerical model implemented in the region (F. Lenartz, personal communication). The selected domain (Fig. 2.18) also contains the Black Sea and parts of the North Atlantic Ocean.

A mesh was created for each standard level (Tab. 2.3) between 0 and 4000 m and stored for further use. The case is particularly interesting, because of the separation of the sea into several basin. Examples of analyzed fields are presented in Fig. 2.19. The separation between the Black Sea cool waters and the Mediterranean Sea water appears

clearly, as well as differences between the eastern and western basins. Note the presence of the Rhodes Gyre (35°N, 28°E), a persistent cyclonic eddy with a radius of about 300 km (Milliff & Robinson, 1992; Robinson *et al.*, 1992). The whole climatology is available at http://gher-diva.phys.ulg.ac.be/gher-data/.

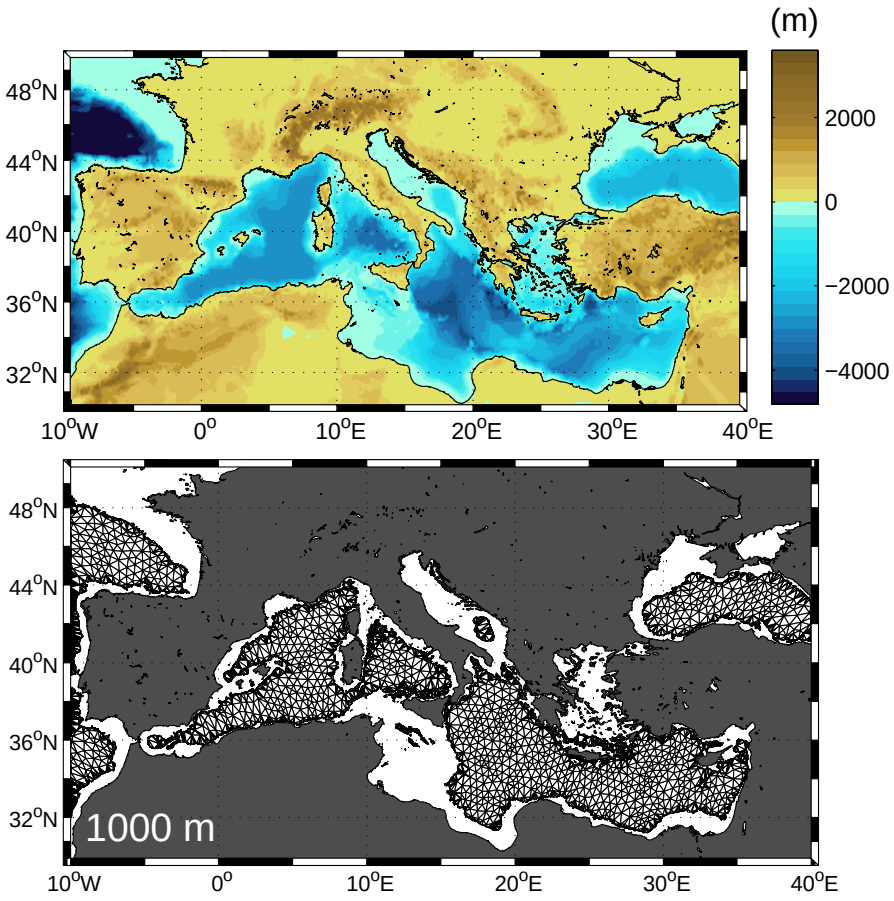

Figure 2.18: Bathymetry of the Mediterranean Sea and finite-element mesh at 1000 m.

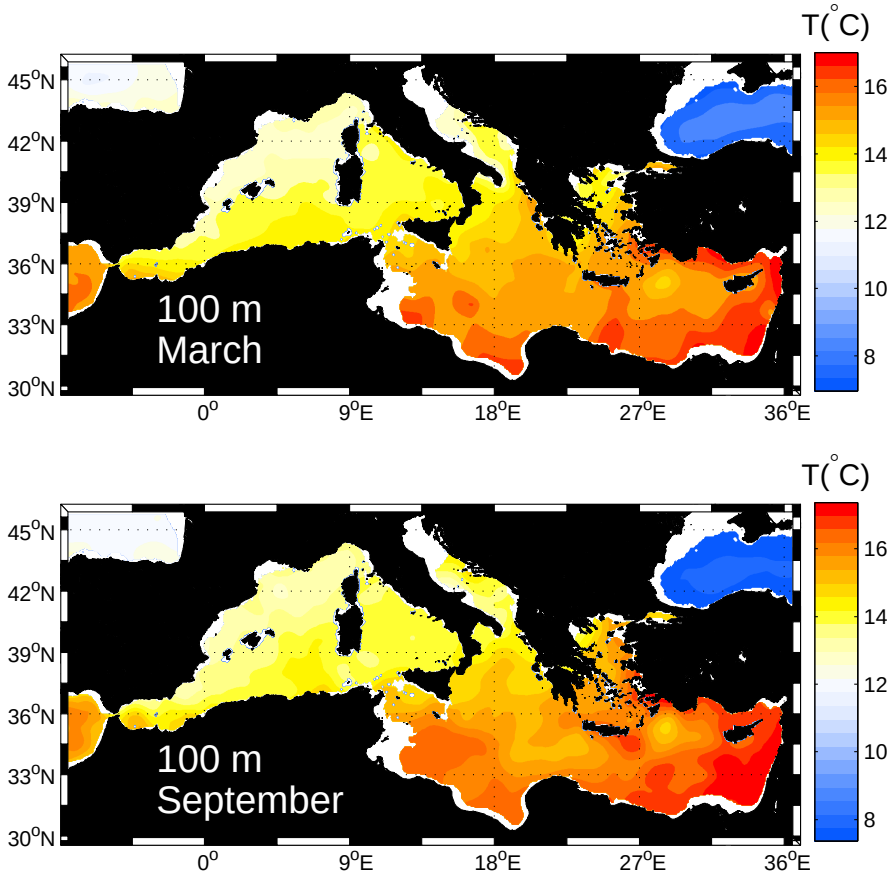

Figure 2.19: Gridded fields of temperature in March (top) and September (bottom) at 100 m.

Acknowledgments

Diva software has been improved in the frame of the SeaDataNet project (http://www.seadatanet.org/), an Integrated Infrastructure Initiative of the EU Sixth Framework Programme. Numerous comments from the users, in particular during the annual Diva workshops, contributed to improve the method.

The Ocean Climate Laboratory (OCL), International Council for the Exploration of the Sea (ICES), HydroBase2, Coriolis and Mediterranean Data Archeology and Rescue (MEDAR) projects greatly helped the production of the present version of the climatology by freely making available the data.

We thank E. Fraile Nuez (IEO, Spain) for his contribution during the preparation of the database and E. Mason (ICM-CSIC, Spain) for his numerous tests of the climatology with a numerical model, which lead to substantial improvement of the final product.

References

Abramowitz, M. & Stegun, I. A. (eds.) (1964). *Handbook of Mathematical Functions with Formulas, Graphs, and Mathematical Tables*. Dover, New York, 1044 pp. ISBN 0-486-61272-4.

Alvera-Azcárate, A., Troupin, C., Barth, A. & Beckers, J.-M. (2011). Comparison between satellite and in situ sea surface temperature data in the Western Mediterranean Sea. *Ocean Dynamics*, **61(6)**: 767–778. doi:10.1007/s10236-011-0403-x.
URL http://www.springerlink.com/content/r5784271357u5400/

Barnes, S. L. (1964). A technique for maximizing details in numerical weather map analysis. *Journal of Applied Meteorology*, **3(4)**: 396–409. doi:10.1175/1520-0450(1964)003<0396:ATFMDI>2.0.CO;2.
URL http://journals.ametsoc.org/doi/abs/10.1175/1520-0450%281964%29003%3C0396%3AATFMDI%3E2.0.CO%3B2

Barth, A., Alvera-Azcárate, A., Troupin, C., Ouberdous, M. & Beckers, J.-M. (2010). A web interface for griding arbitrarily distributed in situ data based on Data-Interpolating Variational Analysis (DIVA). *Advances in Geosciences*, **28**: 29–37. doi:10.5194/adgeo-28-29-2010.
URL http://www.adv-geosci.net/28/29/2010/adgeo-28-29-2010.html

Barton, E. D., Arístegui, J., Tett, P., Cantón, M., García-Braun, J., Hernández-León, S., Nykjaer, L., Almeida, C., Almunia, J., Ballesteros, S., Basterretxea, G., Escánez, J., García-Weill, L., Hernández-Guerra, A., López-Laatzen, F., Molina, R., Montero, M. F., Navarro-Pérez, E., Rodríguez, J. M., van Lenning, K., Vélez, H. & Wild, K. (1998). The transition zone of the Canary Current upwelling region. *Progress in Oceanography*, **41**: 455–504. doi:10.1016/S0079-6611(98)00023-8.

Bennet, A. (1992). *Inverse methods in physical oceanography*. Cambridge Monographs on Mechanics and Applied Mathematics, 368 pp. doi:10.1017/CBO9780511600807. ISBN 0-521-38568-7.

Boyer, T., Levitus, S., Garcia, H., Locarnini, R. A., Stephens, C. & Antonov, J. (2005). Objective analyses of annual, seasonal, and monthly temperature and salinity for the World Ocean on a 0.25° grid. *International Journal of Climatology*, **25(7)**: 931–945. doi:10.1002/joc.1173.

Brankart, J.-M. & Brasseur, P. (1996). Optimal analysis of in situ data in the Western Mediterranean using statistics and cross-validation. *Journal of Atmospheric and Oceanic Technology*, **13**: 477–491. doi:10.1175/1520-0426(1996)013<0477:OAOISD>2.0.CO;2.

Brankart, J.-M. & Brasseur, P. (1998). The general circulation in the Mediterranean Sea: A climatological approach. *Journal of Marine Systems*, **18**: 41–70. doi:10.1016/S0924-7963(98)00005-0.

Brasseur, P. (1994). *Reconstruction de champs d'observations océanographiques par le Modèle Variationnel Inverse: Méthodologie et Applications*. Ph.D. thesis, University of Liège. 267 pp.

Brasseur, P., Beckers, J.-M., Brankart, J.-M. & Schoenauen, R. (1996). Seasonal temperature and salinity fields in the Mediterranean Sea: Climatological analyses of a historical data set. *Deep-Sea Research I*, **43**: 159–192. doi:10.1016/0967-0637(96)00012-X.

Brasseur, P. & Haus, J. (1991). Application of a 3-D variational inverse model to the analysis of ecohydrodynamic data in the Northern Bering and Southern Chukchi Seas. *Journal of Marine Systems*, **1**: 383–401. doi:10.1016/0924-7963(91)90006-G.

Calder, C. A. & Cressie, N. (2007). Some topics in convolution-based spatial modeling. In *Proceedings of the 56th Session of the International Statistics Institute*. Lisbon, Portugal.

Chang, C.-W. J. & Chao, Y. (2000). A comparison between the World Ocean Atlas and Hydrobase climatology. *Geophysical Research Letters*, **27**: 1191–1194. doi:10.1029/1999GL002379.

Chassignet, E. P., Smith, L. T., Halliwell, G. R. & Bleck, R. (2003). North Atlantic simulations with the Hybrid Coordinate Ocean Model (HYCOM): Impact of the vertical coordinate choice, reference pressure, and thermobaricity. *Journal of Physical Oceanography*, **33**: 2504–2526. doi:10.1175/1520-0485(2003)033<2504:NASWTH>2.0.CO;2.

Cleveland, W. S. & Devlin, S. J. (1988). Locally weighted regression: An approach to regression analysis by local fitting. *Journal of the American Statistical Association*, **83**: 596–610. doi:10.2307/2289282.

Conkright, M., O'Brien, T., Boyer, T. P., Stephens, C., Locarnini, R. A., Garcia, H., Murphy, P. P., Johnson, D., Baranova, O., Antonov, J. I., Tatusko, R. & Gelfeld, R. (2002). World Ocean Database 2001 CD-Rom data set documentation. Tech. rep., National Oceanographic Data Center, Washington, D.C.

Denis-Karafistan, A., Martin, J.-M., Minas, H., Brasseur, P., Nihoul, J. & Denis, C. (1998). Space and seasonal distributions of nitrates in the Mediterranean Sea derived from a variational inverse model. *Deep-Sea Research*, **45**: 387–408. doi:10.1016/S0967-0637(97)00089-7.

Fichaut, M., Garcia, M., Giorgetti, A., Iona, A., Kuznetsov, A., Rixen, M. & Medar Group (2003). MEDAR/MEDATLAS 2002: A Mediterranean and Black Sea database for operational oceanography. In *Building the European Capacity in Operational Oceanography, Proceedings of the Third International Conference on EuroGOOS*, vol. 69, pp. 645–648. doi:10.1016/S0422-9894(03)80107-1.

Gabric, A. J., García, L., van Camp, L., Nykjaer, L., Eifler, W. & Schrimpf, W. (1993). Offshore export of shelf production in the Cap Blanc giant filament as derived from CZCS imagery. *Journal of Geophysical Research*, **98**: 4697–4712. doi:10.1029/92JC01714.

Gandin, L. S. (1965). *Objective analysis of meteorological fields*. Israel Program for Scientific Translations, Jerusalem, Israel, 242 pp.

Gouretski, V. V. & Koltermann, K. P. (2004). WOCE Global Hydrographic Climatology. *Berichte des Bundesamtes für Seeschifffahrt und Hydrographie*, **35**: 52 pp.

Gyory, J., Mariano, A. J. & Ryan, E. H. (2011). Ocean surface currents: The Labrador Current. http://oceancurrents.rsmas.miami.edu/atlantic/labrador.html. Accessed April 12, 2011.

Hanawa, K., Rual, P., Bailey, R., Sy, A. & Szabados, M. (1994). Calculation of new depth equations for expendable bathythermographs using a temperature-error-free method (Application to Sippican/TSK T-7, T-6 and T-4 XBTs). Technical Series 42, Intergovernmental Oceanographic Commission. 46 pp.

Hanawa, K. & Yasuda, T. (1992). New detecton method for XBT depth error and relationship between depth error and coefficients in the depth-time equation. *Journal of Oceanography*, **48**: 221–230. doi:10.1007/BF02239006.

Higdon, D. (1998). A process-convolution approach to modelling temperatures in the North Atlantic Ocean. *Environmental and Ecological Statistics*, **5**: 173–190. doi:10.1023/A:1009666805688.

Higdon, D., Swall, J. & Kern, J. (1998). Non-stationary spatial modeling. In J. M. Bernardo, J. O. Berger, A. P. Dawid & A. F. M. Smith (eds.), *Bayesian Statistics 6*, p. 880. Oxford University Press. ISBN 0-19-850485-3.

Hunter, P. & Macnab, R. (2003). The GEBCO Digital Atlas published by the British Oceanographic Data Centre on behalf of IOC and IHO. North Atlantic region.
URL http://www.gebco.net/

Johnson, D. R., Boyer, T. P., Garcia, H. E., Locarnini, R. A., Mishonov, A. V., Pitcher, M. T., Baranova, O. K., Antonov, J. I. & Smolyar, I. V. (2006). World Ocean Database 2005 documentation. In S. Levitus (ed.), *NODC Internal Report 18*, p. 163. U.S. Government Printing Office, Washington D.C.
URL http://www.nodc.noaa.gov/OC5/WOD05/docwod05.html

Karafistan, A., Martin, J.-M., Rixen, M. & Beckers, J.-M. (2002). Space and time distributions of phosphates in the Mediterranean Sea. *Deep-Sea Research I*, **49**: 67–82. doi:10.1016/S0967-0637(01)00042-5.

Kim, H.-S., Gangopadhyay, A., Rosenfeld, L. K. & Bub, F. L. (2007). Developing a high-resolution climatology for the Central California coastal region. *Continental Shelf Research*, **27**: 2135–2161. doi:10.1016/j.csr.2007.05.011.

Lazier, J., Hendry, R., Clarke, A., Yashayaev, I. & Rhines, P. (2002). Convection and restratification in the Labrador Sea, 1990-2000. *Deep-Sea Research*, **49**: 1819–1835. doi:10.1016/S0967-0637(02)00064-X.

Lemos, R. T. & Sansó, B. (2006). Spatio-temporal variability of ocean temperature in the Portugal Current System. *Journal of Geophysical Research*, **111**: C04010. doi:10.1029/2005JC003051.

Lemos, R. T. & Sansó, B. (2009). A spatio-temporal model for mean, anomaly, and trend fields of North Atlantic sea surface temperature. *Journal of the American Statistical Association*, **104(485)**: 5–18. doi:10.1198/jasa.2009.0018.

Lentz, S. J. & Limeburner, R. (1995). The Amazon River plume during AMASSEDS: Spatial characteristics and salinity variability. *Journal of Geophysical Research*, **100(C2)**: 2355–2375. doi:10.1029/94JC01411.

Levitus, S. (1982). Climatological Atlas of the World Ocean. Tech. rep., NOAA Professional Paper 13. US. Government Printing Office, Washington, D.C.

Levitus, S. & Boyer, T. P. (1994). World Ocean Atlas 1994: Volume 4: Temperature. NOAA Atlas NESDIS 4. Tech. rep., NOAA, US Government Printing Office, Washington, D.C.

Locarnini, R. A., Mishonov, A. V., Antonov, J. I., Boyer, T. P. & Garcia, H. E. (2006). World Ocean Atlas 2005, Volume 1: Temperature. Tech. rep., NOAA, US Government Printing Office, Washington, D.C. 182 pp.

Locarnini, R. A., Mishonov, A. V., Antonov, J. I., Boyer, T. P. & Garcia, H. E. (2010). World Ocean Atlas 2009, Volume 1: Temperature. s. levitus, ed. Tech. rep., NOAA Atlas NESDIS 68, U.S. Government Printing Office, Washington, D.C. 184 pp.

Lozier, M. S., Owens, W. B. & Curry, R. G. (1995). The climatology of the North Atlantic. *Progress in Oceanography*, **36**: 1–44. doi:10.1016/0079-6611(95)00013-5.

Marchesiello, P., McWilliams, J. C. & Shchepetkin, A. (2003). Equilibrium structure and dynamics of the California Current System. *Journal of Physical Oceanography*, **3**: 753–783. doi:10.1175/1520-0485(2003)33<753:ESADOT>2.0.CO;2.

Mason, E., Colas, F., Molemaker, J., Shchepetkin, A. F., Troupin, C., McWilliams, J. C. & Sangrà, P. (2011). Seasonal variability of the Canary Current: a numerical study. *Journal of Geophysical Research*, **116**: C06001. doi:10.1029/2010JC006665.
URL http://www.agu.org/journals/jc/jc1106/2010JC006665/2010JC006665.pdf

Mason, E., Molemaker, J., Shchepetkin, A. F., Colas, F., McWilliams, J. C. & Sangrà, P. (2010). Procedures for offline grid nesting in regional ocean models. *Ocean Modelling*, **35(1-2)**: 1–15. doi:10.1016/j.ocemod.2010.05.007.

McIntosh, P. C. (1990). Oceanographic data interpolation: Objective analysis and splines. *Journal of Geophysical Research*, **95(C8)**: 13529–13541. doi:10.1029/JC095iC08p13529.

Milliff, R. F. & Robinson, A. R. (1992). Structure and dynamics of the Rhodes gyre system and dynamical interpolation for estimates of the mesoscale variability. *Journal of Physical Oceanography*, **22(4)**: 317–337. doi:10.1175/1520-0485(1992)022<0317:SADOTR>2.0.CO;2.
URL http://journals.ametsoc.org/doi/abs/10.1175/1520-0485%281992%29022%3C0317%3ASADOTR%3E2.0.CO%3B2

Reiniger, R. & Ross, C. (1968). A method of interpolation with application to oceanographic data. *Deep-Sea Research*, **15**: 185–193. doi:10.1016/0011-7471(68)90040-5.

Reynolds, R. W., Rayner, N. A., Smith, T. M., Stokes, D. C. & Wang, W. (2002). An improved in situ and satellite SST analysis for climate. *Journal of Climate*, **15**: 1609–1625. doi:10.1175/1520-0442(2002)015<1609:AIISAS>2.0.CO;2.

Ridgway, K. R., Dunn, J. R. & Wilkin, J. L. (2002). Ocean interpolation by four-dimensional weighted least squares – Application to the waters around Australasia. *Journal of Atmospheric and Oceanic Technology*, **19**: 1357–1375. doi:10.1175/1520-0426(2002)019<1357:OIBFDW>2.0.CO;2.

Rixen, M., Beckers, J.-M., Brankart, J.-M. & Brasseur, P. (2000). A numerically efficient data analysis method with error map generation. *Ocean Modelling*, **2**: 45–60. doi:10.1016/S1463-5003(00)00009-3.

Rixen, M., Beckers, J.-M., Levitus, S., Antonov, J., Boyer, T., Maillard, C., Fichaut, M., Balopoulos, E., Iona, S., Dooley, H., Garcia, M.-J., Manca, B., Giorgetti, A., Manzella, G., Mikhailov, N., Pinardi, N., Zavatarelli, M. & the Medar Consortium (2005a). The Western Mediterranean Deep Water: a proxy for global climate change. *Geophysical Research Letters*, **32**: L12608. doi:10.1029/2005GL022702.

Rixen, M., Beckers, J.-M., Maillard, C. & the MEDAR Group (2005b). A hydrographic and bio-chemical climatology of the Mediterranean and the Black Sea: a technical note on the use of coastal data. *Bollettino di Geofisica Teorica e Applicata*, **46(4)**: 319–328.

Robinson, A., Malanotte-Rizzoli, P., Hecht, A., Michelato, A., Roether, W., Theocharis, A., Ünlüata, U., Pinardi, N., Artegiani, A., Bergamasco, A., Bishop, J., Brenner, S., Christianidis, S., Gacic, M., Georgopoulos, D., Golnaraghi, M., Hausmann, M., Junghaus, H.-G., Lascaratos, A., Latif, M., Leslie, W., Lozano, C., Oguz, T., Özsoy, E., Papageorgiou, E., Paschini, E., Rozentroub, Z., Sansone, E., Scarazzato, P., Schlitzer, R., Spezie, G.-C., Tziperman, E., Zodiatis, G., Athanassiadou, L., Gerges, M. & Osman, M. (1992). General circulation of the Eastern Mediterranean. *Earth-Science Reviews*, **32(4)**: 285–309. doi:10.1016/0012-8252(92)90002-B.
URL http://www.sciencedirect.com/science/article/B6V62-489RH68-G7/2/e9b170d6800ddf21abcf14dc38bf1b54

Saunders, P. M. (1981). Practical conversion of pressure to depth. *Journal of Physical Oceanography*, **11**: 573–574. doi:10.1175/1520-0485(1981)011<0573:PCOPTD>2.0.CO;2.

Schlitzer, R. (2002). Interactive analysis and visualization of geoscience data with Ocean Data View. *Computers & Geosciences*, **28(10)**: 1211–1218. doi:10.1016/S0098-3004(02)00040-7.
URL http://www.sciencedirect.com/science/article/B6V7D-46TB0P2-C/2/49937e4939d29fab010dc7f0af310bc8

Stephens, C., Antonov, J. I., Boyer, T. P., Conkright, M. E., Locarnini, R. A. ., O'Brien, T. D. & Garcia, H. E. (2002). World Ocean Atlas 2001 Volume 1: Temperature, Levitus S (ed.). NOAA Atlas NESDIS 49. Tech. rep., NOAA, US Government Printing Office, Washington, D.C.

Swall, J. (1999). *A process convolution approach to modeling non-stationary spatial dependence*. Ph.D. thesis, Duke University.

Troupin, C., Sirjacobs, D., Rixen, M., Brasseur, P., Brankart, J.-M., Barth, A., Alvera-Azcárate, A., Capet, A., Ouberdous, M., Lenartz, F., Toussaint, M.-E. & Beckers, J.-M.

(2011). Advanced Data Interpolating Variational Analysis. Application to climatological data. *Ocean Modelling*. Submitted.

Tyberghein, L., Verbruggen, H., Klaas, P., Troupin, C., Mineur, F. & De Clerck, O. (2011). ORACLE: a global environmental dataset for marine species distribution modeling. *Global Ecology and Biogeography*, **20**. doi:10.1111/j.1466-8238.2011.00656.x. URL http://onlinelibrary.wiley.com/doi/10.1111/j.1466-8238.2011.00656.x/pdf

Uu, D. V. & Brankart, J. M. (1997). Seasonal variation of temperature and salinity fields and water masses in the Bien Dong (South China) sea. *Mathematical and Computer Modelling*, **26(12)**: 97–113. doi:10.1016/S0895-7177(97)00243-4. URL http://www.sciencedirect.com/science/article/B6V0V-3SNYRT4-8/2/a740446d0ae6e9c8b8f5839e7c639ea4

van Aken, H. M. (2000a). The hydrography of the mid-latitude Northeast Atlantic Ocean I: The deep water masses. *Deep-Sea Research I*, **47**: 757–788. doi:10.1016/S0967-0637(99)00092-8.

van Aken, H. M. (2000b). The hydrography of the mid-latitude Northeast Atlantic Ocean II: The intermediate water masses. *Deep-Sea Research I*, **47**: 789–824. doi:10.1016/S0967-0637(99)00112-0.

van Aken, H. M. (2001). The hydrography of the mid-latitude Northeast Atlantic Ocean - Part III: The subducted thermocline water mass. *Deep-Sea Research I*, **48**: 237–267. doi:10.1016/S0967-0637(00)00059-5.

Van Camp, L., Nykjaer, L., Mittelstaedt, E. & Schlittenhardt, P. (1991). Upwelling and boundary circulation off Northwest Africa as depicted by infrared and visible satellite observations. *Progress in Oceanography*, **26**: 357–402. doi:10.1016/0079-6611(91)90012-B.

Wahba, G. & Wendelberger, J. (1980). Some new mathematical methods for variational objective analysis using splines and cross validation. *Monthly Weather Review*, **108**: 1122–1143. doi:10.1175/1520-0493(1980)108<1122:SNMMFV>2.0.CO;2.

Ward, R. (2010). General Bathymetric Charts of the Ocean. *Hydro International*, **14(5)**. URL http://www.hydro-international.com/issues/articles/id1218-General_Bathymetric_Charts_of_the_Ocean.html

Chapter 3

Numerical modeling of the Cape Ghir upwelling filament

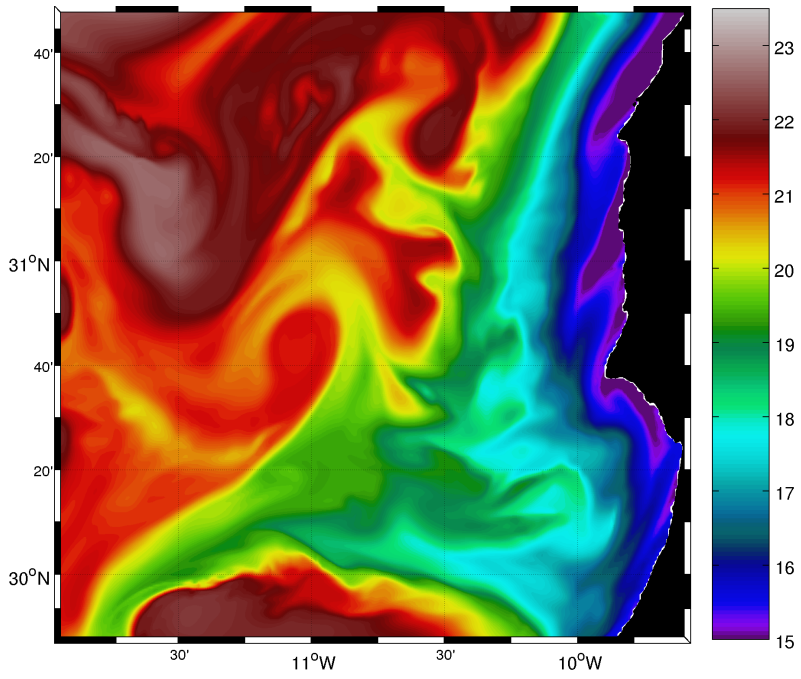

Model simulated temperature at 10 m on September 3.

The object of this chapter is the description of the results obtained with the ROMS numerical model, implemented in a region around Cape Ghir. In particular, we concentrate our effort on the study of the mechanisms responsible for the generation of upwelling filaments at that particular location. The originality of the work is the implementation of the model with a high-resolution ($\mathcal{O}$(1.5 km)) in this region, the use of an original boundary condition scheme (Mason *et al.*, 2010) and the process-oriented experiments.

A paper focused on these aspects of the filament is under revision:

Troupin, C., E. Mason, J.-M. Beckers and P. Sangrà, Generation of the Cape Ghir upwelling filament: a numerical study, to be published in *Ocean Modelling*, doi:10.1016/j.ocemod.2011.0

Contents

3.1 Introduction

As we have seen in Section 1.1.4, the Eastern Boundary Upwelling Systems (EBUS) constitute high-productivity regions (e.g., Fig. 1.8) of the World Ocean (e.g, Ryther, 1969; Durand *et al.*, 1998; Jennings *et al.*, 2001, and Section 1.1.5). They are driven by large scale wind patters (Fig. 1.5) responsible for coastal upwelling, resulting in increased nutrient concentrations in the surface layers. The examination SST maps covering the EBUS reveals the presence of narrow ($\mathcal{O}$ (10 km)), elongated ($\mathcal{O}$(100 km)) structures of cool water extending offshore in the upper surface layer ($\mathcal{O}$(100 m)), preferentially near the irregularities of the coastline. Such structures are referred to as *upwelling filaments*. Associated with the low temperature signal, high chlorophyll concentrations are frequently observed through satellite imagery (Fig. 1.6), bearing the important biological activity fueled by filaments.

Numerous observational (Section 1.2.2) and numerical studies (Section 1.3) were focused on the filaments. Nevertheless, there is still no clear agreement on the physical mechanism(s) leading to their formation. Most of the previous modeling studies (Section 1.3) were not able to reproduce correctly the spatial and temporal characteristic of the Cape Ghir filament. Here, a high-resolution numerical model was implemented to study the filament and the mechanisms generating it. To this end, several process-oriented numerical experiments were conducted. The numerical results prove that the wind shear is the main mechanism for the formation of filaments, while the bathymetry plays the role of a trigger. For the different experiments, climatological solutions were considered, in order to focus on intrinsic variability of the system, not on the varying forcing.

The chapter is organized as follows: The numerical model implementation (domain, forcing, validation) is described in Section 3.2. A mechanism based on the conservation of potential vorticity is proposed (Section 3.3). Section 3.4 describes the process-oriented experiments and discusses the results in the light of the potential vorticity balance. Conclusions and future work are presented in Section 3.5.

3.2 Numerical model implementation

The Regional Ocean Modeling System (ROMS, Shchepetkin & McWilliams, 2005, 2009, UCLA version) is employed to simulate the Cape Ghir filament and to perform numerical experiments to support the generation mechanism explained in section 3.3. The present section is focused on the model configuration and forcing. The solution obtained with this reference configuration will be used as the baseline experiment when comparing and discussing the results of the different numerical experiments (Section 3.4).

ROMS model consists of a terrain-following, free-surface primitive equations ocean model: the equations are discretized on the vertical using stretched terrain-following coordinates (Shchepetkin & McWilliams, 2009); an algorithm for reducing the error in the evaluation of the horizontal pressure gradient in sigma-coordinates is implemented (Shchepetkin & McWilliams, 2003). A staggered Arakawa C-grid (Arakawa, 1966) is used for the horizontal discretization.

The main reason for the choice of this model is that ROMS uses high-order, weakly-diffusive numerical schemes (Shchepetkin & McWilliams, 2003; Haidvogel *et al.*, 2008), which are suitable for the representation of small scale processes that are critical for the generation of coastal upwelling filaments. Another argument in favor of ROMS is the implementation existing in the northeast Atlantic Ocean (Mason *et al.*, 2008, 2011).

3.2.1 Nested domains

In atmospheric and ocean sciences, *nesting* refers to a local increase of resolution through the use of a group of progressively finer but less-extended grids. The lateral boundary conditions of a fine grid, called the *child grid*, are provided by a coarser grid, the *parent grid*. Nesting has to be distinguished from *grid refinement*, which can be performed using a single grid with refined regions. As the spatial step decreases, the time step has to decrease as well (CFL condition, Courant *et al.*, 1967). The temporal advancement of parent and child grids is made by a recursive procedure.

Such nesting procedures are necessary to represent small-scale processes: indeed, it is not currently possible to run a global ocean model with adequate spatial resolution, at least with the computing power at our disposal. Instead of using the parent grid solution to provide boundary conditions to the child one, another option would be to work with a regional climatology in the area of interest. However, Barth *et al.* (2008) showed that the gradients provided by the climatology are often too weak and suggested the use of a large-scale ocean model rather than the climatology.

With the objectives of having a fine spatial resolution of the filament and correctly reproduce the large-scale features, the model is successively run in embedded domains, as depicted in Fig. 3.1. The solution is progressively downscaled from domain $\mathcal{D}_1$ to domain $\mathcal{D}_3$ using the one-way off-line nesting method *roms2roms* (Mason *et al.*, 2010). Their method is designed to reduce unwanted boundary effects, such as spurious currents or wave reflection. The *roms2roms* method has already been successively applied in other regions (e.g., Boé *et al.*, 2011; Capet *et al.*, 2008; McWilliams *et al.*, 2009).

The different domains, summarized in Tab. 3.1, are as follows:

- In $\mathcal{D}_1$ (large domain), a 15 km-resolution North Atlantic solution is produced (Mason *et al.*, 2008). The procedures applied to obtain this solution are identical to those described in Mason *et al.* (2011), although the choice of the domain and the horizontal resolution slightly differ. This configuration is run for a period of 19 years. The solution corresponding to the last 7 years provides initial and boundary conditions to $\mathcal{D}_2$.

- In $\mathcal{D}_2$ (intermediate domain), simulations are run at a horizontal resolution of 4.5 km and for a period of 7 years, in order to reach an equilibrium situation. The last 4 years are used for downscaling to the domain $\mathcal{D}_3$. The results are stored as 3-day averages.

- $\mathcal{D}_3$ (small domain), simulations are run at a resolution of 1.5 km during a period of 4 years and the results are stored as 24-hour averages. $\mathcal{D}_3$ extends more than

200 km off the coast. The extension of the domain is intentionally small, so as to to spatially limit the effects of the modifications in the process-oriented experiments (Section 3.4). In some cases, the filament will not be entirely captured within the domain. However, this does not constitute an issue since we are more concerned by the generation mechanism than the offshore dynamics.

Table 3.1: Domain characteristics.

Domain	Grid size	Spatial resolution (km)	Running period (years)
$\mathcal{D}_1$	222×324	15.0	19
$\mathcal{D}_2$	258×290	4.5	7
$\mathcal{D}_3$	162×162	1.5	4

In this work, we will mostly focus on domains $\mathcal{D}_2$ and $\mathcal{D}_3$. The choice of these domains comes from the need to correctly reproduce the regional circulation features, essential for the modeling of the upwelling filament. The transfer of information from the parent grid to the child grid is achieved through one-way off-line nesting:

- *One-way* means the exchange of information is only from the parent to the child grid, in contrast with two-way nesting, where the coarser grid also receives information from the fine grid.
- *Off-line* means that the two grid configurations are run independently (the parent grid is run first, then initial and boundary conditions are extracted and used for the child grid), in contrast with on-line nesting, where both configurations have to be run synchronously.

The key elements of Mason *et al.* (2010)'s method are the accurate interpolation of data from parent to child grid-points, the corrections applied to normal velocities (both baroclinic and barotropic) to enforce volume conservation and the modification of the child topography over a small region in order to match the parent topography. The method has the advantages of limiting wave reflection at the boundaries and the anomalous currents occurring along the open boundaries (referred to as *rim currents*). It also permits flexibility in the choice of the domains: there is no constraint on the resolutions or positions of the domains, hence arbitrarily rotated grids are allowed.

In terms of mesoscale structures such as filaments or eddies, we fully expect these to be passed from parent to child in our configuration. The realism of the dynamics along the boundary in an off-line forcing configuration with *roms2roms* depends on factors such as:

- The ratio between parent and child grid resolutions: Blayo & Debreu (2005) suggest that 5 may be the upper limit. In our implementation, this ratio is 3 if we consider domains $\mathcal{D}_2$ and $\mathcal{D}_3$ (Tab. 3.1).

- The frequency of updates at the boundary: child domain $\mathcal{D}_3$ (see Fig. 3.1) is forced with 3-day averages from $\mathcal{D}_2$. This is in line with the experiments of Mason *et al.* (2010).

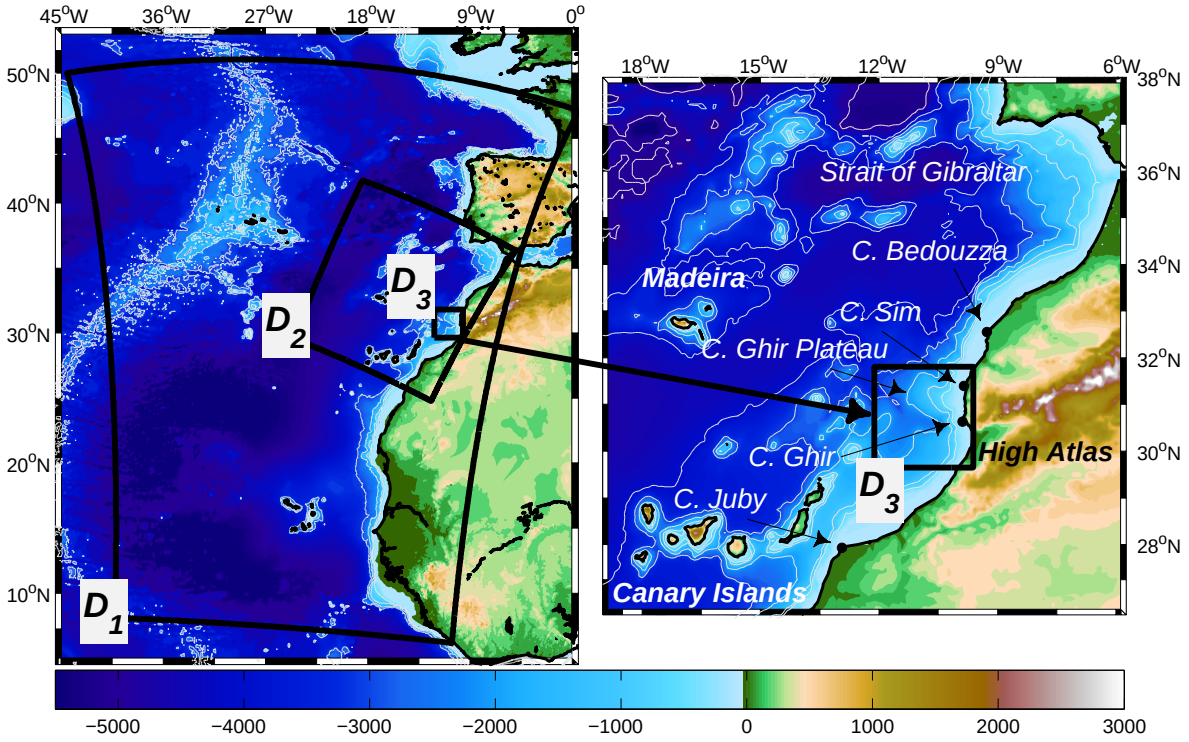

Figure 3.1: Topography (in meters) and nested domains (thick black lines) used for the filament modeling, referred to as: the large domain $\mathcal{D}_1$, the intermediate domain $\mathcal{D}_2$ and the small domain $\mathcal{D}_3$. The main topographic features are indicated in the close-up view (right). Isobaths 500, 1000, 2000 and 3000 m (thin white lines) are superimposed on both maps.

3.2.2 Atmospheric forcing

The grid and forcing files (heat and freshwater fluxes, wind stress) are prepared using the ROMS tools package (Penven *et al.*, 2008). The rivers in the studied area have weak rates of flow and thus are not taken into account in the model. The climatological forcing is preferred to inter-annual forcing, in agreement with the objectives set up in this work.

Wind

Most off the filament studies point to the wind as a responsible factor for filament formation (e.g. Kelly, 1986; Hagen *et al.*, 1996; Castelao & Barth, 2007), thus the importance of working with the highest spatial resolution possible. For the baseline experiment, the Scatterometer Climatology of Ocean Winds (SCOW, Risien & Chelton, 2008) is considered. It consists of climatological monthly-mean wind fields at a 0.25°-resolution.

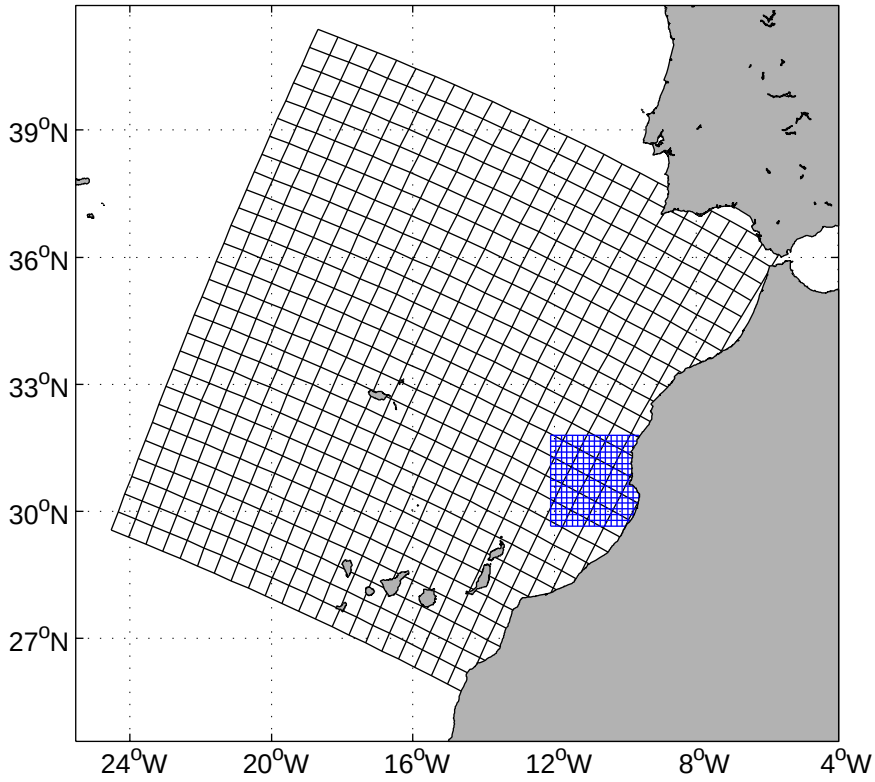

Figure 3.2: Illustration of the nesting for domains $\mathcal{D}_2$ and $\mathcal{D}_3$: the black and blue grids are referred to as parent and child grids, respectively. The resolution has been artificially decreased by a factor 10 for both grids, in order to make the mesh discernible.

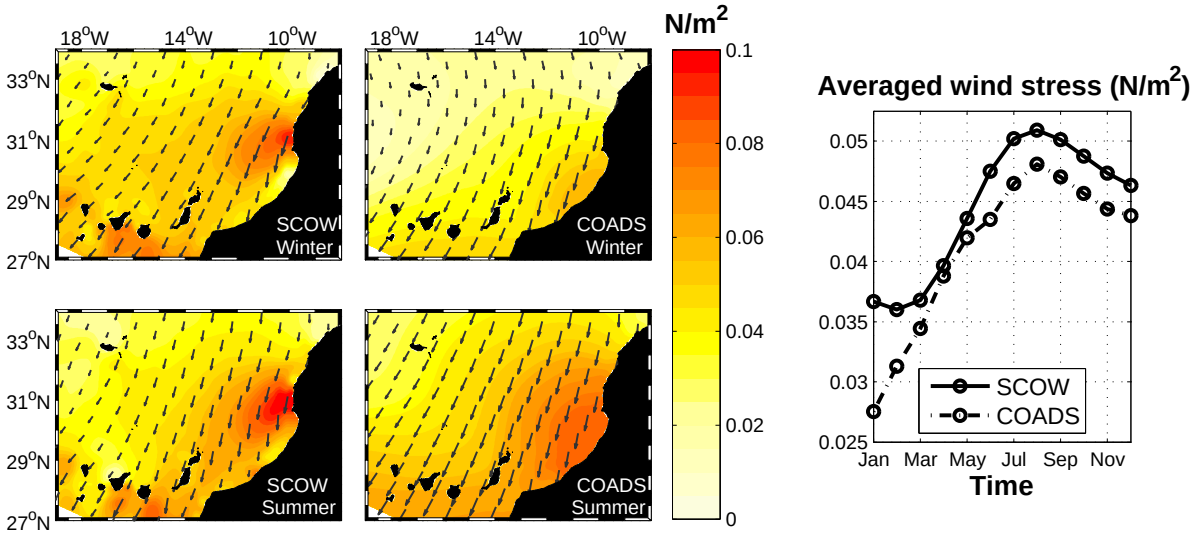

Figure 3.3: SCOW and COADS wind stress fields in winter (top) and summer (bottom) interpolated on the numerical grid $\mathcal{D}_2$. The seasonal cycle (right) is obtained by spatially averaging the wind stress over the domain.

Summer and winter wind stress fields, along with the mean seasonal cycle, are shown in Fig. 3.3 in a limited region around Cape Ghir. In a zone situated between Cape Ghir and Cape Sim (see Fig. 3.1) and that extends a few kilometers offshore, wind intensity is increased, both in summer and winter. The most probable explanation of the wind increase is the presence of a particular topography in this area (High Atlas mountains). As the wind direction is principally equatorward, the wind increase produces a larger Ekman transport and therefore a stronger upwelling. This situation contrasts with other upwelling area, such as the California Current System or the Iberian Peninsula, where winds are poleward in winter, so the upwelling takes place mainly during summer. South of Cape Ghir, a zone of calm winds extends until Cape Juby, certainly because of the change of the coastline orientation. The seasonal cycle (Fig. 3.3, right panel) is in agreement with the large-scale atmospheric situation: winds are upwelling favorable all year long, but are more intense during summer, because of the northward migration of the Azores high (Wooster *et al.*, 1976).

Heat flux

Fields of net heat fluxes are extracted from the 2005 Comprehensive Ocean-Atmosphere Data Set (COADS, Woodruf *et al.*, 1998; Worley *et al.*, 2005). They display an overall southwest gradient (Fig. 3.4), with maximal values located near the Morocco coasts. In winter, the flux is negative (i.e., from ocean to atmosphere) for most of the domain. During that period, one can expect a convective mixing to take place, leading to a deep mixed layer. In summer, the flux is positive everywhere, with the maximal values (160 W/m^2) taking place just south of Cape Ghir. Due to relief, this area is sheltered from the wind, as shown in the wind plot of Fig. 3.3. The seasonal cycle (Fig. 3.4, right panel) shows the contrast between the April-September and October-March periods. The period of maximum heat flux corresponds to the period of strongest winds.

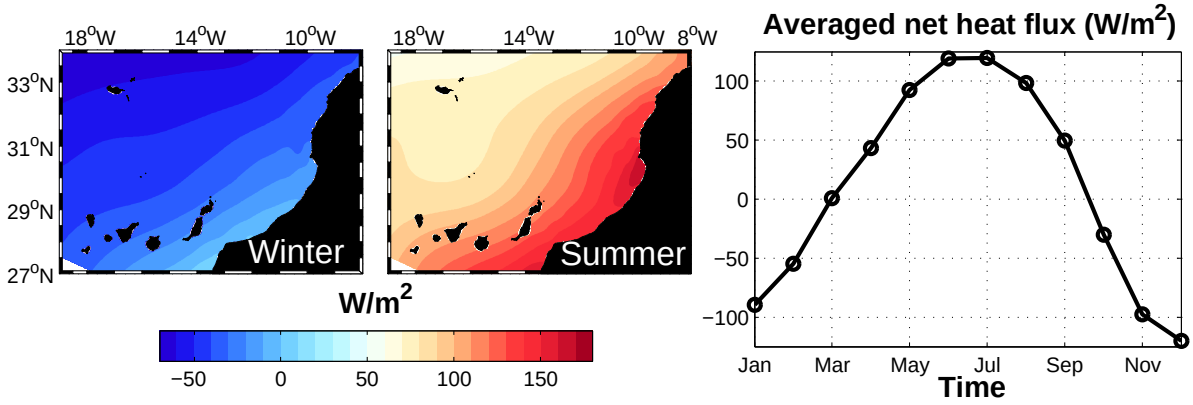

Figure 3.4: COADS heat fluxes in winter (left) and summer (middle) interpolated on the numerical grid $\mathcal{D}_2$ and mean seasonal cycle (right).

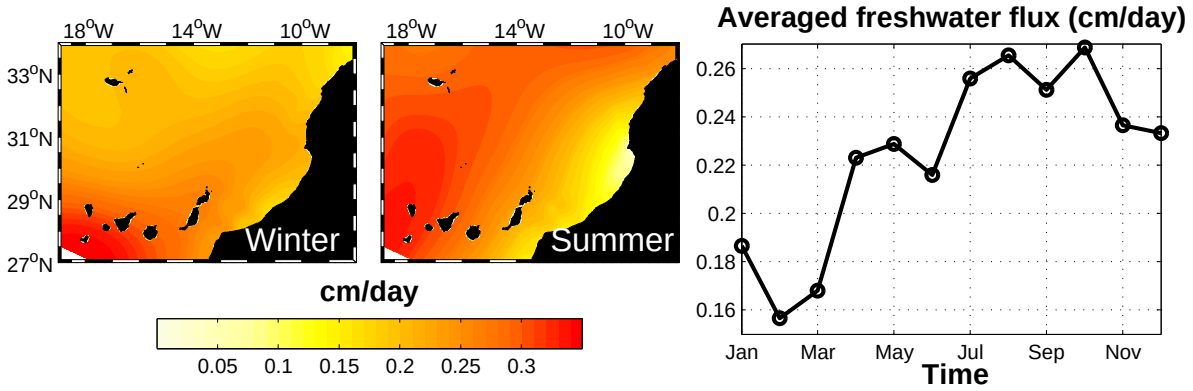

Figure 3.5: COADS freshwater fluxes in winter (left) and summer (middle) interpolated on the numerical grid $\mathcal{D}_2$ and mean seasonal cycle (right).

Freshwater flux

The freshwater flux is computed as the difference between precipitation and evaporation. Figure 3.5 points out the weak values of precipitation throughout the year, in comparison with temperate regions. Minimal values are observed in summer south of Cape Ghir. The combination of intense heat flux and weak precipitation generates a high salinity in the surface layer.

3.2.3 Bathymetry

The General Bathymetric Charts of the Oceans (GEBCO, Hunter & Macnab, 2003; Ward, 2010) provide high-resolution (up to 30 arc-second) bathymetry of the world ocean. For numerical concern, the bathymetry is modified as follows: all the depths lower than a given threshold h_{min} = 25 m are set to this value. The bathymetry is then spatially averaged to remove the possible sources of aliasing. Finally, a smoothing filter is applied repeatedly on the logarithm of the depth h, in order to reduce $r = \|\nabla h\|/h$, the ratio between the depth gradient and the depth, to a value $r_{max} = 0.20$.

3.2.4 Baseline simulation

As the solution of this configuration will be used as a reference for further comparisons (Section 3.4), it is essential to describe its solution and to demonstrate that it is capable to reproduce mesoscale structures similar to those observed in nature. Although our objective is centered on processes, the proper simulation of the upwelling filament constitutes a first achievement. In particular, with the climatological configuration implemented here, it is demonstrated that forcing with multi-year averaged fields is sufficient to generate filaments at the right location and with realistic spatial and temporal dimensions, in agreement with the results of Batteen *et al.* (2000).

Nevertheless, the role of high-frequency wind variations cannot be discarded: off the Oregon coast, experiments with temporally variable winds (Durski & Allen, 2005), with relaxed and sustained winds (Durski *et al.*, 2007) or with a time-periodic winds (Durski *et al.*, 2008) underlined their role in the creation of alongshore-scale instabilities and large-scale disturbances in the upwelling front. A set of new experiments with more realistic wind fields will be the subject of a future work.

Intermediate domain

In order to match the model horizontal resolution, we extracted satellite images from the Medspiration project database (`http://www.medspiration.org`): the SST measurements are acquired by the AVHRR sensor with a 2-km spatial resolution. In Fig. 3.6a, the model results on domain $\mathcal{D}_3$ are overlaid on the $\mathcal{D}_2$ for the period 10 to 12 May, while Fig. 3.6b compares the $\mathcal{D}_2$ solution and satellite SST for the period 4 to 6 September, in both case for the last year of simulation (Fig. 3.6). The satellite SST is also averaged over these periods, here for the year 2009. The left panel of Fig. 3.6a demonstrates the compatibility of the solutions in $\mathcal{D}_2$ and $\mathcal{D}_3$:

- the coastal upwelling has similar width and temperature across the boundary between the two domains;
- the eddy structure is correctly passed between the child and the parent grids.

From 10 to 12 May, the model produces a broad filament, with a length exceeding 100 km. The coastal upwelling off Africa is weaker in the satellite composite. We attribute this discrepancy to the difference in the wind forcing. Away from the coasts, the model SST appears to be lower than what is observed by satellite. Again, the different atmospheric forcing can be invoked to justify this difference. Moreover, time series of temperature maps (both for satellite and model; not presented here) tend to show that the surface heating is very rapid in May and June.

From 4 to 6 September, the overall distribution of SST in the region is well reproduced by the model. Highest SST values are observed in the southwestern part of the domain and around the Strait of Gibraltar. The upwelling is clearly recognizable as a band of cool water, that extends along the NW Africa coast until 33°N. The model also reproduces well the Cape Ghir filament location, just north of Cape Ghir. The offshore extension and

width of the filament obtained with the model also match well with those of the satellite image. The location where the filament detaches, just north of Cape Ghir, is similar in both cases. The mesoscale structures are well captured by the model, suggesting that the numerical grid choice, the climatological configuration and the forcing implemented here are suitable to simulate the filament.

Small domain

SST in $\mathcal{D}_3$ corresponding to base line model is presented: results are shown as a daily average (Fig. 3.7a) and as an average over the first two weeks of September (Fig. 3.7b) during the last year of simulation. The filament structure is identified by a tongue of cool water that propagates offshore, at a latitude slightly higher than that of Cape Ghir, and turns northward around 11°15'W. It extends about 180 km offshore and develops a negative anomaly of 2.5°C with respect to the open ocean temperature. The average width is between 10 and 20 km. The maximal velocities are on the order of 0.5 m s^{-1}, in agreement with the observations of Hagen *et al.* (1996) and Pelegrí *et al.* (2005). The shape of the filament is highly variable. The SST composite constructed from AVHRR measurements (Fig. 3.7c) confirms that the model results in $\mathcal{D}_3$ are plausible.

Time series of model and remote sensed SST (not shown here) indicate that the filament is a quasi-permanent feature, more frequently observed in summer and early fall, when the trade winds and the upwelling peak (e.g., Haynes *et al.*, 1993; Johnson & Stevens, 2000). During these periods, its offshore extension is also maximal and the gradients between filament and non-filament waters are stronger because of the stronger stratification provoked by the intense heat flux (Fig. 3.4). On the contrary, the winter deep mixed layer may reduce the contrast between filament upwelled waters and open ocean waters. The behavior of the mixed layer was examined with the 1-dimension version of the ROMS model, at a location with similar atmospheric conditions (south of the Canary islands) by Troupin *et al.* (2010) (also see Fig. 1.19 in the first chapter).

It is worth noting the small-scale instabilities taking place on the southern part of the filament, specially visible on the daily field (Fig. 3.7a). With the multi-year simulations, it was observed that filament location, shape and dimensions are consistent from one year to another.

3.3 Generation mechanism

3.3.1 Formulation

The proposed mechanism is developed in the framework of the Ertel's potential vorticity (PV; Section 1.3.1) conservation theorem (e.g., Müller, 1995). This theorem states that if the fluid is homogeneous, inviscid, and if no frictional forces are applied, then PV is conserved along streamlines or inversely, the water parcels must flow along constant PV lines. For an homogeneous, rotating fluid Ertel's theorem can be formulated as

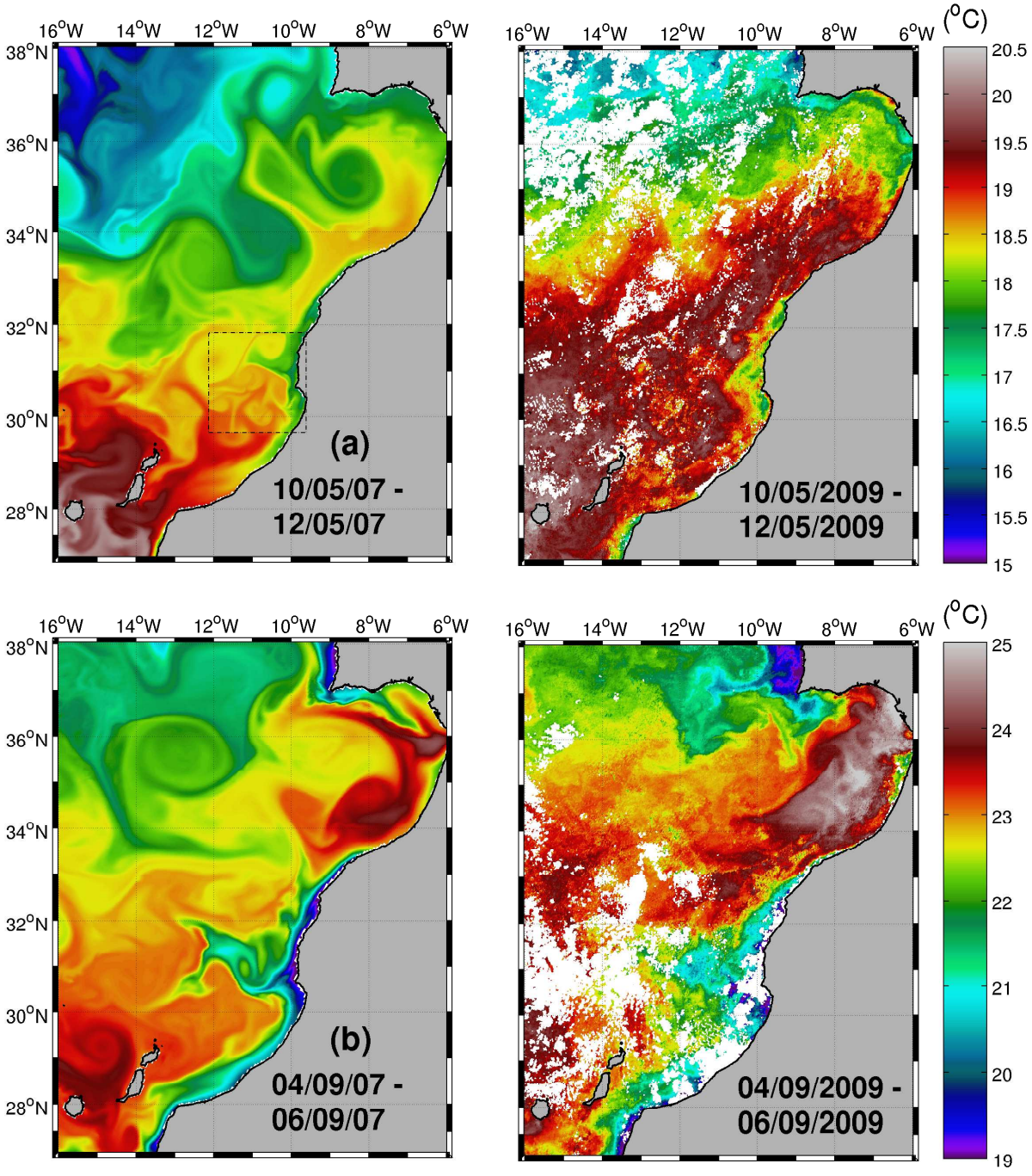

Figure 3.6: Model (left) and satellite (right) sea surface temperature averaged from 10 to 12 May (a) and from 4 to 6 September (b). $\mathcal{D}_3$ solution (dashed square) is superimposed on $\mathcal{D}_2$ solution. Model solutions correspond to the last year of run (7th year for $\mathcal{D}_2$, 4th year for $\mathcal{D}_3$).

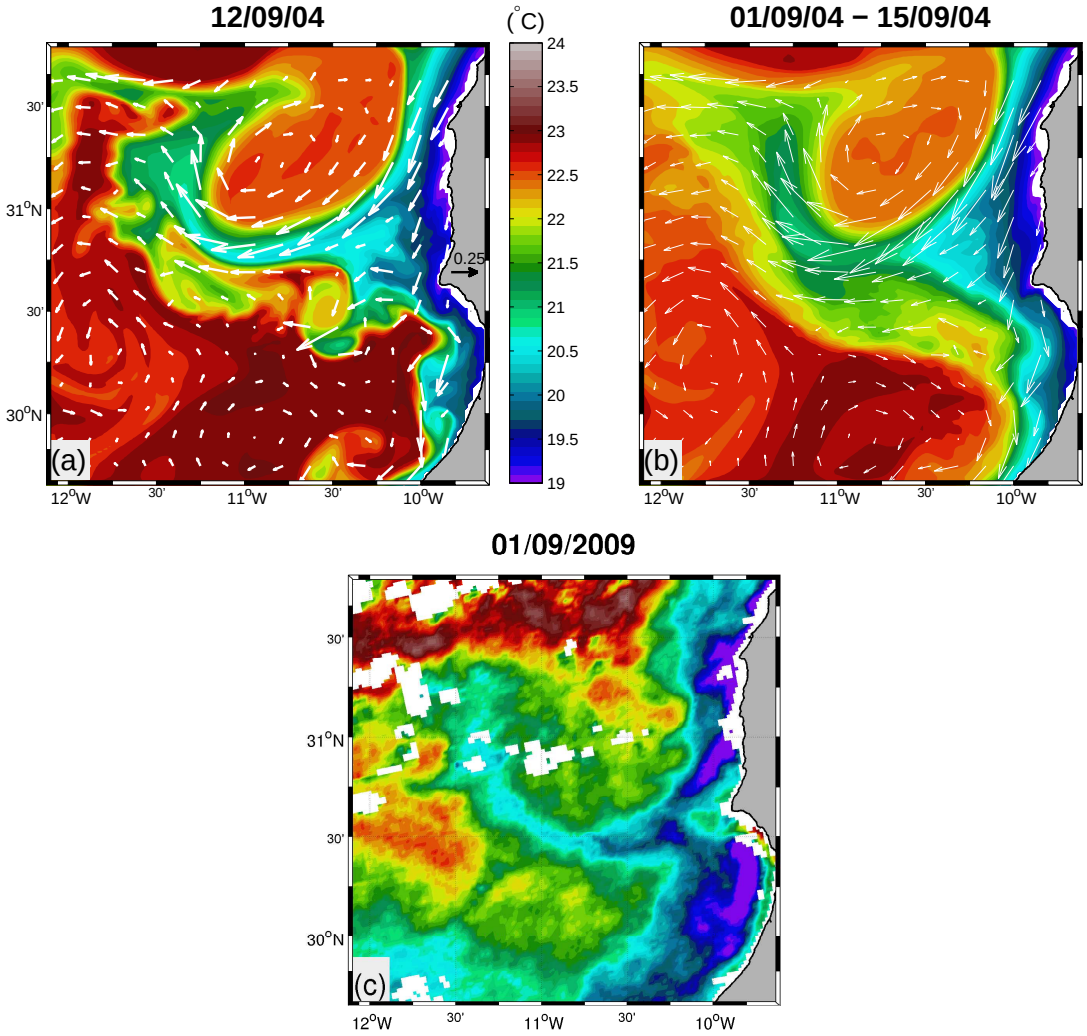

Figure 3.7: Snapshot of the SST on September 12 (a), 15-day averaged SST (1-15 September) (b) obtained during the 4th year of simulation in $\mathcal{D}_3$ and composite produced from AVHRR measurements on September 1, 2009 (c). The color scale is common for the three sub-figures.

$$\frac{dq}{dt} = \frac{d}{dt}\frac{f+\zeta}{h} = 0, \tag{3.1}$$

where q is the PV, f the planetary vorticity, ζ the relative vorticity and h the depth of the water column. Obviously, the aforesaid conditions are not completely fulfilled in our case, but the conservation of PV is a reasonable working hypothesis if we limit ourselves to the surface layer.

Laiz *et al.* (2001) studied the drainage of the subtropical gyre by the NW Africa upwelling system. Following the quasi-geostrophic dynamics (e.g., Pedlosky, 1987) and Ertel's theorem, they stated that water parcels must flow along a meridional band of homogeneous PV on their way toward the equator through the upwelling jet. Since planetary vorticity decreases equatorward, the relative vorticity of the flow has to increase in order to preserve its PV. The relative vorticity of the jet is negative, therefore its absolute value decreases when going south.

The PV for the large domain and the relative vorticity for the intermediate domain are represented in summer (Fig. 3.8) for the baseline configuration (Section 3.2). The figure shows that:

- The dominance of the planetary vorticity over the relative vorticity outside the coastal area, as evidenced by the structure of the equal-PV lines in the large domain (Fig. 3.8a).
- The band of lower PV (corresponding to negative relative vorticity) along the African coastline related to the upwelling jet and its overall decrease toward the equator (in particular with the intermediate domain, Fig. 3.8b).

Laiz *et al.* (2001) showed that the PV value in the homogeneous meridional band is approximately equal to the value at the point of detachment of the flow, where planetary vorticity is the lowest. For the Canary Current system, the latitude where the current detaches from the coast is close to 20°N (e.g., Stramma, 1984; Stramma & Schott, 1999), more than 1000 km to the south of Cape Ghir.

Now, for the Cape Ghir filament to form, it is assumed that the jet receives an external input of PV, preventing the flow to migrate equatorward along the meridional band of homogeneous PV. In order to accommodate the PV increase, the flow detaches from the coast and propagates offshore, towards higher values of PV, in the open ocean.

Going back to formula (3.1), we notice that h, the water column depth, has not been taken into account yet. When the jet starts propagating offshore, it has to overcome an augmentation of depth, from the shelf to the open ocean. It is not the real depth (bathymetry) that has to be considered, but the thickness of the surface layer (see next Section). The consideration of depth can provide an explanation of the preference of the filament to uprise over the Cape Ghir Plateau (CGP), north of Cape Ghir; there, the shelf is wider, and the motion toward the ocean is made easier.

In summary, the hypothesis is twofold:

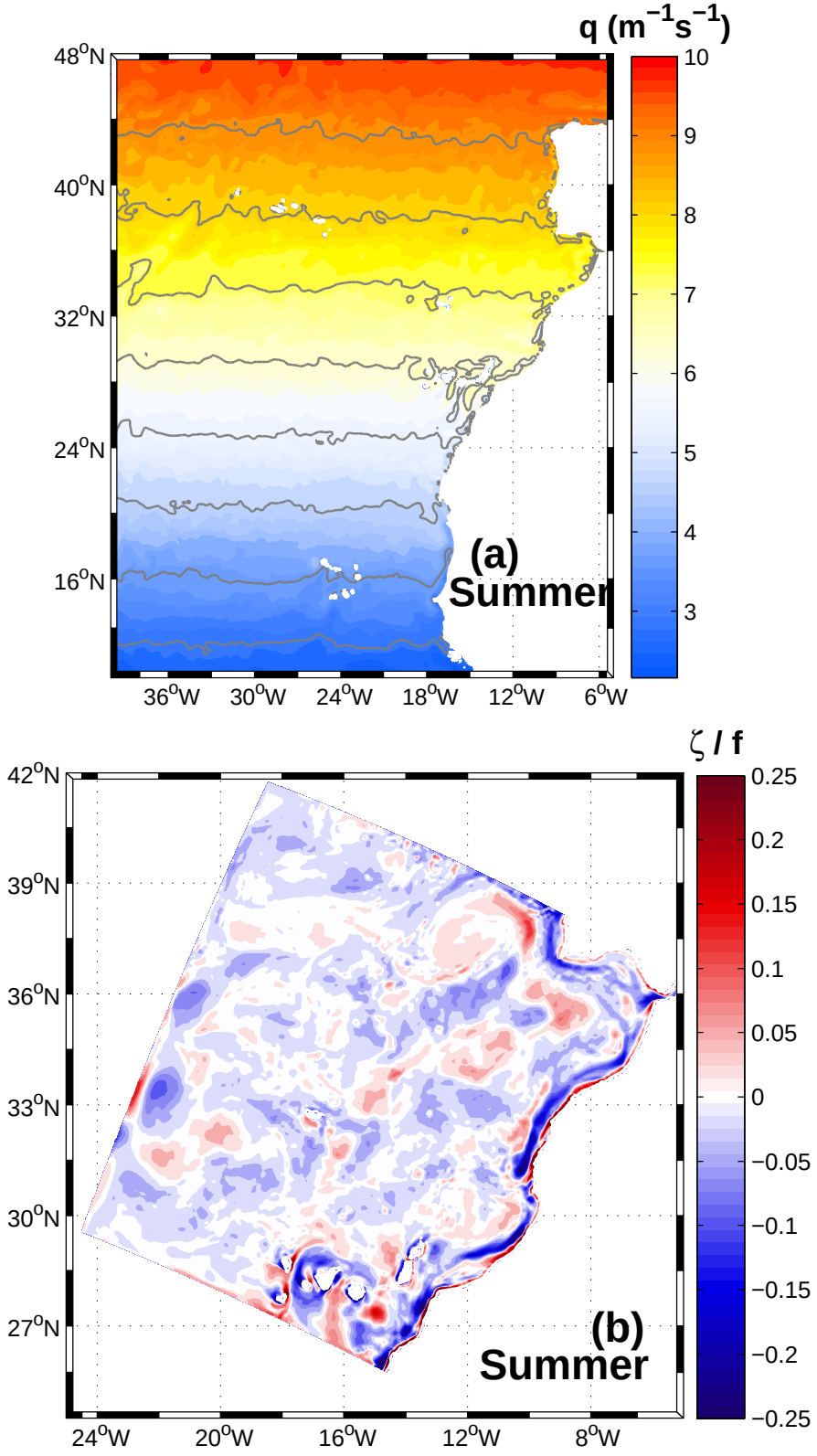

Figure 3.8: Potential vorticity (normalized by 10^{-6}) in summer for domains $\mathcal{D}_1$ (a) and relative vorticity (normalized by f) in domain $\mathcal{D}_2$ (b). PV-lines are separated by 10^{-6} $m^{-1}s^{-1}$.

1. To be able to migrate southward, water parcels must flow along a meridional band of homogeneous PV, where its value is lower that the corresponding value of the ocean interior, until they reach the latitude of detachment of the flow.

2. A local injection of positive relative vorticity by the wind curl increases locally the PV of the flow, forcing the water parcels to leave the homogeneous band of lower PV and travel westward.

3.3.2 Analysis of orders of magnitude

Before the application of the numerical model, the order of magnitude of the different contributions to the PV are examined. The decrease of planetary vorticity Δf due to the southward motion from Cape Ghir to the point of westward turning of the Canary Current (at the latitude of Cape Blanc, e.g., Stramma & Schott, 1999) is easily computed:

$$\Delta f = 2\Omega \left(\sin \lambda_{\text{C.Ghir.}} - \sin \lambda_{\text{C.Blanc}}\right) = 2.25 \times 10^{-5} s^{-1}, \tag{3.2}$$

where Ω is the Earth rotation speed and λ the latitude. Now, to estimate the relative vorticity imparted by the wind to the flow, a reduced-gravity model forced by a wind stress $\boldsymbol{\tau}$ is used. Such a model fits well to the case of a coastal upwelling, as it permits the capture of the structure within the main thermocline. The equations for the momentum and for the mass conservation read:

$$\frac{\partial u}{\partial t} + u\frac{\partial u}{\partial x} + v\frac{\partial u}{\partial y} - fv = -g'\frac{\partial h}{\partial x} + \frac{\tau^x}{\rho_0 h}, \tag{3.3}$$

$$\frac{\partial v}{\partial t} + u\frac{\partial v}{\partial x} + v\frac{\partial v}{\partial y} + fu = -g'\frac{\partial h}{\partial y} + \frac{\tau^y}{\rho_0 h}, \tag{3.4}$$

$$\frac{\partial h}{\partial t} + \frac{\partial}{\partial x}(hu) + \frac{\partial}{\partial y}(hv) = 0, \tag{3.5}$$

with h, the surface layer thickness, $g' = \dfrac{\delta\rho}{\rho_0} g$, the reduced gravity and ρ_0, the reference density. Note that these equations are a more general version of the system (1.8a)-(1.8c) (Section 1.3.2). To derive an equation for the relative vorticity, we take $\dfrac{\partial}{\partial x}(3.4)-$ $\dfrac{\partial}{\partial y}$(3.3) and obtain:

$$\frac{\partial \zeta}{\partial t} + \left(u\frac{\partial}{\partial x} + v\frac{\partial}{\partial}y\right)\zeta = \frac{1}{\rho_0}\underbrace{\left[\frac{\partial}{\partial x}\left(\frac{\tau^y}{h}\right) - \frac{\partial}{\partial y}\left(\frac{\tau^x}{h}\right)\right]}_{(*)}, \tag{3.6}$$

where $\zeta = \dfrac{\partial v}{\partial x} - \dfrac{\partial u}{\partial y}$ is the vertical component of the relative vorticity. The term $(*)$ can be rewritten into:

$$
\begin{aligned}
(*) &= \frac{\partial}{\partial x}\left(\frac{\tau^y}{h}\right) - \frac{\partial}{\partial y}\left(\frac{\tau^x}{h}\right) \\
&= \frac{1}{h}\frac{\partial \tau^y}{\partial x} - \frac{\tau^y}{h^2}\frac{\partial h}{\partial x} - \frac{1}{h}\frac{\partial \tau^x}{\partial y} + \frac{\tau^x}{h^2}\frac{\partial h}{\partial y} \\
&= \frac{1}{h}\left[\underbrace{\left(\partial\frac{\tau^y}{\partial x} - \frac{\partial \tau^x}{\partial y}\right)}_{(**)} + \underbrace{\left(\frac{\tau^x}{h}\frac{\partial h}{\partial y} - \frac{\tau^y}{h}\frac{\partial h}{\partial x}\right)}_{(***)}\right].
\end{aligned} \tag{3.7}
$$

Similarly to Lee *et al.* (2001), we define the terms $(**)$ as the torque acting over the surface of the water column and $(***)$ as the slope-induced torque: $\boldsymbol{\tau}/h$ represents a volume force applied on the whole water column, of which the effect depends on the slope.

Filaments have typical lifetime of a few days, velocity between 0.1-1 m s^{-1}, a length of a few hundred kilometers, a width of a few ten kilometers and a depth of a few hundred meters (see Tab. 1.2). The wind stress curl is estimated from the SCOW climatology (Section 3.2.2). Using the typical lengths of the filament, we have:

$$
(**) = \frac{1}{\rho_0 h}\left(\frac{\partial \tau^y}{\partial x} - \frac{\partial \tau^x}{\partial y}\right) = \mathcal{O}(10^{-9} - 10^{-10})\ s^{-2}. \tag{3.8}
$$

The zonal variations of depth dominates the meridional variations ($\partial h/\partial x \ll \partial h/\partial y$), and the wind stress is about one order of magnitude stronger in the meridional direction than in the zonal one ($\tau^y = \mathcal{O}(10^{-1})$ N/m^2). With these simplifications, the slope-induced stress is recast into:

$$
(***) \approx -\frac{\tau^y}{\rho_0 h^2}\frac{\partial h}{\partial x}. \tag{3.9}
$$

The slope $\partial h/\partial x$ is replaced by $\Delta h/\Delta x$, where Δh is the variation of depth when crossing the shelf off Cape Ghir: on the shelf, h is the real depth (topography), where the stratification is weak, while offshore, h the surface layer thickness. In this case, the isopycnal 27.3 kg/m^3 is selected as an indicator of the surface layer. For this isopycnal, the model diagnostics indicate a depth around 250 m near to the coast, while further offshore, it is almost uniform with values around 150 m. Note that in the first 50 km from the coast, the depth of the isopycnal 27.3 kg/m^3 is not defined, since all the densities are lower in this area. Based on these values, the slope is estimated as:

$$
\frac{\partial h}{\partial x} \approx \frac{\Delta h}{\Delta x} \approx \frac{100\ m}{10\ km} = 10^{-2} \tag{3.10}
$$

and

$$
\frac{\tau^y}{\rho_0 h^2}\frac{\partial h}{\partial x} = \frac{10^{-1}}{10^3 10^4}10^{-2} = \mathcal{O}(10^{-10})\ s^{-2}. \tag{3.11}
$$

We conclude that:

- The variations of PV of the flow either by changing its latitude, or by increasing the layer depth, can be explained by the relative vorticity provided by the wind.
- Both the wind stress curl and the slope-induced torque contribute to the injection of relative vorticity in the jet, but with a predominance of the wind stress curl.

3.3.3 Procedure

In the next section, a set of numerical experiments performed in the domain $\mathcal{D}_3$ is presented. For both experiments, two characteristic variables are selected: temperature and relative vorticity. Temperature allows one to describe and compare the signal of the filament, while relative vorticity acts as the main dynamical variable.

The fields are extracted at a depth of 10 m, in order to concentrate on the near-surface variability, in agreement with the filament general characteristics.

3.3.4 Sources of vorticity variations

In this section, we review several works related to flow detachment and vorticity conservation, in order to identify possible mechanisms related to input of vorticity. Albeit the cases considered hereinafter are based on assumptions not fully compatible with the flow off Cape Ghir, they provide an insight of the processes that come into the picture.

For simplicity's sake, a barotropic case is first considered: Signell & Geyer (1991) made the hypothesis of a shallow ocean with homogeneous water and the hydrostatic approximation to study the formation of eddies around headlands. It arises from their analytical developments that the vorticity is modified through the following processes:

1. The *speed torque*:

$$\frac{C_D\left(\mathbf{u}\times\boldsymbol{\nabla}\|\mathbf{u}\|\right)\cdot\mathbf{e}_z}{H^2},$$

   where C_D is the drag coefficient for the depth-averaged flow, $\mathbf{u}$, the depth-averaged velocity, H, the height of the water column, $\mathbf{e}_z$, a vertical unitary vector. $\boldsymbol{\nabla}$ and $\times$ stand for the gradient and vector product operators, respectively. The speed torque is maximum when the velocity is normal to the velocity gradient, as stronger flows tend to feel relatively more the effects of friction than weak flows. This situation is characteristic of upwelling jets, which often have intense horizontal shear.

2. The *dissipation by bottom friction*:

$$-\frac{C_D\|\mathbf{u}\|\zeta}{H^2},$$

   where ζ is the relative vorticity. This term is proportional to the drag coefficient and to the bottom velocity, and has a stronger influence for shallow depths.

3. The *slope torque*:

$$-\frac{C_D\|\mathbf{u}\|}{H^3}\left(\mathbf{u}\times\boldsymbol{\nabla}H\right)\cdot\mathbf{e}_z,$$

with a maximum when the flow is parallel to the isobaths (hence it vanishes in case of shelf-slope only) and for shallow depth, since the flow feels greater friction at shallow depths.

4. The *diffusion of vorticity* due to horizontal mixing processes:

$$\frac{1}{H}\mathcal{A}_H\Delta\zeta,$$

with $\mathcal{A}_H$, the horizontal eddy viscosity.

Although the assumptions made by Signell & Geyer (1991) may not be applicable in the region of Cape Ghir, where the baroclinic nature of the flow has certainly to be considered, these developments yield an analytical expression of the influence of the jet velocity and the topography on the relative vorticity.

Separation of boundary currents (BC) from the coastal area has been a topic of strong interest, in particular the Gulf Stream, which flow northward along U.S. East Coast until detachment upstream of Cape Hatteras (e.g., Iselin, 1936). Even if the situations are different (western versus eastern boundary current), interesting conclusions can be drawn. Marshall & Tansley (2001) studied the BC separation using an integrated vorticity budget with natural coordinates. Three processes are shown to contribute to the separation:

1. The β effect: in the case of an eastern boundary current (EBC), the planetary vorticity gradient tends to decelerate the current and thus enhances the separation.

2. The vortex stretching: $\mathbf{u}\cdot\boldsymbol{\nabla}h$. It enhances the separation of anticyclonic slope currents (i.e., currents flowing in the direction where the depth decreases), but inhibits the separation of cyclonic slope currents. As described in the introduction, the topography around Cape Ghir is characterized by the CGP, located north of the cape. It is then expected that this feature plays a role in the filament generation.

3. The coastline curvature: the coastline can counteract the stabilization of a western BC due to the β effect or the vortex stretching and then provoke the separation, when the radius of curvature is less than a threshold value $r_{\min}$. This threshold is estimated as

$$r_{\min}=\left(\frac{U}{\beta^*}\right)^{1/2},$$

with U, the velocity of the boundary current and $\beta^*=\partial f/\partial s$, the gradient of the Coriolis parameter in the downstream direction (s being the along-current coordinate). However, as an EBC is not stabilized by the β effect, a minimal radius of curvature for the coastline is not effective.

Lee *et al.* (2001) concentrated their study on the role of the slope on the western boundary currents, but their conclusions are still valid for EBC's. They use a depth-integrated vorticity equation to demonstrate that cross-isobath flows are responsible for the stretching or squashing of vortex tube, in agreement with the statements established by Marshall & Tansley (2001). The influence of the bottom stress on the vorticity is decomposed in two parts:

$$\frac{\partial}{\partial x}\left(\frac{\tau_{by}}{h}\right) - \frac{\partial}{\partial y}\left(\frac{\tau_{bx}}{h}\right) = \frac{1}{h}\left[\left(\frac{\partial \tau_{by}}{\partial x} - \frac{\partial \tau_{bx}}{\partial y}\right) + \left(\frac{\tau_{bx}}{h}\frac{\partial h}{\partial y} - \frac{\tau_{by}}{h}\frac{\partial h}{\partial x}\right)\right],$$

where τ_{bx} and τ_{by} are the horizontal components of the bottom stress. The decomposition is the following:

1. The bottom stress curl (first term) is proportional to the torque acting over the bottom face of the water column of constant depth;
2. The slope-induced bottom stress (second term) is a volume force applied by the bottom stress. This contribution depends on the shape of the bottom topography, as indicated by the derivative of h.

Apart from geometric consideration, it is also required to examine the influence of the wind stress. Castelao & Barth (2007) studied the jet separation at a cape with the help of a numerical model and showed that an increase of the wind curl intensity induces an earlier separation. When the wind stress intensity is increased, the upwelling is enhanced, but the jet separation is not facilitated. The geometry of the cape is also analyzed: the rounder the cape (i.e., large radius of curvature), the longer takes the separation to occur.

Although this review of physical mechanism related to the vorticity injection is not exhaustive, it has the merit to evidence a set of processes and parameters that will have to be further investigated with a numerical model for understanding their role in the generation of filaments near Cape Ghir.

3.4 Process-oriented numerical experiments

Several numerical experiments were designed in order to demonstrate that the generation of Cape Ghir filament is related to the gradient of planetary vorticity (β effect) and to the injection of positive relative vorticity by the wind curl. For these experiments, surface fields averaged over the first two weeks of September are considered as diagnostics. This period was selected because the filament appear more frequently and the water column is well stratified, so the filament SST signature is stronger. With the averaging of the fields, high-frequency variability is filtered out. It is then easier to show whether or not a coherent filament is generated.

For the process-oriented simulations, only one modification with respect to the baseline configuration (Section 3.2) is done at a time, similarly to the approach of Batteen *et al.* (2007). The numerical experiments combine the different forcing conditions and bathymetries described in the following and summarized in Tab. 3.2.

The baseline experiment (E0) used the reference climatological atmospheric forcing and bathymetry of Section 3.2. In experiment E1, planetary vorticity is kept uniform over the domain $\mathcal{D}_3$, in order to prove that the filament generation is related with the constraint of PV conservation. The wind effects are analyzed in experiments E2–E3, so as to demonstrate that wind curl constitutes the main source of positive relative vorticity. Experiments E4-E5 are centered on the topographic effects.

Table 3.2: Descriptions of the process-oriented experiments.

Exp.	Description	Wind	Bathymetry
E0	Reference	SCOW (1/4°)	GEBCO
E1	β-effect	SCOW (1/4°)	GEBCO
E2	Wind curl	Uniform	GEBCO
E3	Wind resolution	COADS (1°)	GEBCO
E4	Topography smoothing	SCOW (1/4°)	Smoothed GEBCO
E5	Shelf-slope only	SCOW (1/4°)	Flattened GEBCO

3.4.1 Baseline experiment (E0)

The results of this experiment were previously presented in Section. 3.2.4. Here, the attention is centered on the temperature (Fig. 3.9a) and relative vorticity maps (Fig. 3.9b) for the first 15 days of September of the fourth year of simulation in $\mathcal{D}_3$. These two variables display very similar features. For comparison with the structures observed with the next experiments, the following characteristics define a filament:

1. strong surface temperature gradient (> 2°C),
2. low aspect ratio (length on the order of 100 km, width on the order of 10 km),
3. core characterized by strong positive relative vorticity (as shown in Fig. 3.9b).

This positive relative vorticity is consistent with the hypothesis that the filament is generated because of a local gain of positive relative vorticity preventing the flow from continuing its way southward. Close to the coast, the vorticity is predominantly positive, with maximal values reached near the irregularities of the coastline. The fields presented here are 15-day averages, hence the signal is not as sharp as in daily results. However, even with this averaging, the temperature signature is still clear, meaning that the process is intense and well localized.

3.4.2 Planetary vorticity effect (E1)

A simple experiment to test the hypothesis of vorticity balance presented in Section 3.3 is to see how the circulation is modified when planetary vorticity is set constant (f-plane)

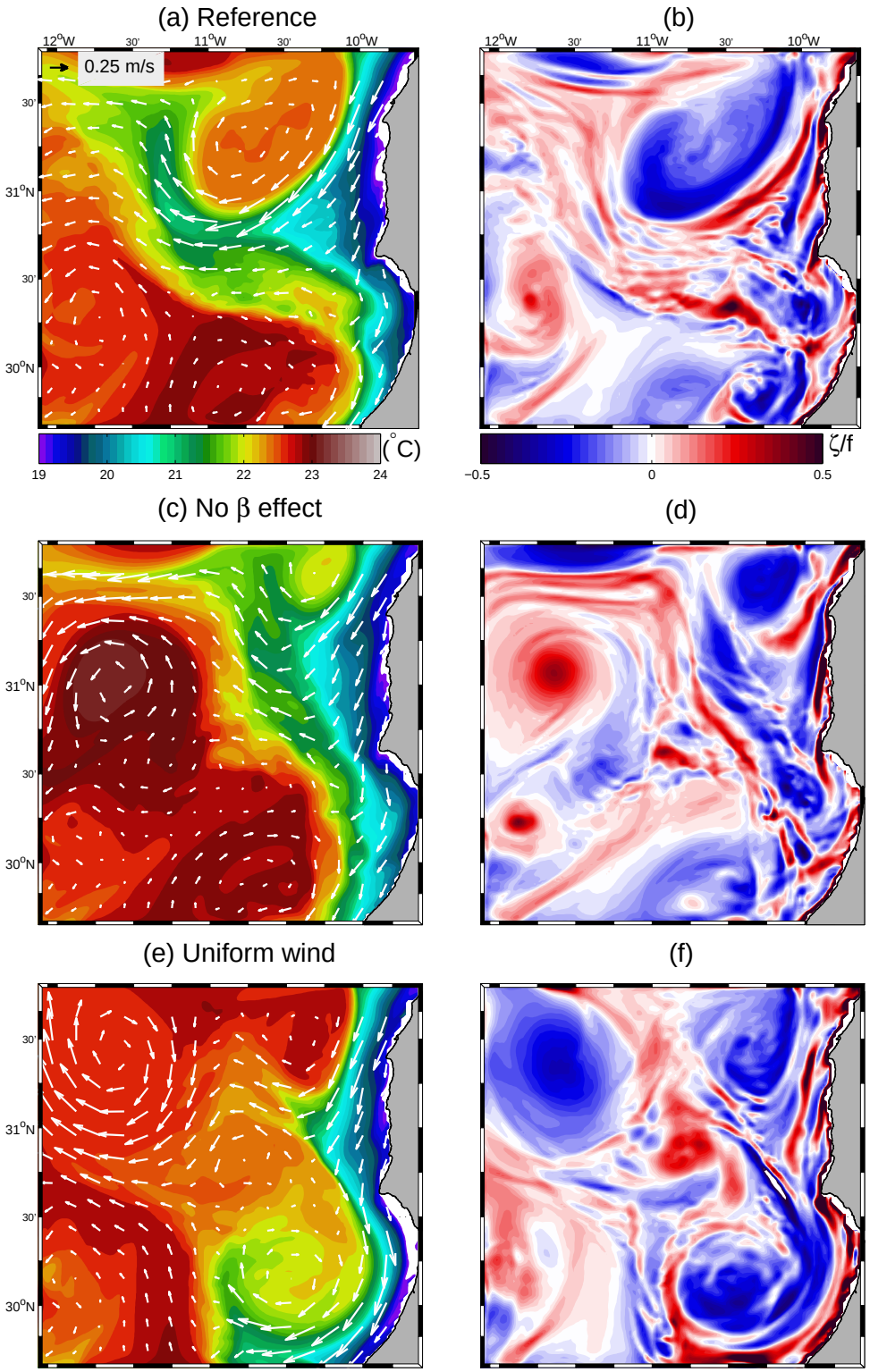

Figure 3.9: Temperature and velocity fields (left column) and normalized relative vorticity (right column) at 10 m in domain $\mathcal{D}_3$, averaged over the first 15 days of September: (a)-(b) baseline configuration (E0), (c)-(d) No β-effect (E1), (e)-(f) Uniform wind (E2).

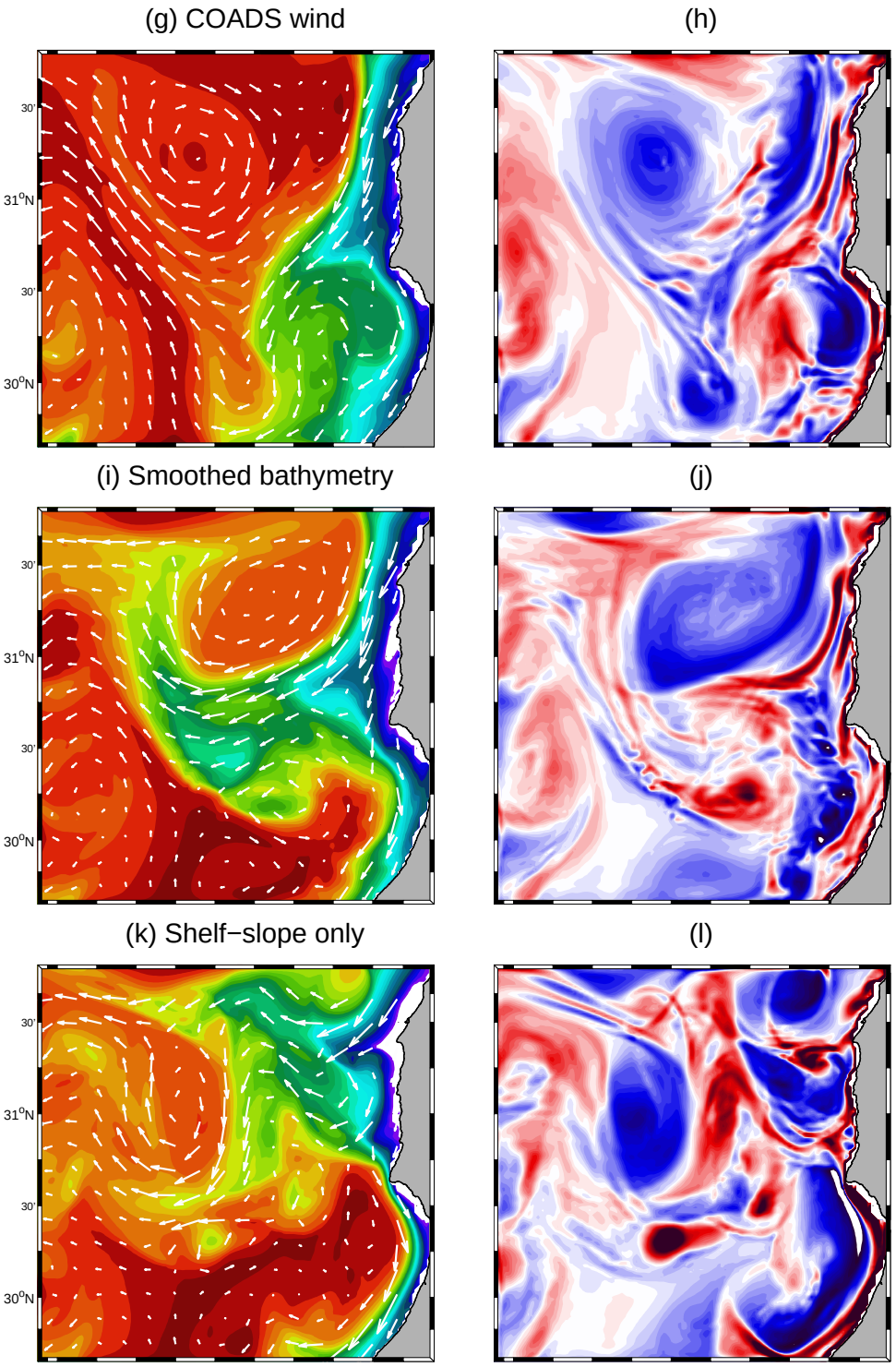

Figure 3.9: Continued: (g)-(h) COADS wind (E3), (i)-(j) Smoothed topography (E4), (k)-(l) shelf-slope only (E5).

compared to the case where planetary vorticity varies with latitude (β-plane). Simulating a situation without β-effect is easily carried out with a numerical model: all the grid points are assigned with a uniform f value, corresponding to the mean latitude of the domain. Now the constraint from Ertel's theorem (3.1) that the meridional flow must accommodate its relative vorticity to decreasing planetary vorticity values no longer applies and there is no restriction for the equatorward flow, even if there is an injection of positive relative vorticity by the wind.

Temperature (Fig. 3.9c) shows that coastal upwelling still develops with the same intensity as in E0, but no filament forms near Cape Ghir. The band of positive relative vorticity is visible (Fig. 3.9d), but there is not clear offshore propagation, in the manner of the baseline experiment. This supports the importance of the vorticity balance to explain the filament formation. These observations are in agreement with the theory of Marshall & Tansley (2001), who demonstrated that β-effect enhances the separation of the jet from the coast in case of eastern boundary currents.

Near Cape Sim (31°23'N), a weak westward flow develops, with an anticyclonic eddy north of it. However, this feature does not fit with the previous definition of the filament, because of its spatial scale (limited offshore development). It is probably due to an instability of the upwelling jet, provoked by the coastline curvature.

Obviously, modifying the Coriolis frequency f does not only induce changes in the coastal area, but also in the large-scale circulation. Nevertheless, the choice of a very small nested domain around Cape Ghir shall limit the influence of the modification of f. This remark remains valid for the other experiments.

3.4.3 Wind forcing effects (E2-E3)

In the EBUS, it was shown that wind curl is a determinant factor in the near-surface dynamics (e.g., Enriquez & Friehe, 1995; Münchow, 2000; Capet *et al.*, 2004; Castelao & Barth, 2007): a positive wind curl creates enhancement of the upwelling (through Ekman pumping) and is responsible for an injection of positive relative vorticity, through squeezing of the water column. Wind stress curls computed in summer using SCOW and COADS wind fields (Fig. 3.10), are characterized by a band of positive values close to the coast and negative values offshore. This feature is common to the four EBUS (Bakun & Nelson, 1991; Risien & Chelton, 2008).

The first wind experiment (E2) consists in working with spatially homogeneous fields. These fields are obtained by spatially averaging the SCOW fields over the domain $\mathcal{D}_3$. Doing so, the wind curl effects are removed. The intensity and the direction of this artificial wind field are computed for each month as the spatial averages. The resulting wind direction is still favorable to coastal upwelling (equatorward), but the injection of positive relative vorticity does not take place anymore.

Again, the upwelling characteristics (width and temperature gradient) are comparable to the baseline experiment (Fig. 3.9e-f), meaning that the general circulation is not strongly perturbed. The main difference is the absence of the filament between Cape Ghir and Cape Sim: the jet tends to follow the isobaths except at 31°N, where a slight deflec-

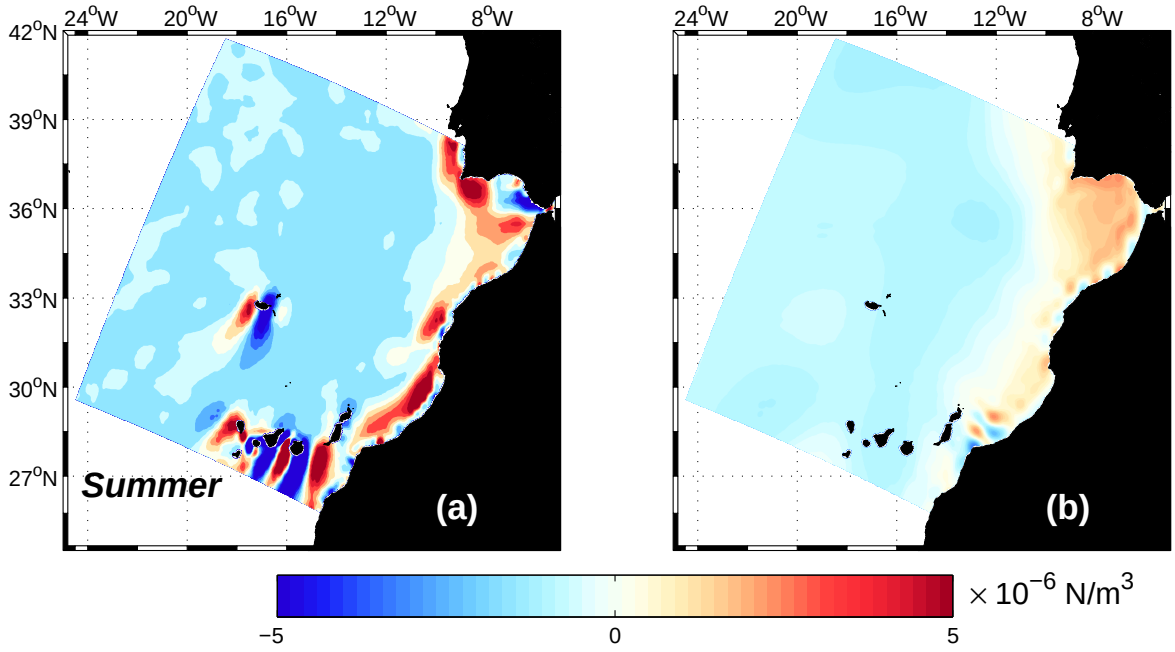

Figure 3.10: Summer wind stress curl for SCOW (a) and COADS winds (b).

tion takes place. The relative vorticity map shows that the largest values appear near the coast, particularly close to the capes. The difference with the baseline experiment is that none of the bands of positive vorticity is able to detach from the coastal jet and propagate offshore.

These results underline the role of wind through its curl in the generation of the Cape Ghir filament: when the curl is null, no additional relative vorticity is added to the flow, which can continue its way south.

In the second wind experiment, fields extracted from COADS are considered. The spatial resolution of these wind fields is lower than that of SCOW. The differences are evident when comparing the fields in Fig. 3.3: COADS fields do not capture the area of accelerated winds centered at 31°N close to the coast, nor leeward of the Canary islands. The area of calm winds south of Cape Ghir is visible in summer, though the contrast with offshore winds is very weak. The annual cycle for SCOW and COADS are generally close, except for January and June: COADS averaged values are much weaker than SCOW ones. Concerning the wind curl, large differences are identified for the width and the intensity of the positive wind-curl band (Fig. 3.10b): with COADS winds, positive values extend more offshore than with SCOW, but do not exceed 0.5×10^{-6}N/m^3, about 25% of the intensity of SCOW wind curl in the coastal area.

The results (Fig. 3.9g) show the development of a westward jet near 31°30'N, but the typical filament structure does not appear. The jet turns southward at the same latitude as Cape Ghir. The relative vorticity plot (Fig. 3.9h) displays the detachment of the positive relative vorticity band north of Cape Ghir as well as the anticyclonic eddy centered at 31°15'N. Even if no filament is produced, there seems to be a trigger effect: the jet starts to turn offshore, but cannot follow the westward direction. The trigger can

be reasonably attributed to the interactions of the flow with the topography.

Although this experiment does not bring direct insight into the filament dynamics, it highlights the necessity of a wind forcing with a sufficient spatial resolution in order to reproduce the main filament features.

3.4.4 Topographic effects (E4-E5)

In order to assess the role of the bathymetry, some modifications are made on the original one (Fig. 3.11a). The CGP (Fig. 3.1) constitutes an obstacle for the upwelling jet and consequently it is able to modify the direction of the flow. In order to evaluate the role of the CGP, the r-ratio is further reduced ($r = 0.05$ instead of $r = 0.20$) by the application of a smoothing filter. The corresponding bathymetry is represented in Fig. 3.11(b). The biggest changes are localized close to the coast (around 50 km offshore), whereas the differences offshore are negligible.

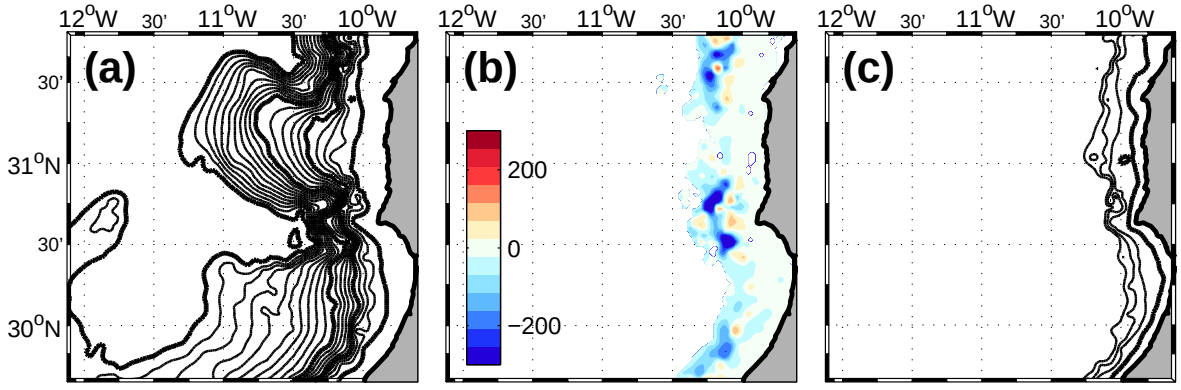

Figure 3.11: Original model bathymetry (a), difference between over-smoothed and original bathymetries (b) and shelf-slope only bathymetry (c). Thin lines are separated by 100 m, while thick lines represent isobaths 100, 500, 1000 and 2000 m.

The resulting temperature and vorticity fields are plotted in Fig. 3.9(i)-(j). Only a difference of intensity can be observed where the filament turns northward, near 11°20'W: temperature is higher than in the baseline experiment. Despite these modifications, the filament remains very similar in both cases. Even if it is involved in the generation mechanism, the topography does not appear to have an influence as strong as the wind field. In a recent study, Meunier *et al.* (2010) attributed the filament formation only to the interaction of the upwelling current with a promontory on the sea floor. However, as their wind field was uniform, they could not assess their role on the vorticity injection.

The last experiment conducted with the topography employs a shelf-slope only bathymetry, constructed this way: a hyperbolic tangent transformation is applied to the original depths, so that the maximal depth is set to 500 m and the minimal depth to 50 m. The hyperbolic function allows a smooth transition between the 500 m and 50 m-deep regions (Fig. 3.11c).

In this case, the differences with the original bathymetry are significant both near-shore and offshore. With these conditions, the model was able to reproduce the typical

features of the filament, except its position, which is about 50 km north of what is normally observed (Fig. 3.9k-l). The absence of the CGP certainly plays an essential role: in the results of E0, the filament was flowing just south of this topographic feature. The reason why the filament uprise at a location more at the north is again interpreted in terms of PV conservation: in the region covered by the upwelling jet, the bathymetry underwent a decrease of the bottom depth (absolute value) with respect to the original one. Then the water column is vertically squeezed, and the vorticity balance requires the development of an anticyclonic motion, leading to the formation of a filament.

Modifying the minimum depth (set to 25 m) will affect the bottom friction and change the behavior of the relative vorticity in the inner shelf region. However, this will only affect a very narrow region when compared to the whole domain, so that this effect will be local and not affecting qualitatively the domain-scale balance of potential vorticity.

The conclusion from these topography-related experiments, is that the Cape Ghir (and its prolongation under sea surface, the CGP), plays the role of a trigger for the filament. The main contribution to the domains-scale balance of potential vorticity is the relative vorticity injected by the wind curl, while the contributions of the bottom torque and related bottom friction are weaker.

3.5 Conclusions

The Cape Ghir filament is a recurrent feature of the Canary Current upwelling system. This study aims at numerically simulating the characteristics of the filaments and examining the mechanisms of generation. Filaments are frequently observed north of Cape Ghir through satellite imagery, but few modeling efforts could accurately represent its location and characteristic dimensions.

The baseline configuration, fed with realistic forcing conditions and boundary conditions from a larger domain, was capable to reproduce the main features of the filament (spatial and temporal scales, temperature gradient, location) with a good degree of realism. The spatial resolution (1.5 km) proves to be sufficient for the objective of our study. In another work in progress, a set of experiments was run with a finer horizontal resolution (800 m). The results were quite similar concerning the general filament dynamics, while frontal instabilities developed along the filament edges. These instabilities may play a role in the dissipation of the filament and in the transfer of water properties, but are not expected to influence the mechanism of formation.

The different experiments focused on the mechanisms of generation were defined by modifying the conditions of the baseline experiment. They were designed to assess the role of wind, geometry (bottom and coastline) and planetary vorticity on the dynamics of the filament. The proposed mechanism is based on the conservation of PV within the upwelling jet. The experiment with the uniform f parameter (no β effect) did not produce any filament, as the restriction of an equatorward flow was eliminated. This confirms the validity of the vorticity balance assumption, even if such a condition on the Coriolis frequency is not feasible in reality.

The experiments dedicated to the wind effects (E2-E3) underline its role on the fila-

ment formation, through the injection of positive relative vorticity into the flow. In the uniform wind experiment (E2), the injection of vorticity by the wind is removed. According to the proposed mechanism (Section 3.3), since the jet did not receive relative vorticity, it continued its way along the coast. When interpolated onto the model grid, COADS winds (E3) display a wider but weaker band of positive wind curl along the coast of NW Africa. It results in a flow without any filament during the studied period, although some meandering of the jet is observed north of Cape Ghir. A situation without any wind at all have been tested, but did not provide meaningful results, since with no wind, the upwelling itself disappears. This is why our experiments have in common that the wind is perturbed in a way that allows the main circulation characteristics to subsist.

The bathymetry is considered as a trigger to the filament formation: numerous observational studies confirm that their location is related to the coast irregularities. When the bathymetry is slightly modified (E4), the resulting fields are still very close to the reference case, meaning that filament formation is not strongly sensitive to the variation in the bathymetry. In this experiment, the trigger effect of Cape Ghir is slightly affected, hence the same wind field creates a filament at the same location. It is probable that once the filament has been generated, its trajectory is more dependent on the topographic features of the bottom. When the sea floor is made flat, except in the vicinity of the coast, a filament is still produced, but a location that does not correspond to real observations. This discrepancy is again explained by effects on the PV. We conclude that a realistic bathymetry is necessary to achieve to trigger the filament detachment at the correct location, even if the sensitivity to this parameter is much lower than to wind.

From these experiments, it is believed that the key ingredient to better resolve the filament dynamics is the interactions between wind and topography: Cape Ghir is not only a coastal geographical feature, but has continuation below (the CGP) and above sea surface (High Atlas range). The general direction and intensity of the wind is modified at the latitude of Cape Ghir (Fig. 3.3). The coupling with an atmospheric model would certainly give a better insight of the role of wind and relate its intensity to the land relief.

The wind spatial resolution appears as a essential issue: real observations indicate that, within an area of a few tenths of km offshore, wind intensity tends to diminish when approaching the coast (e.g., in California, Dorman *et al.*, 2006). This drop-off is not properly represented with a resolution of 0.25°. Yet it certainly plays a role in the filament dynamics, through an additional generation of positive wind stress curl and an influence on the upwelling intensity (Enriquez & Friehe, 1995; Capet *et al.*, 2004; Dever *et al.*, 2006).

The application of the same methodology (climatological run and modified conditions) to the other filaments in the Canary Current System (e.g., Cape Blanc, Cape Bajador, Cape Saint Vincent) or in another EBUS would allow one to determine if the proposed mechanism is generally applicable, or typical of Cape Ghir. Of particular interest are the California Current System and the Iberian Peninsula, where wind is favorable to upwelling all year long.

Acknowledgments

We thank J. Molemaker and F. Colas for their suggestions on the preparation of the simulations and I. Laiz for her contribution to the mechanism.

References

Arakawa, A. (1966). Computational design for long-term numerical integration of the equation of fluid motion: Two-dimensional incompressible flow. Part I. *Journal of Computational Physics*, **1(1)**: 119–143. doi:10.1016/0021-9991(66)90015-5.
URL http://www.sciencedirect.com/science/article/B6WHY-4DDR4NR-T0/2/c526d9b9e8bf9c2a5871a29de6f1cda7

Bakun, A. K. & Nelson, C. S. (1991). The seasonal cycle of wind-tress curl in subtropical eastern boundary current regions. *Journal of Physical Oceanography*, **21**: 1815–1834. doi:10.1175/1520-0485(1991)021<1815:TSCOWS>2.0.CO;2.

Barth, A., Alvera-Azcárate, A. & Weisberg, R. H. (2008). Benefit of nesting a regional model into a large-scale ocean model instead of climatology. Application to the West Florida Shelf. *Continental Shelf Research*, **28(4-5)**: 561–573. doi:10.1016/j.csr.2007.11.004.

Batteen, M. L., Martinez, J. R., Bryan, D. W. & Buch, E. J. (2000). A modeling study of the coastal eastern boundary current system off Iberia and Morocco. *Journal of Geophysical Research*, **105(C6)**: 14173–14195. doi:10.1029/2000JC900026.

Batteen, M. L., Martinho, A. S., Miller, H. A. & McClean, J. L. (2007). A process-oriented modelling study of the coastal Canary and Iberian Current system. *Ocean Modelling*, **18(1)**: 1–36. doi:10.1016/j.ocemod.2007.02.006.

Blayo, E. & Debreu, L. (2005). Revisiting open boundary conditions from the point of view of characteristic variables. *Ocean Modelling*, **9(3)**: 231–252. doi:10.1016/j.ocemod.2004.07.001.
URL http://www.sciencedirect.com/science/article/pii/S1463500304000447

Boé, J., Hall, A., Colas, F., McWilliams, J., Qu, X., Kurian, J. & Kapnick, S. (2011). What shapes mesoscale wind anomalies in coastal upwelling zones? *Climate Dynamics*, pp. 1–13. doi:10.1007/s00382-011-1058-5.
URL http://www.springerlink.com/content/q585253243k40h87/fulltext.pdf

Capet, X., Campos, E. J. & Paiva, A. M. (2008). Submesoscale activity over the Argentinian shelf. *Geophysical Research Letters*, **35**: L15605. doi:10.1029/2008GL034736.
URL http://www.agu.org/journals/gl/gl0815/2008GL034736/

Capet, X. J., Marchesiello, P. & McWilliams, J. C. (2004). Upwelling response to coastal wind profiles. *Geophysical Research Letters*, **31**: L13311. doi:10.1029/2004GL020123.

Castelao, R. M. & Barth, J. A. (2007). The role of wind stress curl in jet separation at a cape. *Journal of Physical Oceanography*, **37**: 2652–2671. doi:10.1175/2007JPO3679.1.

Courant, R., Friedrichs, K. & Lewy, H. (1967). On the partial difference equations of mathematical physics. *IBM Journal of Research and Development*, **11(2)**: 215–234. doi:10.1147/rd.112.0215.

Dever, E. P., Dorman, C. E. & Largier, J. L. (2006). Surface boundary-layer variability off Northern California, USA, during upwelling. *Deep-Sea Research II*, **53(25-26)**: 2887–2905. doi:10.1016/j.dsr2.2006.09.001.

Dorman, C. E., Dever, E. P., Largier, J. & Koracin, D. (2006). Buoy measured wind, wind stress and wind stress curl over the shelf off Bodega Bay, California. *Deep-Sea Research II*, **53**: 2850–2864. doi:10.1016/j.dsr2.2006.07.006.

Durand, M.-H., Cury, P., Mendelssohn, R., Roy, C., Bakun, A. & Pauly, D. (eds.) (1998). *Global versus Local Changes in Upwelling Systems*. ORSTOM, Paris, 594 pp. ISBN 2-7099-1389-5.

Durski, S. M. & Allen, J. S. (2005). Finite-amplitude evolution of instabilities associated with the coastal upwelling front. *Journal of Physical Oceanography*, **35(9)**: 1606–1628. doi:10.1175/JPO2762.1.
URL http://journals.ametsoc.org/doi/abs/10.1175/JPO2762.1

Durski, S. M., Allen, J. S., Egbert, G. D. & Samelson, R. M. (2007). Scale evolution of finite-amplitude instabilities on a coastal upwelling front. *Journal of Physical Oceanography*, **37(4)**: 837–854. doi:10.1175/JPO2994.1.
URL http://journals.ametsoc.org/doi/abs/10.1175/JPO2994.1

Durski, S. M., Samelson, R. M., Allen, J. S. & Egbert, G. D. (2008). Normal-mode instabilities of a time-dependent coastal upwelling jet. *Journal of Physical Oceanography*, **38(9)**: 2056–2071. doi:10.1175/2008JPO3803.1.
URL http://journals.ametsoc.org/doi/abs/10.1175/2008JPO3803.1

Enriquez, A. G. & Friehe, C. A. (1995). Effects of wind stress and wind stress curl variability on coastal upwelling. *Journal of Physical Oceanography*, **25**: 1651–1671. doi:10.1175/1520-0485(1995)025<1651:EOWSAW>2.0.CO;2.

Hagen, E., Zülicke, C. & Feistal, R. (1996). Near surface structures in the Cape Ghir filament off Morocco. **19(6)**: 577–598.

Haidvogel, D. B., Arango, H., Budgell, W. P., Cornuelle, B. D., Curchitser, E., di Lorenzo, E., Fennel, K., Geyer, W. R., Hermann, A. J., Lanerolle, L., Levin, J., McWilliams, J. C., Miller, A. J., Moore, A. M., Powell, T. M., Shchepetkin, A. F., Sherwood, C. R., Signell, R. P., Warner, J. C. & Wilkin, J. (2008). Ocean forecasting in terrain-following coordinates: Formulation and skill assessment of the Regional Ocean Modeling System. *Journal of Computational Physics*, **227(7)**: 3595–3624. doi:10.1016/j.jcp.2007.06.016.

Haynes, R., Barton, E. D. & Pilling, I. (1993). Development, persistence and variability of upwelling filaments off the Atlantic coast of the Iberian Peninsula. *Journal of Geophysical Research*, **98**: 22681–22692. doi:10.1029/93JC02016.

Hunter, P. & Macnab, R. (2003). The GEBCO Digital Atlas published by the British Oceanographic Data Centre on behalf of IOC and IHO. North Atlantic region.
URL http://www.gebco.net/

Iselin, C. (1936). A study of the circulation of the western North Atlantic. *Papers in Physical Oceanography and Meteorology*, **4**: 101 pp. doi:10.1575/1912/1087.
URL http://hdl.handle.net/1912/1087

Jennings, S., Kaiser, M. & Reynolds, J. D. (2001). *Marine Fisheries Ecology*. Blackwell Science Ltd, Oxford. ISBN 978-0-632-05098-7.

Johnson, J. & Stevens, I. (2000). A fine resolution model of the eastern North Atlantic between the Azores, the Canary Islands and the Gibraltar Strait. *Deep-Sea Research I*, **47**: 875–899. doi:10.1016/S0967-0637(99)00073-4.

Kelly, K. (1986). The influence of winds and topography on sea surface temperature patterns over the Northern California slope. *Journal of Geophysical Research*, **90**: 11783–11798. doi:10.1029/JC090iC06p11783.

Laiz, I., Sangrà, P., Pelegrí, J. L. & Marrero-Díaz, A. (2001). Sensitivity of an idealised subtropical gyre to the eastern boundary conditions. *Scientia Marina*, **65**: 187–194. doi:10.3989/scimar.2001.65s1187.

Lee, S.-K., Pelegrí, J. L. & Kroll, J. (2001). Slope control in western boundary currents. *Journal of Physical Oceanography*, **31**: 3349–3360. doi:10.1175/1520-0485(2001)031<3349:SCIWBC>2.0.CO;2.

Marshall, D. P. & Tansley, C. E. (2001). An implicit formula for boundary current separation. *Journal of Physical Oceanography*, **31**: 1633–1638. doi:10.1175/1520-0485(2001)031<1633:AIFFBC>2.0.CO;2.

Mason, E., Colas, F., Molemaker, J., Shchepetkin, A., Sangrà, P. & McWilliams, J. C. (2008). Seasonal variability of the Canary Current system. In *Eastern boundary upwelling ecosystems: integrative and comparative approaches*. Las Palmas de Gran Canaria, Spain.
URL http://www.confmanager.com/main.cfm?cid=845&nid=7276

Mason, E., Colas, F., Molemaker, J., Shchepetkin, A. F., Troupin, C., McWilliams, J. C. & Sangrà, P. (2011). Seasonal variability of the Canary Current: a numerical study. *Journal of Geophysical Research*, **116**: C06001. doi:10.1029/2010JC006665.
URL http://www.agu.org/journals/jc/jc1106/2010JC006665/2010JC006665.pdf

Mason, E., Molemaker, J., Shchepetkin, A. F., Colas, F., McWilliams, J. C. & Sangrà, P. (2010). Procedures for offline grid nesting in regional ocean models. *Ocean Modelling*, **35(1-2)**: 1–15. doi:10.1016/j.ocemod.2010.05.007.

McWilliams, J. C., Colas, F. & Molemaker, M. J. (2009). Cold filamentary intensification and oceanic surface convergence lines. *Geophysical Research Letters*, **36**: L18602. doi:10.1029/2009GL039402.
URL http://www.agu.org/pubs/crossref/2009/2009GL039402.shtml

Meunier, T., Rossi, V., Morel, Y. & Carton, X. (2010). Influence of bottom topography on an upwelling current: Generation of long trapped filaments. *Ocean Modelling*, **35(4)**: 277–303. doi:10.1016/j.ocemod.2010.08.004.

URL http://www.sciencedirect.com/science/article/B6VPS-50W1TPD-2/2/eac751cd6591c014f49603f2dea97c87

Müller, P. (1995). Ertel's potential vorticity theorem in physical oceanography. *Reviews of Geophysics*, **33(1)**: 67–97. doi:10.1029/94RG03215.

Münchow, A. (2000). Wind stress curl forcing of the coastal ocean near Point Conception, California. *Journal of Physical Oceanography*, **30**: 1265–1280. doi:10.1175/1520-0485(2000)030<1265:WSCFOT>2.0.CO;2.

Pedlosky, J. (1987). *Geophysical Fluid Dynamics*. Springer-Verlag, 2nd edn., 728 pp. ISBN 0-387-96387-1.

Pelegrí, J. L., Marrero-Díaz, A., Ratsimandresy, A., Antoranz, A., Cisneros-Aguirre, J., Gordo, C., Grisolía, D., Hernández-Guerra, A., Laíz, I., Martínez, A., Parrilla, G., Pérez-Rodríguez, P., Rodríguez-Santana, A. & Sangrà, P. (2005). Hydrographic cruises off northwest Africa: the Canary Current and the Cape Ghir region. *Journal of Marine Systems*, **54(1-4)**: 39–63. doi:10.1016/j.jmarsys.2004.07.001.
URL http://www.sciencedirect.com/science/article/pii/S0924796304002064

Penven, P., Marchesiello, P., Debreu, L. & Lefèvre, J. (2008). Software tools for pre- and post-processing of oceanic regional simulations. **23**: 660–662. doi:10.1016/j.envsoft.2007.07.004.

Risien, C. M. & Chelton, D. B. (2008). A global climatology of surface wind and wind stress fields from 8 years of QuikSCAT scatterometer data. *Journal of Physical Oceanography*, **38**: 2379–2413. doi:10.1175/2008JPO3881.1.

Ryther, J. H. (1969). Photosynthesis and fish production in the sea. *Science*, **166(3901)**: 72–76. doi:10.1126/science.166.3901.72.
URL http://www.jstor.org/stable/1727735

Shchepetkin, A. F. & McWilliams, J. C. (2003). A method for computing horizontal pressure-gradient force in an oceanic model with a nonaligned vertical coordinate. *Journal of Geophysical Research*, **108(C3)**: 3090. doi:10.1029/2001JC001047.

Shchepetkin, A. F. & McWilliams, J. C. (2005). The regional oceanic modeling system (ROMS): a split-explicit, free-surface, topography-following-coordinate oceanic model. *Ocean Modelling*, **9**: 347–404. doi:10.1016/j.ocemod.2004.08.002.

Shchepetkin, A. F. & McWilliams, J. C. (2009). Correction and commentary for "Ocean forecasting in terrain-following coordinates: Formulation and skill assessment of the regional ocean modeling system" by Haidvogel et al., J. Comp. Phys. 227, pp. 3595-3624. *Journal of Computational Physics*, **228(24)**: 8985–9000. doi:10.1016/j.jcp.2009.09.002.

Signell, R. & Geyer, W. (1991). Transient eddy formation around headlands. *Journal of Geophysical Research*, **96**: 2561–2575. doi:10.1029/90JC02029.

Stramma, L. (1984). Geostrophic transport in the warm water sphere of the eastern subtropical North Atlantic. *Journal of Marine Research*, **42**: 537–558. doi:10.1357/002224084788506022.

Stramma, L. & Schott, F. (1999). The mean flow field of the tropical Atlantic Ocean. *Deep-Sea Research II*, **46**: 279–303. doi:10.1016/S0967-0645(98)00109-X. URL http://www.ingentaconnect.com/content/els/09670645/1999/00000046/00000001/art00109

Troupin, C., Sangrà, P. & Arístegui, J. (2010). Seasonal variability of the oceanic upper layer and its modulation of biological cycles in the Canary Island region. *Journal of Marine Systems*, **80(3-4)**: 172–183. doi:10.1016/j.jmarsys.2009.10.007.

Ward, R. (2010). General Bathymetric Charts of the Ocean. *Hydro International*, **14(5)**. URL http://www.hydro-international.com/issues/articles/id1218-General_Bathymetric_Charts_of_the_Ocean.html

Woodruf, S. D., Diaz, H. F., Elms, J. D. & Worley, S. J. (1998). COADS release 2 data and metadata enhancements for improvements of marine surface flux fields. *Physics and Chemistry of the Earth*, **23(5-6)**: 517–526. doi:10.1016/S0079-1946(98)00064-0.

Wooster, W. S., Bakun, A. & McLain, D. R. (1976). The seasonal upwelling cycle along the eastern boundary of the North Atlantic. *Journal of Marine Research*, **34**: 131–140.

Worley, S. J., Woodruff, S. D., Reynolds, R., Lubker, S. J. & Lott, N. (2005). ICOADS release 2.1 data and products. *International Journal of Climatology*, **25**: 823–842. doi:10.1002/joc.1166.

Chapter 4

CAIBEX–Cape Ghir cruise

Top: On board Sarmiento de Gamboa during CAIBEX-Cape Ghir. Retrieving a drifting buoy. August 26, 2009.
Bottom left: Sloane's viperfish (Chauliodus sloani).
Bottom right: zooplankton: krill, gastropods, copepods, ...
Courtesy of Álvaro Roura (IIM, Vigo).

The CAIBEX project (**Ca**naries-**Ib**erian marine ecosystem **Ex**changes, http://www.iim.csic.es/~barton/caibex/index.html) was carried out in summer 2009 in the Canary Current upwelling system. The Cape Ghir component of the cruise took place off northwest Africa aboard research vessel *Sarmiento de Gamboa*, from August 16 to September 5, 2009. The main objective was the physical and biochemical sampling of the Cape Ghir upwelling filament.

Data collected during the cruise are presented and analyzed using interpolation and property diagrams. The maps serve to describe the filament properties and to make comparisons with the results obtained with the numerical model (Chapter 3). The most interesting feature is a subsurface anticyclonic eddy, detected north of Cape Ghir, at depths between 200 and 400 m. A mechanism is proposed to explain the generation of such an eddy.

Remote-sensed measurements of SST and wind speed are extracted in order to validate the observations.

Contents

4.1 Data acquisition

Water properties were measured through a conductivity-temperature-depth (CTD) instrument (56 casts), a SeaSoar towed vehicle (9 meridional tracks) and drifting buoys (6 deployments). The locations of these measurements are presented in Fig. 4.1, along with the numerical model temperature that was used to design the sampling strategy. In the course of the cruise, SST satellite images were acquired in near real time. They confirmed the presence of a long upwelling filament developing north of Cape Ghir and extending westward more than 100 km, but with a position that significantly changed during the three weeks of the cruise. The parameters that will be considered during this analysis phase are: temperature, salinity, fluorescence, oxygen concentration and transmittance.

Velocities were determined with Acoustic Doppler Current Profilers (ADCP) operating at 75 and 150 kHz. According to Hummon & Firing (2003), range and velocity measurement noise vary inversely with frequency and depend on the sea condition. It turned out that the 150 kHz ADCP measurements were limited to a depth about 200 m, while the 75 kHz ADCP provided measurements until a depth of about 800 m.

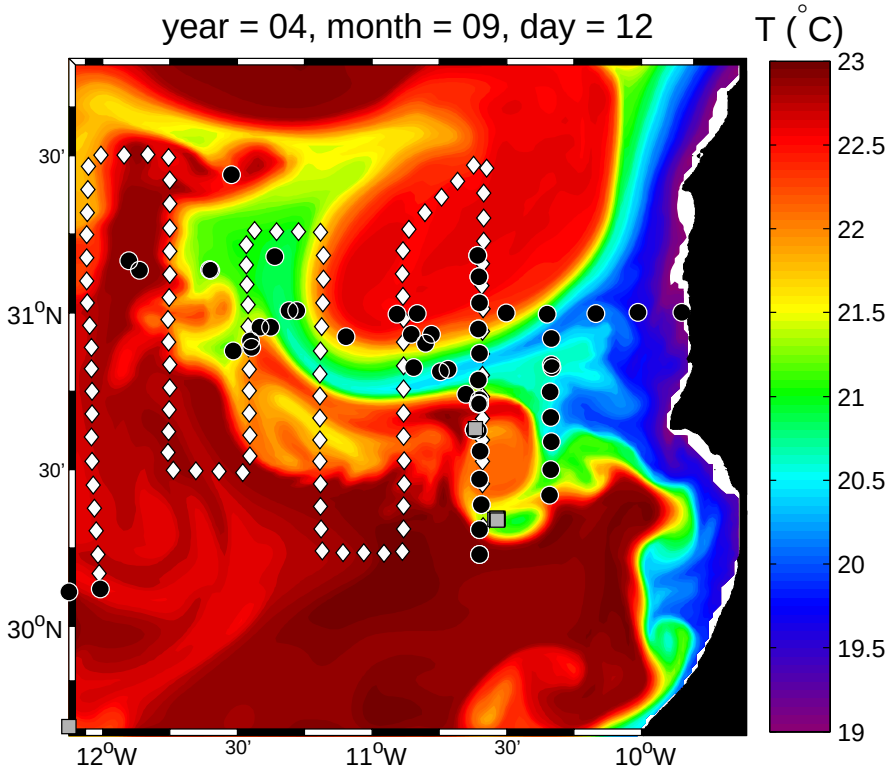

Figure 4.1: SeaSoar tracks (white diamonds), CTD casts (black dots) and drifter release positions (grey squares) overlaid on the regional model surface temperature (12 September, 4th year of simulation in the small domain $\mathcal{D}_3$). Though the model was forced with climatological fields, its results helped us to define a sampling strategy.

4.1.1 CTD

Fifty-six CTD casts were made (Fig. 4.1 and Tab. 4.1) in a region that encompasses Cape Ghir. Raw data files were processed with Sea-Bird SEASOFT software (http://www.seabird.com/software/softrev.htm) and data were vertically filtered by averaging adjacent measurements into bins of 0.5 m.

Since the measurements were made during a three-week span, it is delicate to perform direct interpolation on them without precaution (i.e., with a large signal-to-noise ratio). This will be further discussed in Section 4.2.3.

The meridional transect, carried at 10°36'W from 25 to 27 August, is of particular interest: the data where all acquired during a short period, so that local ocean properties have not undergone significant variations.

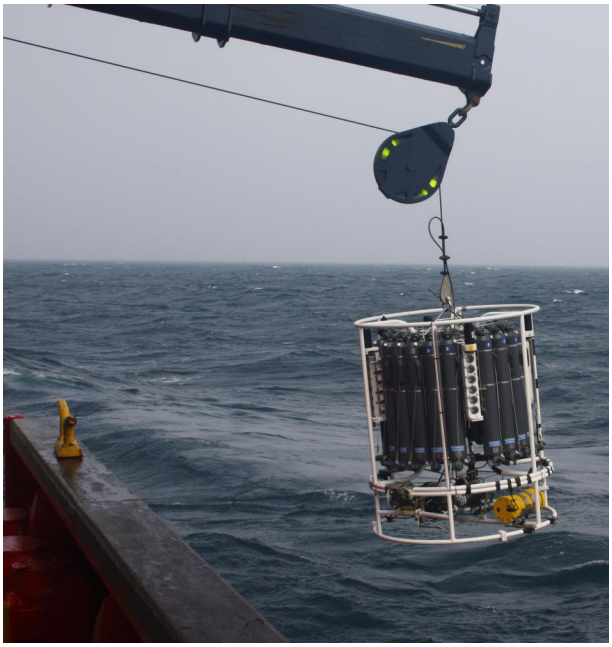

Figure 4.2: Deployment of the CTD rosette on August 20, 2009. The measured parameters are: temperature, conductivity, pressure, oxygen concentration, turbidity, transmittance, fluorescence, irradiance, and surface irradiance.

Locations

CTD measurements were carried out all the cruise long with various objectives. According to these objectives, they are classified in different categories (Fig. 4.3):

HPS (high-pressure sensors): these measurements were performed in order to test a new biological sensor. They were only made far away from the coast, where the bottom depth was sufficiently large (>2000 m).

Bongo: made after a collect with the bongo net (net used to determine the type and concentration of plankton).

Table 4.1: CTD casts performed during CAIBEX-Cape Ghir. Maximal depth is estimated from the ship instruments. Coordinates correspond to the beginning of the cast.

Station		Cast	Date	Max. Depth (m)	Latitude	Longitude	Comment
0		FIL001	17/8/2009	2091	30°07'05"	12°00'29"	
1		FIL002	20/8/2009	1074	30°25'07"	10°20'24"	HPS
2	(M12)	FIL003	20/8/2009	1749	30°29'59"	10°20'07"	Monitoring 12
3		FIL004	20/8/2009	1448	30°35'15"	10°20'05"	HPS
4		FIL005	20/8/2009	760	30°39'55"	10°20'09"	
5	(M11)	FIL006	20/8/2009	1302	30°44'47"	10°20'21"	Monitoring 11
6		FIL007	20/8/2009	1172	30°50'04"	10°19'59"	Bongo net 1
7		FIL008	20/8/2009	950	35°55'04"	10°20'06"	
8	(M1)	FIL009	21/8/2009	–	31°00'03"	9°50'57"	Monitoring 1
9	(M2)	FIL010	21/8/2009	–	31°00'01"	10°00'47"	Monitoring 2
10	(M3)	FIL011	21/8/2009	369	30°59'49"	10°10'10"	Monitoring 3
11		FIL013	23/8/2009	2113	30°43'19"	10°36'00"	Incubation
12		FIL014	23/8/2009	1724	30°44'20"	10°39'05"	Nitrogen incubation
14	(M4)	FIL015	23/8/2009	537	30°59'44"	10°20'55"	Monitoring 4
15		FIL016	24/8/2009	1631	30°49'12"	10°43'00"	Bongo net
16		FIL017	24/8/2009	1882	30°48'43"	10°44'45"	Physical buoy
17		FIL018	24/8/2009	1785	30°54'12"	10°48'07"	Nitrogen
18		FIL019	24/8/2009	2160	30°49'28"	10°50'41"	HPS
19	(M5)	FIL020	24/8/2009	710	30°59'56"	10°30'06"	Monitoring 5
20		FIL021	24/8/2009	1486	30°55'49"	10°46'46"	Physical buoy
21		FIL022	25/8/2009	1811	30°55'53"	10°51'14"	Incubations
22		FIL023	25/8/2009	1523	30°59'45"	10°54'28"	Nitrogen, phys. buoy
23		FIL024	25/8/2009	2088	30°55'27"	11°05'43"	HPS
24	(M6)	FIL025	25/8/2009	1579	30°59'50"	10°49'56"	Monitoring 6
25		FIL026	25/8/2009	1529	30°49'32"	10°19'55"	Station 6
26	(T1)	FIL027	26/8/2009	687	31°10'59"	10°36'27"	Transect T1
27	(T2)	FIL028	26/8/2009	725	31°06'51"	10°36'11"	Transect T2
28	(T3)	FIL029	26/8/2009	866	31°01'51"	10°36'05"	Transect T3
29	(T4)	FIL030	26/8/2009	–	30°56'54"	10°36'18"	Transect T4
30	(T5)	FIL031	26/8/2009	1211	30°52'11"	10°36'06"	Transect T5
31	(T6)	FIL032	26/8/2009	1656	30°47'05"	10°36'16"	Transect T6
32	(T7)	FIL033	27/8/2009	2270	30°42'35"	10°36'01"	Transect T7
33	(T8)	FIL034	27/8/2009	2140	30°37'36"	10°37'12"	Transect T8, HPS
32b	(T7b)	FIL035	27/8/2009	2221	30°42'35"	10°36'15"	Transect T7 (repeat.)
34	(T9)	FIL036	27/8/2009	1665	30°33'26"	10°35'54"	Transect T9
35	(T10)	FIL037	27/8/2009	2076	30°28'07"	10°36'04"	Transect T10
36	(T11)	FIL038	27/8/2009	1777	30°23'15"	10°35'42"	Transect T11
37	(T12)	FIL039	27/8/2009	1652	30°18'30"	10°36'00"	Transect T12
38	(T13)	FIL040	27/8/2009	1561	30°13'45"	10°36'01"	Transect T13
39		FIL041	28/8/2009	2265	31°00'22"	11°16'45"	Phys. buoy, incub.
40		FIL042	28/8/2009	2305	31°00'23"	11°18'29"	Phytoplankton net
41		FIL043	28/8/2009	2072	31°10'42"	11°21'36"	HPS
42		FIL044	28/8/2009	2494	31°26'25"	11°31'20"	Bongo net
43		FIL045	29/8/2009	2338	30°57'16"	11°22'30"	Incubations
44		FIL046	29/8/2009	2353	30°57'15"	11°25'00"	Nitrogen
45		FIL047	29/8/2009	3042	31°08'09"	11°35'54"	HPS
46		FIL048	29/8/2009	2925	31°08'09"	11°51'46"	Bongo net
47		FIL049	30/8/2009	2502	30°54'34"	11°27'06"	Incubations
48		FIL050	30/8/2009	2560	30°53'22"	11°26'45"	Nitrogen
49		FIL051	30/8/2009	2888	31°08'16"	11°36'11"	HPS
50		FIL052	30/8/2009	2983	31°09'54"	11°54'07"	Bongo net
51		FIL053	30/8/2009	2891	30°52'42"	11°30'53"	Bongo net
52		FIL054	31/8/2009	2136	29°39'40"	13°26'42"	HPS
53		FIL055	3/9/2009	1860	30°37'26"	10°36'21"	Station T8

Incubation: made every time the buoy for the biological study was picked up (Lagrangian study; not presented here).

Monitoring: measurements made at fixed locations at different times of the year, during other campaigns.

Transect: meridional track approximatively along 10°36'W (25-27 August 2009).

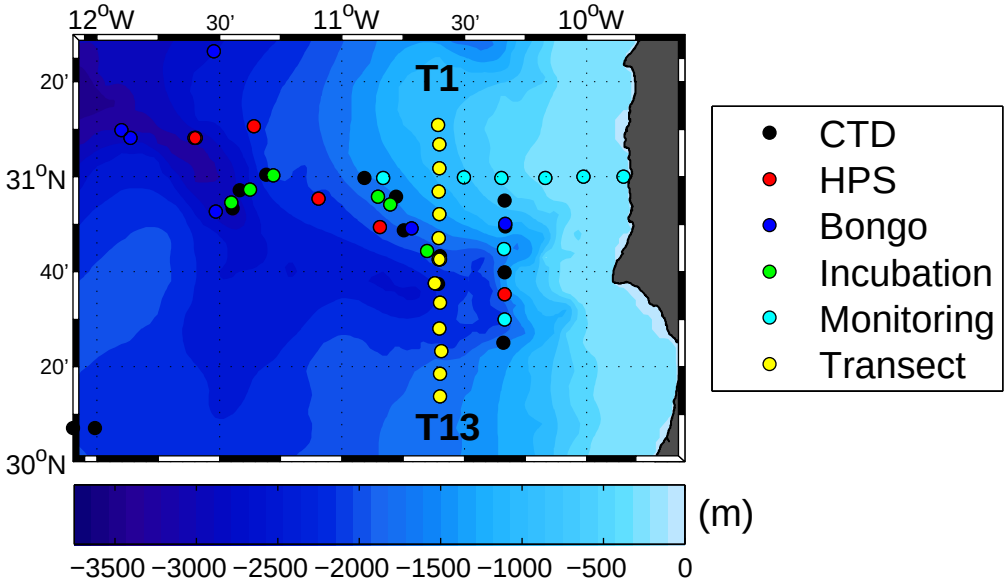

Figure 4.3: Locations and types of the CTD casts, superimposed on the regional bathymetry extracted from GEBCO. T1 and T13 denote the first and last casts of the meridional transect, respectively.

Measurements

Fluorescence is measured by CTD and SeaSoar and constitutes a good proxy of the chlorophyll *a* concentration. The relation between the two variables is known as the *Kautsky effect* (Kautsky *et al.*, 1960): a plant exposed to light displays variations in its fluorescence, and these variations are related to photosynthesis (e.g., Falkowski & Kiefer, 1985; Harris, 1980; Maxwell & Johnson, 2000).

In order to work with chlorophyll *a* concentrations, a calibration would have to be made. However, as this chapter is focused on qualitative results, preliminary analyzes are made using fluorescence. Fluorescence are expressed in FUs (standing for *fluorescence units*) and are unitless.

Transmittance is the fraction of incident light, at a specified wavelength, that passes through a sample, in this case a layer of water at a given depth.

The measurements obtained in the meridional transect (yellow dots in Fig. 4.3) are shown in the form of scatter plots, for the first 400 m of the water column (Fig. 4.4). On average, two successive profiles were separated by a distance of 9.6 km, providing a high-resolution sampling of the filament properties.

Stations T9 and T10 have the lowest near-surface temperatures (Fig. 4.4a), a possible signal of the filament crossing. A close-up view of the first 40 m is provided in Fig. 4.5a (note the different color bars). The strong horizontal gradient is obvious: at 20 m depth, the temperature at T9 and T10 is more than 1°C lower than in the other stations. T8 temperatures are relatively low in comparison with the others. For these stations, the thermal stratification is weaker in comparison with the other profiles.

Figure 4.5a also shows that at stations T4 and T5, a rise of cold water (with respect to stations T1 to T7) takes place. Corresponding to this cool water, a small increase of fluorescence (Fig. 4.5b) is observed around 35 m, with values larger than 0.25.

If we now focus on stations T9 and T10, we observe that:

- the salinity (Fig. 4.4b) and oxygen concentration (Fig. 4.4c) do not show any particular feature, except a small increase of salinity at T10 between 50 and 100 m.
- the transmittance (Fig. 4.4d) is minimal between 5 and 40 m. This diminution is attributed to an increase concentration of suspended matter in that zone.
- the fluorescence (Fig. 4.5b) displays large values, mainly between 20 and 30 m. As measurements are not available in the first meters of the water column, we do not know whether the signal reaches the surface and is thus detectable using remote sensing imagery.

From this first set of raw observations, two features catch our attention:

1. The probable signal of an upwelling filament centered at 30°30'N, characterized by cool, nutrient-rich and low-transmittance waters.
2. An input of cool waters at station T5, associated with a slight subsurface increase of chlorophyll *a* concentration .

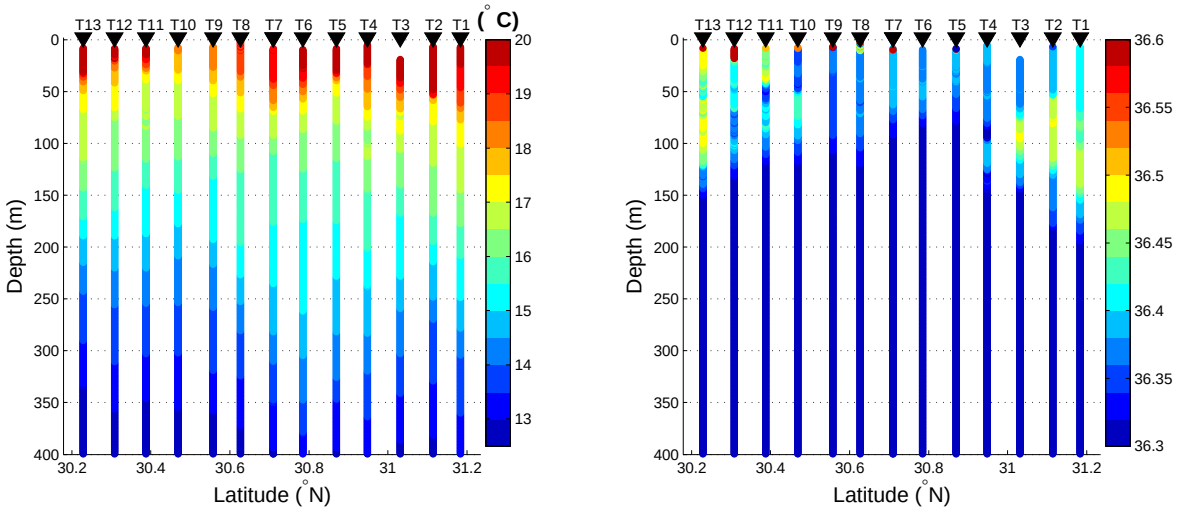

(a) (b)

Figure 4.4: Scatter plots of the CTD measurements made in the meridional transect: (a) temperature, (b) salinity.

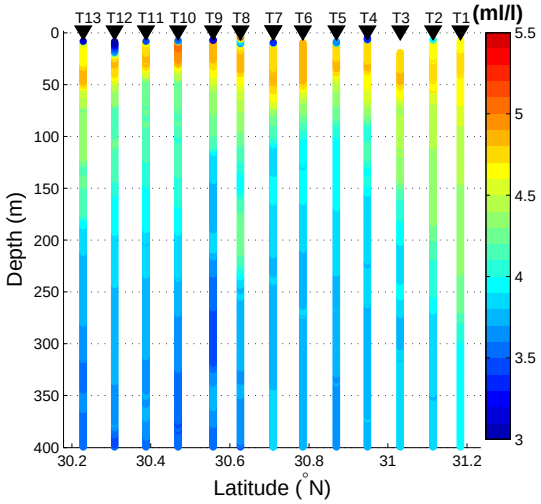

(c)

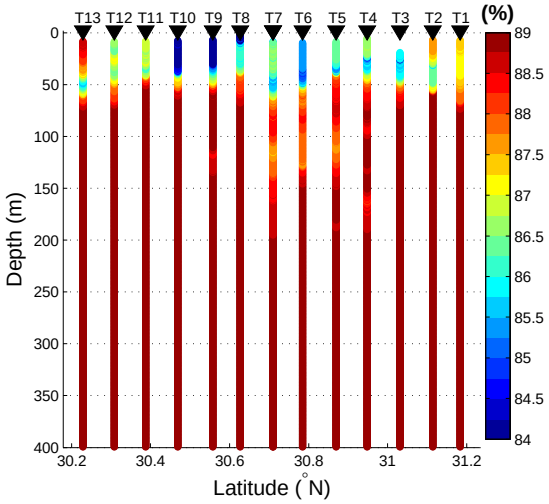

(d)

Figure 4.4: continued: (c) oxygen concentration and (d) transmittance.

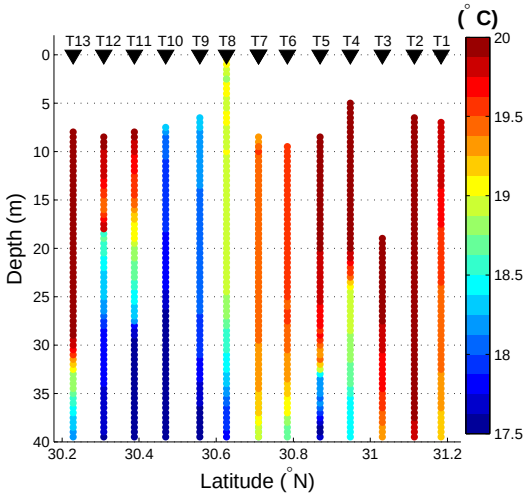

(a)

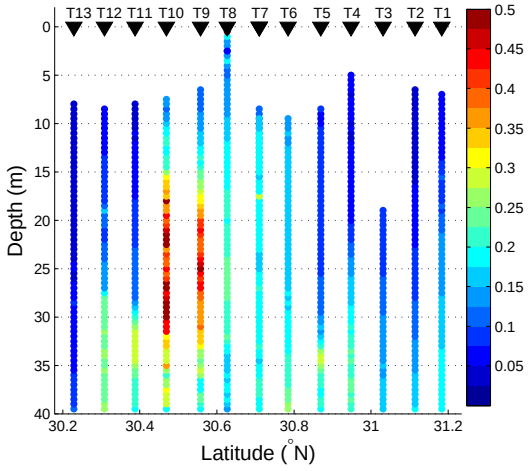

(b)

Figure 4.5: Scatter plot of the CTD measurements from 0 to 40 m: (a) temperature, (b) fluorescence. Stations T9 and T10 display a low-temperature, high-chlorophyll signal.

4.1.2 Seasoar

The SeaSoar is a towed vehicle that measures the water properties by undulating between the surface and a depth ranging between 400 and 500 m (Fig. 4.6). Its advantages are the high spatial and temporal resolutions, which are particularly adapted to the study of upwelling filaments. SeaSoar vehicles were previously employed in other upwelling regions, mainly the California Current upwelling system (e.g., Huyer *et al.*, 1998; Barth *et al.*, 2000) and along the Iberian Peninsula (Haynes & Barton, 1990). To our knowledge,

it is the first time that this high-resolution device was used in the upwelling system off NW Africa.

Throughout the cruise, most of the measurements with the SeaSoar were made between 15 m and 410 m deep, with the deepest measurements at 429 m. The mean distance between two successive meridional sections (Fig. 4.7) was 28 km, while the mean vertical resolution was 0.72 m. For safety reasons, no track was performed closer than 100 km from the coast in order to avoid collision with the bottom. Indeed, the bathymetry is known with a limited spatial resolution. Temperature, salinity, and Seapoint fluorescence (http://www.seapoint.com/scf.htm) were acquired.

Figure 4.6: The SeaSoar Mk II vehicle employed for the measurements has the following characteristics: length: 2 m; height: 0.98 m; width: 1.60 m, weight: 150 kg; maximal speed: 12 kn (22 km/h). Technical document available at http://www.chelsea.co.uk/Factsheets/SeaSoar04.pdf

Locations

Three series of SeaSoar tracks (Fig. 4.7) were conducted at different times of the cruise:

1. August 17-20 (tracks no. 1–6): six meridional tracks progressively going closer to the coast, starting approximatively along 12°W and finishing along 10°30'W. The westernmost and easternmost tracks are referred to as no. 1 and no. 6, respectively. The idea of this first series, made at the beginning of the cruise, was to obtain a synoptic picture of the filament, before performing further measurements with the CTD.

2. August 22-23 (track no. 7): a meridional track close to 10°30'W (around the same longitude as track no. 6) for determining the variation of the filament position over a period of 2-3 days.

3. September 2-3 (tracks no. 8 and 9): two meridional tracks completed again at the same longitude, just before the end of the cruise, in order to examine changes with respect to the initial conditions of the cruise.

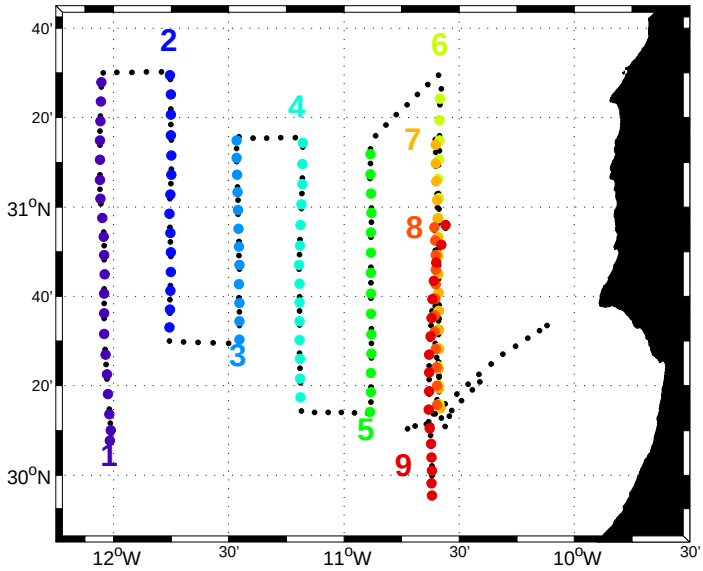

Figure 4.7: The SeaSoar course (black dots) is made up of meridional tracks (colored dots) approaching the coast. Tracks 6 to 9 are repeated at different times at approximatively the same longitude.

Measurements

Prior to their interpolation, data are simply represented in the forms of scatter plots. This provides a visual quality check and evidences the regions void of data. These will have to be considered with caution after the data griding. During track 8 and the beginning of track 9, the speed of the ship was not sufficient (due to rough sea conditions), hence the SeaSoar could not come close enough to sea surface. This explains why measurements stop close to 50 m below the surface. Hence we will have less confidence in the gridded fields in this part of the water column.

Scatter plots of T, S and fluorescence are shown in Figs. 4.8, 4.9 and 4.10, respectively. With the high spatial resolution, interesting features can be directly observed. In track 6, between 30.6°N and 30.9°N, the near-surface temperature is more than 2°C cooler than at other latitude. A similar observation is made for track 9, but at a lower latitude (between 30.35 and 30.50°N).

Overall, salinity decreases with depth, at least for the layers sampled by the SeaSoar. This is typical from subtropical regions, where evaporation is enhanced by strong heating and wind in summer, and precipitations are weak through the year. Variations of salinity near the surface do not allow an easy identification of the filament. Still, meridional variability is apparent for the deeper layers (200-400 m). They will be examined in Section 4.2.4.

For tracks 1 to 7, the fluorometer was not correctly calibrated, resulting in abnormally high values (Fig. 4.10). Concretely, most of the measurements are higher than 0.2, even at 400 m. The contrast is clearly seen by comparing the color scale of the first seven tracks with the last two ones. The measurements corresponding to these tracks have to be treated with caution. Nevertheless, they were not discarded from the data collection,

since they still contain qualitative information. For instance in track 3, an increase of fluorescence is detected between 30.85°N and 31°N below 300 m. The fluorescence values are not realistic, the higher values probably translate a process has occurred in that zone.

The bad calibration was noticed before the end of the cruise after the construction of the scatter plots. The fluorometer was fixed before the end of the cruise and the last two tracks provided realistic measurements (values close to zero below 100 m). Unfortunately, whilst the calibration was corrected, almost no measurements were available close to surface because of the sea state.

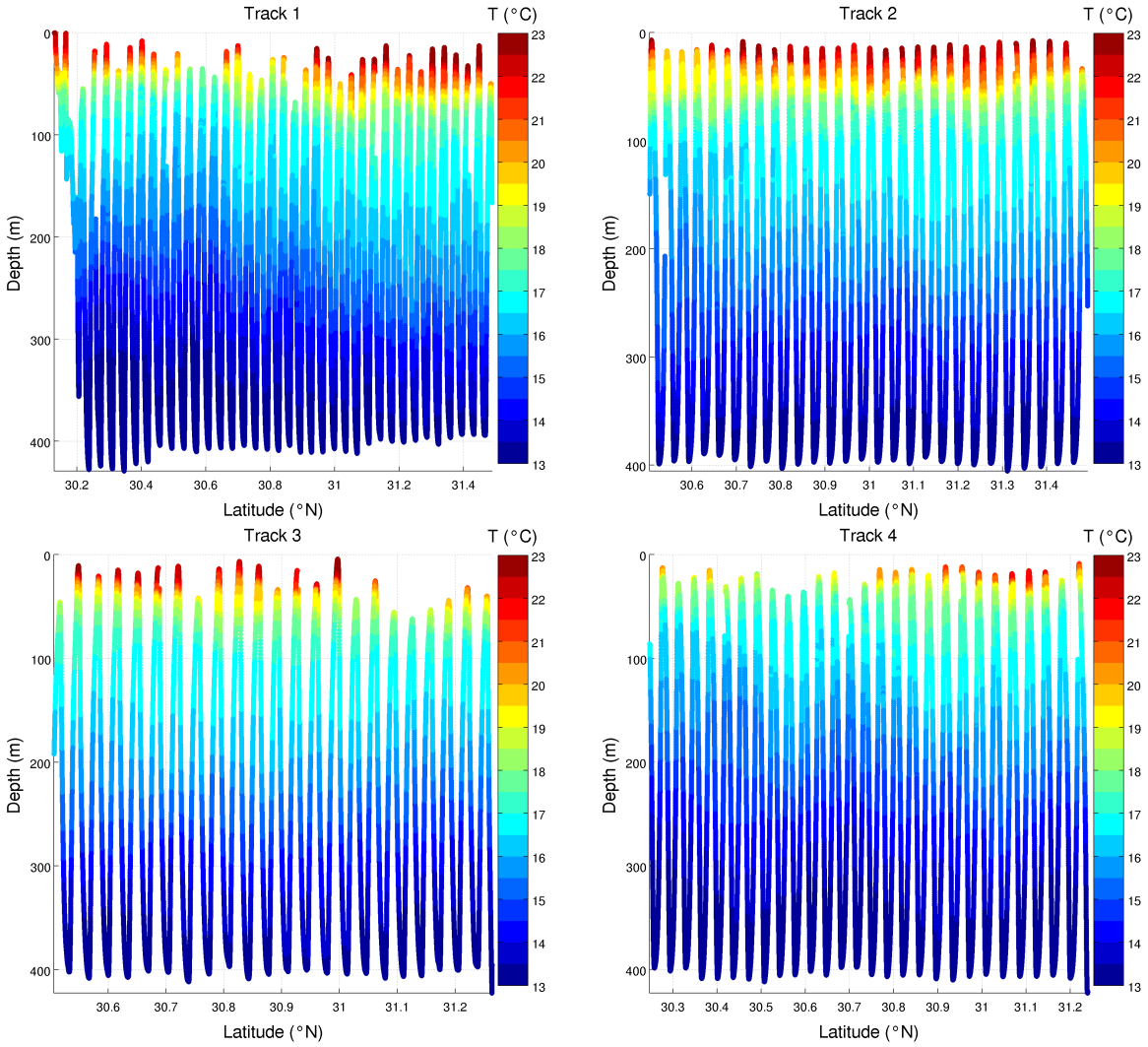

Figure 4.8: Measurements of temperature by the SeaSoar provide information on the structures crossed during the tracks. Here tracks 1 to 4.

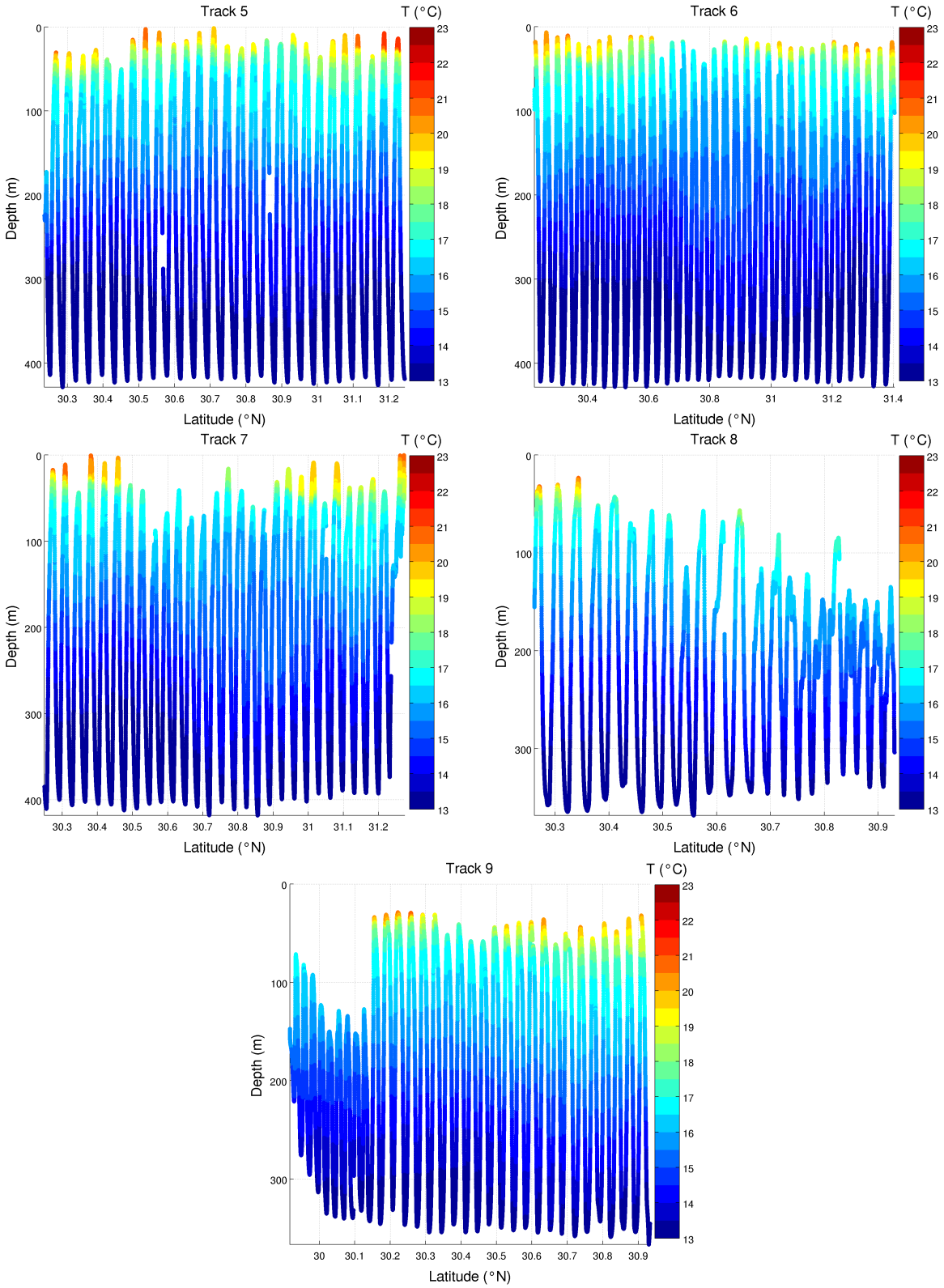

Figure 4.8: continued: tracks 5 to 9.

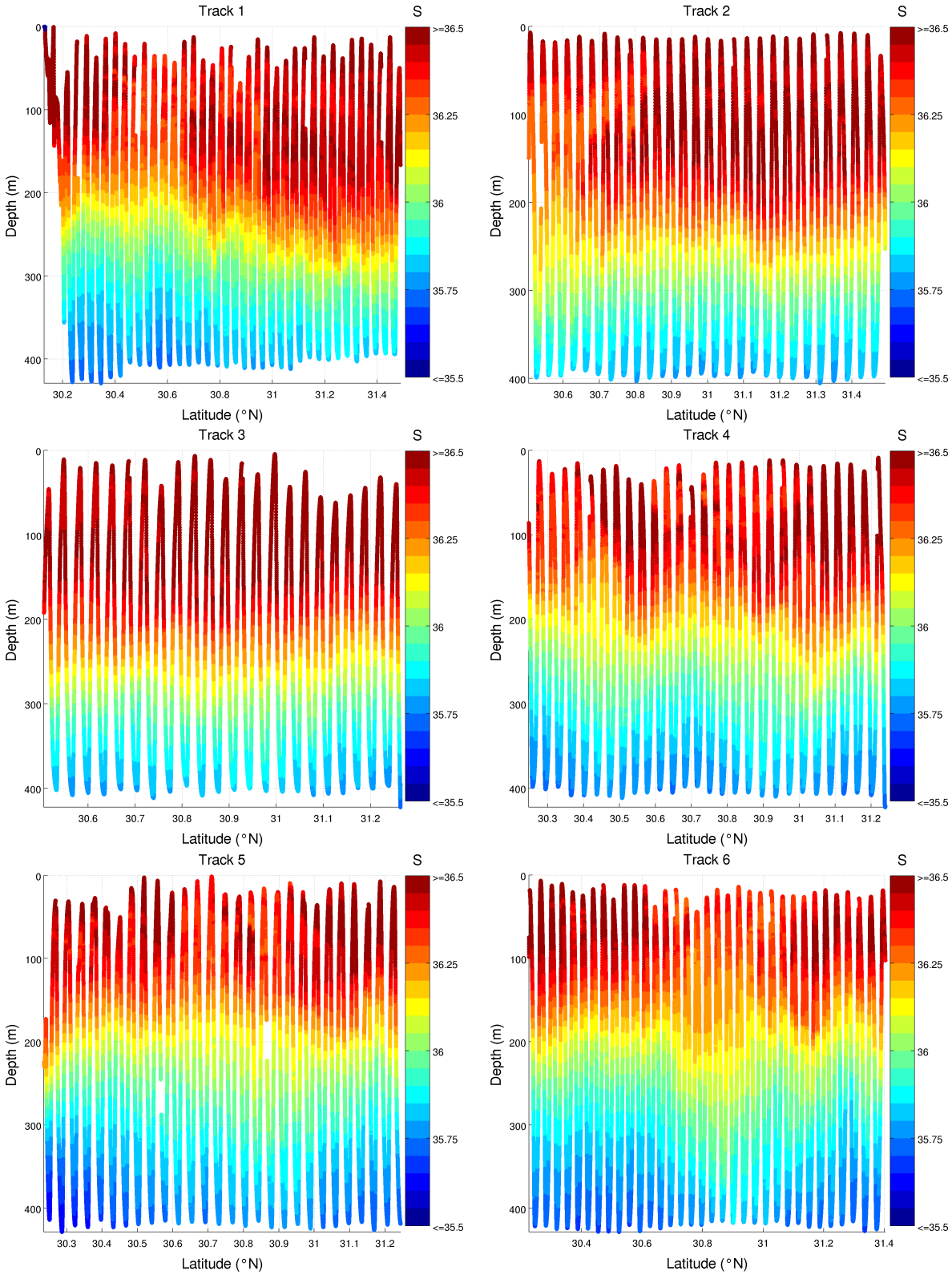

Figure 4.9: SeaSoar salinity measurements for tracks 1 to 6.

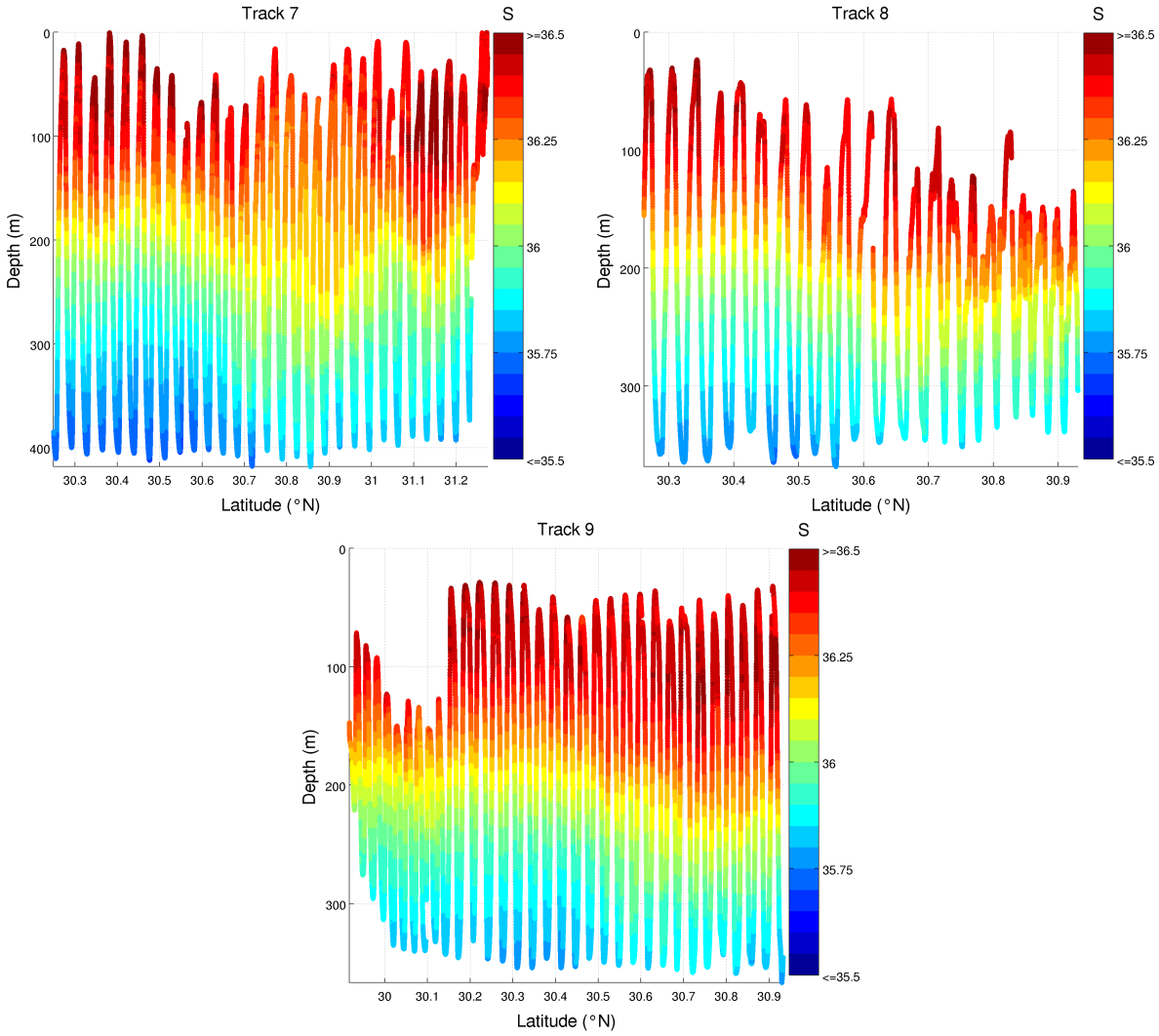

Figure 4.9: continued: tracks 7 to 9. Due to rough sea, the ship velocity was not sufficient, and the SeaSoar could not come close enough to the surface.

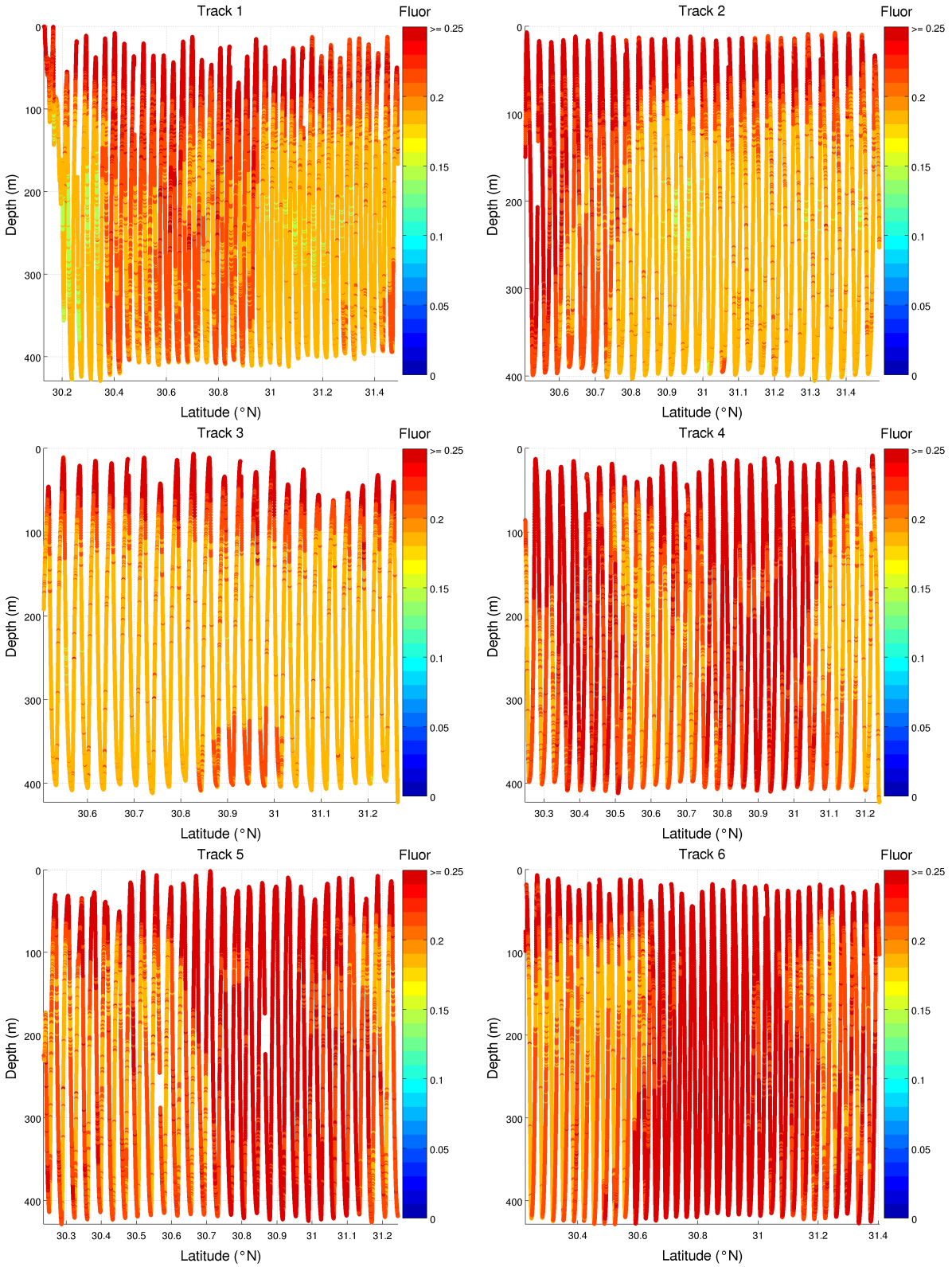

Figure 4.10: SeaSoar fluorescence measurements for tracks 1 to 6. The raw measurements highlight the calibration issue for tracks 1 to 7: the fluorescence is unrealistically high in this part of the water column. Tracks 8 and 9 benefited from the adjustment of the sensor.

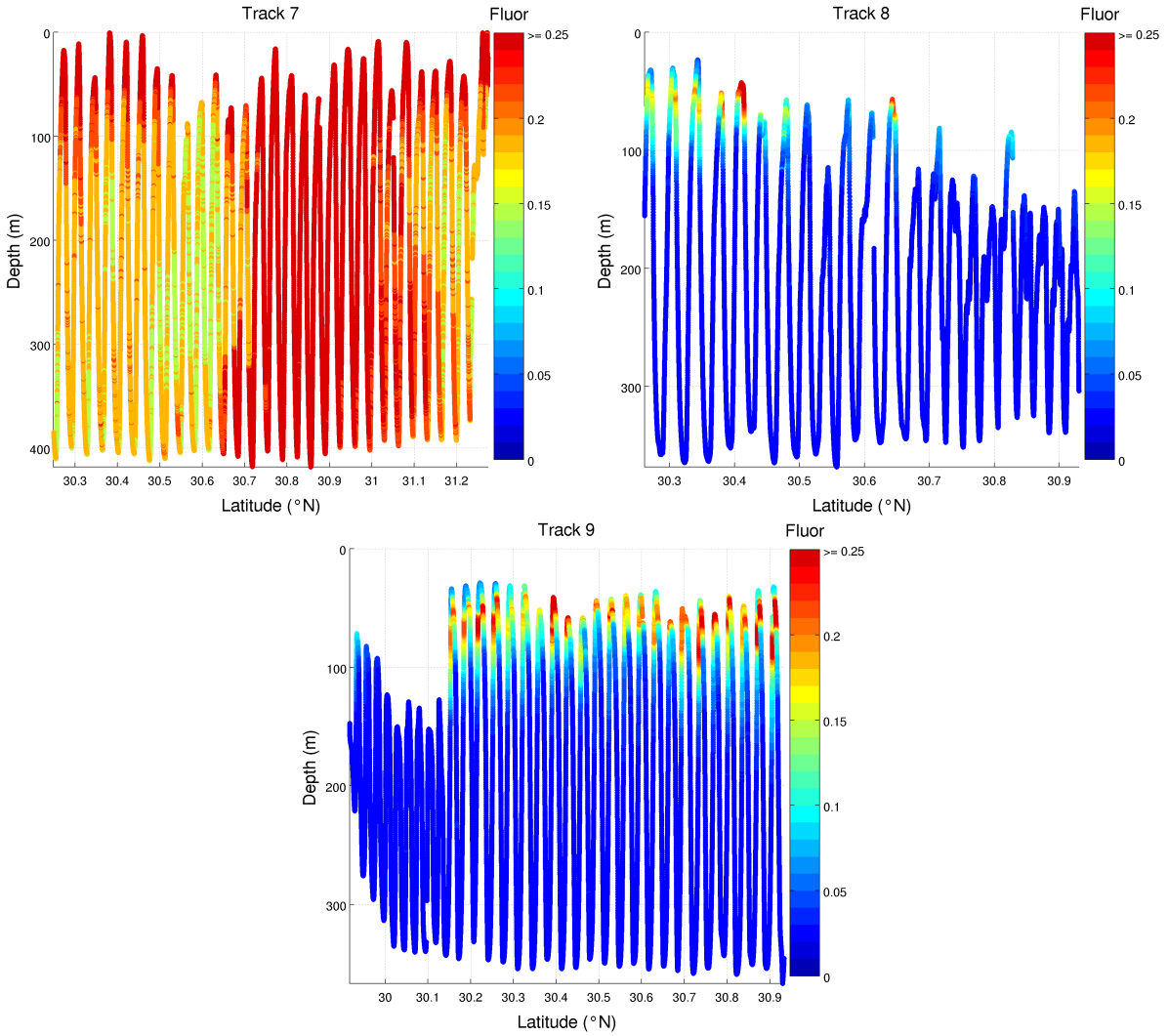

Figure 4.10: continued: tracks 7 to 9. The correction of the calibration is evident in the last two tracks.

4.1.3 ADCP velocities

The processing of the ADPC raw measurements was performed by B. Barreiro González (Instituto de Investigaciones Marinas, Consejo Superior de Investigaciones Científicas, Vigo, Spain) with the "Common Oceanographic Data Access System" (CODAS) software. The procedure is not detailed here, but will be in an article (in preparation) describing the measurements of the physical parameters during the 3rd leg of CAIBEX.

4.1.4 Drifters

On September 3, 2009, we decided to launch six drifting buoys (Fig. 4.11) with the objective of following the current at given depths: five buoys had their drogue at 10 m and were launched in the core of the filament; one had the the drogue at 300 m and was dropped north of the filament, in the convergence zone. Because the satellite images did not allow us to determine the filament position that day, we had to exploit the SeaSoar data of the 9th track in near real-time.

Each of them transmits a radio signal, allowing the ARGOS satellites to determine their position several times a day. In this case, 80-90 minutes separated two valid positions. No sensor was mounted on the drifters, thus the only information provided is the set of trajectories.

Figure 4.11: The radio-wave emitting parts of the Argos drifting buoys are located in the gray spheres. A drogue (not shown here) was attached to each of them in order to follow the current.

The near-surface drifters were intended to study the possible generation of westward-propagating eddies by the Cape Ghir filament, in the so-called *Eddy Corridor* (Sangrà *et al.*, 2009). With the 300 m-drogue drifter, we wanted to confirm the existence of a subsurface anticyclonic eddy north of the filament, as suggested by our measurements. The positions for the deployment of the drifters were directly deduced from the SeaSoar measurements performed on the same day (track no. 9). Yet, the lack of near-surface data made the decision complicated. The use of temperature and salinity provided by

the thermosalinograph, mounted close to the water intake of the ship, could have been a valuable additional source of information. However, such data were not available at the time the decision had to be made.

The raw trajectories of the six drifters are displayed in Fig. 4.12. Acquisition of positions was stopped by end of October, as the drifters had left the region of interest. Some of them were previously taken to the coast, probably by fishing vessels. They were not released afterwards.

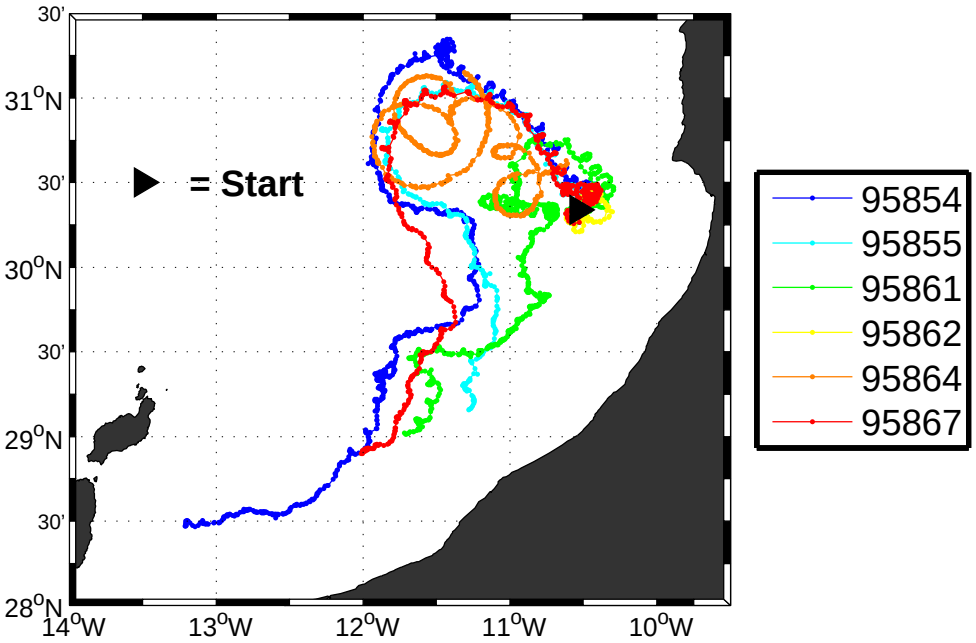

Figure 4.12: The drifter trajectories from September 3 to October 31, 2009, show an overall northwestward displacement, followed by a cyclonic loop and a southward motion. Drifter no. 95864 (orange line) has the drogue at 300 m. Artificial displacements (i.e., due to ships) are not displayed.

4.2 Data analysis

Most of the collected raw data have been described and displayed in the previous sections without any processing. In the present section, basic analysis and interpolations are performed, in order to extract information about the filament properties.

4.2.1 Mean CTD profiles

Averaging all the profiles measured with the CTD provides a general view of the water characteristics and the variability of its properties in the studied region. It is also a way to spot suspect profiles or measurements. For all the variables, the scattering around the

mean profiles is rather limited (Fig. 4.13), demonstrating the consistency of the measurements. Only a few values of fluorescence at depths (Fig. 4.13c), appearing as *spikes*, seem suspect.

In the first 100 m, temperature sharply decreases from its surface value (20-22°C) to about 17°C. Until 1000 m, the decrease continues, but at a lower rate until approximatively 1000 m where it reaches between 8 and 9°C. From 1000 to 1500 m, the contribution of intermediate water masses modifies the shape of the curve: temperatures slightly increase and reach a local maximum around 1200 m. Finally, between 1500 and 3000 m, temperature decreases again, and the variability is even lower. Minimal values are lower than 4°C.

Salinity also decreases with depth, except between 800 and 1200 m, again under the influence of intermediate water masses. Near the surface, a great variability is observed. This is probably due to the time necessary for the stabilization of the CTD probe during the descent. The values in the first meters of the water column have to be considered with precaution. The lowest observed values (below 35) correspond to the deepest measurements.

Below 150 m, fluorescence variations are very weak, therefore we concentrate on the surface layers (Fig. 4.14a). For the individual profiles, the maximal fluorescence occurs generally between 20 and 60 m. For the mean profile, the maximum is located between 30 and 50 m, with a mean fluorescence around 0.18.

Close to the surface, oxygen has concentrations around 4.8 ml/l (Fig. 4.14b). This concentration decreases and reaches its minimum between 700 and 800 m. At greater depths, the values encountered are similar to those of the surface.

4.2.2 Property diagrams and water masses

A water mass refers to a body of water with a common formation history, for example, convection caused by surface cooling, having its origin in a particular region of the ocean (e.g., Tomczak, 1999). They are identified by their temperature, salinity, and other properties such as nutrients or oxygen content.

The potential temperature-salinity diagrams ($\theta - S$, Fig. 4.15) are constructed from the CTD and the SeaSoar measurements presented in Section 4.1.2. Both isopycnals and *isospices* (lines of equal *spiciness*, Flament, 2002) are represented on the diagrams. Spiciness is an indicator of diffusive stability and permits the distinction between water masses.

Near-surface waters are characterized by a large variability, with temperatures between 16°C and 23°C and salinity between 36.25 and 36.6. The low salinity is attributed to the contribution of upwelled coastal waters. In the main thermocline, the North Atlantic Central Water (NACW) is characterized by a weak scattering; its temperature ranges from 10°C to 16°C.

Below the main thermocline, two water masses are identified, though they are slightly diluted: the Antarctic Intermediate Water (AAIW) and the Mediterranean Water (MW).

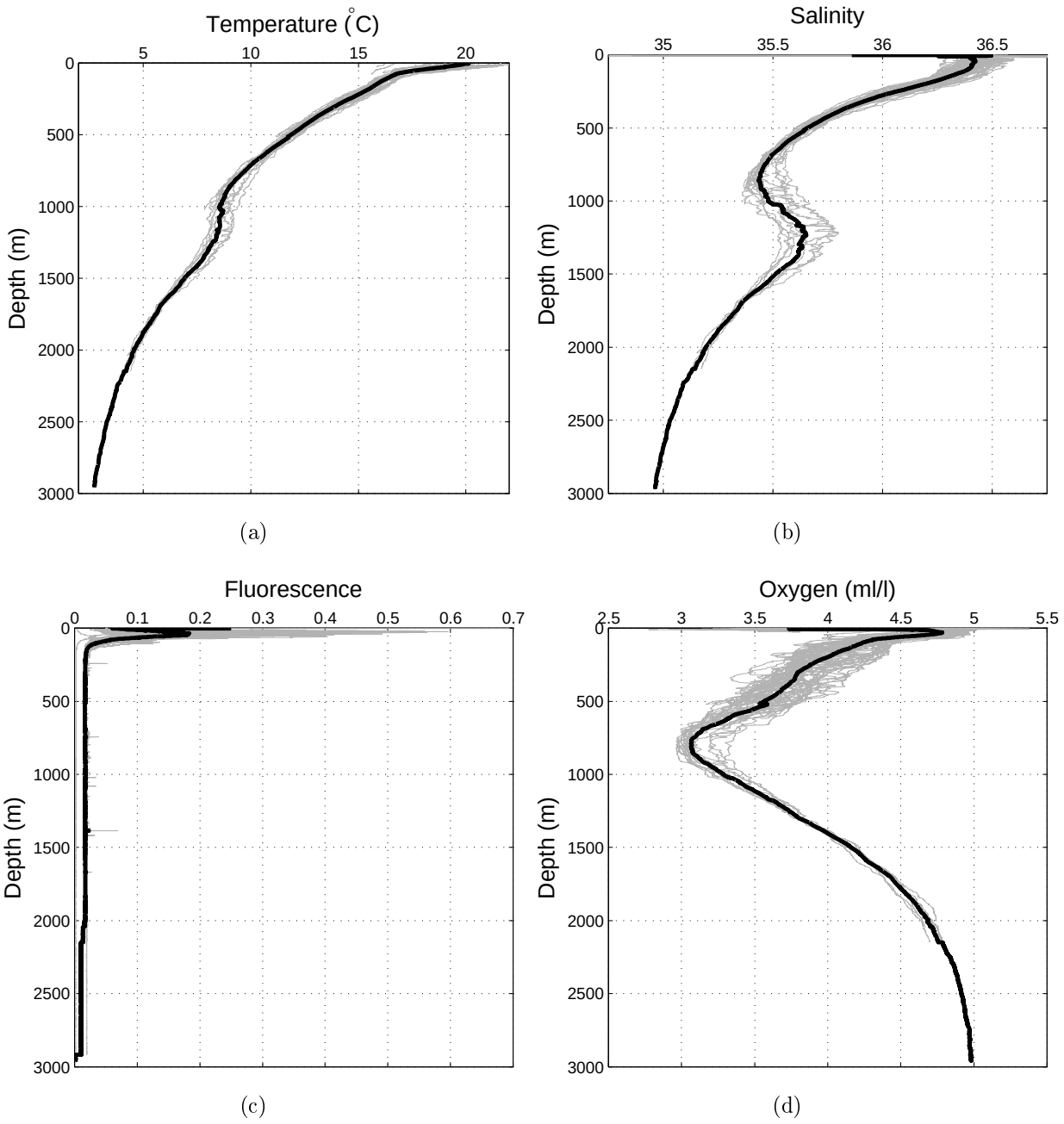

Figure 4.13: Temperature, salinity, fluorescence and oxygen concentrations measured by the CTD. Gray curves indicate individual profiles, while thick black curves show their average. Apart from some fluorescence peaks below 200 m, no obvious outliers are visible.

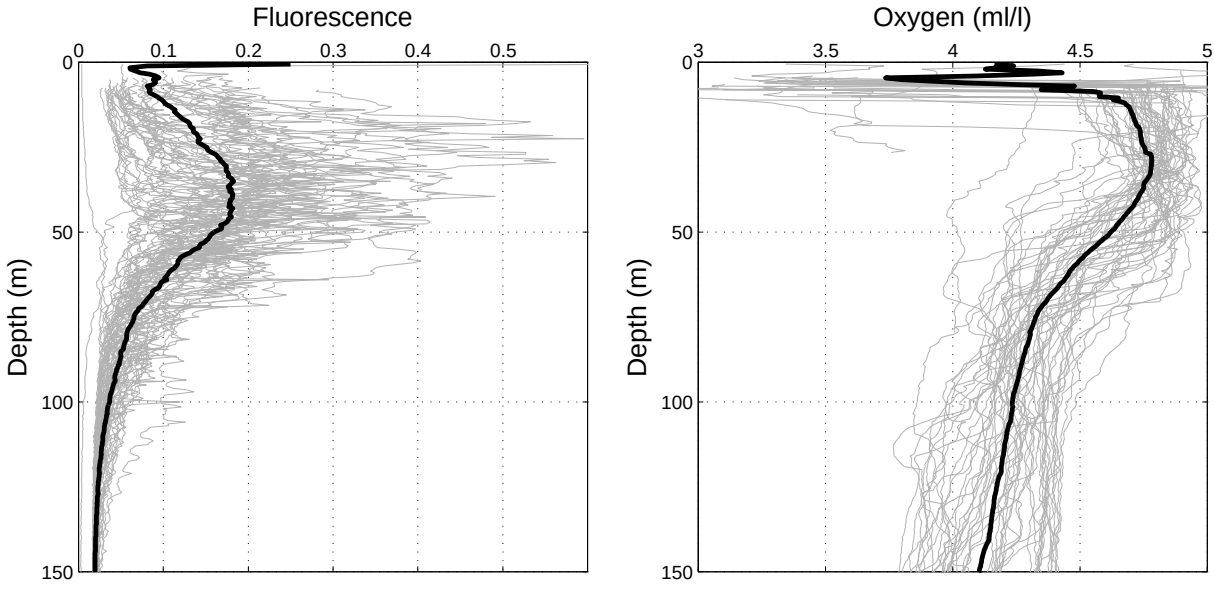

(a) (b)

Figure 4.14: Close-up view of fluorescence (a) and oxygen concentrations (b) in the first 150 m of the water column. The chlorophyll maximum occurs at depths between 20 and 60 m.

The MW is identified by its high temperature and salinity (> 35.5), while the AAIW displays a salinity minimum between 700 and 1000 m.

At greater depths (below 1000 m), the North Atlantic Deep Water (NADW) has a tight $\theta - S$ relation. The minimal temperature and salinity were close to $3°C$ and 35, respectively.

The $\theta - S$ diagram presented here is similar to Fig. 1.20 presented in the first chapter, except that here the signal of MW and AAIW is less marked. This can be explained by the limited depths at which CTD were dropped at some occasions (less than 500 m), or simply to the absence of MW in the sampled region.

The diagram (Fig. 4.16) constructed using the fluorescence and the potential temperature measured by the CTD shows that the fluorescence maxima are observed for temperature between 16 and 20°C. This is in agreement with Head *et al.* (1996), who measured the maximal chlorophyll for temperature between 17 and 19°C off Cape Ghir. The leftmost profile seems suspect, since all the fluorescence values are well below the corresponding values for the other profiles. After identifying this profile, we concluded that it did not influence the results of our interpolations, due to its position.

4.2.3 Horizontal sections

The objective of the horizontal sections is to get an overall representation of the physical structures present in the region of interest, over the duration of the cruise. To this end, all the Seasoar and CTD data are used. Data are vertically interpolated on a set of standard depths (Tab. 4.2). The method used for the analysis is Diva, extensively described in Chapter 2.

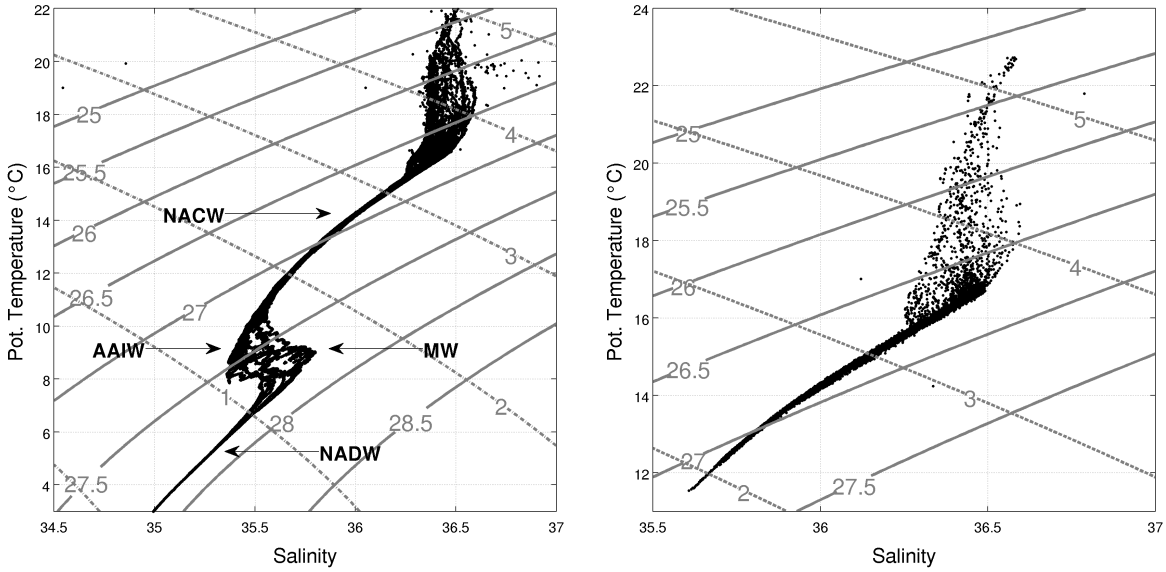

Figure 4.15: $\theta - S$ diagram based on the CTD (left) and SeaSoar measurements (right). Gray plain lines indicate isopycnals, while gray dashed lines indicate isospices.

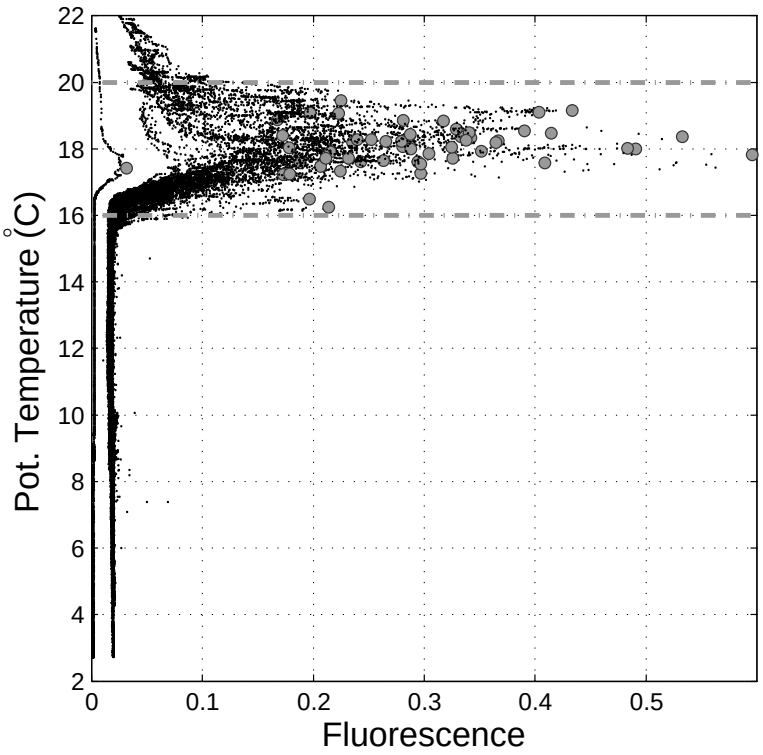

Figure 4.16: Fluorescence-potential temperature diagram based on the CTD measurements. Grey dots indicate the fluorescence maximum for each profile.

Table 4.2: Depth levels selected for the horizontal analysis.

Layer no.	1	2	3	4	5	6	7	8	9	10	11
Depth (m)	5	10	15	20	25	50	75	100	150	200	250
Layer no.	12	13	14	15	16	17	18	19	20	21	22
Depth (m)	300	400	500	750	1000	1250	1500	1750	2000	2500	3000

Choice of the parameters

As the number of data is not large enough to infer good estimates of the parameters with the methods described in Chapter 2, several tests were carried out with different value for correlation length (L) and signal-to-noise ratio (λ). For both parameters, three values were used: a large, an intermediate and a small one, leading to a total of 9 test cases. For L, we tested the values 0.25, 0.75 and 5°, while for λ, we tested 1, 3 and 10.

The three analyzes with the largest L values only display a zonal gradient of temperature, thus these analyzes are not interesting to visualize smaller-scale features, namely the coastal upwelling and the filament. The choice of a relatively low signal-to-noise ratio is imposed by the conditions of the cruise: all the data were collected for a 3-week span, thus the representativity error is as important as in climatology constructions (Section 2.3.2). The final choice is $L = 0.75$ and $\lambda = 3$.

Results

Analyzed fields are produced for temperature, salinity, oxygen concentration and fluorescence, for all depths of Tab. 4.2. Results for a set of selected depths are described subsequently. Data points are overlaid on the maps, in order to see their coverage and the agreement with the interpolated fields.

Temperature: In the layers close to the surface (5–25 m), both the upwelling and the filament are visible. Between 50 and 100 m, the influence of the filament cool waters is still present, but the upwelled waters are not visible in the northeast part of the domain. This can be simply due to a lack of data in that zone: where no data are available, the analyze tends to a reference field, which is, in this case, the linear regression of the data. From 150 to 400 m, a structure of relatively warm water, centered at 31°N and close to the coast, is observed. The different maps confirmed that this structure is not an artifact of the interpolation, as several data points present this characteristic of warmer water. Further analyzes are necessary to identify its origin.

Salinity: Overall, the salinity maps display the same structures as temperature. The upwelling (cool waters) is associated with lower salinity. This is explained by the decrease of salinity with depth observed in the area (e.g., Section 4.1.2). Again, a small structure located at 31°N is observed between 150 and 400 m, this time characterized by a positive anomaly of salinity.

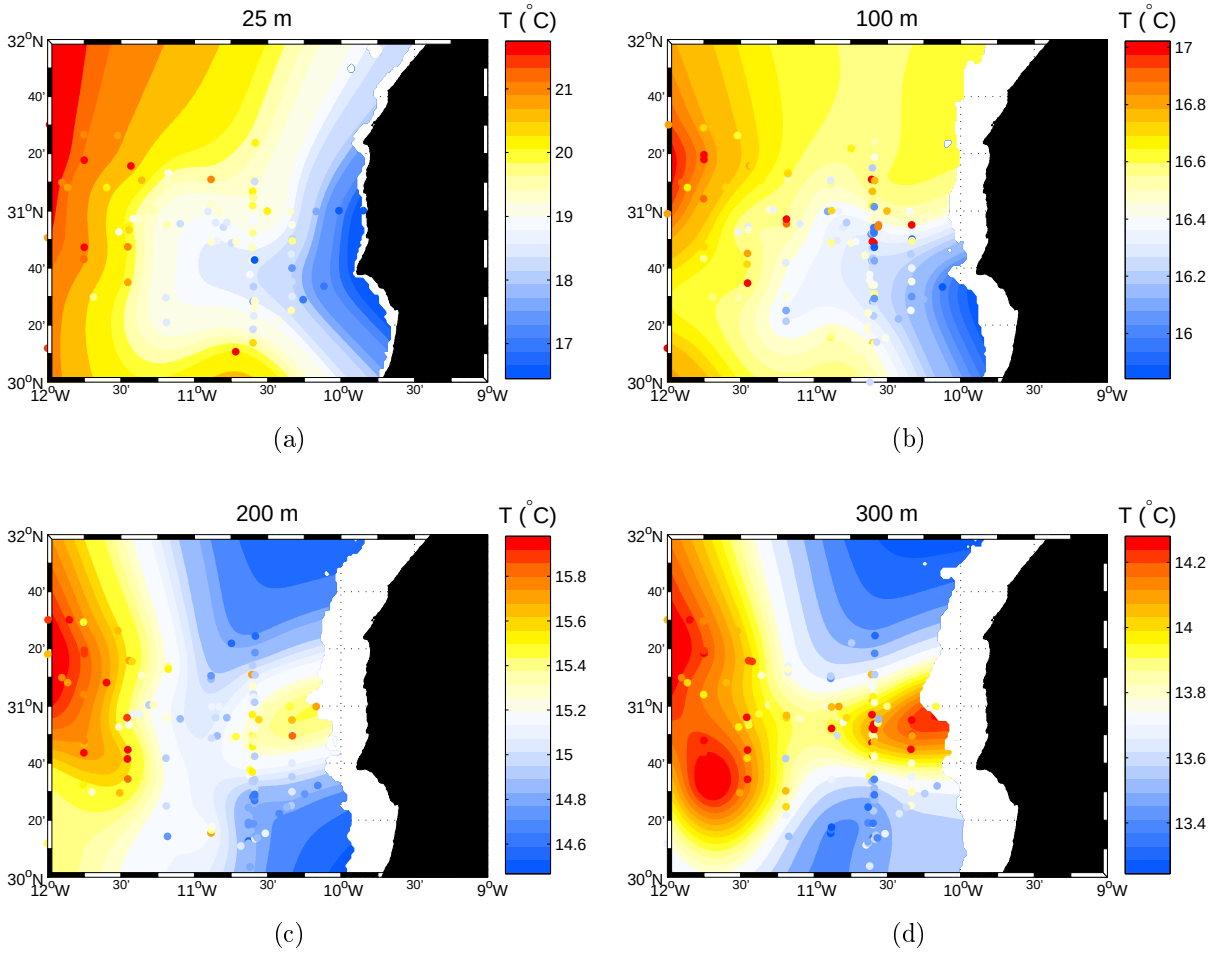

Figure 4.17: Horizontal analyzes of temperature using the combined data set (CTD and SeaSoar) at 25 m (a) 100 m (b), 200 m (c) and 300 m (d). The original values of the data points are superimposed on the fields. The offshore propagation of cool water (25 and 100 m) is interpreted as the signal of a filament, while the warm core is attributed to a subsurface anticyclonic eddy.

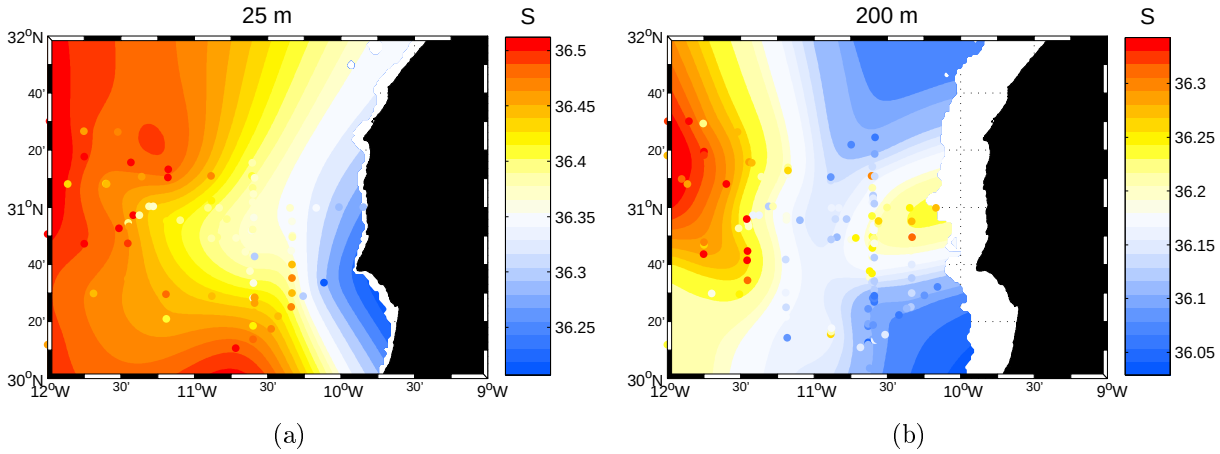

Figure 4.18: Horizontal analyzes of salinity using the combined data set (CTD and SeaSoar) at 25 m and 200 m (b). The original values of the data points are superimposed on the fields.

4.2.4 Vertical sections

Vertical section maps are produced using the data obtained during the CTD (Section 4.1.1) or the SeaSoar transects (Section 4.1.2). The difficulty of such analysis is the difference between vertical (H) and horizontal scales L. Contrary to the horizontal case, the assumption of anisotropy cannot be formulated. An artificial transformation has to be applied to the vertical coordinates in order to take into account the difference between horizontal and vertical scales.

The value of L is the characteristic length of the processes that are surveyed, typically, a few kilometers. It may also be estimated as the mean distance between two consecutive profiles. H is much smaller, since the vertical variability is generally higher. The analysis parameters are chosen for taking into account these specificities and several sensitivity tests were performed prior to the production of the maps presented later.

SeaSoar

The tracks used for these analyzes are those of Fig. 4.7. For each track, temperature, salinity and fluorescence are available. As stated before, the fluorescence sensor had a problem of calibration in the tracks 1 to 7, hence the corresponding gridded fields are not discussed here. Figure 4.19 shows temperature fields for tracks 1-9.

Tracks 1–3: at the north end of the track (30.9-31.5°N), we observe warm water near the surface ($T \simeq 23$°C) and a descent of the isotherms in tracks 1 and 2. This may be the signal of an anticyclonic eddy. Numerical model results suggest that such an eddy is present north of the filament.

Tracks 4–7: in these tracks, the filament becomes progressively more visible: the rise of the isotherms towards the surface indicates the front between cool filament water and open ocean water. Another interesting feature is the descent of the isotherms that happens between 200 and 400 m, particularly visible in tracks 5, 6 and 7. Its position is just a few kilometers north of the filament, hence it is reasonable to think that the two structures are related. Hagen (2001) suggested that the poleward flowing undercurrent may have an influence on the generation or maintenance of the filament. The isotherm deformation is the vertical signal of the warm water pool observed in the horizontal sections (Fig. 4.17). The salinity analysis for track 7 (Fig. 4.20a) also displays a deformation of the isohalines at the same location (30.8°N).

Tracks 8–9: during these sections, rough sea conditions impeded the ship from having a sufficient velocity. For this reason the SeaSoar vehicle was not able to go sufficiently close to the surface and the results in this zone have to be considered with caution. The near-surface signature of the filament is not identifiable as in the previous tracks. Between 200 and 350 m, the descent of the isotherms is again visible, between 30.6°N and 30.8°N in both tracks. In track 9, a rise of the isotherm, corresponding to the filament, is located around 30.4°N.

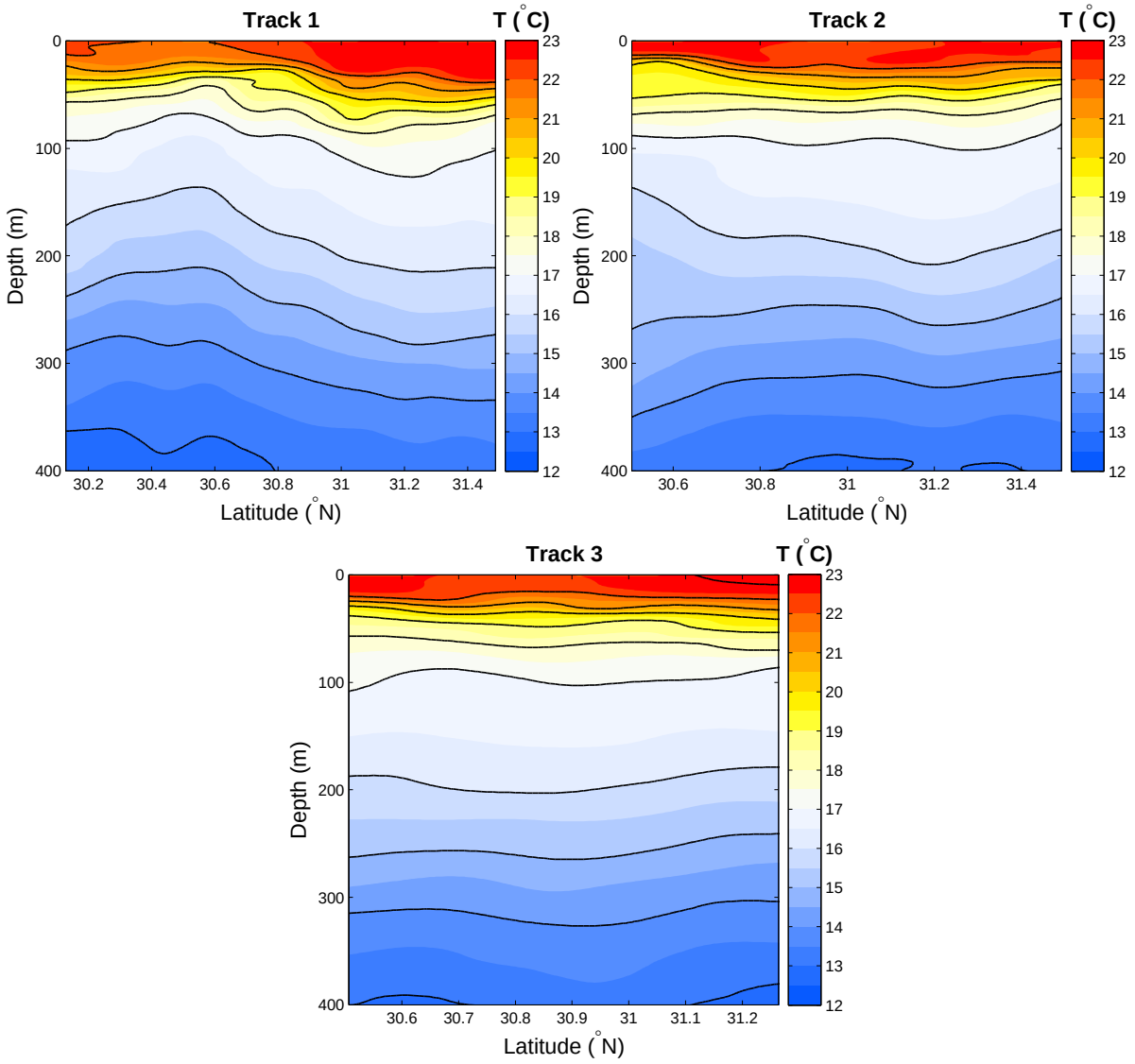

Figure 4.19: Vertical analyzes of SeaSoar temperature for tracks 1-3. The black lines are distant of 1°C.

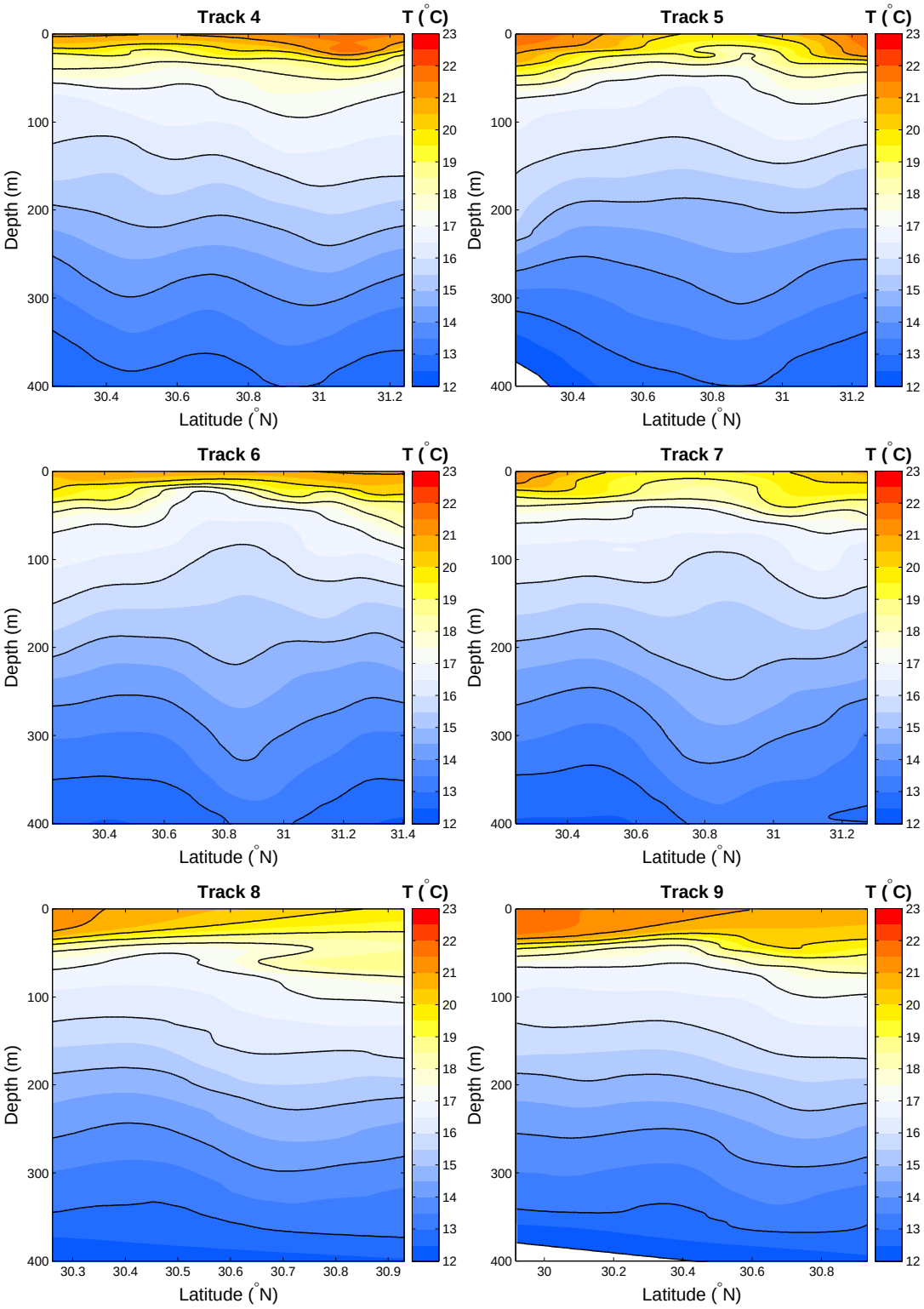

Figure 4.19: continued: tracks 4-9

For these tracks, the fluorescence sensor was fixed by the technician and worked properly. The corresponding analysis (Fig. 4.21) in the upper layers show that the highest values appear at a depth of 40 m, over a large range of latitudes. The problem, mentioned previously, is the lack of measurements between 50 m and the surface, making difficult the interpolation in this zone. For track 9, the situation is slightly better. The maximal fluorescence is found at 30.4°N at 40 m depth.

These vertical analyzes of SeaSoar data provides relevant characteristics of the physical structure in the close to the filament. Unfortunately, because of the lack of simultaneous temperature and fluorescence measurements, physical and biological processes cannot be related.

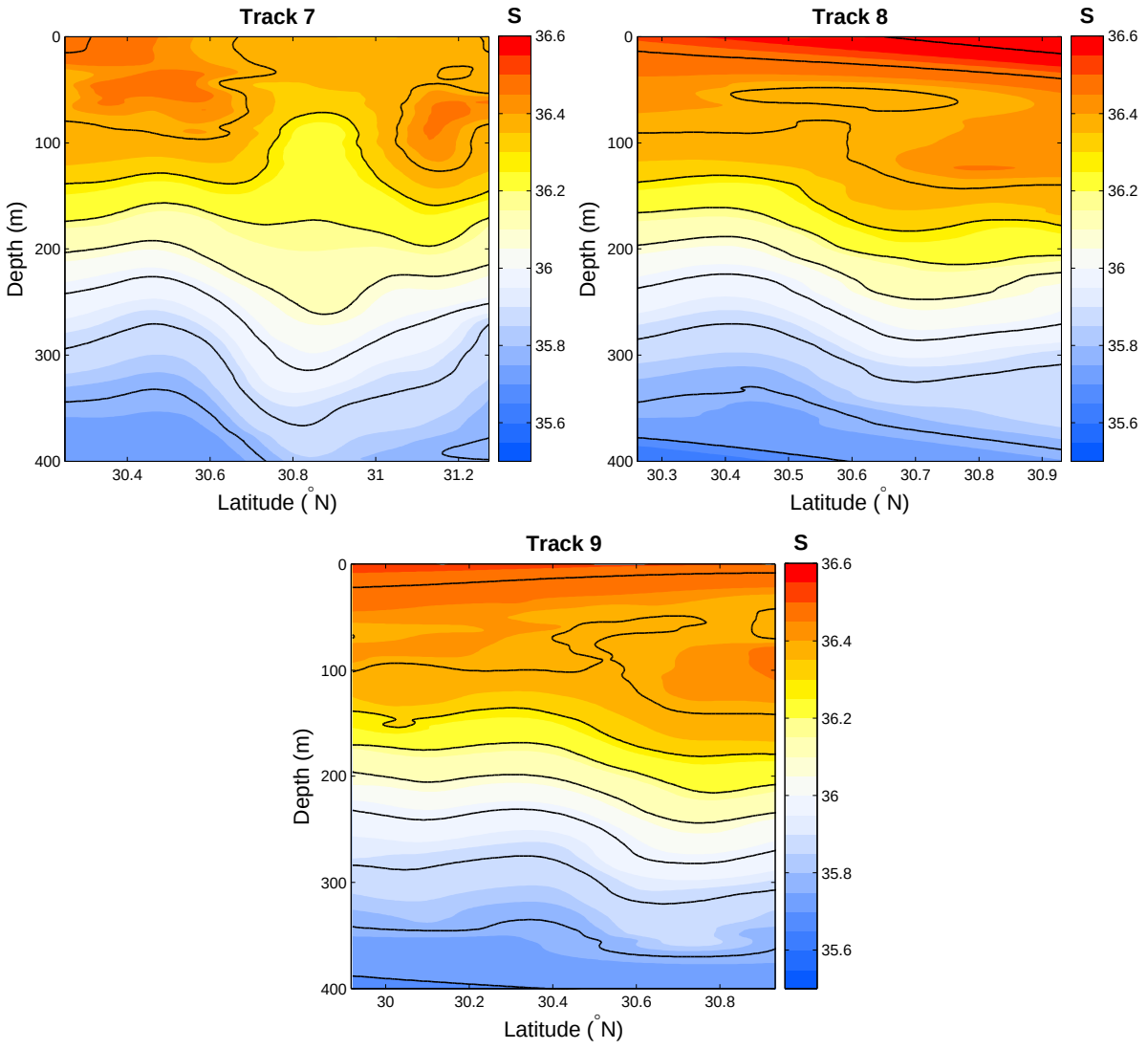

Figure 4.20: Vertical analyzes of SeaSoar salinity for tracks 7-9. The black lines draw salinity increments of 0.1.

CTD

After processing the SeaSoar data, we focus on the CTD data obtained through the transect at 10°36'W (Fig. 4.3). The corresponding data were presented in Fig. 4.4. Although

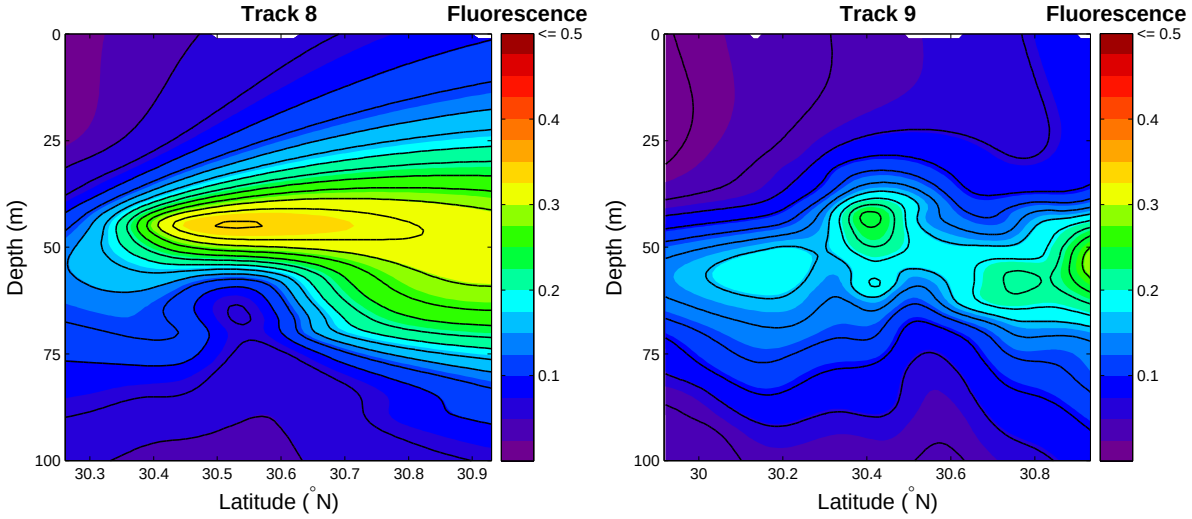

Figure 4.21: Vertical analysis of SeaSoar fluorescence for tracks 8-9.

the spatial resolution is lower than with the SeaSoar, CTD will provide better quality fluorescence measurements and ensure values near the surface, almost independently on the sea conditions (contrary to SeaSoar).

The localization of the filament is easy with the help of Fig. 4.22: the low surface temperatures visible between T8 and T10 are the signal of upwelled waters exported offshore. Surface temperature vary from slightly more than 20°C at stations T2-T4 and T12-T13, to 18°C in the core of the filament. In the same area, Pelegrí *et al.* (2005) measured a temperature of 17.6°C within the filament. Yet, the salinity map (Fig. 4.22b) does not allow for an easy identification of the filament.

As the studied processes are located near the surface, the analyzes are focused on the upper layers: from 0 to 400 m for temperature, salinity and oxygen concentration, and from 0 to 100 m for fluorescence (Fig. 4.23). Since the CTD measurements have a lower resolution than the SeaSoar, it is not expected to discover new structures, but rather to confirm the observations made before. In particular, the descent of the isotherms (Fig. 4.23a) and isohalines (Fig. 4.23b) north of the filament appears clearly between T5 and T7.

The biological repercussions of the filament are examined by mean of fluorescence of oxygen concentration provided by the CTD. Highest surface fluorescence occurs between T7 and T9, just north of the core of the filament, possibly in the frontal zone between filament fresh upwelled waters and open ocean warmer waters. Below the surface, a maximum of fluorescence takes place at 25 m and corresponds to the location of the filament core. For the other stations, the deep fluorescence maximum (DFM) is approximatively centered at 50 m. The DFM is a well-known feature in the Canary Island waters; Tett *et al.* (2002) showed that the DFM had increasingly shallowed values when approaching the coast.

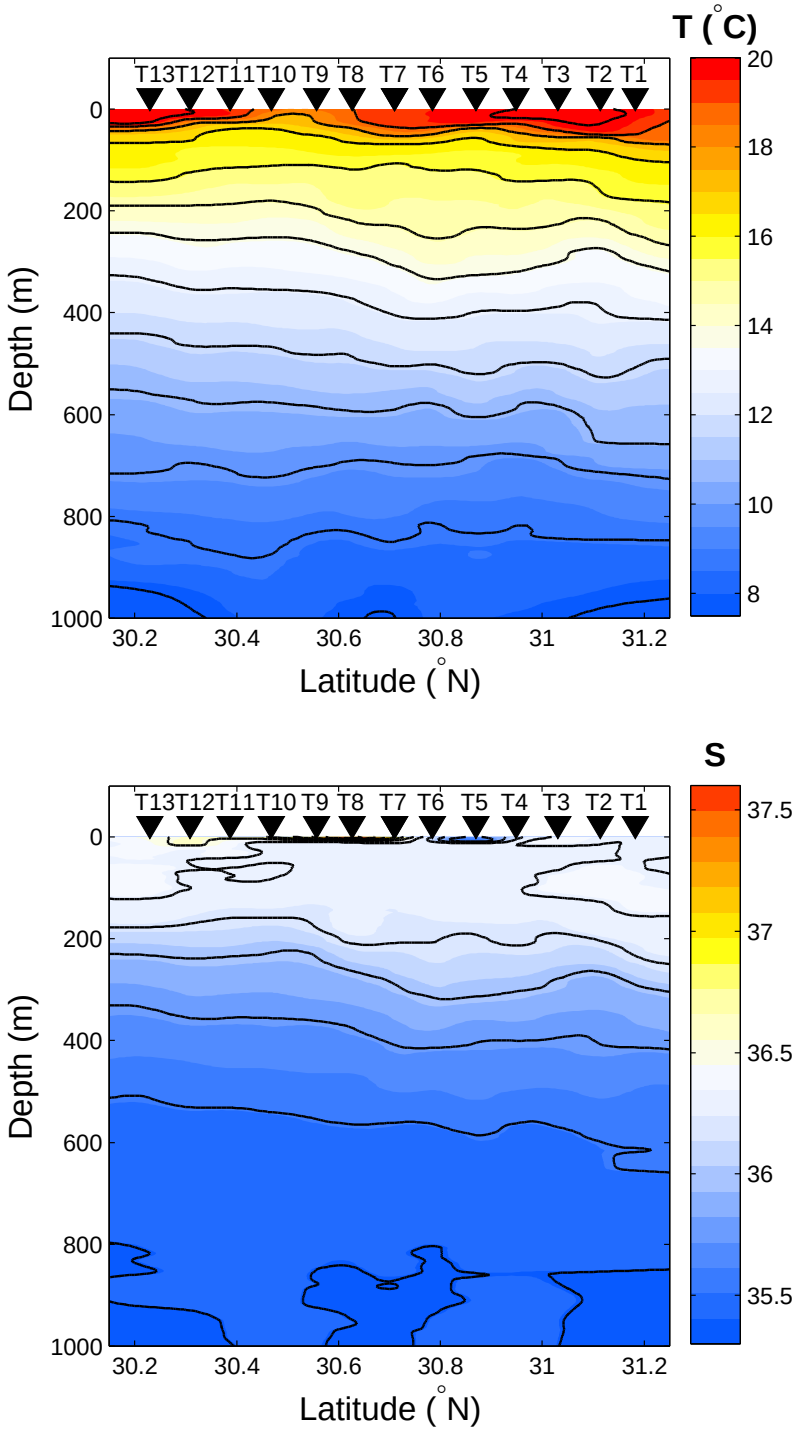

Figure 4.22: Vertical analyzes of the CTD transect data at 10°36'W for temperature and salinity between surface and 1000 m. Triangles indicate cast positions. The black lines draw temperature increments of 1°C.

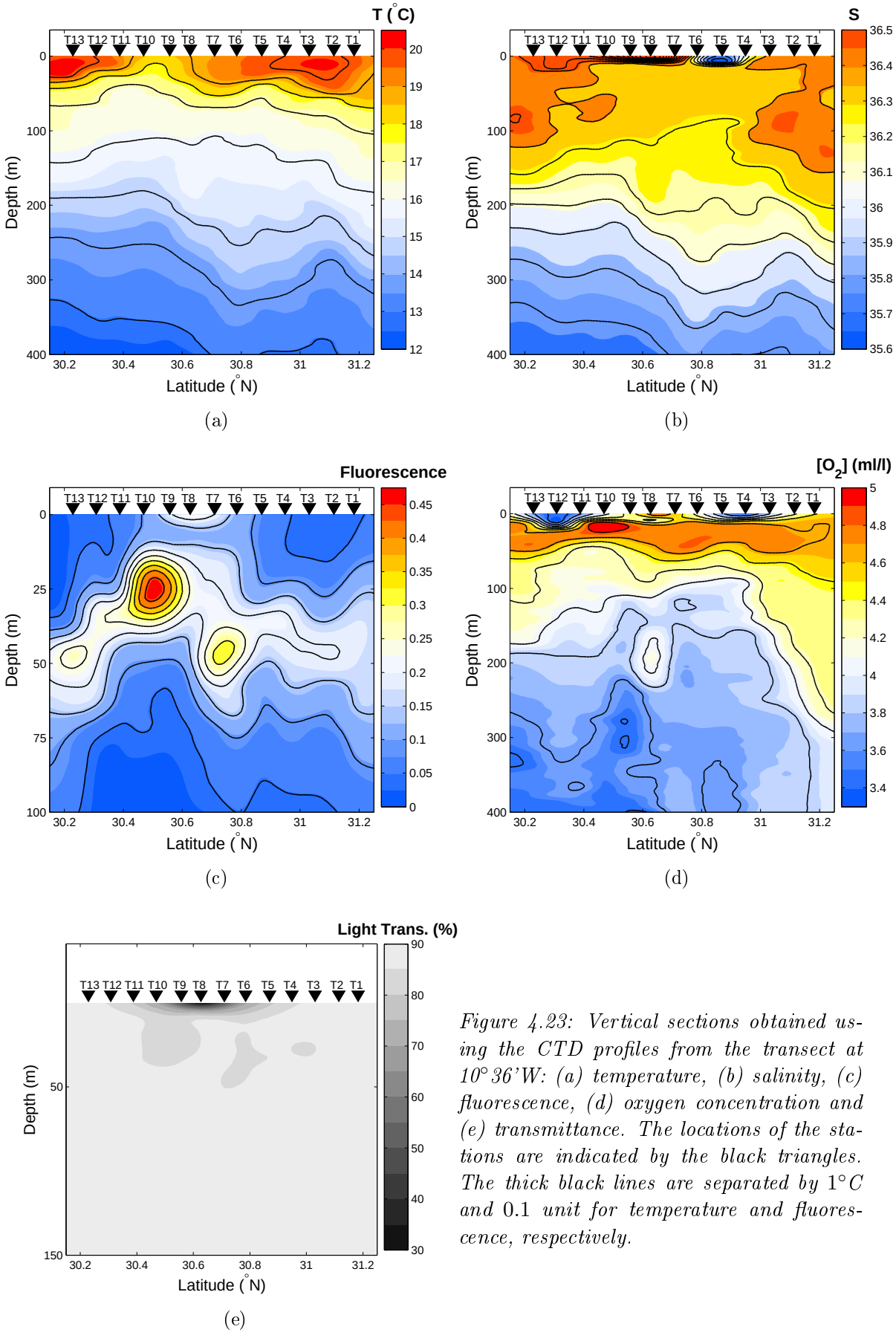

Figure 4.23: Vertical sections obtained using the CTD profiles from the transect at 10° 36'W: (a) temperature, (b) salinity, (c) fluorescence, (d) oxygen concentration and (e) transmittance. The locations of the stations are indicated by the black triangles. The thick black lines are separated by 1°C and 0.1 unit for temperature and fluorescence, respectively.

4.2.5 ADCP velocities

These results are preliminary and are mainly aimed to show the correspondence between temperature/salinity and velocity features, as well as to confirm the order of magnitude of the velocities obtained with the numerical model.

Velocities along the CTD transect

The zonal component of the velocity (Fig. 4.24) is mainly westward, with the exceptions of:

- the surface flow north of 30.8°N,
- a subsurface flow, centered at 400 m, at a latitude of 30.8°N,
- the flow in the northern part of the transect, for depths between 0 and 400 m.

As previously stated, the 75 kHz ADCP provides velocities at higher depths than the 150 kHz ADCP. However, we also noted that the 75 kHz ADCP does not give measurements in the near-surface layer (typically between 0 and 50 m). This is why we will use the 150 kHz measurements for layers between 0 and 100 m and 75 kHz measurements for deeper layers.

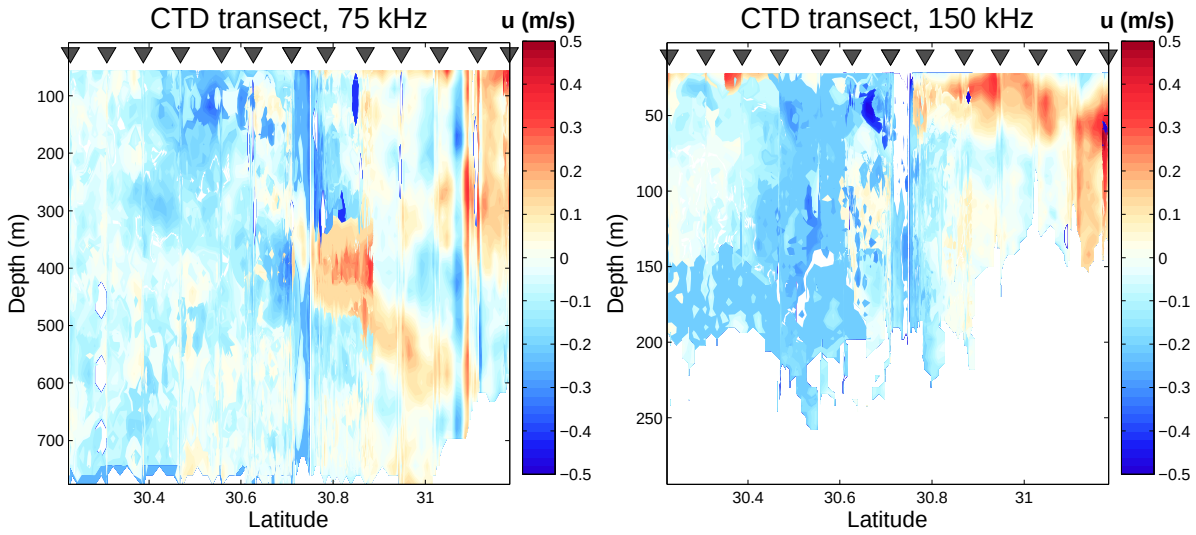

Figure 4.24: Zonal component of the velocity along the CTD transect for the 75 kHz (left) and 150 kHz (right) ADCPs. Positive values indicate eastward velocities. Triangles indicate the CTD positions.

We now concentrate on individual depth layers. Velocities are vertically averaged over given layers. Then, for visualization purpose, they are spatially interpolated (linear interpolation on horizontal planes) on a 0.01° regular grid at a longitude of 10°36'W, which is the mean longitude of the transect.

In the surface layer (0-25 m, Fig. 4.25a), the maximal velocity (0.55 m s^{-1}) occurs at a latitude around 30°40'N, where the current is mostly westward. This value of velocity is in agreement with the measurements made during previous cruises (e.g. Pelegrí *et al.*, 2005) and the model results (Figs. 3.7a-b). In the southern part of the transect (south of 30°30'N), the flow if directed toward the coast, with a velocity exceeding 0.35 m s^{-1}. A similar flow pattern was also present in the model results (Fig. 3.7), where an anticyclonic circulation is visible south of the filament.

In the layer 25-50 m (Fig. 4.25b), we observe a strong shear at 30°45'N. We believe that this shears corresponds to the front on the northern flank of the filament. In the 300-350 m layers (Fig. 4.25c), currents are weaker, as expected. In the southern part of the transect, we observe northeastward velocities, while there is a shear at station T5. Going back to Figs. 4.23a-b, we notice that the signal of the anticyclonic eddy is centered between stations T5 and T6. Hence the observation of this shear is compatible with the existence of the eddy.

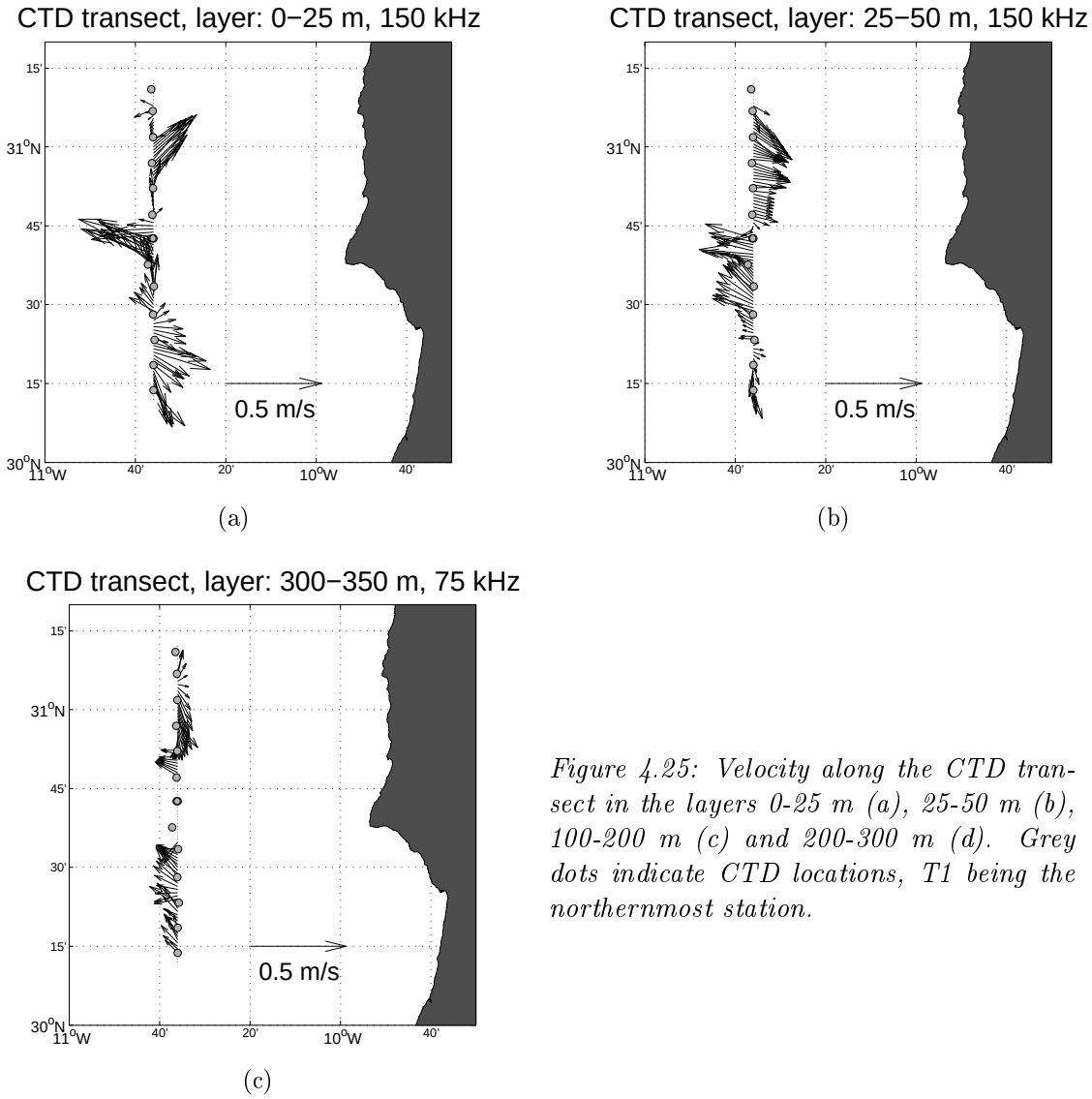

Figure 4.25: Velocity along the CTD transect in the layers 0-25 m (a), 25-50 m (b), 100-200 m (c) and 200-300 m (d). Grey dots indicate CTD locations, T1 being the northernmost station.

Velocity along the SeaSoar tracks

The next figures display the velocities measured along the first seven SeaSoar tracks. Unrealistically high velocities were removed from the data (southern part of track 3).

Tracks 1-6: in the layer 0-50 m (Fig. 4.26a), we observe the highest velocities in tracks 1 and 4. The velocities are mainly directed to the west. Steep changes of velocity direction occur in most of the tracks, especially tracks 2 and 3. We attribute them to mesoscale eddies. In the 100-200 m layer (Fig. 4.26b), velocities have decreased, especially in the westernmost tracks. In the layer 300-350 m layer (Fig. 4.26c), we looked for the signal of the descent of the isotherms and the resulting anticyclonic circulation in the track 6, as mentioned in Section 4.2.4. We observe a change in the velocity direction approximatively at 31°50'N, though velocities are relatively low in this area.

Track 7: the strong westward velocities between 30°20'N and 30°40'N (Fig. 4.27a) may correspond to the location of the filament core. In the 300-350 m layer, velocities are oriented northwestward in most of the track, except in its northern part. There, similarly to track 6, the vectors tend to be directed toward the coast, confirming that the existence of an anticyclonic eddy is plausible.

Tracks 8: due to rough sea conditions, this track was shorter than the previous ones. The southwestward flow (Fig. 4.28a) may be an indication of the filament, though the absence of near-surface measurements (Fig. 4.8) does not allow us to confirm it. The 300-350 m layer (Fig. 4.28a) does not yield any particular feature.

Tracks 9: between 0 and 50 m, the velocities are predominantly directed westward, with an increased intensity north of 30°20'N (Fig. 4.29a). The vectors in the 300-350 m layer exhibit a counter-flow south of 30°20'N (Fig. 4.29b).

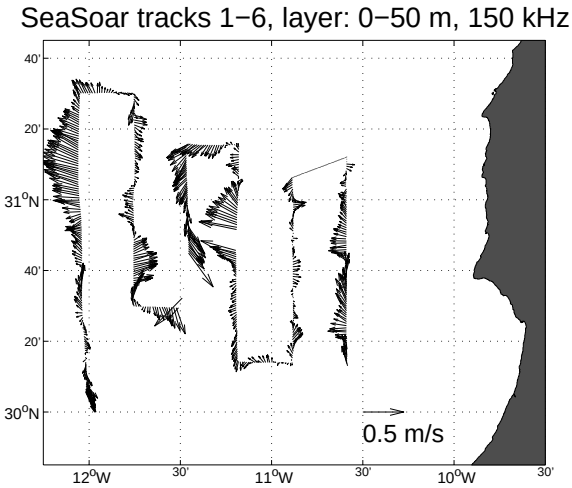

(a)

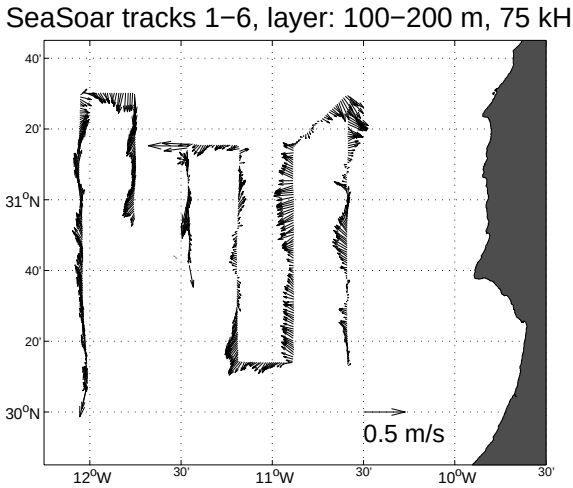

(b)

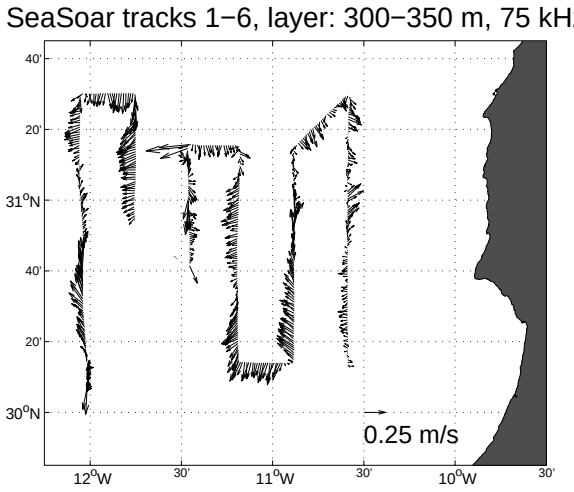

(c)

Figure 4.26: Velocity along the SeaSoar tracks 1-6 in the layers 0-50 m (a), 100-200 m (b) and 300-350 m (c).

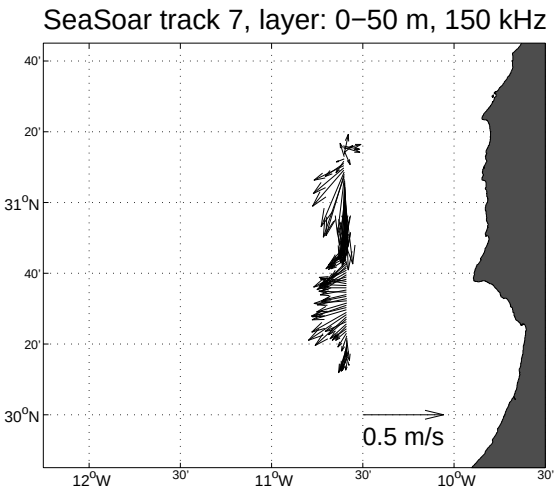

(a)

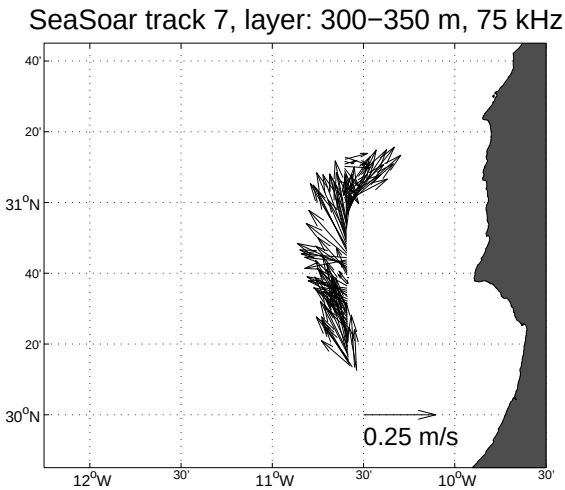

(b)

Figure 4.27: Velocity along the SeaSoar track 7 in the layers 0-50 m (a) and 300-350 m (b).

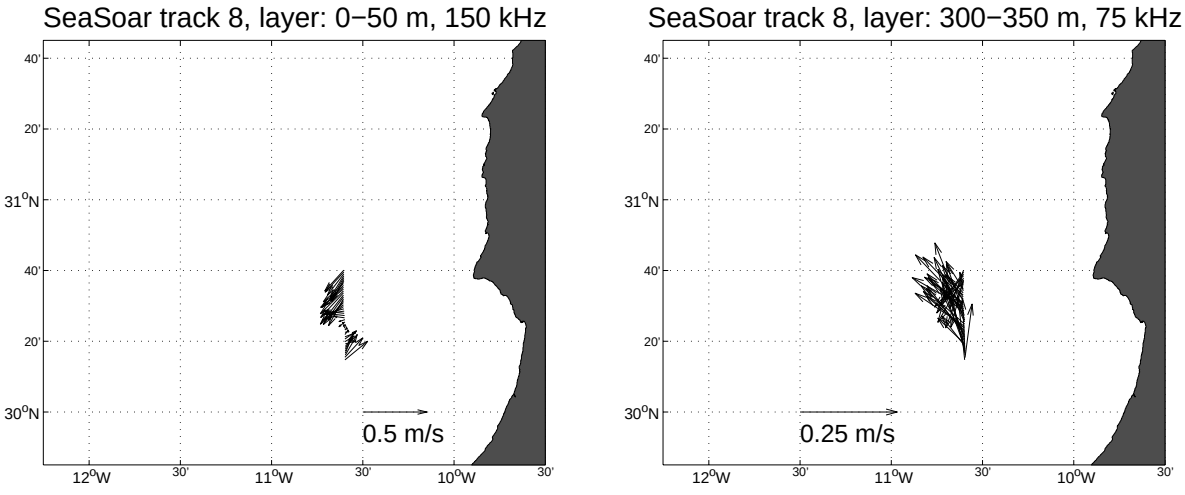

(a) (b)

Figure 4.28: Velocity along the SeaSoar track 8 in the layers 0-50 m (a) and 300-350 m (b).

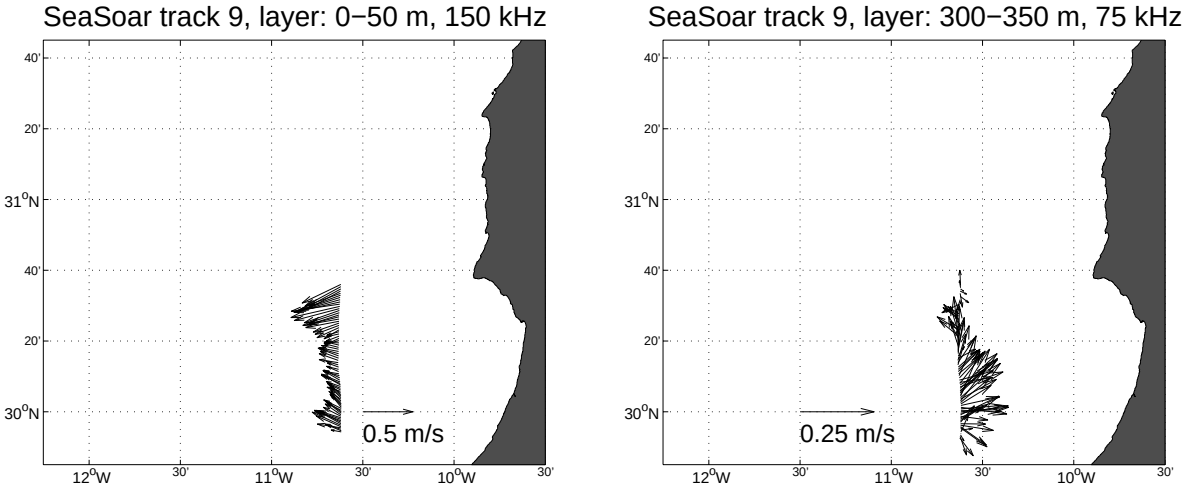

(a) (b)

Figure 4.29: Velocity along the SeaSoar track 9 in the layers 0-50 m (a) and 300-350 m (b).

4.2.6 Drifter trajectories

Albeit launched at very close locations, near-surface drifters followed relatively different paths. The temporal availability of the positions allows one to display the inertial oscillations, characterized with a theoretical period of 23h56', if we consider a mean latitude of 30°N.

After a 10–15 day-period of weak motions, drifters no. 95854, 95855 and 95867 started a northwestward motion, possibly entrained by the filament. Between 31°N and 31°30'N, they underwent a cyclonic trajectory with the westernmost position close to 12°W. They followed their course with a southwest direction, towards the passage between Africa and the easternmost Canary Islands. Their estimated median velocity is on the order of 0.35 m/s. The highest velocities occurred in the northern part of the cyclonic turning.

The 300 m-drogue drifter (no. 95864) described a series of cyclonic loops with a rotation period $T \simeq$ 5-6 days and a radius $R \simeq$ 30-40km. The estimated median velocity for this drifter is on the order of 0.15 m/s. Unfortunately, this drifter aimed to find a subsurface anticylonic eddy, instead of a cyclonic one. As these experiments were performed during the very last days of the cruise, it was not possible to make additional tries. The confirmation of this subsurface eddy may be undertaken during forthcoming cruises in the same area.

4.3 Subsurface anticyclonic eddy

Using the previous vertical and horizontal sections, we proposed that the characteristics in the temperature and salinity fields observed between 200 and 400 m deep, north of the filament core, are the representation of a subsurface anticyclonic eddy. Such an eddy, responsible for a downward velocity, would explain the presence of warmer and saltier water in a determined area (e.g., Figs. 4.17c-d and 4.18b).

The mechanism is still to be explained, but similar observations were made during previous cruises in the same area:

- from September 29 to October 3, 1992, on board R/V *Hudson* and *Humboldt* (Hagen *et al.*, 1996),
- from October 5 to 15, 1995, on board R/V *Hespérides* (Pelegrí *et al.*, 2005) and
- from September 27 to October 1, 1997 (Pelegrí *et al.*, 2005).

As this eddy was observed during different years and months, it suggests that it is a recurrent feature, at least during summer-fall. The available historical data collected from the World Ocean Database 2009 (Boyer *et al.*, 2009) in the Cape Ghir region in winter-spring are not sufficient to confirm whether the subsurface eddy is seasonal or not.

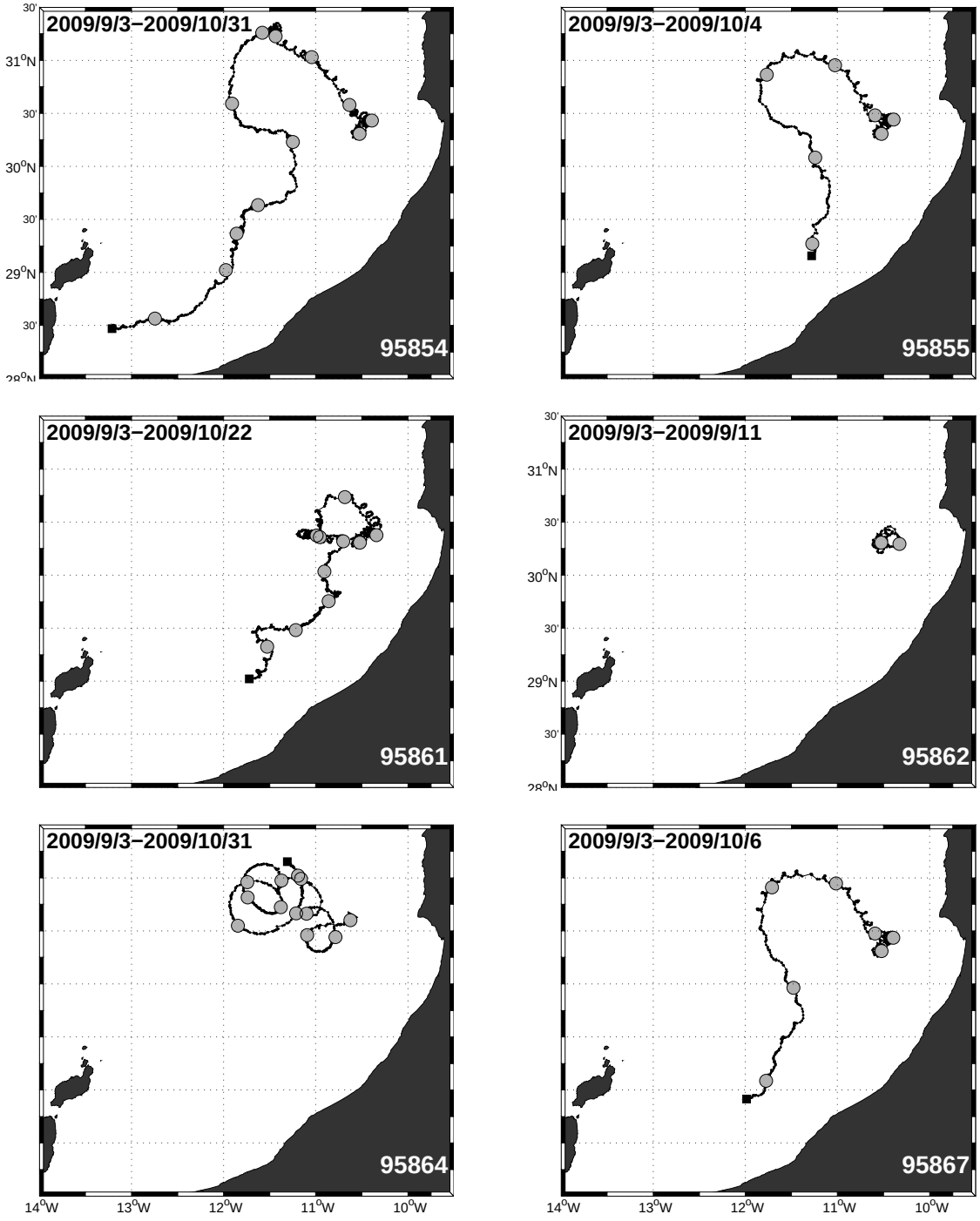

Figure 4.30: Individual trajectories of Argos drifters. Final drifter positions are indicated by black squares. Grey disks are separated by approximatively five days. Start and end dates of activity are indicated in the top-left corners. The drifter no. 95864 had its drogue at 300 m.

4.3.1 Comparison with model results

The objective is not a direct comparison of the model fields with the cruise measurements: this would not make sense, since the model uses climatological forcing (see Chapter 3). It is preferred to make a comparison of the typical features deduced from the in situ measurements: if the model is capable of reproducing such features, then it means it contains the necessary ingredients for the intended purpose, even if the values of the fields are not always similar. Comparison of model results with satellite SST fields was made in Sections 3.2.4 and 3.2.4.

With the help of horizontal and vertical sections extracted from the numerical fields, particular attention is paid to the subsurface anticyclonic eddy and the upwelling undercurrent.

Model horizontal sections

The temperature and relative vorticity are extracted from the model results, at a depth of 300 m (Fig. 4.31). The time when the fields are extracted corresponds to a situation where the filament was well developed in September. The purpose is to be in conditions close to those of the cruise. Between 200 and 400 m deep, the horizontal analyze (Fig. 4.17) showed a pool of warm water close to the coast. In the model, a similar feature is also present, centered at a latitude of 31°15'N. The modeled temperature at 300 m is higher ($\simeq 15.8$°C) than the measured one ($\simeq 14.2$°C), and the position of the warm water area is a few kilometers more to the north. Still, the results are qualitatively in agreement with the observations.

The corresponding vorticity map (Fig. 4.31) underlines the presence of a anticylonic eddy, with vorticity of $0.2 - 0.25f$. Along the coast, a narrow band of warmer water is visible. It is the probable signal of the poleward undercurrent, characteristic of the upwelling. Corresponding to this warm water, a band of negative vorticity is found along the coast. Negative values of vorticity are also compatible with the presence of an undercurrent: velocities tend to decrease when approaching the border, due to the frictional forces. The order magnitude for the vorticity in the undercurrent is similar to that of the anticyclonic eddy.

Model vertical sections

For the examination of the vertical variations of the properties across the filament, two sections are extracted from the model results: a meridional section **AB**, similar to the CTD transect (Fig. 4.3), and a zonal section **CD**, at the same latitude as the monitoring CTD. The tracks where the fields are extracted are overlaid on the model fields in Fig. 4.32.

Zonal section: the upwelling is visible in a confined area (≈ 50 km width) near the coast (Fig. 4.33a). It is recognizable by the up-sloping isotherms. The minimal temperature appears very close to the coast (19°C). The filament lies about 120 km from the shore, with surface values of 21°C. It is thin (≈ 25 km) and shallow (50 m). Dooming of the

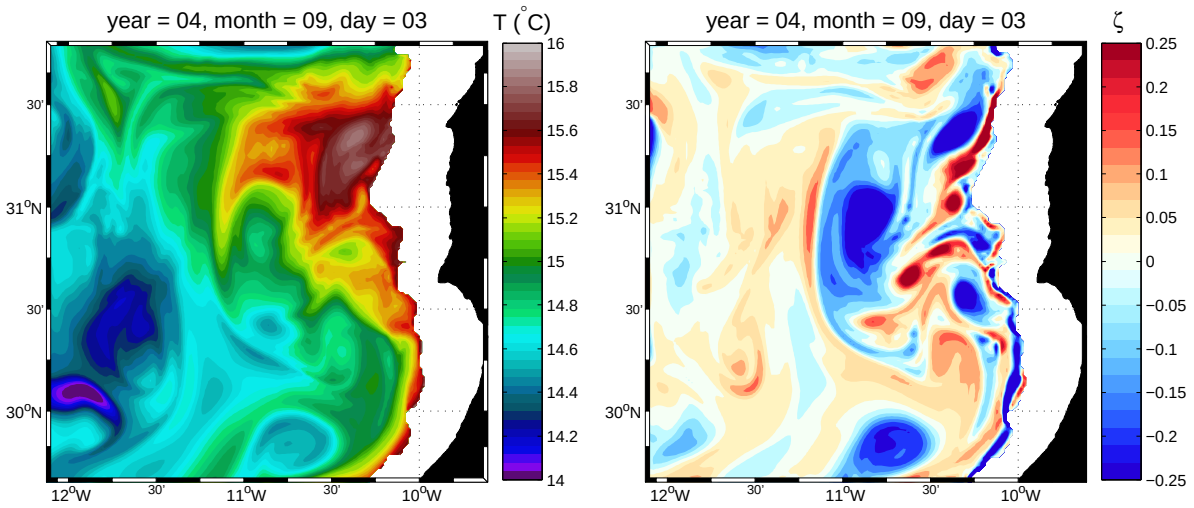

Figure 4.31: Temperature (left) and relative vorticity normalized by f (right) at 300 m on September 3, showing the signal of an anticyclonic eddy centered at 31° N 11° W.

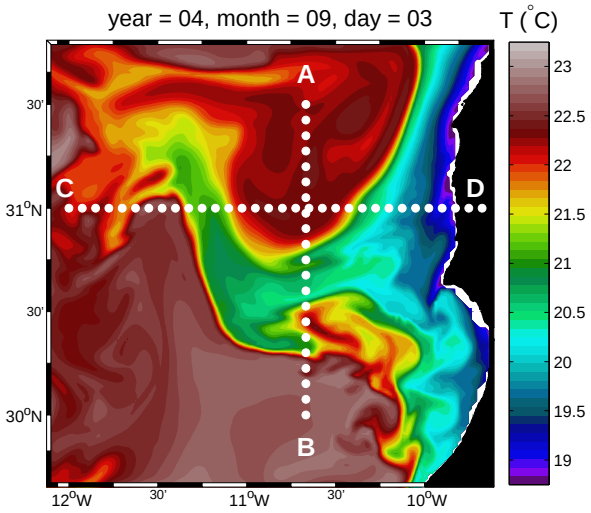

Figure 4.32: Locations of the vertical sections extracted from the 3-dimensional fields. The temperature field corresponds to the surface on September 3rd.

isotherms take place at around 200 m depth at two locations: below the filament and at 50 km from the coast.

The meridional velocity (Fig. 4.33b) reaches values up to 0.3 m/s, in the core of the filament, after its northward turn. This is compatible with the values observed during previous cruises, where values exceeding 0.5 m/s were reported. The maximal southward velocities lie in the first 100 km off the coast, near the surface. A weak poleward undercurrent ($v < 0.05$ m/s) appears below 75 m. The anticyclonic circulation of the filament is visible at distances between 50 and 150 km.

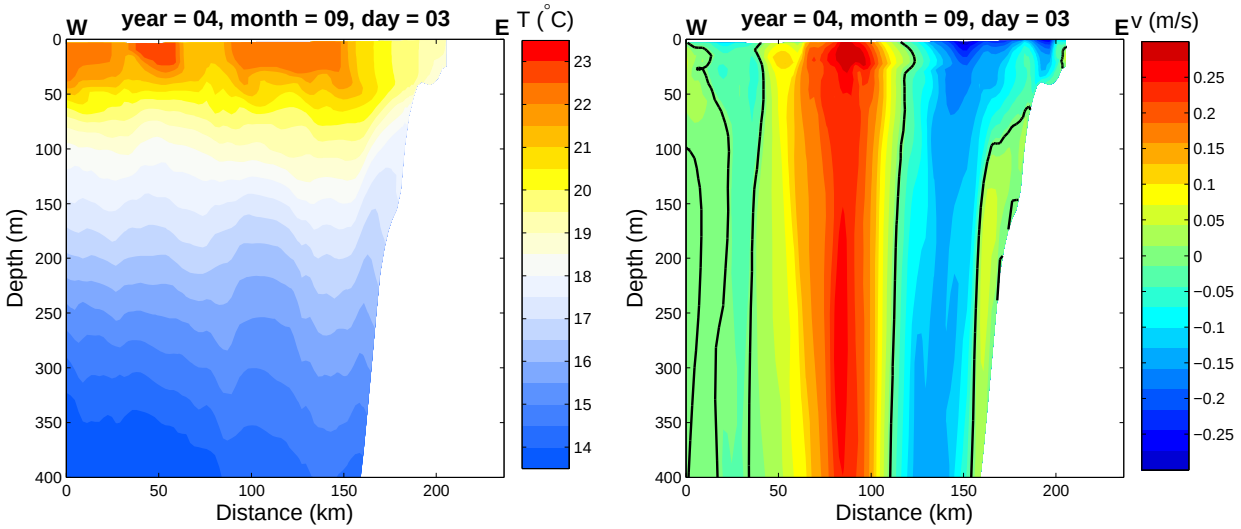

(a) (b)

Figure 4.33: Zonal sections at 31°N for temperature (a) and meridional velocity (b) on September 3. Positive values denote northward velocities. Black contours indicate null velocity.

Meridional section: it is extracted at less than 100 km from the coast. Temperature allows the identification of three branches of the filament (Fig. 4.34a): the main one, centered at 75 km from the beginning of the section, and two secondary ones, located north and south of the core. This was already visible in Fig. 4.32: it shows that the filament is a complex structure, one which frontal instabilities tend to develop. The signal of an anticyclonic eddy appears from 200 m to 400 m, although it is clearer at depths. The maximal offshore velocities are reached near surface, within the filament and to its north (Fig. 4.34b). It is worth noting that the intense current associated with the filament is relatively deep, if compared with the temperature characteristics.

4.3.2 Generation mechanism for the anticyclonic eddy

The model results agree well with the observations, in terms of processes. However, it is not obvious to detect the subsurface anticyclonic eddy using vertical sections. The region is rich in eddies and other small-scale processes, hence a lot of variability is present around the filament. The horizontal sections at 300 m (Fig. 4.31) clearly display the anticylonic eddy and the corresponding warmer water.

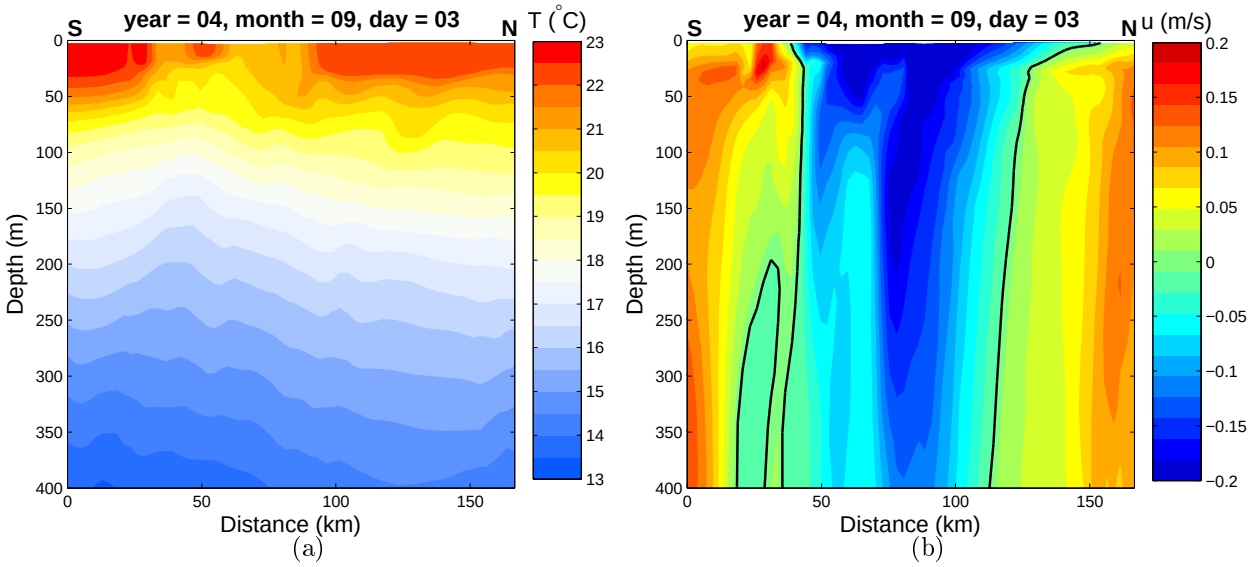

Figure 4.34: Meridional sections at 10°40'W for temperature (a) and zonal velocity (b) on September 3. Positive values denote eastward velocities. Black contours indicate null velocity.

The sequence of vorticity maps at 300 m (not shown) makes us believe that the anti-cyclonic eddies are generated where the coastline changes its orientation, approximatively at the 31°N, a few kilometers north of Cape Ghir. The undercurrent, visible as a band of negative vorticity, detaches from the shore and generate the eddy. A similar mechanism was proposed by Peliz *et al.* (2002) for the Iberian Peninsula and Molemaker *et al.* (2010) for the California Current system. As both systems bear common characteristics (as eastern-boundary upwelling systems), this generation mechanism may also be valid for our area of study.

In order to confirm it with in situ measurements, one or several drifters with the drogue between 200 and 400 m could be launched during futures cruises taking place close to Cape Ghir. During CAIBEX cruise, only one such drifter has been deployed, but the choice of the release position was not optimal due to the lack of SeaSoar measurements near the surface.

4.4 Remote-sensing data analysis

Although satellite SST and chlorophyll concentrations were acquired in near-real time during the cruise, these data were not always available or were sometimes affected by clouds. Hence they were not helpful to take decisions concerning the sampling strategy. In this section, we use satellite images of SST and wind intensity to confirm our in situ observations a posteriori.

4.4.1 Data sources and processing

SST

Along-track (L2P products) sea-surface temperature (SST) is measured by the Advanced Very High Resolution Radiometer (AVHRR). The L2P data files are downloaded from the U.S. National Oceanographic Data Center at ftp://data.nodc.noaa.gov/pub/data.nodc/ghrsst/L2P/. The selected products are the GHRSST-PP L2P Near Atlantic Regional (NAR) 17 and 18, originally produced by the ESA Medspiration project (www.medspiration.org/). L4 products (regional, cloud-free maps) do not serve our purpose, since the technique applied to fill the holes creates artifacts in the SST field.

The maps presented hereinafter are produced by selecting the passes (ascending and descending) of satellites NOAA 17 and NOAA 18 with the best data coverage (Tab. 4.3).

Table 4.3: Satellites and passes selected for the SST maps.

Date	Satellite	Pass
17-08-2009	NOAA 18	ascending
18-08-2009	NOAA 18	ascending
20-08-2009	NOAA 17	descending
23-08-2009	NOAA 17	descending
26-08-2009	NOAA 17	descending
02-09-2009	NOAA 18	ascending
03-09-2009	NOAA 18	ascending

Wind speed

Along-track sea wind speed is measured by the Quick Scatterometer (QuikSCAT, http://winds.jpl.nasa.gov/missions/quikscat/index.cfm) satellite. Data files are acquired from the Physical Oceanography Distributed Active Archive Center (PODAAC) of the Jet Propulsion Laboratory (JPL) at ftp://podaac.jpl.nasa.gov/pub/ocean_wind/quikscat/L2B12/data/.

Each daily map is produced by combining the fourteen swaths of the satellite.

4.4.2 SST and wind measurements

SeaSoar tracks

The trajectories were presented in Section 4.1.2 and the analysis in Section 4.2.4. The first six tracks (August 17-20) are overlaid on the satellite SST corresponding to August 18 and 20, 2009 (Fig. 4.35). The images reveals that the first track started in an area of cooler water, which seems linked to the main filament. A low-temperature signal was visible in Fig. 4.19 in the southern part of the track. The third track came close to the filament but did not cross it.

Tracks 4-6 went across the cool waters of the filament, which had a broad surface signature at that time (≈ 50 km), as confirmed by temperature maps of Fig. 4.19. Between August 20 and 23 (Fig. 4.36), the filament weakened (offshore extension and breadth). Track 7, repeated at the same longitude as track 6, was also performed in the filament.

The last track (September 3, 2009) did not provide any measurements close the surface. The SST image (Fig. 4.37) indicates that the filament was centered at a latitude around 30°30'N, in the middle of the track. The filament core was narrower in comparison with other days (e.g., August 20, 2009, Fig. 4.35), probably because of a period of wind relaxation during the previous days, as shown by the wind intensity maps (Fig. 4.38).

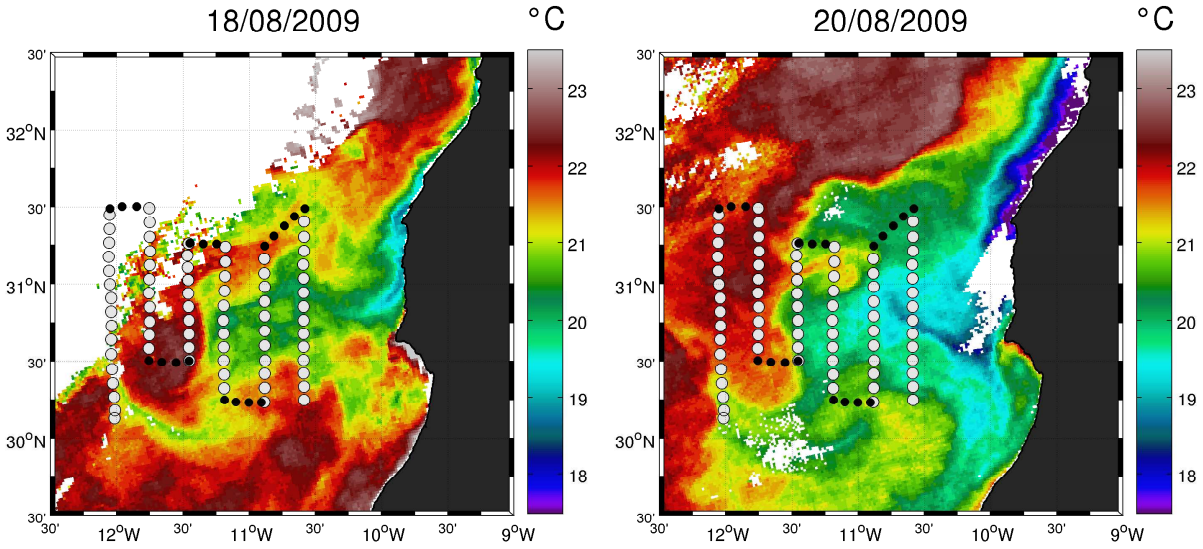

Figure 4.35: SST on August 18 and 23, 2009 and SeaSoar tracks no. 1-6 (white dots).

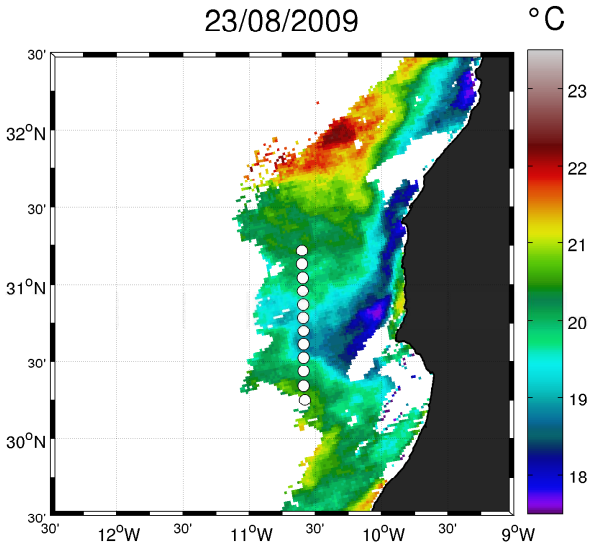

Figure 4.36: SST on August 23, 2009 and SeaSoar track no. 7.

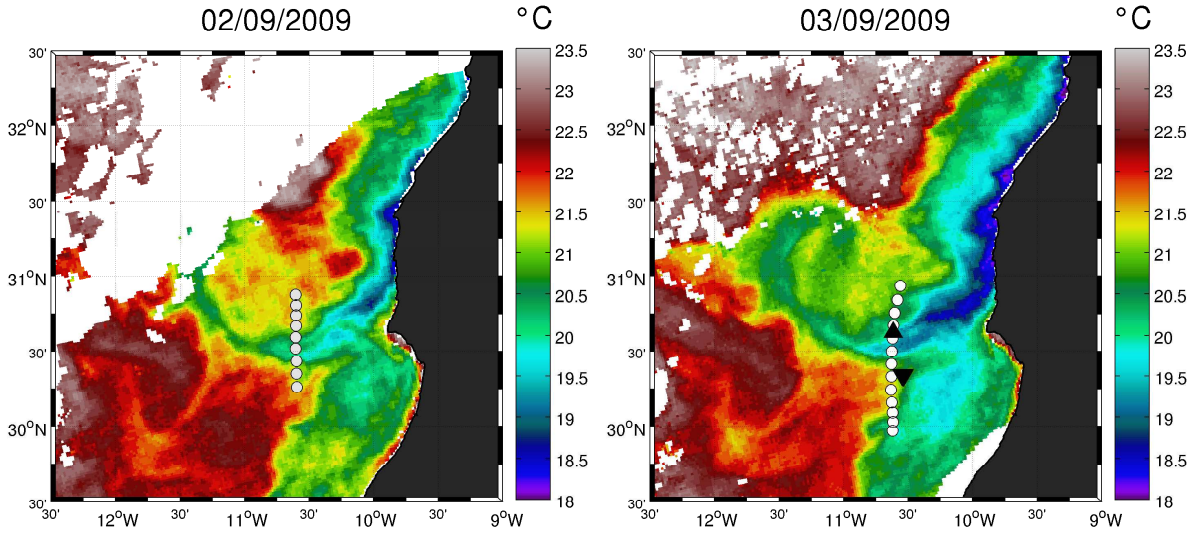

Figure 4.37: SST on September 2 and 3, 2009, with SeaSoar tracks 8 (left) and 9 (right). Release positions of the 10 m drifters and 300 m drifter are indicated by the ▼ and ▲, respectively.

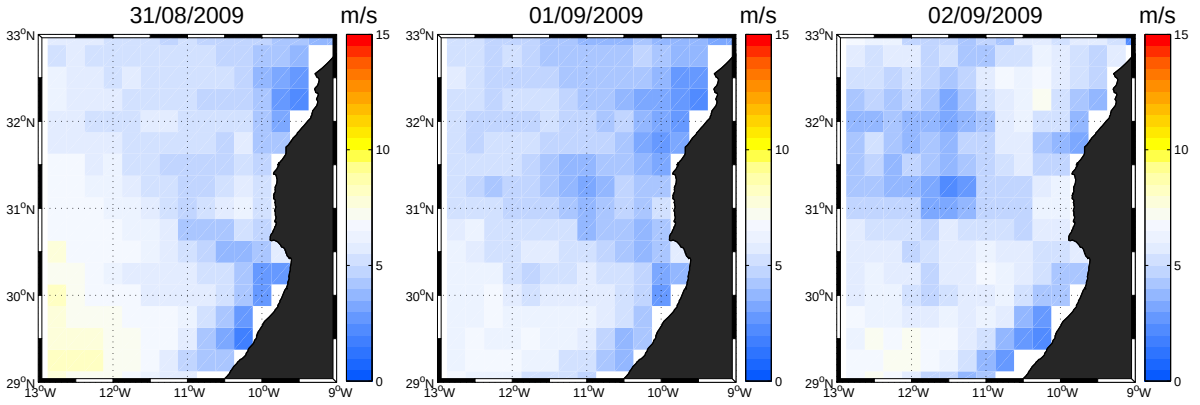

Figure 4.38: Wind intensity derived from QuikSCAT measurements from August 31 to September 2, 2009.

CTD meridional transect

We performed the meridional track between August 25 and 27, 2009 (Section 4.1.1). During that time span, the filament was well developed (Fig. 4.39) and the wind was intense, especially near the coast north to Cape Ghir (Fig. 4.40). The SST map confirms the position of the filament core, between stations T8 and T9 (Figs. 4.22 and 4.23). Our measurements exhibit lower temperature than the AVHRR data. This is explained by the fact that the first CTD measurements are obtained a few meters below the surface, while the SST can suffer from *skin temperature* effects due to diurnal heating. The position of the subsurface anticylonic eddy, centered on station T6 (Fig. 4.23), seems to correspond to the northern flank of the filament.

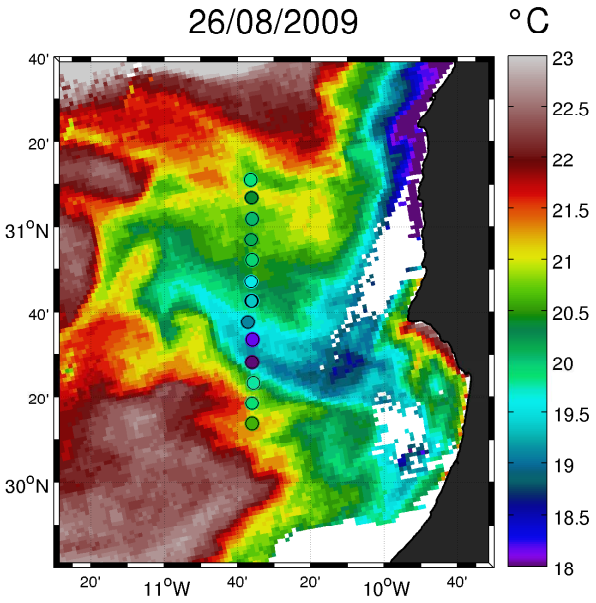

Figure 4.39: SST and near-surface temperature measured during the CTD meridional transect on August 26, 2009.

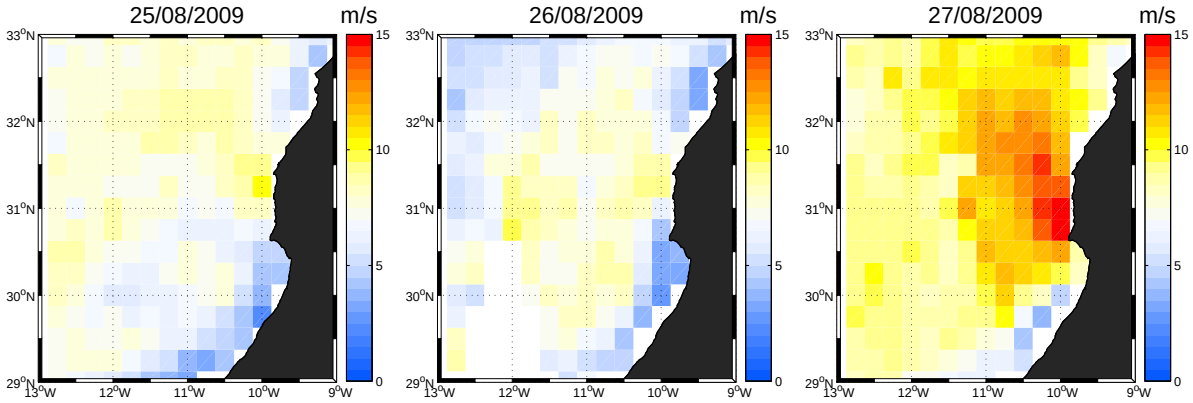

Figure 4.40: Wind intensity derived from QuikSCAT measurements from August 25 to 27, 2009.

4.5 Conclusions

A set of data acquired during the CAIBEX cruise have been processed and analysed. Three types of measurements have been used: CTD casts, SeaSoar tracks, and drifter trajectories. Vertical analyzes (Section 4.2.4) have been performed on the nine SeaSoar tracks and on the CTD transects, while horizontal analysis (Section 4.2.3) have been performed on the combined data set. From the interpolated maps, we were able to detect the filament signal, characterized by strong horizontal gradients in the surface layers. On average, the filament core was found at 30.8°N, slightly to the south of Cape Ghir.

North of the filament, the signal of a subsurface anticyclonic eddy was found. It was visible in the vertical sections as a downward dooming of the isotherms and isohalines, particularly in the SeaSoar tracks no. 6 and 7 (Fig. 4.19) and in the CTD transect (Fig. 4.23(e)). The horizontal sections between 200 and 400 m (Fig. 4.17) indicated an area of warmer water close to the coast, attributed to the downward velocity generated by the anticyclonic eddy.

The model results were examined at depths where the eddy is assumed to occur. At 300 m, a similar area of warmer water is observed above 31°N and an anticyclonic eddy around 100 km offshore, with vorticity close to $-0.25\ f$. The vertical sections obtained from the model (Figs. 4.33 and 4.34) confirmed the dooming of the isotherms observed with the in situ measurements.

Considering the relative positions of the filament and the anticyclonic eddy, we think that both structures are related (as suggested by Peliz *et al.* (2002)), though the coincidence may be simply due to the presence of topographic features responsible for the filament near surface and for the eddy between 200 and 400 m. Similar studies on other filaments in the same upwelling system (e.g., Cape Blanc, Cape Juby) or in other regions of the world ocean would help to state if the subsurface anticyclonic eddy is specific to Cape Ghir, or is a general feature associated with upwelling filaments.

Acknowledgments

We are grateful to the captain and the crew of the *Sarmiento the Gamboa* and the Spanish Ministry of Education and Science for funding the CAIBEX project (CTM2006-02293). Beatriz Barreiro González (IIM-CSIC, Spain) processed the ADCP data.

References

Barth, J. A., Pierce, S. D. & Smith, R. L. (2000). A separating coastal upwelling jet at Cape Blanco, Oregon and its connection to the California Current system. *Deep-Sea Research II*, **47**: 783–810. doi:10.1016/S0967-0645(99)00127-7.

Boyer, T. P., Antonov, J. I., Baranova, O. K., Garcia, H. E., Johnson, D. R., Locarnini, R. A., Mishonov, A. V., O'Brien, T. D., Seidov, D., Smolyar, I. V. & Zweng, M. M. (2009). World Ocean Database 2009, Chapter 1: Introduction. Tech. rep., National Oceanographic Data Center, Ocean Climate Laboratory, Washington, D.C. 216 pp.
URL ftp://ftp.nodc.noaa.gov/pub/WOD09/DOC/wod09_intro.pdf

Falkowski, P. & Kiefer, D. A. (1985). Chlorophyll a fluorescence in phytoplankton: relationship to photosynthesis and biomass. *Journal of Plankton Research*, **7(5)**: 715–731. doi:10.1093/plankt/7.5.715.
URL http://plankt.oxfordjournals.org/content/7/5/715.abstract

Flament, P. (2002). A state variable for characterizing water masses and their diffusive stability: spiciness. *Progress in Oceanography*, **54**: 493–501. doi:10.1016/S0079-6611(02)00065-4.

Hagen, E. (2001). Northwest African upwelling scenario. *Oceanologica Acta*, **24**: 1–17. doi:10.1016/S0399-1784(00)01110-5.

Hagen, E., Zülicke, C. & Feistal, R. (1996). Near surface structures in the Cape Ghir filament off Morocco. *Oceanologica Acta*, **19(6)**: 577–598.

Harris, G. P. (1980). The relationship between chlorophyll *a* fluorescence, diffuse attenuation changes and photosynthesis in natural phytoplankton populations. *Journal of Plankton Research*, **2(2)**: 109–127. doi:10.1093/plankt/2.2.109.

Haynes, R. & Barton, E. D. (1990). A poleward flow along the Atlantic coast of the Iberian Peninsula. *Journal of Geophysical Research*, **95**: 11425–11442. doi:10.1029/JC095iC07p11425.

Head, E. J. H., Harrison, W. G., Irwin, B. I., Horne, E. P. W. & Li, W. K. W. (1996). Plankton dynamics and carbon flux in an area of upwelling off the coast of Morocco. *Deep-Sea Research I*, **43(11-12)**: 1713–1738. doi:10.1016/S0967-0637(96)00080-5.
URL http://www.sciencedirect.com/science/article/B6VGB-3VWNK3M-9/2/5d86723cc8986a91d60ed856bd29ff5f

Hummon, J. M. & Firing, E. (2003). A direct comparison of two RDI shipboard ADCPs: A 75-khz Ocean surveyor and a 150-khz narrow band. *Journal of Oceanic and Atmospheric Technology*, **20**: 872–888. doi:10.1175/1520-0426(2003)020<0872:ADCOTR>2.0.CO;2.

Huyer, A., Barth, J. A., Kosro, P. M., Shearman, R. K. & Smith, R. L. (1998). Upper-ocean water mass characteristics of the California Current, summer 1993. *Deep-Sea Research II*, **45**: 1411–1442. doi:10.1016/S0967-0645(98)80002-7.

Kautsky, H., Appel, W. & Amann, H. (1960). Chlorophyllfluorescenz und Kohlensaureassimilation. XIII. Die Fluorescenzkurve und die Photochemie der Pflanze. *Biochemische Zeitschrift*, **322**: 277–292.

Maxwell, K. & Johnson, G. N. (2000). Chlorophyll fluorescence–a practical guide. *Journal of Experimental Botany*, **51(345)**: 659–668. doi:10.1093/jexbot/51.345.659.
URL http://jxb.oxfordjournals.org/content/51/345/659.abstract

Molemaker, M. J., McWilliams, J. C. & Dewar, W. K. (2010). Submesoscale generation of mesoscale anticyclones in the California undercurrent. In *AGU Ocean Science meeting*. Portland (OR), U.S.A.

Pelegrí, J. L., Marrero-Díaz, A., Ratsimandresy, A., Antoranz, A., Cisneros-Aguirre, J., Gordo, C., Grisolía, D., Hernández-Guerra, A., Laíz, I., Martínez, A., Parrilla, G., Pérez-Rodríguez, P., Rodríguez-Santana, A. & Sangrà, P. (2005). Hydrographic cruises off northwest Africa: the Canary current and the Cape Ghir region. *Journal of Marine Systems*, **54(1-4)**: 39–63. doi:10.1016/j.jmarsys.2004.07.001.
URL http://www.sciencedirect.com/science/article/pii/S0924796304002064

Peliz, A., Rosa, T. L., Santos, A. M. P. & Pissarra, J. L. (2002). Fronts, jets, and counter-flows in the Western Iberian upwelling system. *Journal of Marine Systems*, **35**: 61–77. doi:10.1016/S0924-7963(02)00076-3.

Sangrà, P., Pascual, A., Rodríguez-Santana, A., Machín, F., Mason, E., McWilliams, J. C., Pelegrí, J. L., Dong, C., Rubio, A., Arístegui, J., Marrero-Díaz, A., Hernández-Guerra, A., Martínez-Marrero, A. & Auladell, M. (2009). The Canary Eddy Corridor: A major pathway for long-lived eddies in the subtropical North Atlantic. *Deep-Sea Research*, **56(12)**: 2100–2114. doi:10.1016/j.dsr.2009.08.008.
URL http://www.sciencedirect.com/science/article/pii/S0967063709001733

Tett, P., Arístegui, J., Barton, D., Basterretxea, G., Armas, J. D. D., Escánez, J. E., Hernández-León, S., Lorenzo, L. M. & Montero, N. (2002). Steady-state DCM dynamics in Canaries waters. *Deep-Sea Research II*, **49(17)**: 3543–3559. doi:10.1016/S0967-0645(02)00097-8.

Tomczak, M. (1999). Some historical, theoretical and applied aspects of quantitative water mass analysis. *Journal of Marine Research*, **57(2)**: 275–303. doi:10.1357/002224099321618227.

Chapter 5

Time evolution of the Canary Current upwelling system

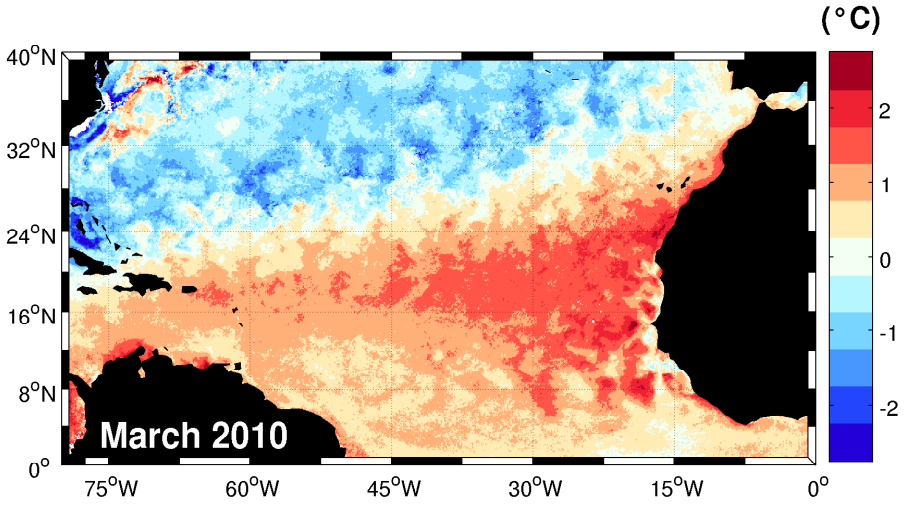

SST anomalies in March 2010.

After the analysis of the climatological situation in the northeast Atlantic (Chapter 2), the examination of the mechanism responsible if the filament with a numerical model (Chapter 3) and the presentation of in situ data collected during the CAIBEX cruise (Chapter 4), we study the time evolution of temperature in the domain of interest. As stated in the introduction, upwelling systems play an important role in the fishing industry, therefore the changes occurring in these specific area have to be analyzed with care.

During the first months of 2010, the tropical and subtropical North Atlantic displayed anomalously high temperatures, with values seldom observed during the last decades. In situ and remote sensing data are used to evaluate horizontal, vertical and temporal extensions of the anomalies. The repercussions on the seasonal evolution of the mixed layer are examined; in particular, we show that the northwest Africa coastal upwelling is significantly weakened in comparison to previous years. The consequences on the biological variables are examined by means of satellite-derived measurements. A simple mechanism related to changes in wind intensity is proposed in order to explain our observations.

Contents

Some of the results presented in this chapter are the subject of the article:

C. Troupin and F. Machín, Evidences of wind-induced temperature anomalies in the tropical and subtropical North Atlantic in winter-spring 2010, *in preparation.*

5.1 Introduction

In the subtropical northeast Atlantic Ocean, the seasonal cycle of physical properties is mainly driven by air-sea interactions, namely wind stress and net heat flux. In winter the net heat flux reaches negative values (i.e., transfer from ocean to atmosphere), responsible for the deepening of the thermocline. A late winter phytoplankton bloom is associated to this physical process (Yoder *et al.*, 1993, and references therein). In summer, trade winds intensify due to the northward motion of the Azores high (Wooster *et al.*, 1976), while the net heat flux reaches its maximum. The result of these two counteracting processes is a strong stratification of the ocean surface layers. A shallow mixed layer prevents the injection of nutrients from deeper waters (see for example Fig. 1.19).

Recent observations depict significant changes of the described seasonal cycle during the first months of 2010. As an illustration, we represented the SST field in January 2009 and 2010 (Fig. 5.1). The inspection of the shape of different isotherms reveals that the spatial structures are dissimilar, especially east of 45°W. The SST in the Cape Ghir area also exhibits large differences between 2009 and 2010.

It is of primary importance to examine these changes, because of the coupling between biological and physical cycles (Arístegui *et al.*, 2001; Troupin *et al.*, 2010) and the influence of SST on the hurricane activity in the Atlantic Ocean (e.g., Goldenberg *et al.*, 2001). Moreover, as we related the filaments to the coastal upwelling, it is relevant to assess the variations of the upwelling intensity.

5.2 Data and methods

5.2.1 Sources

The region of study is limited by the region 0°W-80°W, 0°N-40°N. All the data come from free-access data bases (Tab. 5.1).

1. Remote-sensing data: level 3 monthly SST, chlorophyll *a* concentration, particulate organic carbon (POC) and particulate inorganic carbon (PIC) are extracted from Moderate Resolution Imaging Spectroradiometer (MODIS, `http://modis.gsfc.nasa.gov/about/`) on NASA's Aqua and Terra satellites (`http://oceancolor.gsfc.nasa.gov/cgi/l3`). The available images have a pixel size of 4 km or 9 km. As the region of interest is relatively extended, the 9 km-resolution turns out to be sufficient.

2. In situ measurements: all the available data for the year 2010 are extracted from the World Ocean Database 2009 (WOA09, Boyer *et al.*, 2009), available at `http://www.nodc.noaa.gov/OC5/SELECT/dbsearch/dbsearch.html`. Since new data are progressively added to the database, it is advised to check for updates periodically. The last download made was on February 28, 2011. At that time, we obtained at total of 11723 casts, broken down as follows:

    - 121 CTD casts,

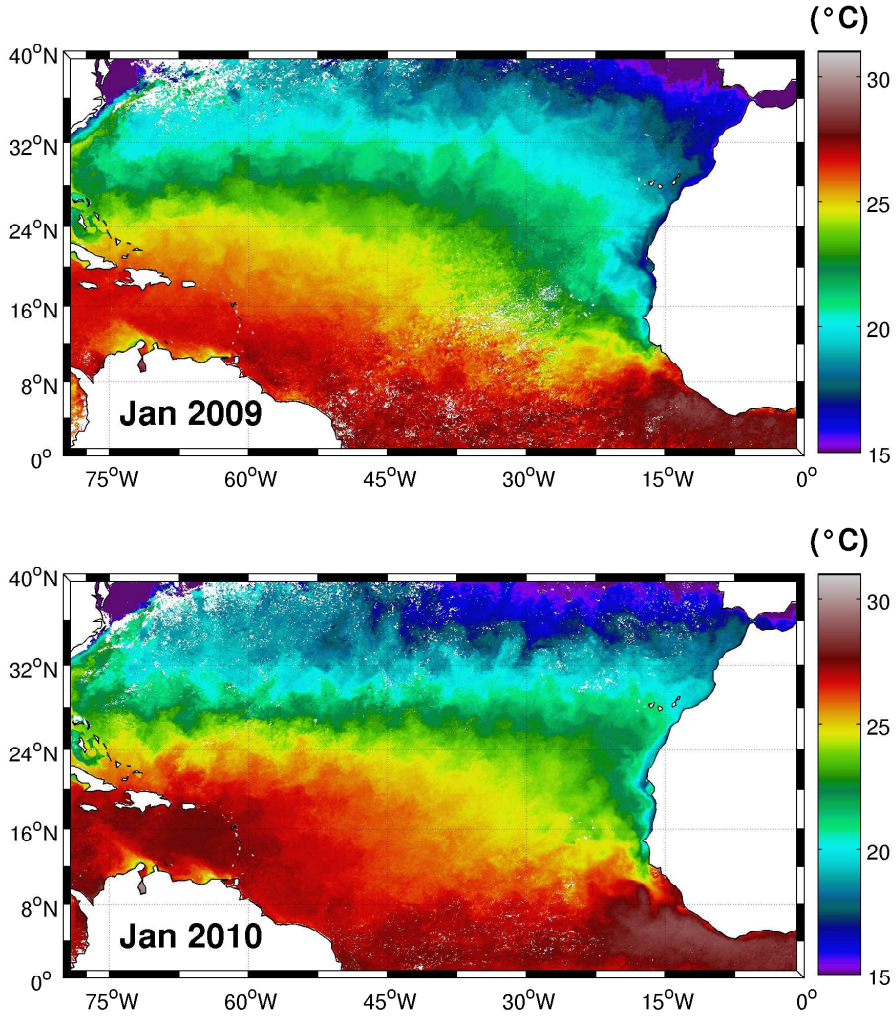

Figure 5.1: SST in January 2009 (left) and 2010 (right) from MODIS Aqua. Note the difference of aspect of the fields in the eastern part of the domain.

- 2665 expendable bathythermograh (XBT) casts,
- 5094 profiling floats (PFL) casts,
- 2419 moored buoys (MRB) casts,
- 1424 glider (GLD) casts.

Only the good-flagged data are retained, in order to guarantee their quality.

3. ARGO profilers: a set of profilers are selected in the U.S. Global Ocean Data Assimilation Experiment (GODAE, http://www.usgodae.org/) data catalog, according to their location and to their life time.

4. Hydrographic climatology: the World Ocean Atlas 2009 (WOA09, Locarnini *et al.*, 2010) temperature fields are extracted in the region of interest on the 33 depth levels, ranging from surface to 5500 m.

5. Atmospheric fields: zonal and meridional wind components at 10 m are obtained from the European Centre for Medium-Range Weather Forecasts (ECMWF) Interim Re-analysis Data Archive as monthly means of daily means (http://data-portal.ecmwf.int/data/d/interim_moda/).

6. North Atlantic Oscillation (NAO) station-based indices are obtained from the National Center for Atmospheric Research (NCAR) Climate and Global Dynamics (CDG) Climate Analysis Section (http://www.cgd.ucar.edu/cas/jhurrell/indices.html) for the winter season (defined here as the period from December to March).

7. Monthly fields of net primary production (NPP, see also Section 1.1.5 and Fig. 1.8) are obtained from the Ocean Productivity home page of the Oregon State University.

Table 5.1: Data used for the analysis.

Data type	Product	Provider & References
Remote sensing	MODIS-Aqua L3	NASA Ocean Color (Feldman & McClain, 2010)
SST climatology	OI SST	NOAA (Reynolds *et al.*, 2002; Smith *et al.*, 2008)
In situ profiles	WOD09	US NODC (Boyer *et al.*, 2009)
Profilers	ARGO	US GODAE
Climatology	WOA09 temperature	US NODC (Locarnini *et al.*, 2010)
	WOA09 salinity	US NODC (Antonov *et al.*, 2010)
Wind velocity	ERA-40 Re-analysis	ECMWF (Uppala *et al.*, 2005)
	Interim Re-analysis	ECMWF (Simmons *et al.*, 2006; Uppala *et al.*, 2008)
Heat fluxes	Daily Re-analysis	NCEP/NCAR (Kalnay *et al.*, 1996)
NAO index	Station-based index	NCAR CDG's Climate Analysis Section (Hurrel, 1995)
Net primary production	VGPM NPP	Oregon State Ocean Productivity (Behrenfeld & Falkowski, 1997)

5.2.2 Processing

The processing essentially consists of averaging, anomaly calculation and spatial interpolations. We considered level 3 products, that is to say, geophysical parameters that have been specially and/or temporally re-sampled (http://podaac.jpl.nasa.gov/Glossary).

Anomalies of SST, chlorophyll *a*, POC, PIC and NPP are computed for each month and season of 2009 and 2010, by subtracting the climatological mean computed using data from 2002 to 2008. Wind speed anomalies are computed with respect to the 1989-2008 monthly averages.

A time series of monthly mean values of SST is obtained by averaging the NOAA OI SST over the area of interest (Fig. 5.3).

A quality control is applied to profiler data prior to their mapping (Fig. 5.5(a)). Mixed-layer depth is computed using the criterion of 0.2°C decrease with respect to the temperature at 10 m (Kara *et al.*, 2000).

Climatological values at the locations of the profiles are obtained by horizontal interpolation of the WOA09 gridded fields. In situ anomalies (Fig. 5.7) are calculated by interpolating the WOD vertical profiles onto standard isobaric levels using the weighted parabolic method (WPI, Reiniger & Ross, 1968) and subtracting the climatological value (WOA09) horizontally interpolated at the corresponding profile location.

Wind velocities (Fig. 5.13) are averaged over the area of study; a Butterworth low-pass filter is applied to the wind time-series to remove high-frequency variability.

5.3 Results

The temperature anomalies are presented in a progressive way: first the horizontal extension is examined by mean of satellite images; secondly, the temporal dimension is considered using a time series of spatially-averaged monthly fields; the vertical extension is studied with ARGO profilers and vertical profiles.

5.3.1 Spatial structure of the anomalies

Remote-sensing images provide high-resolution information on the ocean surface, with an almost daily global coverage. They constitute a first tool to examine the changes of the ocean physical and biological characteristics. SST anomalies with respect to the 2002-2008 period are derived using measurements from the MODIS sensor on the Aqua satellite. SST anomalies are shown for the months of 2010 in the north subtropical and tropical Atlantic Ocean (Fig. 5.2).

In November-December 2009, an area of anomalously warm water extends from America to Africa coasts, the anomalies being more homogeneous in December. In January-February, the transition between the two areas is sharp and takes place along a line joining

the Strait of Gibraltar (36°N) to the Caribbean islands (20°N). Positive anomalies are particularly high along the NW Africa coast, between 12°N and 32°N. This region coincides with the Canary Current upwelling system.

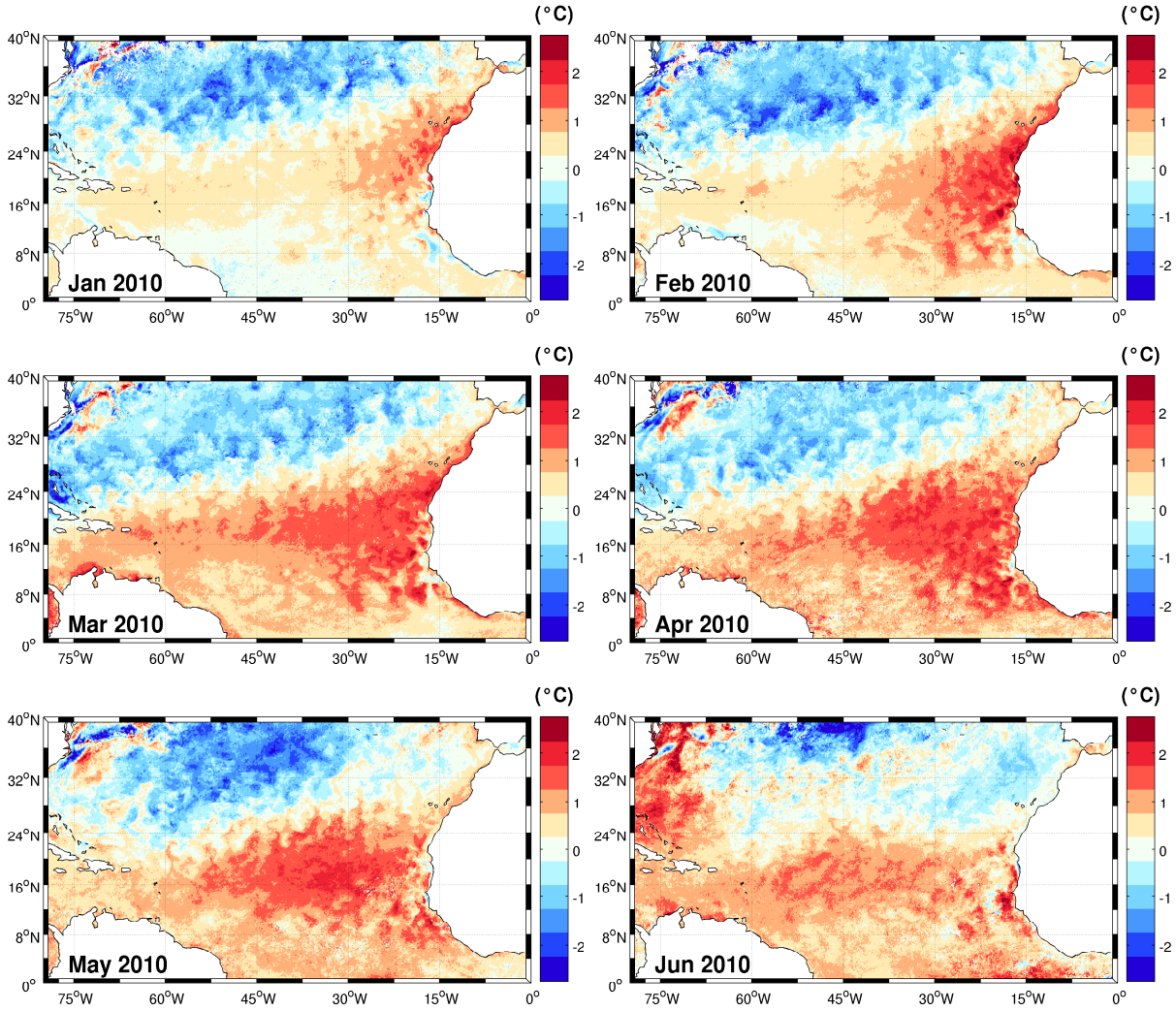

Figure 5.2: Monthly SST anomalies from January to June 2010. Maximal values take place off NW Africa.

5.3.2 Time series analysis

In order to assess the evolution of the anomalies over the past three decades, NOAA Optimum Interpolation SST analysis (Reynolds *et al.*, 2002) is considered. The domain-averaged values were computed for each month until December 2010 (Fig. 5.3). The climatological cycle in the studied region is as follows: the minimal temperatures are reached in February-March, when the mixed layer is the deepest, under the effect of convective mixing. The temperature starts to increase in spring, when the net heat flux becomes positive again. Maximal values are reached in August-September and correspond to the shallowest mixed layer (e.g., Troupin *et al.*, 2010).

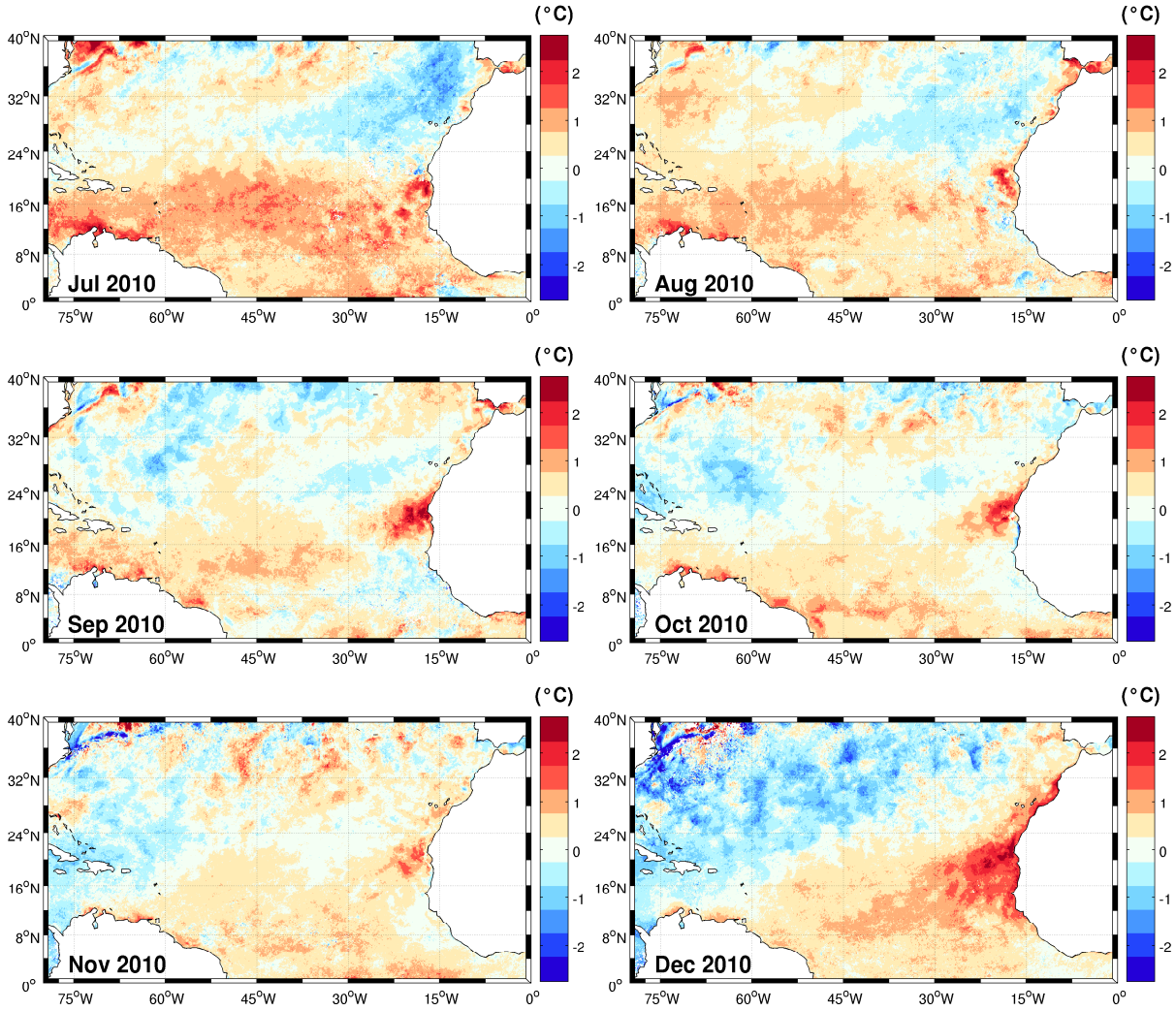

Figure 5.2: Continued: from July to December 2010.

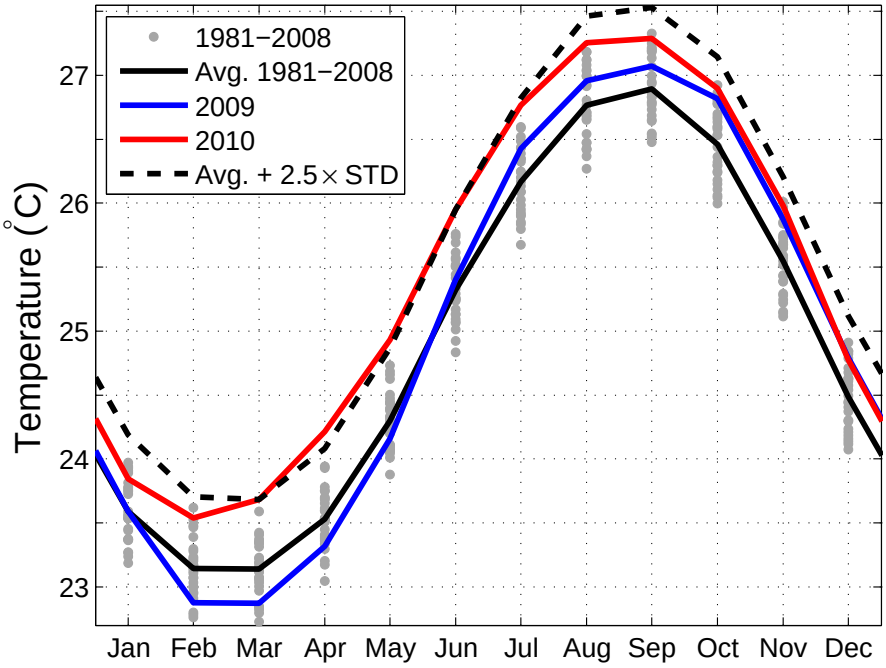

Figure 5.3: Annual cycle of SST computed in the control area. Gray dots show the individual monthly averages from 1981 to 2008, blue, red and black lines represent 2009, 2010 and 1981-2008 averaged cycles, respectively.

During the first half of 2009, surface temperatures were slightly below the long-term mean, with a difference not larger than 0.25°C. The changes started in June 2009, when temperatures became higher than the 1981-2008 average. In early 2010, the deviation with respect to the climatology further increased: the mean value for February 2010 (23.3°C) was only reached between April and May 2009. Furthermore, from March to August 2010, the monthly mean temperatures were higher than the values of any of the corresponding month during the 30 previous years. From March to May, the anomalies with respect to the 1981-2008 average exceed 2.5 standard deviations. From September to December, the situation seems to normalize, as the 2010 values are getting closer to those of 2009.

Vertical extension

After the inspection of the anomaly recurrence in time, we analyze their vertical extension. In situ profiles from the WOD09 (Boyer *et al.*, 2009) and profilers from the GODAE data catalog are considered. A set of three profilers located south of the Canary archipelago was selected. They were chosen because of their location and their long lifetime (Fig. 5.4). Their displacements are relatively short and principally zonal over the considered period. The seasonal cycle measured by profiler no. 4900825 (Fig. 5.5(a)) is similar to the description made previously: lowest temperatures appear in late winter under the effect of the thermocline erosion. During this period, the mixed layer frequently reaches depths well below 100 m. The computed MLD in 2010 displays a distinct behavior in 2010: the winter values remain close to summer time MLD, around 50 m, with the deepest values not below 75 m. Again, it is confirmed that winter 2010 surface temperatures are 2°C higher

than past years. The mean profile of density also leads to striking observations: in winter 2010 the density was lower than spring 2010 density by about 0.5 kg/m^3, whereas the climatological profile shows the opposite. It is of particular importance, as the biological productivity is essentially concentrated in winter. A similar seasonal cycle is observed with the other profilers (Fig. 5.5b-c).

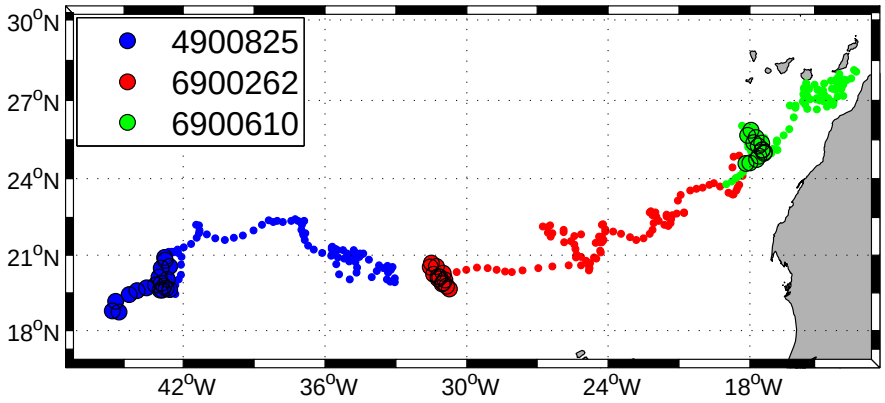

Figure 5.4: Trajectories of the three selected profilers. Large dots indicate position after January 1, 2010.

Profilers provide a good representation of the seasonal cycle of the mixed layer. It remains to confirm the vertical extension of the area affected by the anomalies. To this end, we computed anomalies of in situ profiles extracted from the WOD09 with respect to the WOA09 climatology. The winter 2010 anomalies at 75 m (Fig. 5.7) confirm the extension of the positive-anomaly area, in agreement with the structure determined with the help of satellite images (Fig. 5.2). Several points off NW Africa display anomalies up to 4°C with respect the climatology, in particular between Canary and Cabo Verde archipelagos.

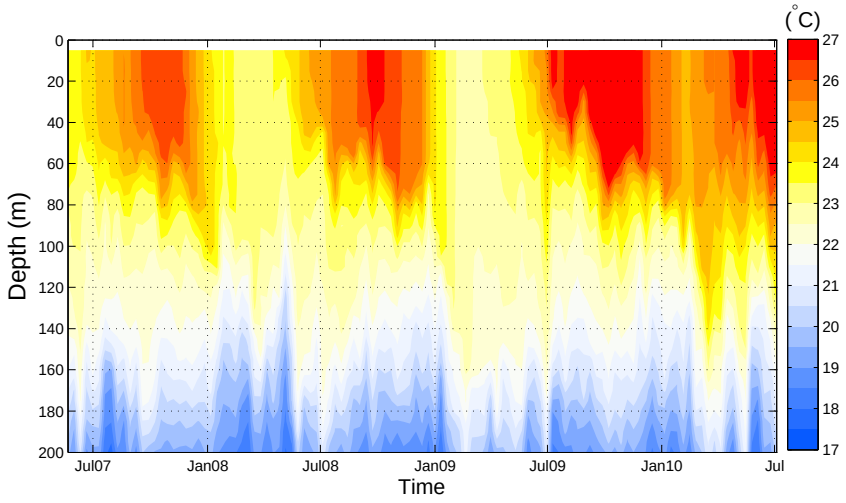

(a) 4900825

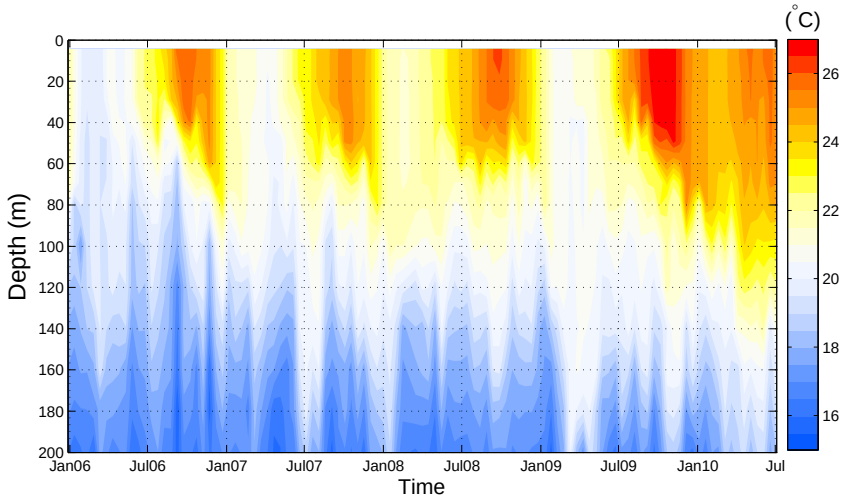

(b) 6900262

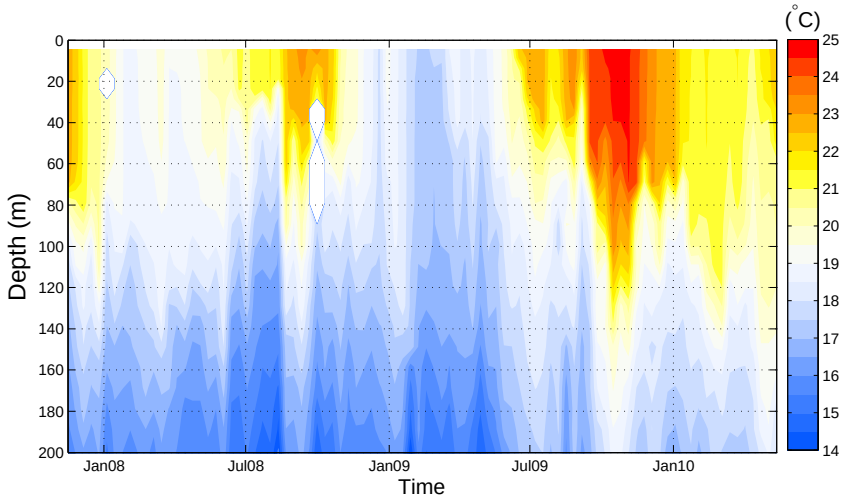

(c) 6900610

Figure 5.5: Evolution of temperature measured by profilers no. 4900825, 6900262 and 6900610.

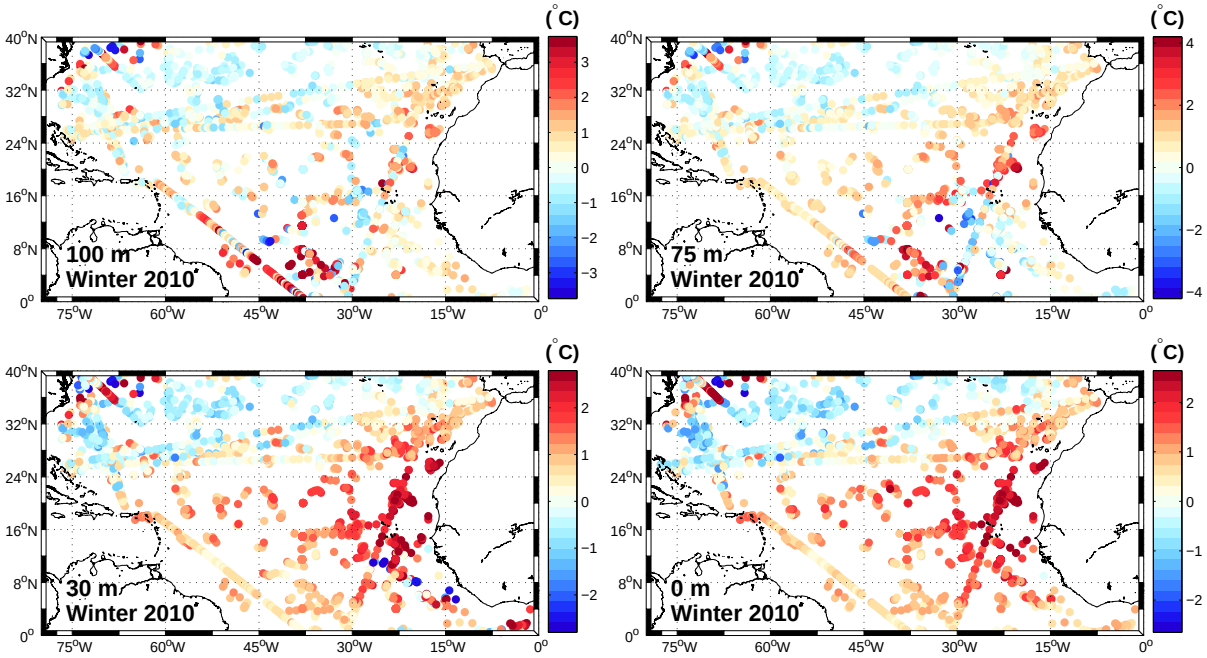

Figure 5.6: Temperature anomalies with respect to WOA09, obtained for the available in situ data in winter 2010 at 100, 75, 30 m and at surface.

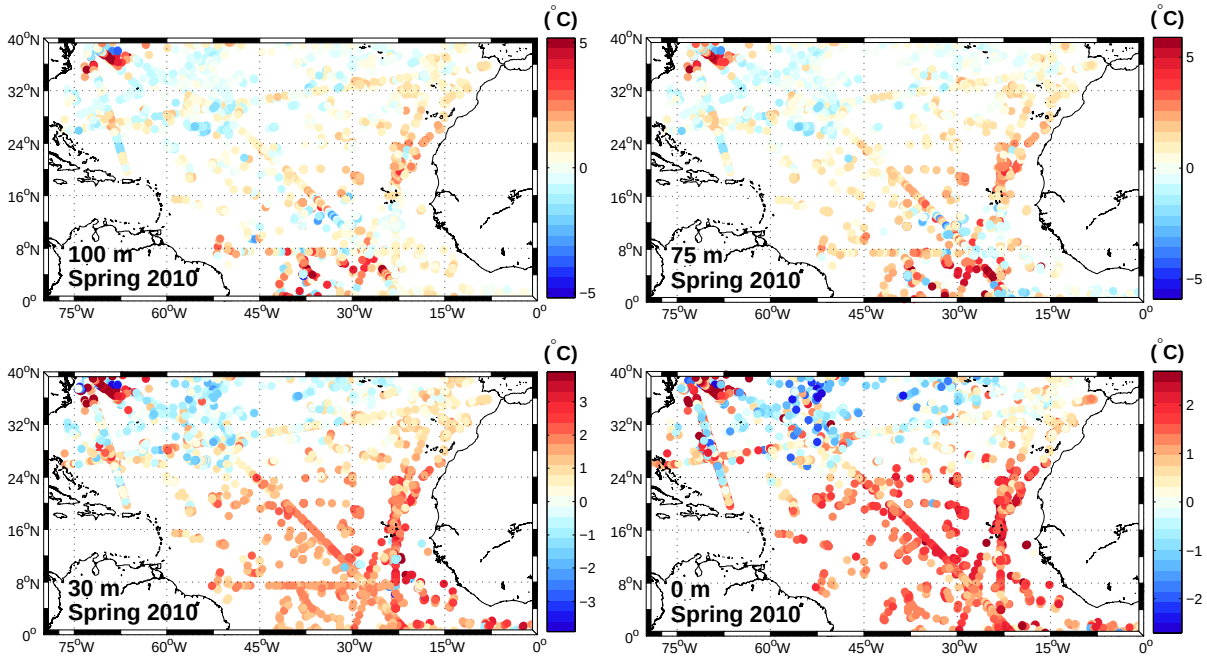

Figure 5.7: Temperature anomalies with respect to WOA09, obtained for the available in situ data in spring 2010 at 100, 75, 30 m and at surface.

5.3.3 Effects on the biological cycles

In the Canary Current upwelling system, the biological cycles are strongly influenced by the mixed-layer evolution (e.g., Troupin *et al.*, 2010). It is then relevant to examine satellite-derived chlorophyll *a* concentrations. Winter 2010 anomalies (Fig. 5.8) can be broken up into three subregions: the open ocean, where the anomalies are low, a narrow band of increased concentration around 32°N and a coastal area off NW Africa, with strongly negative anomalies. Comparison with the SST anomaly maps (Fig. 5.2) highlights a correspondence between the areas of positive (negative) temperature anomalies with negative (positive) chlorophyll *a* concentration anomalies. In particular, the upwelling area exhibits a substantial decrease of the chlorophyll *a* concentration, as a result of a weakened biological activity, especially between Cape Ghir (31°N) and south of Cape Roxo (12°N). Similar spatial distributions are obtained for POC (Fig. 5.9) and PIC (Fig. 5.10) measured by the MODIS sensor.

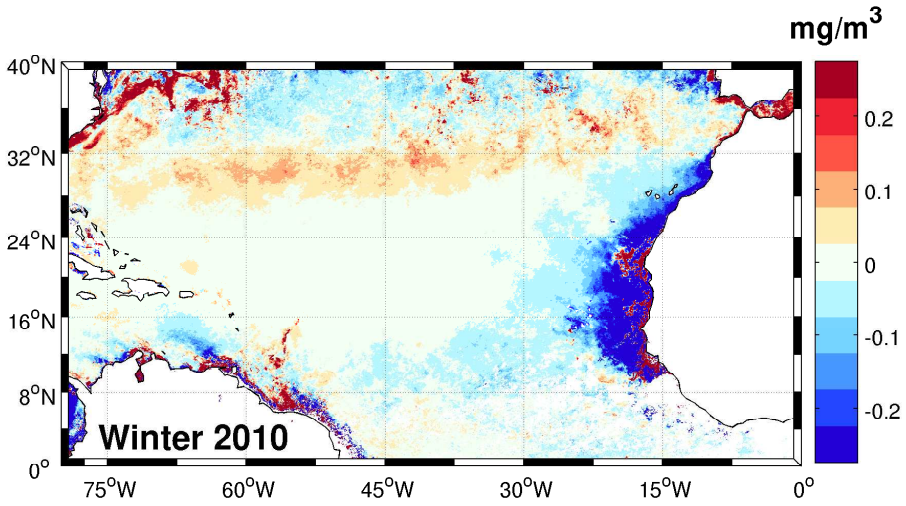

Figure 5.8: Chlorophyll a concentration anomalies for winter 2010. Blue area denotes zone of decreased concentration.

5.3.4 Effects on the productivity

The NPP anomalies for 2010 computed for the region of interest are presented in Fig. 5.11. In the open ocean, the anomalies are weak, since in this area, productivity is weak, whatever the conditions. Off northwestern Africa, a zone of negative anomalies extends up to several hundred kilometers from the coast. The order of magnitude of these anomalies is 10^3 mg C/m^2/day. It is particularly important in terms of fisheries: Chassot *et al.* (2010) showed that primary production constrains fisheries catches worldwide, at the scale of Large Marine Ecosystems, over both short and longer time scales. This means that a diminution of fish catches can be expected in the area. However, we are still lacking such data to study the possible changes in the fish catches.

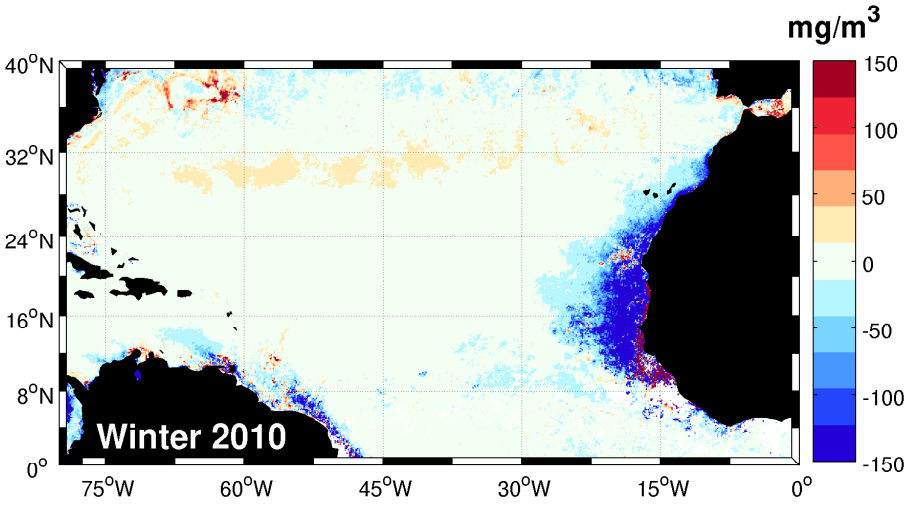

Figure 5.9: Anomalies of POC concentrations in winter 2010.

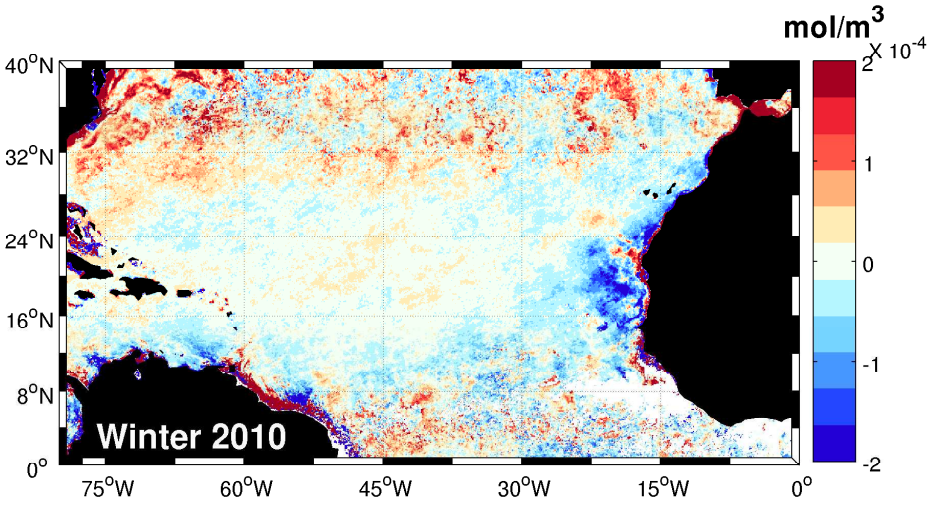

Figure 5.10: Anomalies of PIC concentrations in winter 2010.

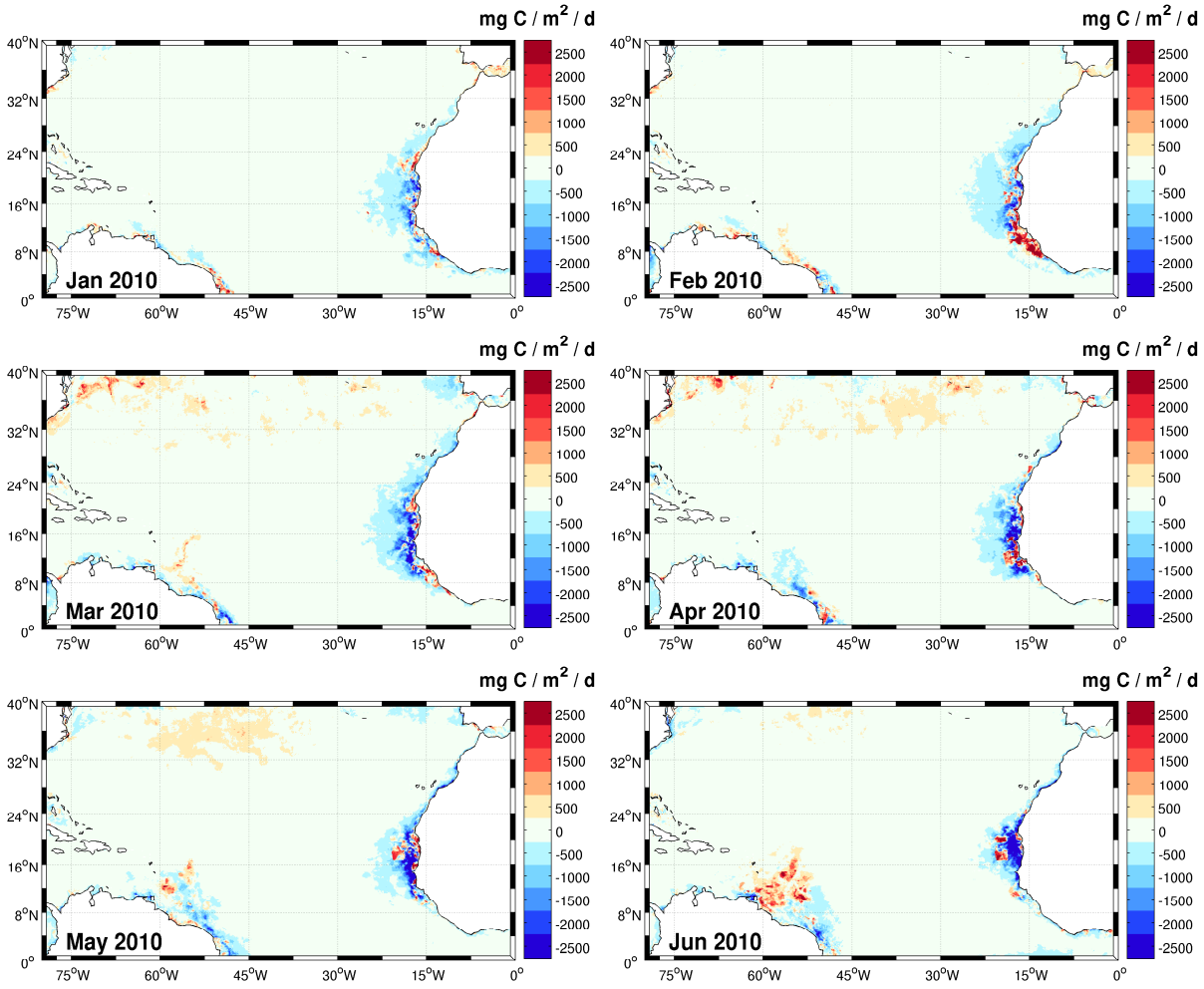

Figure 5.11: Monthly NPP anomalies from January to June 2010.

5.4 Mechanism

A mechanism that accounts for the observed changes is proposed hereafter. As coastal upwelling intensity depends on wind strength and orientation, wind intensity anomalies are computed in the studied area. The resulting isopleths are superimposed on the SST map (Fig. 5.12): the region of negative wind anomalies shows a remarkable similitude with the region of warmer temperatures. Another possible explanation might be a variation in the net heat flux penetrating the water column. To verify this hypothesis, we examined heat flux components over the last three decades. The results (not shown here) demonstrate that the net heat flux did not undergo significant variations in order to contribute to the temperature change described here.

However, the latent and sensible components of the net heat flux are dependent on the wind intensity (e.g., Charnock, 1967; Kondo, 1975; Yu *et al.*, 2004). Hence in the area of negative wind anomaly, these components have a reduced intensity and then the lost of heat by the ocean is decreased. This possible interaction between latent and sensible heat fluxes with SST was proposed by Cayan (1992). On the contrary, the long-wave heat flux is an increasing function of the ocean temperature. Thus in the region of positive SST anomalies, this component tends to increase the lost of heat by the ocean. All in all, the variations of the heat flux components roughly compensate one each other, and the interannual variations are relatively weak.

To sum up, the mechanism we propose is as follows: in a portion of the north Atlantic Ocean, the wind intensity decreases and provokes different consequences, according to the region:

1. Off northwest Africa, where it is climatologically equatorward, the wind is responsible for a weakening of the coastal upwelling, resulting in warmer than normal temperature, and lower than normal chlorophyll *a* concentrations.

2. In the open ocean, it causes a shallowing of the mixed layer. As a same heat flux is supplied to a smaller quantity of water (comprised between the surface and the mixed layer depth), the temperature increases. Yet, chlorophyll *a* concentration anomalies are not significant is this area, because the productivity is generally low, and the changes in the wind intensity themselves do not constitute a sufficient factor to stimulate the biological activity.

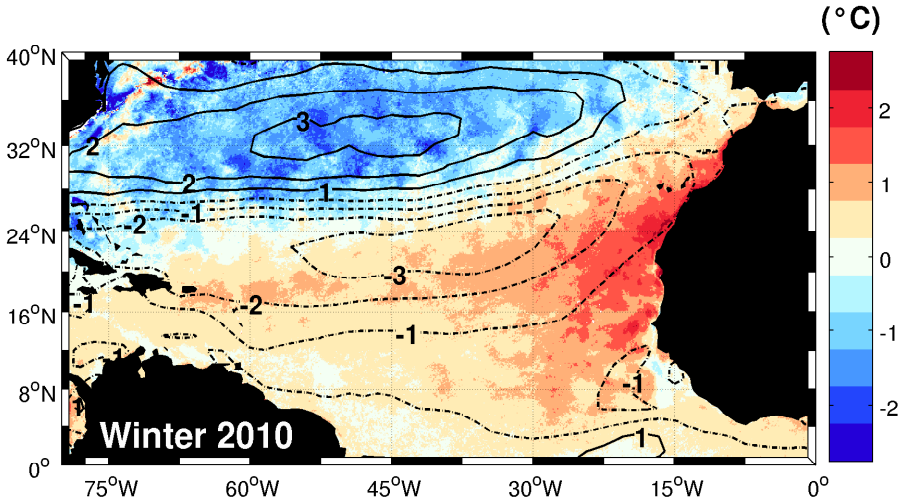

Figure 5.12: SST and wind speed anomalies (contour lines) for winter 2010. Plain (dashed) contours lines denote positive (negative) wind anomalies.

What is still to investigate is the origin of the wind intensity modification. Since the large-scale wind structure in the studied region is notably determined by the Azores high position, it is natural to look at the evolution of the NAO index. The index is based on the difference of normalized sea level pressure between Lisbon (Portugal) and Stykkishólmur/Reykjavik (Iceland).

NAO effects on the North Atlantic Ocean are numerous, both on physical (Wanner *et al.*, 2001; Marshall *et al.*, 2002; Hurrell & Deser, 2009) and ecological bases (Ottersen *et al.*, 2001). Wind and NAO indexes are plotted in Fig. 5.13. Their relationship has already been investigated (e.g., Hurrel, 1995; Marshall *et al.*, 2001), but the implication on the tropical SST is not perfectly understood.

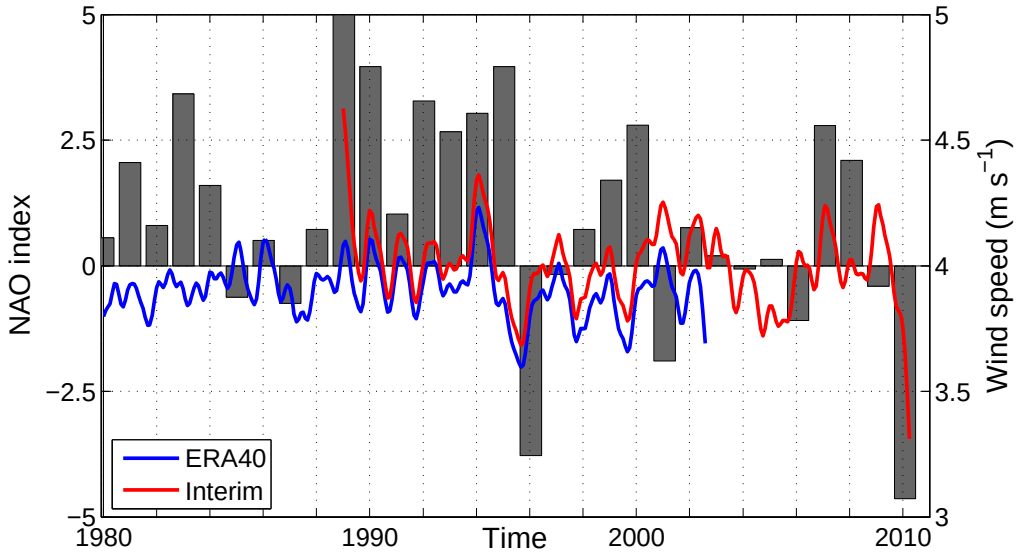

Figure 5.13: Evolution of seasonal NAO index and wind speed from ECMWF 40-year reanalysis and interim product, from 1980 to 2010.

Over the past three decades, the NAO index has been mostly positive. The most notable exceptions are 1996, 2001 and 2010. The negative NAO index phase means that Azores high and Icelandic low are weaker, resulting in a lower number of winter storms, with lower intensity, and more humidity is carried to southern Europe. A negative NAO index is not always correlated to a weakening of the winds, although it is the case for the negative episodes in 1989, 1996 and 2010. The results presented here are in agreement with Santos *et al.* (2005), who showed that warm (cold) mid-latitude SST anomalies were associated to low (high) NAO in the Canary Current system. However, their analysis is limited to a smaller region and restricted to the surface layer. The link between SST and NAO was also showed by Visbeck *et al.* (1998) with an ocean model and by Hurrell & Deser (2009). The latter also report a correspondence between MLD and NAO.

5.5 Conclusions

We analyzed in situ and remote sensing data in the tropical and subtropical North Atlantic in winter and spring 2010. An extended region of positive temperature anomalies develops in the southern part of the domain of interest and reaches its maximum extension in February. A set of profilers launched in the region showed the modifications of the water column properties near the surface: the development of a mixed layer that usually takes place in winter seems to be prevented in 2010. The analysis of in situ profiles confirms the information brought by the remote sensing measurements and permits the determination the vertical extension of the anomalies.

Wind seems to be the main factor for these anomalies: a wind intensity decrease causes a shallower mixed layer and a weaker upwelling in the coastal area of northwest Africa. The wind fields we analyzed are in agreement with this assumption.

Acknowledgments

NASA Ocean Color and US NODC are acknowledged for making the remote sensing and in situ data available, ECMWF for providing the atmospheric fields and J. Hurrel (NCAR) for NAO indices.

References

Antonov, J. I., Seidov, D., Boyer, T. P., Locarnini, R. A., Mishonov, A. V., Garcia, H. E., Baranova, O. K., Zweng, M. M. & Johnson, D. R. (2010). World Ocean Atlas 2009, Volume 2: Salinity. S. levitus, Ed. Tech. rep., NOAA Atlas NESDIS 69, U.S. Government Printing Office, Washington, D.C. 184 pp.

Arístegui, J., Hernández-León, S., Montero, M. F. & Gómez, M. (2001). The seasonal planktonic cycle in coastal waters of the Canary Islands. *Scientia Marina*, **65**: 51–58. doi:10.3989/scimar.2001.65s151.

Behrenfeld, M. J. & Falkowski, P. G. (1997). Photosynthetic rates derived from satellite-based chlorophyll concentration. *Limnology and Oceanography*, **42(1)**: 1–20. URL http://www.jstor.org/stable/2838857

Boyer, T. P., Antonov, J. I., Baranova, O. K., Garcia, H. E., Johnson, D. R., Locarnini, R. A., Mishonov, A. V., O'Brien, T. D., Seidov, D., Smolyar, I. V. & Zweng, M. M. (2009). World Ocean Database 2009, Chapter 1: Introduction. Tech. rep., National Oceanographic Data Center, Ocean Climate Laboratory, Washington, D.C. 216 pp. URL ftp://ftp.nodc.noaa.gov/pub/WOD09/DOC/wod09_intro.pdf

Cayan, D. R. (1992). Latent and sensible heat flux anomalies over the northern oceans: driving the sea surface temperature. *Journal of Physical Oceanography*, **22(8)**: 859–881. doi:10.1175/1520-0485(1992)022<0859:LASHFA>2.0.CO;2.

Charnock, H. (1967). Flux-gradient relations near the ground in unstable conditions. *Quarterly Journal of the Royal Meteorological Society*, **93(395)**: 97–100. doi:10.1002/qj.49709339508.

Chassot, E., Bonhommeau, S., Dulvy, N. K., Mélin, F., Watson, R., Gascuel, D. & Le Pape, O. (2010). Global marine primary production constrains fisheries catches. *Ecology Letters*, **13(4)**: 495–505. doi:10.1111/j.1461-0248.2010.01443.x.

Feldman, G. C. & McClain, C. R. (2010). Ocean Color Web, http://oceancolor.gsfc.nasa.gov/. NASA Goddard Space Flight Center, Eds. Kuring, N., Bailey, S. W., Franz, B. F., Meister, G., Werdell, P. J., Eplee, R. E., accessed October 4, 2010.

Goldenberg, S. B., Landsea, C. W., Mestas-Nunez, A. M. & Gray, W. M. (2001). The recent increase in Atlantic hurricane activity: Causes and implications. *Science*, **293(5529)**: 474–479. doi:10.1126/science.1060040. URL http://www.sciencemag.org/cgi/content/abstract/293/5529/474

Hurrel, J. W. (1995). Decadal trends in the North Atlantic Oscillation: Regional temperatures and precipitation. *Science*, **269(5224)**: 676–679. doi:10.1126/science.269.5224.676.

Hurrell, J. W. & Deser, C. (2009). North Atlantic climate variability: The role of the North Atlantic Oscillation. *Journal of Marine Systems*, **78(1)**: 28–41. doi:10.1016/j.jmarsys.2008.11.026. URL http://www.sciencedirect.com/science/article/B6VF5-4VNH3V7-M/2/0e9a811d09352ed34865a43c0d124fb1

Kalnay, E., Kanamitsu, M., Kistler, R., Collins, W., Deaven, D., Gandin, L., Iredell, M., Saha, S., White, G., Woollen, J., Zhu, Y., Leetmaa, A., Reynolds, R., Chelliah, M., Ebisuzaki, W., Higgins, W., Janowiak, J., Mo, K. C., Ropelewski, C., Wang, J., Jenne, R. & Joseph, D. (1996). The NCEP/NCAR 40-year reanalysis project. *Bulletin of the American Meteorological Society*, **77(3)**: 437–471. doi:10.1175/1520-0477(1996)077<0437:TNYRP>2.0.CO;2.
URL http://journals.ametsoc.org/doi/abs/10.1175/1520-0477%281996%29077%3C0437%3ATNYRP%3E2.0.CO%3B2

Kara, A. B., Rochford, P. A. & Hurlburt, H. E. (2000). An optimal definition for ocean mixed layer depth. *Journal of Geophysical Research*, **105**: 16803–16821. doi:10.1029/2000JC900072.

Kondo, J. (1975). Air-sea bulk transfer coefficients in diabatic conditions. *Boundary-Layer Meteorology*, **9**: 91–112. doi:10.1007/BF00232256.

Locarnini, R. A., Mishonov, A. V., Antonov, J. I., Boyer, T. P. & Garcia, H. E. (2010). World Ocean Atlas 2009, Volume 1: Temperature. S. levitus, Ed. Tech. rep., NOAA Atlas NESDIS 68, U.S. Government Printing Office, Washington, D.C. 184 pp.

Marshall, J., Johnson, H. & Goodman, J. (2001). A study of the interaction of the North Atlantic Oscillation with ocean circulation. *Journal of Climate*, **14(7)**: 1399–1421. doi:10.1175/1520-0442(2001)014<1399:ASOTIO>2.0.CO;2.
URL http://journals.ametsoc.org/doi/abs/10.1175/1520-0442%282001%29014%3C1399%3AASOTIO%3E2.0.CO%3B2

Marshall, J., Kushnir, Y., Battisti, D., Chang, P., Czaja, A., Dickson, R., Hurrell, J., McCartney, M., Saravanan, R. & Visbeck, M. (2002). North Atlantic climate variability: phenomena, impacts and mechanisms. *International Journal of Climatology*, **21(15)**: 1863–1898. doi:10.1002/joc.693.
URL http://www3.interscience.wiley.com/journal/89016692/abstract

Ottersen, G., Planque, B., Belgrano, A., Post, E., Reid, P. C. & Stenseth, N. C. (2001). Ecological effects of the North Atlantic Oscillation. *Oecologia*, **128**: 1–14. doi:10.1007/s004420100655.

Reiniger, R. & Ross, C. (1968). A method of interpolation with application to oceanographic data. *Deep-Sea Research*, **15**: 185–193. doi:10.1016/0011-7471(68)90040-5.

Reynolds, R. W., Rayner, N. A., Smith, T. M., Stokes, D. C. & Wang, W. (2002). An improved in situ and satellite SST analysis for climate. *Journal of Climate*, **15**: 1609–1625. doi:10.1175/1520-0442(2002)015<1609:AIISAS>2.0.CO;2.

Santos, A. M. P., Kazmin, A. S. & Peliz, A. (2005). Decadal changes in the Canary upwelling system as revealed by satellite observations: Their impact on productivity. *Journal of Marine Research*, **63(21)**: 359–379. doi:10.1357/0022240053693671.

Simmons, A., Uppala, S., Dee, D. & Kobayashi, S. (2006). ERA-Interim: New ECMWF reanalysis products from 1989 onwards. *ECMWF Newsletter*, **110**: 25–35.

Smith, T. M., Reynolds, R. W., Peterson, T. C. & Lawrimore, J. (2008). Improvements to NOAA's historical merged land-ocean surface temperature analysis (1880-2006). *Journal of Climate*, **21**: 2283–2296. doi:10.1175/2007JCLI2100.1.

Troupin, C., Sangrà, P. & Arístegui, J. (2010). Seasonal variability of the oceanic upper layer and its modulation of biological cycles in the Canary Island region. *Journal of Marine Systems*, **80(3-4)**: 172–183. doi:10.1016/j.jmarsys.2009.10.007.

Uppala, S., Dee, D., Kobayashi, S., Berrisford, P. & Simmons, A. (2008). Towards a climate data assimilation system: status update of ERA-Interim. *ECMWF Newsletter*, **115**: 12–18.

Uppala, S. M., Kallberg, P. W., Simmons, A. J., Andrae, U., da Costa Bechtold, V., Fiorino, M., Gibson, J. K., Haseler, J., Hernandez, A., Kelly, G. A. & et al. (2005). The ERA-40 re-analysis. *Quarterly Journal of the Royal Meteorological Society*, **131(612)**: 2961–3012. doi:10.1256/qj.04.176.

Visbeck, M., Cullen, H., Krahmann, G. & Naik, N. (1998). An ocean model's response to North Atlantic Oscillation-like wind forcing. *Geophysical Research Letters*, **25(24)**: 4521–4524. doi:10.1029/1998GL900162.

Wanner, H., Brönnimann, S., Casty, C., Gyalistras, D., Luterbacher, J., Schmutz, C., Stephenson, D. B. & Xoplaki, E. (2001). North Atlantic Oscillation - Concepts and studies. *Surveys in Geophysics*, **22**: 321–381. doi:10.1023/A:1014217317898.

Wooster, W. S., Bakun, A. & McLain, D. R. (1976). The seasonal upwelling cycle along the eastern boundary of the North Atlantic. *Journal of Marine Research*, **34**: 131–140.

Yoder, J. A., McClain, C. R., Feldman, G. C. & Esaias, W. E. (1993). Annual cycles of phytoplankton chlorophyll concentrations in the global ocean: A satellite view. *Global Biogeochemical Cycles*, **7(1)**: 181–194. doi:10.1029/93GB02358.

Yu, L., Weller, R. A. & Sun, B. (2004). Improving latent and sensible heat flux estimates for the Atlantic Ocean (1988-1999) by a synthesis approach. *Journal of Climate*, **17(2)**: 373–393. doi:10.1175/1520-0442(2004)017<0373:ILASHF>2.0.CO;2.
URL http://journals.ametsoc.org/doi/abs/10.1175/1520-0442%282004%29017%3C0373%3AILASHF%3E2.0.CO%3B2

General conclusions

Summary of the results and contributions

Specific conclusions have been presented at the end of each chapter. Here we summarize the main results and insist on the relationships existing between the chapters.

After the general introduction in Chap. 1, we worked on in situ data available in the northeast Atlantic ocean in Chap. 2. The objective was the creation of a high-resolution climatology for temperature and salinity. The benefit brought by the climatology was twofold:

1. It provided an hydrographic atlas of the Canary EBUS with a high spatial resolution and a good coverage of the coastal area.

2. Initial and boundary conditions could be extracted for a regional model implemented in the same area. The model solution was showed to be improved when the regional climatology was used instead of the widespread World Ocean Atlas 2005 (Mason, 2009).

Overall, the developments of this climatology acted as a test-case for the Diva method: the climatology was used directly to feed a numerical model, which was the perfect tool to spot the suspect values of the fields. The weak points of the methodology noted during the preparation of the climatology were taken in consideration and permitted the adaptation of the general procedure (e.g., vertical filtering of the analysis parameters).

Numerical simulations centered on Cape Ghir, with the ROMS model, were described in Chap. 3. Our goal was twofold:

1. To obtain a realistic representation (space and time scales, temperature, ...) of the Cape Ghir filament. Indeed, previous modeling exercises of the filament were not completely satisfying: in some cases, the filaments appeared at wrong positions (i.e., at locations were they were never observed though in situ or satellite observations), in other cases, they did not appear at all. Usually, the main issue was the lack of horizontal resolution, though high-resolution implementations of various models suffered from other issues, for example unrealistic filament size. Our belief is that, apart from the resolution itself, the two other essential ingredients were the accuracy of the atmospheric forcing and the choice of the open boundary conditions.

2. Study the mechanisms at the origin of the filaments at a specific place (north of Cape Ghir, close to the Cape Ghir plateau), by means of a set of experiments in which different parameters (planetary vorticity, wind, topography, ...) were modified. Behind these experiments, the idea was the following: the filament is generated to satisfy the conservation of potential vorticity: the equatorward upwelling jet takes place in a narrow band of uniform potential vorticity, while in the ocean interior, the potential vorticity is controlled by the planetary vorticity f. Near Cape Ghir, positive relative vorticity is injected to the upwelling jet, so that the vorticity balance is broken. The jet has to turn westward toward the ocean interior, where the potential vorticity is higher.

   The numerical results highlighted the role of the planetary vorticity, hence confirming the existing vorticity balance, and showed that the wind curl was the main source of relative vorticity.

In Chap. 4, the measurements made during the 3rd leg of the CAIBEX cruise, focused on the Cape Ghir filament, was analyzed. It is worth noting that the initial sampling strategy was based on the model results described in the previous chapter, although, obviously, changes had to be made to take into account the specific sea conditions that affected us. The preliminary analyzes mainly consisted of quality control and data griding. Using the software Diva described in Chap. 2, horizontal and vertical maps for temperature, salinity, chlorophyll and oxygen concentrations were generated. The signal of a subsurface anticyclonic eddy (200-400 m), located close to the coast, was discovered. Its origin is attributed to the interaction of the undercurrent with the topography. Model results (Chap. 3) were extracted at similar location and depth, and confirmed the presence of the subsurface eddy. We noticed that the eddy was always located below the convergence zone north of the filament, thus we think there is link between the filament and the subsurface eddy. The energy of the eddy seems too weak to be able to entrain the filament, but it may play the role of a trigger. The measurements of biological parameters underlined the role of the filament with its exportation of nutritive matter to the open ocean.

Chapter 5 addressed the time evolution of the Canary upwelling system. We gathered satellite images, in situ data and model reanalysis to examine the changes that underwent the system during the last decades. We discovered that the year 2010 was very atypical: the monthly-averaged SST were higher than any of the corresponding months during the 30 previous years in the tropical and subtropical north Atlantic ocean. The responsible factor seemed to be the wind intensity, which strongly decreased in 2010. Two distinct effects were observed: 1. in the coastal area, where winds are mainly equatorward (hence favorable to upwelling), the decrease of intensity results in a weaker upwelling, evidenced by warmer waters and lower concentration in chlorophyll, particulate organic and inorganic carbon. 2010 was also particular from the point of view of low-pressure systems, which were many during the year. Since they get their energy from the warm ocean ($T \geq 26.5$°C), is is natural to envisage a connection between the warm anomalies and the Atlantic storms.

General discussion

The study of physical processes such as upwelling filaments requires a multi-disciplinary approach: in situ and remote-sensing observations are necessary to detect and characterize the filaments; however, a pure observational approach is not sufficient: satellite images provides only an information on the surface, and are often contaminated by clouds or aerosol particles; in situ data are limited, due to the cost of oceanographic cruises and sometimes to the restriction to access historical data. The decision to construct a regional climatology, although it was not initially planned in this thesis, was a logical step to extract as much information as possible out of a limited amount of data.

Apart from providing us a numerical representation of the filaments, the model allowed us to perform experiments that would not be possible in reality: the modification of the wind conditions, the bathymetry, or the Earth's rotation. A careful selection of the model parameters, boundary and initial conditions, atmospheric forcing helped us to obtain results in agreement with the observations.

The oceanographic cruise was the perfect link between the two previous parts. The large amount of data collected brought us a different point of view on the subject, even if most of the data still need to be processed and exploited in order to provide a coherent view of the filament.

Initially, it was foreseen to analyze the time-evolution of the circulation in the region of interest by means of the numerical model: the forcing conditions would have to modified according to the predictions from the climatic models. However, we believe that this approach would not be fruitful when applied on relatively small numerical domains, like those we had in our simulations. A modification of the atmospheric fields (wind, heat fluxes, precipitations) would certainly have an influence on the basin-scale circulation, hence it would be more efficient to have a model covering the whole Atlantic at our disposal. This constitutes a considerable modeling effort. As this modeling approach was discarded, we turned to available data available among various data bases.

Overall, we think that the way to tackle the theme of upwelling filaments was original and provided an open view on the topic, with contributions in various fields of the oceanography.

Perspectives and future work

Data processing and climatology

Albeit the climatology presented in Chap. 2 showed improvements with respect to other products (global or regional) that covers the same area, the griding method can be modified in order to further enhance the quality of the interpolated fields. The possible modifications are detailed hereinafter. Another valuable option is the extension of the region covered by the climatology, either to the whole Atlantic, or to the World Ocean.

Advection constraint

In the Diva method, the correlation can be increased along specified directions by adding a term to the functional to be minimized (2.4):

$$\tilde{J}_a = \tilde{J}(\varphi) + \frac{\theta}{\mathcal{U}^2} \int_{\tilde{D}} \left[\mathbf{u} \cdot \tilde{\boldsymbol{\nabla}} \varphi \right]^2 d\tilde{D}, \tag{5.1}$$

where $\mathbf{u}$ is the equivalent of a velocity field of scale $\mathcal{U}$ and θ controls the relative weight of the second term called *advection constraint*. An example is the increase of correlation along streamlines or along isobaths. As we have seen previously (Chap. 3), we have at our disposal high-resolution velocity fields provided by the numerical model. Such fields could be used to provide information for the advection constraint.

Another possibility is the extraction of velocities from a drifter climatology (e.g., the 1° resolution climatology by Lumpkin & Garzoli, 2005). The advection constraint will certainly improve the reconstruction in the regions void of data, since the information can carried along streamlines from regions with data. The drawback is that it adds another set of parameters to determine (i.e., the relative importance of the advection term in the variational principle, Troupin *et al.*, 2011). Our opinion is that the constraint by a velocity field should be preferentially applied in the case of synoptic data, for instance data from a cruise, provided that a velocity field with appropriate spatial and temporal resolutions is available (either through drifters, altimetry, or numerical model).

Type of data

In Section 2.2.1, we explained that we had to restrict the choice of data to CTD and bottles, since other sensors suffer from various issues, such as errors in the depth measurements. A proposed solution is the *detrending*: each data point is assigned a class, according to the type of measurements (CTD, XBT, MBT, ...). Let us call C_{CTD}, $C_{\text{XBT}}, \ldots$ the classes containing the CTD, XBT, ... data points, respectively. The misfit term of the functional to be minimized in Diva is now written:

$$\sum_{i \in C_{CTD}} \mu_i \left[d_i - d_{C_{CTD}} - \varphi(x_i, y_i) \right]^2 + \sum_{i \in C_{XBT}} \mu_i \left[d_i - d_{C_{XBT}} - \varphi(x_i, y_i) \right]^2 + \ldots \tag{5.2}$$

where the $d_{C_{\mathrm{CTD}}}, d_{C_{\mathrm{XBT}}}, \ldots$ are new unknowns representing the trend in each class. If $\varphi(x, y)$ is assumed to be known, the minimization with respect to each of the trends d_{C_j} leads to

$$d_{C_j} = \frac{\sum_{i \in C_j} \mu_i \left[d_i - \varphi(x_i, y_i) \right]}{\sum_{i \in C_j}} \mu_i. \tag{5.3}$$

In practice $\varphi(x, y)$ in not known and an iterative method is necessary to determine the trends. The idea here is to use the detrending to take into account the type of measurements and possibly extract a trend for each class. The XBT are known to have a problem in the fall-rate equation (see http://www.nodc.noaa.gov/OC5/XBT_BIAS/bias_intro.html and references therein), hence we hope to be able to correct, at least partially, the errors due to the depth problem.

Multivariate approach

It is common to have less salinity than temperature measurements. The same applies to nutrients data (e.g., nitrate, phosphate, silicate) or chlorophyll concentration. Nevertheless, it is also common to have relations existing between the different variables. A concrete example was presented in the introduction, where the strong relationship between temperature and chlorophyll concentration was highlighted in the coastal area affected by upwelling.

For the Canary basin, a set of salinity-temperature relations were inferred from historical data sets (Marrero-Díaz *et al.*, 2001; Marrero-Díaz *et al.*, 2006). Such relations are particularly useful when working with XBT devices (which provide only temperature), but they are usually valid in a limited area and above a limited depth.

For a larger basin such as the North Atlantic, another solution to exploit the correlations between the variables is the multivariate approach: for a given analyze, two data files with different variables are considered. The two variables are normalized to guarantee they have similar variances.

Modeling aspects

From the modeling point of view, obvious steps for the amelioration of the solution is the increase of the spatial resolution and the extension of the numerical domain. This mainly depends on the computational resources available. If the resolution is sufficiently increased, it will be possible to simulate submesoscale features, such as the frontal instabilities that develop on the flanks of the filament.

Yet the increase of resolution is necessary only if it is justified by the objectives of the study. In the present case, the spatial resolution employed in the simulations was sufficient to allow the correct reproduction of the filament and to run the process-oriented experiments. An enlargement of the domain would certainly improve the representation of the large-scale circulation features (i.e., the main regional currents), but it is not believed to change qualitatively the results presented in Chap. 3.

Now if we concentrate on the physics, several meaningful experiments can be designed, such as an inter-annual simulation or runs with wind field from other databases. Measurements made in the California coastal zone showed that there is a wind drop-off starting at around 50 km from the coast. This is particularly relevant in our application: if the intensity of the equatorward wind decreases when approaching the coast, then its curl is positive. When working with climatological wind database, the spatial resolution ($\simeq$ 25 km) is not sufficient to resolve the wind drop-off, whereas it constitutes a source of positive relative vorticity to the flow. A bypass consist in artificially modifying the wind field, so that a realistic reduction of the intensity takes place in the few ten kilometers off the coast. The wind measurements made during the CAIBEX cruise should help us to determine the order of magnitude of the wind drop-off in the region of study.

The air-sea interactions in the Cape Ghir region also deserves a particular attention, for example:

1. During upwelling, it is frequent to encounter stratus clouds. These clouds may reduce the quantity of heat that reach the sea surface. The heat fields employed in our simulations were not fine enough to resolve this phenomenon.

2. The wind in the upwelling system is driven by the pressure gradient between the oceanic high (Azores high) and the continental thermal low. If the temperature of the ocean increased more than that of the continent, the contrast between the two will be lower and so is the wind. Weaker winds mean weaker upwelling and warmer coastal temperatures.

The use of an atmospheric model coupled to the ocean model is certainly the key to get an insight into these mechanisms. It is planned to implement the Weather Research and Forecasting model (WRF, Skamarock *et al.*, 2008) in a domain encompassing Cape Ghir, Madeira and the Canary Islands. In a first step, the atmospheric model outputs will be used only as forcing fields for the ocean model, the interest being to have a fine representation of the wind field. Then in a second step, the two models will be coupled to allow the study of the aforementioned interactions.

Another interesting direction to follow would be the simulation of a given filament event, namely the filaments observed during the CAIBEX cruise. The positive point is that in numerous situ measurements and satellite images are available for the duration of the cruise, thus providing a data set for validation.

Hydrographic cruises

The sampling strategy for the 3rd leg of CAIBEX was designed according to previous observations and to model results. It is obvious that scientists from distinct disciplines have different expectations regarding the nature of the measurements to be made. The sea conditions also have to be taken into account, as we had to notice during the three weeks of the cruise. Apart from these considerations, some improvements can certainly be made. If I had the opportunity to take part in a similar oceanographic cruise, here are the points I would take care of:

- Consultation and creation of archives containing the weather and wave forecasts on a daily basis.
- Acquisition of weather data at a coastal station, in order to make comparison with the measurements obtained through the ship instruments.
- Better consultation for the maximal depth of the CTD casts.
- Acquisition of hydrographic data closer to the coast.

Obviously, an operational model run over the region of interest, with assimilation of the measurements, would constitute a nice accomplishment.

From the point of view of instruments, the limit is set by the budget. The drifters dropped at the end of the cruise only provided the position, but no information about physical parameters. The SeaSoar proved to be a valuable tool for obtaining almost continuous measurements in the upper water column, though a careful calibration of the different sensors is a step that cannot be neglected.

Autonomous underwater vehicles such as *gliders*, also have to be mentioned. The advantages of gliders are the control of the horizontal position (contrarily to drifters), the possibility to operate under all weather conditions (contrarily to ships) and the cost (in comparison with the cost of a single ship-day). The autonomy of a glider can last several months, a sufficiently long period to study a short-time process such as filaments. The strong fronts and upwelling jets would require the use of fast-moving gliders. Since the drag is approximatively a quadratic function of the velocity, the autonomy of the gliders would be reduced.

High-frequency radar is a possible option for the monitoring of the filament, due to the particular velocity signature of the latter. Again, the cost can be prohibitive, but the radar would provide valuable data both for observation, model validation and possibly data assimilation in the future.

References

Lumpkin, R. & Garzoli, S. L. (2005). Near-surface circulation in the Tropical Atlantic Ocean. **52(3)**: 495–518. doi:10.1016/j.dsr.2004.09.001.

Marrero-Díaz, A., Pelegrí, J. L., Rodríguez-Santana, A. & Sangrà, P. (2001). Applicability of T-S algorithms to the Canary Islands region. **65**: 195–204. doi:10.3989/scimar.2001.65s1195.

Marrero-Díaz, A., Rodríguez-Santana, A., Machín, F. & Pelegrí, J. L. (2006). Analytic salinity-temperature relations for the upper-thermocline waters of the eastern North Atlantic subtropical gyre. **70**: 167–175. doi:10.3989/scimar.2006.70n2.

Mason, E. (2009). *High-resolution modelling of the Canary Basin oceanic circulation*. Ph.D. thesis, Universidad de Las Palmas de Gran Canaria. 275 pp.
URL http://acceda.ulpgc.es/bitstream/10553/5004/1/0620484_00000_0000.pdf

Skamarock, W. C., Klemp, J. B., Dudhia, J., Gill, D. O., Barker, D. M., Duda, M. G., Xiang-Yu, H., Wang, W. & Powers, J. G. (2008). A description of the Advanced Research WRF Version 3. Tech. rep., NCAR, Boulder, Colorado, USA.

Troupin, C., Sirjacobs, D., Rixen, M., Brasseur, P., Brankart, J.-M., Barth, A., Alvera-Azcárate, A., Capet, A., Ouberdous, M., Lenartz, F., Toussaint, M.-E. & Beckers, J.-M. (2011). Advanced Data Interpolating Variational Analysis. Application to climatological data. Submitted.

List of Figures

List of Tables

About this document

This document was prepared with the free software LaTeX (http://www.latex-project.org/) and the editor Texmaker (http://www.xm1math.net/texmaker/. The references were managed with BibTeX (http://www.bibtex.org/) with the help of the software JabRef (http://jabref.sourceforge.net/).

Most of the figures of this thesis are produced by the author. When it is not the case, the `url` is indicated in the figure caption. Photographs of Chapter 4 were taken during the CAIBEX cruise.